TOWARD A USER'S TOOLKIT FOR MODELING SCINTILLATOR PROPORTIONALITY AND LIGHT YIELD

BY

Qi Li

A Dissertation Submitted to the Graduate Faculty of

WAKE FOREST UNIVERSITY GRADUATE SCHOOL OF ARTS AND SCIENCES

in Partial Fulfillment of the Requirements

for the Degree of

DOCTOR OF PHILOSOPHY

Physics

May 2014

Winston-Salem, North Carolina

Approved By:

Richard T. Williams, Ph.D., Advisor

W. Frank Moore, Ph.D., Chair

N. A. W. Holzwarth, Ph.D.

Timo Thonhauser, Ph.D.

K. B. Ucer, Ph.D.

CONTENTS

LIST OF FIGURES vii
LIST OF TABLES xi
ABSTRACT xii

PART I

CHAPTER 1: INTRODUCTION 1
1. Topics and methods comprising my Ph.D. research 1
2. Scintillators for energy-resolved detection of radiation 6
3. The search for what controls scintillator proportionality, and efforts toward development of a predictive model based on material properties 11

PART II: SELECTION OF 6 PUBLISHED PAPERS ON MODELING AND ELECTRONIC STRUCTURE RELATED TO SCINTILLATOR PROPORTIONALITY

CHAPTER 2: THE ROLE OF HOLE MOBILITY IN SCINTILLATOR PROPORTIONALITY 24
1. Introduction 26
2. Modeling method 27
3. Results and discussion 29
4. Conclusions 33
CHAPTER 3: A TRANSPORT-BASED MODEL OF MATERIAL TRENDS IN NONPROPORTIONALITY OF SCINTILLATORS 39
1. Introduction 42
2. Modeling method 47
3. Material trends affecting nonproportionality 52
3.1 Nonlinear dipole-dipole and Auger quenching dependent on min (μ_h,μ_e) 52
3.2 Branching between excitons and independent carriers as a function of μ_h/μ_e .. 58

3.3 Variation of carrier independence along the track when $\mu_h/\mu_e << 1$, leading to the "hump" for halides …… 64
3.4 Trend produced by anisotropy of mobility ……..…… 69
3.5 Simulated local light yield versus excitation density for some model scintillators …… 74
3.6 Effective diffusion coefficient modeled on mixed excitons and free carriers in the track …….. 77
4. Summary and Conclusions …… 84
CHAPTER 4: EXCITATION DENSITY, DIFFUSION-DRIFT, AND PROPORTIONALITY IN SCINTILLATORS ……..…… 92
1. Introduction …… 94
2. Measurement of quenching kinetics at high excitation density ……. 95
2.1 Background and method …… 95
2.2 Intensity-dependent absorption coefficients …… 97
2.3 Experimental results and discussion …….. 100
3. Modeling the competition between fast carrier diffusion and dipole-dipole quenching in CsI and CsI: Tl ……..….. 114
3.1 Modeling method …….. 116
3.2 Values of the material parameters ……. 119
3.3 Modeling results and discussion ……. 120
CHAPTER 5: ELECTRON ENERGY RESPONSE OF SCINTILLATORS CALCULATED FROM CARRIER MOBILITIES AND MEASURED 1st THROUGH 3rd ORDER QUENCHING ……... 129
CHAPTER 6: FIRST PRINCIPLES CALCULATIONS AND EXPERIMENT PREDICTIONS FOR IODINE VACANCY CENTERS IN SrI_2 …….. 141
1. Introduction ……... 143
2. Material parameters and calculation methods ……..… 147
2.1 Crystal structure and experimental parameters ……..…….. 147
2.2 Computational methods ……...…….. 147
2.3 Finite supercell size corrections ……..……...…. 148
2.4 Chemical potentials, formation energies and thermodynamic transitions …. 149

3. Results ……..…… 150
3.1 Crystal structure and experimental parameters ……..…… 150
3.2 Defect formation energies and thermodynamic transition energies ……..… 151
3.3 Lattice relaxation and electron density contours around the iodine vacancy ..153
3.4 Configuration coordinate diagram …….. 156
4. Discussion ……. 158
4.1 Photo-ionization limit and optical absorption transitions of the F center ….. 158
4.2 Thermal trap depth of the F center and thermoluminescence data ……. 162
4.3 Vibrational wavefunctions and modeled optical absorption bands of F and F^- centers in SrI_2 ……..……..…… 164
4.4 Comparison to a particle-in-a-box model and other halide crystals in Mollwo-Ivey plots …….. 166
5. Conclusions ……..…… 168
CHAPTER 7: HOST STRUCTURE DEPENDENCE OF LIGHT YIELD AND PROPORTIONALITY IN SCINTILLATORS IN TERMS OF HOT AND THERMALIZED CARRIER TRANSPORT …… 175

PART III: CHAPTERS ON MY RECENT SCINTILLATOR RESEARCH NOT YET PUBLISHED

CHAPTER 8: FIRST PRINCIPLES CALCULATIONS ON Ce, Sr, Sr-F_A, AND F CENTERS IN $LaBr_3$……... 186
1. Computational details ……..…….. 188
2. Results and discussion …….…….. 189
2.1 Bulk material ……... 189
2.2 Electronic structure and charge localization …….…….. 190
2.3 Formation energies …….……...… 190
2.4 Energy levels and carrier transport analysis ……...…… 192
CHAPTER 9: FIRST PRINCIPLES CALCULATIONS ON SOLID-SOLUTIONS OF ALKALI HALIDES FOR POSSIBLE SCINTILLATOR USE ……..…. 195
1. Introduction ……... 197

2. Computational details 198
2.1 First-principles calculations 198
2.2 Group velocity and electron/hole effective mass 199
2.3 Formation enthalpy and phase diagram 199
3. Results and Discussion 200
3.1 Electronic structures and group velocities of $NaBr_{0.5}I_{0.5}$ and $Na_{0.5}K_{0.5}I$ 200
3.2 Formation enthalpies as a function of composition 203
CHAPTER 10: CALCULATED HOT ELECTRON GROUP VELOCITY AND MONTE-CARLO SIMULATION OF HOT ELECTRON TRANSPORT IN SCINTILLATORS 206
1. Introduction 208
2. Computational details 209
3. Results 212
3.1 Band structures 212
3.2 Group velocity 213
3.3 Monte-Carlo simulations 214
4. Conclusions 216
CHAPTER 11: FIRST PRINCIPLES CALCULATIONS ON GGAG:Ce and GYGAG:Ce SCINTILLATORS..... 218
1. Introduction 220
2. Computational details 221
3. Preliminary results and discussion 222

PART IV

CHAPTER 12: CONCLUSIONS 228

APPENDIX I: AB INITIO ENERGETICS AND KINETICS STUDY OF H_2 AND CH_4 IN THE SI CLATHRATE HYDRATE 231

APPENDIX II: A THEORETICAL STUDY OF THE HYDROGEN-STORAGE POTENTIAL OF H4M IN METAL ORGANIC FRAMEWORK MATERIALS AND CARBON NANOTUBES 236
APPENDIX III: SURFACE MODIFICATION ENABLED CARRIER MOBILITY ADJUSTMENT IN CZTS NANOPARTICLE THIN FILMS 245
APPENDIX IV: FIELD ELECTRON EMISSION OF LAYERED Bi_2Se_3 TOPOLOGICAL INSULATOR 257

Curriculum Vitae 263

LIST OF FIGURES

Chapter 1

1 SLNYCI data …… 8

2 Light yield…… 10

3 Nonproportionality vs. effective diffusion cofficient …… 14

4 Scintillator decision tree…… 18

5 Workflow toward a user's toolkit for Modeling scintillator…… 20

Chapter 2

1 HPGe and CsI diffusion …… 31

2 Auger quenching fraction …… 32

Chapter 3

1 2^{nd} order quenching vs. density …… 53

2 2^{nd} order quenching vs. mobility …… 54

3 Independent carrier fraction vs. mobility …… 59

4 Independent carrier fraction vs. density …… 65

5 Survival fraction vs. density …… 67

6 Simulated local light yield …… 68

7 Cross-section of anistropic diffusion at low density …… 72

8 Cross-section of anistropic diffusion at high density …… 72

9 Survival fraction vs. anistropy …… 73

10 Simulated local light yield vs. anistropy …… 74

11 SLLY of modelled materials …… 76

12 Nonproportionality vs. effective diffusion coefficient …… 82

Chapter 4

1 CsI thin film transmittance vs fluence …….. 98

2 NaI thin film transmittance vs fluence ……. 100

3 CsI:Tl spectrum …… 101

4 CsI STE decay ……. 103

5(a) Expanded STE decay ……... 105

5(b) Convolution of growth and decay ……..... 106

6(a) Bimolecular growth ……. 108

6(b) Bimolecular recombination rate ……... 109

7 NaI STE decay ……..…… 110

8 CsI:Tl Tl+* decay …….…….... 111

9 NaI:Tl Tl+* decay …….…. 112

10 Light yield vs excitation density ……..…… 113

11 Separation of electrons and holes with different mobilities ……..……..….. 118

12 Carrier diffusion profiles ……. 120

13 e^{-1} radius of electron distribution and independent fraction ……..…… 122

14 Independent fraction of electrons and holes vs hole mobility …….. 124

15 e^{-1} radius of electron radial profile vs dE/dx …….…... 125

Chapter 5

1 NaI production yield and local light yield ……...….. 134

2 Calculated electron energy response compared to experiment ……..……. 136

Chapter 6

1 Formation energies ……..…… 151

2 Thermodynamic transition energies ……. 152

3 Energy levels ……..…….…..… 154

4 Electron density contours …….…… 155

5 Configuration coordinate diagram …….……..…… 157

6 Vibrational wavefunction ……..…….. 161

7 Modeled optical absorption bands …… 166

8 Mollwo-Ivey plot ……..…… 168

Chapter 7

1(a) NaI and SrI_2 conduction band structure …… 179

1(b) Group velocity distribution vs energy …….……..179

1(c) Electron track cross sections …….……179

2 Scintillator physical Decision Tree ……..……..... 182

Chapter 8

1 Electron/hole density contours ……. 191

2 Formation energies …….…….. 192

3 Defect energies levels …….…….……. 193

Chapter 9

1 Band structures and partial density of states ……..... 202

2 Hot electron/hole group velocities ……..…….. 203

3 Formation enthalpies ……..... 203

4 Simulated temperature phase diagram ……..…… 203

Chpater 10

1 Band structures ……. 212

2 Group velocity and density of states ……..…….. 213

3 Hot electron thermalization time and diffusion range ……...…... 215

Chpater 11

1 Crystal structure …… 222

2 Band structure and PDOS of GGAG ……..…….. 224

3 PDOS of GYGAG …… 225

4 Optical transition energies …… 226

LIST OF TABLES

Chapter 3

1 Estimated conduction and valence band mobilities of SrI_2……. 71

2 Mobilities and nonproportionaltiy …….……. 81

Chapter 4

1 Parameters obtained from time-resolved measurements ……..…… 110

Chapter 5

1 Physical parameters for NaI:Tl and SrI_2:Eu ……..…….. 135

Chapter 6

1 Lattice constant and band gap …… 151

2 Formation energies ……..…….. 152

3 Vacancy size and force constant ……..……. 153

4 Bader analysis …….. 156

5 Transition energies ……..…… 161

Chapter 9

1 Electron and hole effective masses ……..……... 201

Chapter 10

1 Calculation parameters ……..……..…… 210

2 Group velocity and thermalization range ……..……..……. 215

Chapter 11

1 Lattice constants band gaps ……..……..…… 223

ABSTRACT

Intrinsic nonproportionality is a material-dependent phenomenon that sets an ultimate limit on energy resolution of radiation detectors. In general, anything that causes light yield to change along the particle track (e.g., the primary electron track in γ-ray detectors) contributes to nonproportionality. Most of the physics of nonproportionality lies in the host-transport and transfer-to-activator term. The main physical phenomena involved are carrier diffusion, trapping, drift in internal electric fields, and nonlinear rates of radiative and nonradiative recombination. Some complexity is added by the now well-established fact that the electron temperature is changing during important parts of the physical processes listed above. It has consequences, but is tractable by application of electron-phonon interaction theory and first-principles calculation of trap structures checked by experiment. Determination of coefficients and rate "constants" as functions of electron temperature T_e for diffusion, $D(T_e(t))$; capture on multiple (i) radiative and nonradiative centers, $A_{1i}(T_e(t))$; bimolecular exciton formation, $B_2(T_e(t))$; and nonlinear quenching, $K_2(T_e(t))$, $K_3(T_e(t))$ in specific scintillator materials will enable computational prediction of energy-dependent response from standard rate equations solved in the electron track for initial excitation distributions calculated by standard methods such as Geant4. $T_e(t)$ itself is a function of time. Determination of these parameters can be combined with models describing carrier transport in scintillators, which is able to build a user's toolkit for analyzing any existing and potential scintillators. In the dissertation, progress in calculating electronic structure of traps and activators, diffusion coefficients and rate functions, and testing the model will be described.

CHAPTER 1: INTRODUCTION

1. Topics and methods comprising my Ph.D. research

In 2009, I started my Ph.D. study under supervision of Prof. Thonhauser, from whom I began to learn the idea and applications of first principles calculations based on density functional theory (DFT). This is a major method used in different directions in my Ph.D research. Our main focus at that time was on hydrogen storage materials, specifically, clathrate hydrates and the crystalline form of $(H_2)_4CH_4$ (H4M). Clathrate hydrates are crystalline, ice-like structures formed out of water molecules stabilized by van der Waals interaction. They are formed naturally at the bottom of the ocean, and are normally filled with methane in the cavities formed by water molecules. These deposits mean a tremendous stockpile of energy with less greenhouse gas release. H4M is one of the most promising hydrogen storage materials due to its extremely high mass density and volumetric density of hydrogen. Long range intermolecular interaction plays an important role in these compounds. We used the van der Waals density functional vdW-DF as an accurate description of van der Waals interaction in these systems. Our two-year work resulted in two papers included in this dissertation as Appendices I and II.

Inspired by Prof. Williams, I started to investigate scintillator proportionality related projects from late 2009. My first involved project on this topic was to study the role of carrier diffusion in scintillator proportionality using finite element methods to solve the rate equation of the carriers excited in scintillators in assumed cylindrical track geometry. Scintillators have been used as radiation detector materials for over 80 years, and investigation of the origins of nonproportional response (see below) intensified greatly since about 2000. While carrier diffusion had been noted as a factor in early

treatments [1,2], the quantitative treatment of carrier diffusion in modern-era modeling of scintillator nonproportionality was largely ignored in modeling of electron energy response at the time our work was undertaken in 2009. In 2009, Setyawan et al. published a paper showing empirical correlation of the ratio of electron and hole effective mass from high-throughput bandstructure of scintillators with an experimental measure of nonproportionality in a class of materials comprising mostly oxides [3]. A series of papers (Chapter 2, 3, 4) on results and discussions of our thermalized carrier transport model including charge separation and nonlinear quenching were published in 2010 and 2011. These papers convinced some leading groups in the scintillator field that carrier diffusion is indeed a controlling factor in scintillator proportionality and this idea is now well accepted in the community.

After 2 years' research on scintillators and hydrogen storage materials, I was selected for the Computational Chemistry and Material Science (CCMS) summer institute of Lawrence Livermore National Laboratory (LLNL) with help from Prof. Thonhaser and Prof. Williams in 2011. I worked on a project of simulating self-trapped excitons (STE) in SiO_2 from first principle calculations under supervision of Dr. Babak Sadigh and Dr. Daniel Åberg during the 10 week stay at LLNL. For the first time, I learned how to model point defect systems in different materials using a planewave based code, Vienna Ab-initio Simulation Package (VASP). Excited states of the defect systems are of particular interest from both experimental and theoretical aspects. Traditional density functional theory normally severely underestimates the band gaps of both insulators and semiconductors and hence positions of the energy levels associated with the defects. Moreover, traditional DFT gives qualitatively wrong pictures for charged

defects like self-trapped holes (STH) in alkali halides due to its insufficient capability of localizing charge. In order to get more accurate information for the optical and thermodynamic properties of the defects, I expanded my capability of performing first principles calculations to hybrid functionals and GW approximation level. Furthermore, I was introduced to including excitonic effects in the defect simulations by the Bethe-Salpeter equation. Later in 2013, I learned more on GW and BSE methods in BerkeleyGW 2013 workshop. The research experience I gained from the CCMS institute and Berkeley GW workshop helped me greatly on projects of defects in scintillators with which I have been involved in the later years of my Ph.D. study. A formal collaboration between our group and the Sadigh group of LLNL was established after the summer school. We had many fruitful results and discussions since then, particularly in discussions with Daniel Åberg. Calculations on various defects in scintillators are crucial to scintillator studies in our group. First, the results of the optical transition energies help with interpretation and planning of the picosecond absorption experiments to recogonize various absorption bands in the previously uncharted picosecond absorption spectrum. For example, work on F centers in SrI_2 in Chapter 6 made predictions on the absorption and emission peaks and lineshape for the F centers in different charge states in SrI_2, which is an exceptional scintillator in terms of proportionality and light yield. Although solid experimental data are still lacking, these theoretical results can be used to guide the picosecond absorption experiments for relevant absorption peaks associated with this defect. More importantly, electronic structure calculations on these defects may in our planned future work be used to calculate the capturing cross-section of different defects, which is an important input parameter for either the finite element modeling currently

being performed by Xinfu Lu from our group or a Monte Carlo simulation incorporating capturing mechanisms.

In 2012, several published works of Monte Carlo simulations on hot carrier thermalization and transport from Gao, Kerisit et al. of Pacific Northwest National Laboratory (PNNL) provoked our realization in the effect of hot electron transport in scintillators [4]. This awareness of the importance of hot carriers was concurrently reinforced by the results of interband z-scan experiments performed in our lab in the Ph.D. research of Joel Grim [5], showing for the first time that nonlinear quenching in certain classes of scintillators (mainly the heavier halides) is almost pure 3^{rd} order in its dependence on excitation density, implying free-carrier Auger decay, as opposed to 2^{nd} order quenching by presumed dipole-dipole transfer that was found in the oxides studied. Materials with high optical phonon frequencies (most oxides) exhibit almost pure 2^{nd} order nonlinear quenching while materials with lower optical phonon frequencies (for example, halides) have 3^{rd} order kinetics. Based on the published results from PNNL on hot carrier thermalization and the experimental data, we were able to make a hypothesis as follows. High optical phonon frequencies result in fast hot electron thermalization in general, hence the excited electron-hole pairs in most oxides are able to combine and form excitons during a time scale (< 1ps) shorter than typical nonlinear quenching time scale (~ 10 ps). Therefore 2^{nd} order nonlinear quenching dominates in oxide scintillators. In heavier (non-fluoride) halide materials, hot electron thermalization happens on a longer time scale of a few picoseconds due to lower optical phonon frequencies. Since hot electrons are highly mobile with their extra kinetic energies up to one band gap above the conduction minimum, trapping of the hot electrons on (self-trapped) holes is believed

to be delayed during the nonlinear quenching time regime, so that these materials hence have 3rd order kinetics. Indeed, recent picosecond absorption spectroscopy of self-trapped exciton formation versus initial electron energy has confirmed this hypothesis in CsI [6]. To test our hypothesis and obtain quantitative information on the effect of hot carrier transport, I used first principle calculations again for the phonon properties and hot electron group velocities in selected scintillator materials. These results were all combined in a published work and included as Chapter 6 in this dissertation. A scintillator "decision tree" which is able to categorize scintillators by their optical phonon frequency, band edge mobility, and hot carrier group velocity and make predictions of the proportionality and light yield of each category was constructed. In addition, I developed a Monte Carlo simulation package independently for hot electron thermalization and transport using the group velocity results calculated from first principles. This yet unpublished work is shown in Chapter 10. The results were presented in the International Conference on Inorganic Scintillators and Their Applications (SCINT 2013) in Shanghai.

Besides the work mentioned above, I also did some collaborative projects on my own time during part of the last two years of my Ph.D. study to investigate carrier transport in photovoltaic systems and graphene-like 2-D layered materials. Appendicies III and IV are two manuscripts accepted for publication on these topics. These papers are mainly presenting experimental studies. I used first principles calculations to give theorectical prediction of key parameters as a significant complement of the experimental investigations.

In summary, I have used first principles calculations as a shared method in different fields (energy storage, scintillator nonproportionality, photovoltaics, and

topological insulators) during my Ph.D. research. Scintillator nonproportionality is the central part of my research and main body of this dissertation. Since 2000, chemical and nuclear terrorism threats motivated an upsurge for high resolution scintillator detectors. My work is aimed toward understanding the physical mechanisms that put limits on intrinsic scintillator resolution. Developing a users' modeling toolkit, including necessary measured and/or calculated input parameters for analyzing a broad range of scintillators will be extremely helpful to the scintillator community. The nature of the problem and my research results in support of that goal will be discussed below.

2. Scintillator for energy-resolved radiation detection

Scintillation is a flash of light produced in a transparent material by the stopping of a particle (an electron, an alpha particle, a neutron, or high-energy photon). When a scintillator is excited by the incoming particle, it can emit part of the absorbed energy in the form of (usually visible) light. Scintillator materials are normally coupled with an electronic light sensor such as a photomultiplier tube (PMT) to obtain a scintillator detector. Compared to a normal Geiger counter, scintillator radiation detectors provide spectroscopy response of the incident radiation so that the energy of the radiation and thus the type of the source can be determined. Scintillator radiation detectors have broad applications in particle physics, astronomy, medical imaging, homeland security, oil well logging, and other related fields.

Scintillator detectors have been used for ever 80 years in many different areas. For a long period of time, sensitivity was almost the sole criterion for scintillators and hence high light yield inorganic scintillators like NaI:Tl were popular and remain so for

many applications. But the response time (scintillation decay time) of NaI:Tl is slow. In the early 1990's, a new need for fast scintillators grew as CERN's large hadron collider (LHC) and associated detectors began to be planned and built. Pushed by this need for better speed, $PbWO_4$ became part of a vanguard of new scintillators investigated and developed rather intensively over the last two decades. Over 60,000 $PbWO_4$ crystals were individually grown and incorporated in the Compact Muon Solenoid (CMS) to detect gamma ray showers emanating from the 10^8 bunch crossings per second at LHC. These fast scintillators played an important role in the discovery of the Higgs boson in 2012. Nuclear nonproliferation became an increasingly pressing need after 2001. Discovery of high resolution scintillator detectors, preferably at low cost for wide deployment, is needed to distinguish isotopes and chemical elements in security scanning. Our work aims to elucidate the fundemantal physics that limits the resolution of scintillator detectors.

Proportionality between scintillator light yield and incident gamma-ray energy is a prerequisite for achieving the best energy resolution consistent with counting statistics in a radiation detector. A perfect scintillator material should have a constant ratio between total light emission and the initial energy of the primary electron being stopped inside it. However, fundamental origins like carrier quenching and deep defect trapping usually causes significant nonproportionality to existing scintillator electron response, which limits the overall resolution of the radiation detectors designed from these scintillators. The experimental measurement for the electron response curve is obtained from Scintillator Light Yield Nonproportionality Characterization Instrument (SLYNCI) of Lawrence Berkeley and Larwrence Livermore Laboratories [7]. A set of SLYNCI data

for different scintillators is shown in Fig. 1, almost all of the scintillators diviate from the perfectly horizontal response significantly.

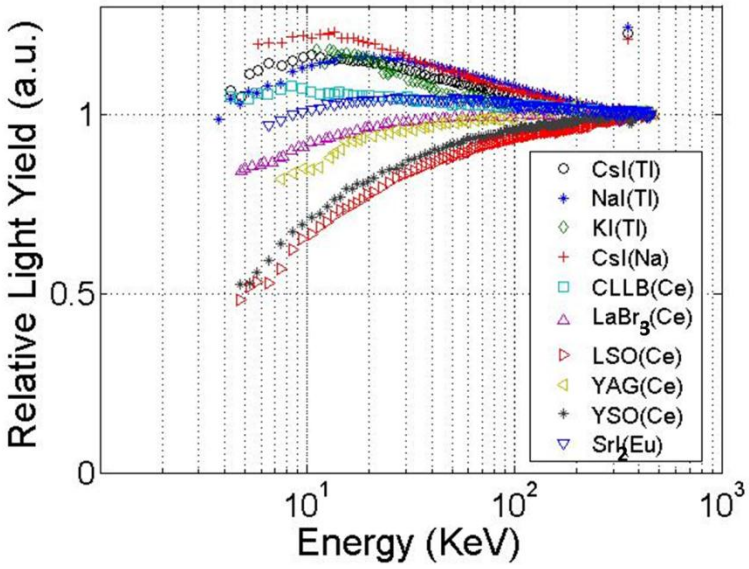

FIG. 1 Light yield from Compton scattering of different scintillators measured by Scintillator Light Yield Nonproportionality Characterization Instrument (SLYNCI), all data are normalized to 662 KeV. Figure plotted from data supplied by G. Bizarri et al. and S. A. Payne et al. Adapted from Ref. [7] with permission of Institute of Electrical and Electronics Engineers.

SLYNCI data is the standard measurement for scintillator proportionality; however it does not contain the information of the origins of the nonproportionality. In Fig. 1, the low electron energy part corresponds to track end region in a real particle track excited in scintillators, and commonly implies high excitation density. The global roll-off part on the left hand side of SLYNCI data is commonly assumed to be related with the nonlinear quenching (2^{nd} order dipole-dipole quenching or 3^{rd} Auger quenching) mechanism among the exciations introduced by the incident particle in the scintillators. Oxides tend to have the more severe nonlinear quenching than halide scintillator materials as shown in Fig. 1. Alkali halides have their typical rising part on the high

electron energy part which also introduces nonproportionality. Currently the leading performers in SLYNCI-type data are in the class of multivalent halide compounds, including $LaBr_3$:Ce and SrI_2:Eu. Such scintillators do not show a strong rising part at the beginning part of the track and the steep nonlinear quenching roll-off occurs only at the highest excitation densities associated with track ends. In addition, Sr co-doped $LaBr_3$:Ce is recently synthesized and has a further improvement in what was already one of the most proportional scintillators, which allows it to have exceptionally high resolution for a scintillator, up to 2% at 662 keV [8].

Another important criterion, partially related to the proportionality, is the total light yield or simply the brightness of a scinllator. The expression for light yield L due to Lempicki, Wojtowicz, and Berman is as follow [9]:

$$L = \beta' SQ \tag{1}$$

where the electron-hole pair creation efficiency β' is determined to be 2 to 3, it is the ratio between the energy needed to create one excitation in a material and the band gap of the material. S is the transfer efficiency for excitations to transfer to activators and Q is the quantum efficiency of the activators. In Fig. 2, the overall light yield for various scintillators grouped by the anions is plotted against their band gaps. The red line is the theoretical limit of the light yield using β' value of 2.5 [10].

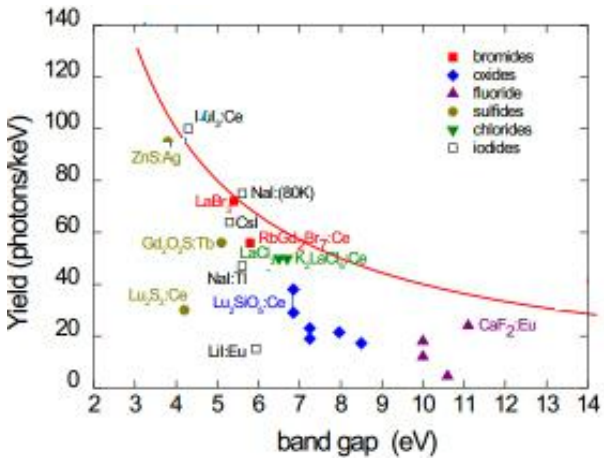

FIG. 2 Overall light yield of different scintillators as a function of their band gaps. The red line is the theoretical limit of light yield. Adapted from Ref. [10] with permission of Institute of Electrical and Electronics Engineers.

An ideal sincillator would have *S* and *Q* values both be 1 and push the light yield to the theoretical limit, this also makes a perfectly proportional scintillator. The light yield and proportionality are related criteria of scintillators. As shown in Fig. 2, proportional scintillators have light yield generally closer to their theoretical limits and vise versa.

Efforts to understand the physical basis of nonproportionality in order to more efficiently discover and design scintillators with better resolution have intensified in the last decade. The motivation comes in part from the need for highly discriminating nuclear material monitoring and some types of secrurity scanning, but improved resolution can also benefit medical molecular imaging and particle physics experiments. It would be very useful if one or more design rules for proportionality could be found. A material design rule is a predictive relationship between one independently measurable material parameter and a trend of response affecting nonproportionality, valid across a broad range of radiation detector materials. Such predictive trends would suggest physical

mechanisms that can be tweaked and engineered for improved scintillator detector resolution.

To actually discover and investigate these important material dependent parameters or design rules, there has been an active and useful subfield of scintillator research known variously as computational modeling of scintillator performance intensified recently. The emphasis has been on "modeling," which connotes the tweaking of included phenomena and searching for the most important material parameters that can reproduce features of experimental electron energy response and total light yields. My dissertation will describe the theoretical study and Modeling of scintillator nonproportionality and light yield developed in our group in stages.

3. The search for what controls scintillator proportionality, and efforts toward development of a predictive model based on material properties

Most of the physics behind nonproportionality is contained in the *S* transport term in Eq. (1). In order to model scintillator proportionality, we put our main focus on the transport of the excited carriers.

In 2009, our group began to study the effect that electron and hole diffusion occurring in thermal equilibrium within the extreme radial concentration gradient of high-energy electron tracks may have upon nonlinear quenching and the branching of electron-hole pairs and independent carriers. This effect was ignored to a large degree in the scintillator field for many decades. It was mentioned as a possibility and included to some degree in very early models [1,2], but had not been analyzed quantitatively in regard to the new interest in proportionality up to the time our Wake Forest group started

numerical modeling of the effects in scintillators. Our interest was provoked partially by the fact that the nonlinear quenching, either 2^{nd} order or 3^{rd} order, is extremely sensitive to a change in the track radius given an initial deposited local carrier concentration on-axis. The carrier density is inversely proportional to the square of the track radius; hence the 2^{nd} order and 3^{rd} order quenching depend on fourth and sixth power. Even modest diffusion can have controlling influence on nonlinear quenching in such a case, and the extreme concentration gradient promotes substantial diffusion effects even on the picosecond time scale on which nonlinear quenching typically occurs. Carrier mobilities therefore become a very important paramenter that can control nonlinear quenching and hence nonproportionality. In Chapter 2, a finite element method is used to simulate the time-dependent radial diffusion and drift in the high carrier concentration gradient characteristic of electron tracks with presence of intermal electric field in scintillators and other radiation detector materials. This work was published in *Nuclear Instruments and Methods in Physics Research A* (2011) [11].

In Chapter 3, the diffusion-drift-quenching model was improved and generalized. It also was the first attempt to simulate the general form of SLYNCI Compton coincidence data without using any fitting parameters. A fast Poission solving algorithm was used to calculate the potential and electric filed and enabled the program to simulate 2-dimensional diffusion for materials with anisotropic mobilities. With the help from the first principles band structure calculations [3], we were able to develop an effective diffusion coefficient model which describes the competition between diffusion and quenching of the mixture of carriers (electrons, holes, and excitons) along an electron track for most oxides, selenides, and semiconductors without self-trapping holes. The

effective diffusion coefficient is defined as follows. It is a single material dependent parameter that describes how efficiently the carriers can transport out of the high carrier density region before significant nonlinear quenching can occur.

$$D_{eff} \approx \frac{kT}{\max(m_h, m_e)} \left[\min\left(\frac{m_e}{m_h}\right) \tau_{EXC} + \left(1 - \min\left(\frac{m_e}{m_h}\right)\right) \tau_e \right] \quad (2)$$

Here, m_e, m_h are electron and hole band masses, τ_{EXC} and τ_e are the scattering time of excitons and independent carriers in the materials. As calculated in Ref. [12], the ratio between electron and hole mobilities defines the branching between the excitons and independent carriers. Eq. (2) is a "two gas" model of excitation transport. The predicted nonproportionality vs. effective diffusion coefficient relation matches experimental data for oxides and smiconductors well as shown in Fig 3. The initial track radius was taken to be 3 nm in agreement with later determinations [4,5]. This work is published in *Journal of Applied Physics* (2011) [12]. The halides cannot be fitted in the same plot by the effective diffusion coefficient model alone, we believe it relates to the hot electron transport in such materials and this issue will be addressed later.

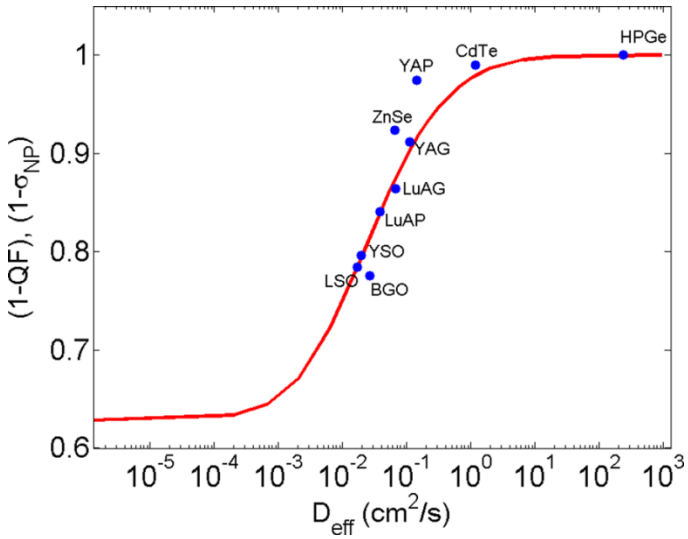

FIG. 3 Empirical measures of proportionality (1-r_{NP}) tabulated by Setyawan et al. [3] for the scintillators shown, together with points for CdTe and HPGe (77 K), are plotted versus effective diffusion coefficient, D_{eff}, deduced from calculated band masses [2] with an assumed exciton scattering time s_{EXC}=8.4×10^{15} s. The red curve is the plot of (1-QF), the survival probability against second-order quenching through 10 ps for on-axis excitation density 10^{20} e-h/cm^3 in a 3 nm Gaussian track. Figure adapted from Ref. [12] with permission of American Institute of Physcis.

The diffusion-drift model is further completed and compared with experimental data from our group in Chapter 4, which is published as a front cover in *Physica Status Solidi B* (2011) [13]. Experimental results like the time window for quenching to happen, nonlinear quenching rates, bimolecular exciton formation rate, and electron capturing (on activators) rate are described in detail. These results were used as inputs for the transport model. The combined theoretical and experimental research enabled us to investigate the interplay of charge separation and nonlinear quenching in a carrier transport framework in determining scintillator nonproportionality.

The simulated local light yield (SLLY) result from Ref. [12] is a function of on-axis carrier density and hence cannot be compared directly with the SLYNCI data which is the light yield as a function of electron energy. To actually compare our simulated data with electron response data (SLYNCI), the Monte Carlo GEANT4 software package was

introduced and provided data for excitation population as a function of carrier density. SLLY and GEANT4 data can be integrated to obtain the simulated electron response curve. The calculated electron response data for NaI:Tl and SrI_2:Eu scintillators corresponds with experimental K-dip data very well as shown in Chapter 5, which was published in *MRS communications* (2012) [14]. This comparison is a strong evidence of the validation of our model.

The master rate equation describing the carrier transport contains the capture on various types of radiative and nonradiative centers. These capturing rates are crucial to the carrier transport processes and through it, the nonproportionality. Despite the importance of the properties of these trapping centers, there is in fact very limited experimental investigation performed at this point. Multiple types of traps always co-exist in a certain material and it is normally difficult to study them from experimental approaches separately and thoroughly. A more feasible and probably better way to get the information of various types of trapping centers in different scintillator materials is electronic structure simulation. To obtain our desired parameters such as capturing center population, capturing cross-section, and capturing rate as a function of electron energy for each type of activator/defect, we perform first principles calculations and study the electronic structures of the defective systems before analyzing the results with approaches which lead us to the rates. Our calculations are based on density functional theory and are carried out in the projector augmented wave (PAW) framework in the Vienna *ab initio* simulation package (VASP). As an example of theoretically investigating defects that are difficult to study using theoretical approaches, the work of Chapter 6 won the Young Researcher Award in 2012 International Conference on

Defects in Insulating Materials (ICDIM) and was published as editor's suggestion in *Physica Status Solidi B* (2013) [15]. In this chapter, we present first principles calculation results for iodine vacancy centers in SrI_2 scintillator. In 2008, SrI_2:Eu scintillator became the focus of intense interest in the search to develop higher-resolution gamma-ray scintillation spectrometers. Part of the motivation of this work is to gain understanding of electron traps contributing to the size of linear quenching fraction in Ref. [12]. We want to characterize the properties of some of the expected common lattice defects in SrI_2. However, SrI_2 is extremely hygroscopic and until recently it was moderately difficult to grow good crystals. As a result of these complicating experimental factors and the absence of a strong driving interest until the recent need for improved gamma-ray detectors, there is very little known about point defects in SrI_2. Our work includes the electronic structure, lattice relaxation, and formation energies of iodine vacancy defects in different charged states in SrI_2. Using the parameters that are calculable from first principles in SrI_2 as a starting point, prediction of absorption energy, vibrational lineshape, thermal trap depth, and Mollwo-Ivey comparison to alkaline-earth fluorides is made.

The transport model established in 2011 has its limitations on predicting the nonproportionality of halide materials like NaI and SrI_2. In 2012, our measurements of nonlinear quenching kinetic order alongside Monte Carlo simulation performed by Wang et al. [4] led us to realize the importance of both hot and thermalized electron transport for scintillator performance. Therefore, we expanded our previous diffusion and nonlinear quenching model to include hot electron transport. Furthermore, we established a more general model predicting scintillator nonproportionality based on optical phonon

frequency, thermalized band edge mobilities, group velocity in the upper conduction bands, and hole self-trapping. A scintillator "decision tree" was concluded from these results as shown in Fig. 4. This paper was published as a front cover in *Physica Status Solidi RRL* (2012) [17], and is included as Chapter 7. In Fig. 4, the criterion at the top level is whether hot electron thermalization is fast compared to picosecond scale of nonlinear quenching. If so, there will be thermalized carriers diffusing with band-edge mobilities during nonlinear quenching and the model in Ref. [12] should apply. The decisive parameter for these materials (almost all oxides) is effective diffusion coefficient. The right-hand branch at the top is toward low optical phonon frequency, thus slow thermalization of hot carriers, thus free carriers during nolinear quenching, and 3rd order Auger quenching should be expected. Experimental evidence of the top level branching between 2nd order quenching and 3rd order quenching is obtained from the z-scan experiments done in our lab. The second level branch on the right is between small and large hot electron group velocity, corresponding to small and large hot-electron range. Thermalization rate (top level) combines with group velocity to determine hot electron range. If hot electrons have a small thermalization range, their collection in the electric field of the self-trapped holes in the track core will not encounter many traps. Thus light yield will be high and the typical "halide hump" [8] will be small.

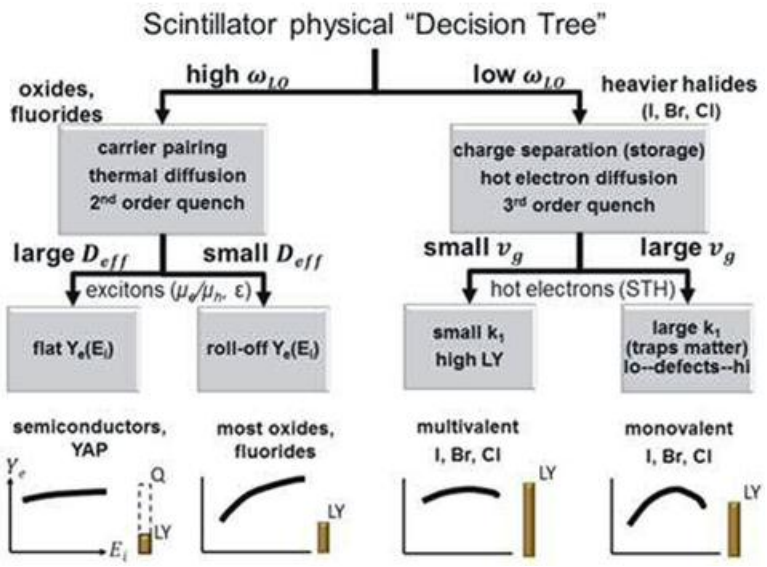

FIG. 4 How classes of general behavior in electron energy response (curves) and light yield (LY) illustrated along the bottom may result from physical parameter values: ω_{LO} deciding electron thermalization rate: fast to the left with thermalized diffusion versus slow to the right with hot free carriers; subsequent branching in the thermalized half is governed by band-edge diffusion coefficient D_{eff} [3]; whereas the non-thermalized half is controlled by hot-electron velocity and range depending on host structure. Adapted from Ref. [17] with permission of John Wiley and Sons.

In Chapter 8, three different centers, F center, Sr-F_A center and Ce activator are all simulated and compared using first principle techniques. As described in Ref. [8], $LaBr_3$:Ce co-doped with Sr^{2+} can achieve almost perfectly proportional electron response and high light yield up to 75,000 ph/MeV which is at the theoretical limit of $LaBr_3$. The central question of the effect of the co-doping is how a small amount of Sr co-do-ping (160 ppm) can have a controlling effect over Ce activators with much larger population (50,000 ppm). Our calculation shows that the geometric size of the hole density contour of the Sr-F_A center is larger than Ce center, which may imply that Sr-F_A centers have bigger hole capturing cross-section. However, more evidence is needed to prove that the holes are captured on Sr-F_A centers with a much faster rate compared with Ce centers. We are planning to simulate multi-phonon capturing process described in [16] based on

the electronic structure calculations performed, which will strengthen the analysis of carrier capturing features of these centers and give answers to the capturing parameters we would like to use in the transport model.

A. Gektin summarized the literature on light yield in mixed-crystal scintillators, showing that light yield is often improved in mixed crystals. This suggests a route to new scintillators with good band edge mobilities and modest conduction band group velocity, just like one of the best scintillators SrI_2. We first took alkali halide mixed crystals NaI_xBr_{1-x} and $Na_xK_{1-x}I$ ternaries as a starting point. The calculations show that $Na_xK_{1-x}I$ is a very promising material in terms of hot electron group velocity. In Chapter 9, the results are discussed.

In Chapter 10, a detailed discussion of the modeling of hot electron transport combined with usage of parameters calculated from first principles calculations or directly from experiments is presented. A Monte-Carlo simulation package developed independently from our group for hot electron transport is used for results on the thermalization time and diffusion range [18].

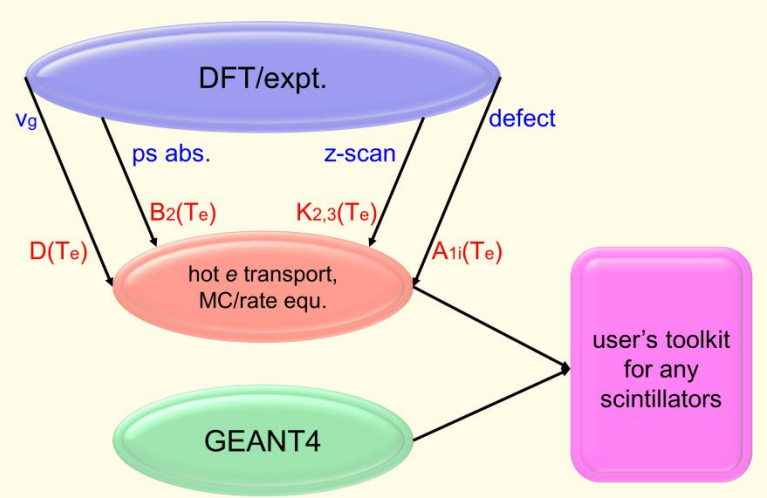

FIG. 5 Workflow toward a user's toolkit for scintillator nonproportionality and light yield. The group velocity, defect electronic structure calculated from density functional theory is translated to diffusion coefficient $D(T_e)$ and capturing rate $A_{1i}(T_e)$ for various centers as a function of electron temperature T_e. Similarly, bimolecular exciton formation rate $B_2(T_e)$ and nonlinear quenching rates $K_2(T_e)$, $K_3(T_e)$ are extracted from picosecond absorption and z-scan experiments. These input parameters can be used in a Monte-Carlo simulation or a finite element rate equation solver to simulate hot electron transport processes to predict local light yield as a function of carrier density. The resulted simulated local light yield can be combined with GEANT4 data to get the electron response for any existing/potential scintillators.

The current model contains the hot electron diffusion using group velocities calculated from first principles band structure calculations and the optical/acoustic phonon frequencies from phonon calculations. Internal electric field is also considered. To make this model more generalized and be able to eventually make predictions of scintillator light yield, we need the information of other rates from either experiments or calculations. In the near future, the nonradiative capturing by different centers through multiphonon emission will be worked out. At this point, our group is able to acquire the bimolecular exciton formation rate B_2 from picosecond absorption experiments and nonlinear quenching rates K_2 and K_3 from z-scan experiments. To sum up, the workflow of our planned user's toolkit for Modeling scintillator nonproportionality and light yield is presented in Fig. 5. Based on the foregoing discussion, all the rate constants used in the

modeling for local light yield are now a function of electron temperature. The bimolecular exciton formation rate and nonlinear quenching rates can be obtained from experiments done in our lab. First principles calculations can provide information of the group velocities and optical phonon frequencies so the diffusion coefficient is also solved naturally by using these parameters in a Monte Carlo simulation. Electronic structure calculations on various defects can be performed as in Chapter 8. These calculations can result in actual capturing rates as a function of electron energies which will be used in rate equation or Monte Carlo simulations. These simulations will be done as a function of on-axis carrier density, and local light yield will be predicted. One can then combine the simulated local light yield with GEANT4 data to get the simulated electron response for scintillators.

This dissertation contains 11 chapters and 4 appdendices comprising 15 published or “in preparation” papers out of a total 23 papers (19 of which are already published) and manuscripts on which I am a co-author. A full list of publications is included in the Curriculum Vitae.

REFRENCES

[1] S. A. Payne, W. W. Moses, S. Sheets, L. Ahle, N. J. Cherepy, B. Sturm, and S. Dazeley, "Nonproportionality of scintillator detectors: theory and experiment. II," IEEE Trans. Nucl. Sci. **58**, 3392 (2011).

[2] R. B. Murray and A. Mayer, "Scintillation Response of Activated Inorganic Crystals to Various Charged Particles," Phys. Rev. **112**, 815 (1961).

[3] W. Setyawan, R. M. Gaume, R. S. Feigelson, and S. Curtarolo, "Compariative study of nonproportionality and electronic band structure features in scintillator materials," IEEE Trans. Nucl. Sci. **56**, 2989 (2009).

[4] Z. Wang, Y. Xie, L. W. Campbell, F, Gao, and S. Kerisit, "Monte Carlo simulations of electron thermalization in alkali iodide and alkaline-earth fluoride scintillators," J. Appl. Phys. **112**, 014906 (2012).

[5] J. Q. Grim, K. B. Ucer, A. Burger, P. Bhattacharya, E. Tupitsyn, E. Rowe, V. M. Buliga, L. Trefilova, A. Gektin, G. A. Bizarri, W. W. Moses, and R. T. Williams, "Nonlinear quenching of densenly excited states in wide-gap solids," Phys. Rev. B **87**, 125117 (2013).

[6] K. B. Ucer, G. Bizarri, A. Burger, A. Gektin, L. Trefilova, and R. T. Williams, "Electron thermalization and trapping rates in pure and doped alkali and alkaline-earth iodide crystals studied by picosecond optical absorption," Phys. Rev. B **89**, 165112 (2014).

[7] G. Hull, W. S. Choong, W. W. Moses, G. A. Bizarri, J. D. Valentine, S. A. Payne, N. J. Cherepy, and B. W. Reutter, "Measurements of NaI:Tl electron electron response: comparison of different samples," IEEE Trans. Nucl. Sci. **56**, 331 (2009).

[8] M. S. Alekhin, D. A. Biner, K. W. Kramer, and P. Dorenbos, "Improvement of $LaBr_3$:5%Ce scintillation properties by Li^+, Na^+, Mg^{2+}, Ca^{2+}, Sr^{2+}, and Ba^{2+} co-doping," J. App. Phys. **113**, 224904 (2013).

[9] Lempicki, A. J. Wojtowicz, and E. Berman, "Fundamental limits of scintillator performance," Nucl. Instrum. Meth. A **333**, 304-311 (1993).

[10] I. V. Khodyuk, P. A. Rodnyi, and P. Dorenbos, "Nonproportionality scintillation response of NaI:Tl to low energy x-ray photons and electrons," J. Appl. Phys. **107**, 8 (2010).

[11] Qi Li, J. Q. Grim, R. T. Williams, G. A. Bizarri, and W. W. Moses, "The Role of Hole Mobility in Scintillator Proportionality," Nuc. Inst. Meth. Phys. Res. A **652**, 288 (2011).

[12] Qi Li, J. Q. Grim, R. T. Williams, G. A. Bizarri, and W. W. Moses, "A transport-based model of material trends in nonproportionality of scintillators," J. Appl. Phys. **109**, 123716-1-17 (2011).

[13] R. T. Williams, J. Q. Grim, Qi Li, K. B. Ucer, and W. W. Moses, "Excitation density, diffusion-drift, and proportionality in scintillators," Feature Article, Phys. Status Solidi B **248**, 426 (2011).

[14] J. Q. Grim, Qi Li, K.B. Ucer, R. T. Williams, G. A. Bizarri and W.W. Moses, "Electron energy response of NaI: Tl and SrI2: Eu calculated from carrier mobilities and measured first-and third-order quenching," MRS Communications **2**, 139 (2012).

[15] Qi Li, R. T. Williams, and D. Åberg, "First principles calculations and experiment predictions for iodine vacancy centers in SrI2," Editor's Choice, Phys. Status Solidi B **250**, 233 (2013).

[16] A. Alkauskas, Q. Yan, and C. G. Van de Walle, "First-principles theory of nonradiative carrier capture via multiphonon emission," presented in APS 2014, Denver.

[17] Qi Li, J. Q. Grim, K. B. Ucer, A. Burger, G. A. Bizarri, W. W. Moses, and R. T. Williams, "Host structure dependence of light yield and proportionality in scintillators in terms of hot and thermalized carrier transport," Front Cover, Phys. Status Solidi RRL **6**, 346 (2012).

[18] Qi Li, J. Q. Grim, N. A. W. Holzwarth, and R. T. Williams, "Hot electron velocity, relaxation time, and range in ultraviolet- and electron-excited scintillators," presented in SCINT 2013, Shanghai.

CHAPTER 2: THE ROLE OF HOLE MOBILITY IN SCINTILLATOR PROPORTIONALITY

Qi Li, Joel Q. Grim, R. T. Williams, G. A. Bizarri, W. W. Moses

The following manuscript was published in *Nuclear Instruments and Methods in Physics Research Section A* in 2011. Qi Li performed all finite element method calculations. Qi Li and R. T. Williams developed the diffusion-drift model and prepared the manuscript. I thank G. A. Bizarri and W. W. Moses of Lawrence Berkeley Lab for helpful discussions and reading of the manuscript. Manuscript is reproduced with permission of Elsevier. Stylistic variations are due to the requirements of the journal.

ABSTRACT

Time-dependent radial diffusion and drift are modeled in the high carrier concentration gradient characteristic of electron tracks in scintillators and other radiation detector materials. As expected, the lower mobility carrier (typically the hole) controls the ambipolar diffusion. Carrier separation when electron and hole mobilities are unequal produces a built-in radial electric field near the track analogous to an *n-intrinsic* semiconductor junction. The diffusion is shown to have significant effects on both the low-dE/dx and high-dE/dx ends of electron light-yield curves and their respective contributions to nonproportionality. In CsI:Tl, it is shown that electron confinement toward the end of the track accentuates high-order quenching such as Auger recombination or dipole-dipole transfer, while in HPGe extremely rapid (< 1 fs) dilution of carrier concentration by radial diffusion renders Auger quenching negligible. Separation of geminate carriers is accentuated in the beginning of the track if electron and hole mobilities are widely unequal as in CsI:Tl, leading to bimolecular recombination of trapped carriers by slower thermal hopping routes as the favored channel at low dE/dx.

1. Introduction

It is generally assumed that the root cause of nonproportionality in scintillators is nonradiative electron-hole recombination (quenching) that depends nonlinearly on the ionization density, coupled with the variability of local ionization density from beginning to end of an electron track. In order to relate *dE/dx* to a volume density of excitations that enter the 2nd and 3rd order nonradiative decay rates associated with dipole-dipole transfer and Auger recombination, it is necessary to know the (time-dependent) radius of the distribution of excitations. For example if one models the linear deposition *dE/dx* locally as distributed in a cylindrical track of radius r_t, then the excitation density at any location along the track is proportional to $(dE/dx)/r_t^2$ at that point. Clearly, the nonlinear quenching processes are very sensitive to $r_t(t)$, being 4th order in r_t for dipole-dipole and 6th order for Auger quenching.

We can associate three characteristic time ranges of changing $r_t(t)$ with different physical processes of radial diffusion: (1) ballistic transport of carriers created with kinetic energy in excess of *kT*, lasting for a thermalization time of fs to ps, during which the carriers diffuse a thermalization length $\mathbf{l}_t$ [1]; (2) diffusion of carriers with band mobilities in thermal equilibrium, commencing at the end of ballistic transport and continuing until the carrier is recombined with a partner or reduced to slow thermal hopping transport after becoming trapped; (3) thermal hopping / detrapping on a time scale of nanoseconds to microseconds in room-temperature scintillators.[2] Process (1) of ballistic transport is often folded into the definition of an initial track radius. Vasil'ev has estimated a thermalization length $\mathbf{l}_t$ = 3 nm as typical for scintillator materials.[1] It

is the process (2) of band diffusion in thermal equilibrium that is the topic of this paper, having importance in ~ 20 ps down to ~ 1 fs depending on mobilities. If diffusion/drift produces a significant dilution of concentration on this time scale, it can exert a strong influence on the outcome of Auger and dipole-dipole quenching, flattening the roll-off of light yield at high dE/dx. If it introduces spatial separation of electrons and holes, it can influence the path of radiative recombination kinetics and trap-mediated quenching. The diffusive separation of electrons and holes due to unequal mobilities will be shown to be favored at low dE/dx, especially when holes are immobile (self-trapped). In this way diffusive band transport of electrons relative to holes on the picosecond time scale can explain why the depression of light yield at low dE/dx is a feature peculiar to halide scintillators and is especially strongly expressed in NaI:Tl, CsI:Tl, and CsI:Na where holes are known to be strongly self-trapped. To illustrate these effects, we will compare diffusion simulations in a scintillator with nearly zero hole mobility on the relevant time scale (CsI:Tl) and in high-purity germanium (HPGe) semiconductor detector material having very high hole and electron mobilities.

2. Modeling Method

Time-step finite-element analysis was used to solve for the diffusion and drift currents, electric field, and local carrier concentration in cylindrical symmetry around the track of a charged particle. The equations used are

$$\vec{J}_e(\vec{r},t) = -D_e \nabla n_e(\vec{r},t) - \mu_e n_e(\vec{r},t)\vec{E}(\vec{r},t) \qquad (1)$$

$$\frac{\partial n_e(\vec{r},t)}{\partial t} = -\nabla \cdot \vec{J}_e(\vec{r},t) \qquad (2)$$

for electrons and an equivalent set of equations for holes, where the variables and constants have their usual meanings. Poisson equation

$$(\vec{r},t) = \frac{\rho}{\varepsilon\varepsilon_0} \qquad (3)$$

serves to evaluate electric field for insertion back into the diffusion/drift equation. The Einstein relation $D = \mu k_B T/e$ gives the diffusion coefficients for electrons and holes in terms of their mobilities μ_e and μ_h. The static dielectric constant ε of the material is used in Gauss's law.

The finite-element evaluation is applied to cylindrical shells around a starting distribution which is taken to be a Gaussian radial profile initially identical for electrons and holes. The electron and hole number in each cylindrical shell is updated in each time step according to the diffusion and drift currents across the cell boundaries. When it is desired to evaluate Auger quenching, a 3rd-order loss corresponding to Eq. (4) is included in the right side of Eq. (2) for evaluation in each cell and time step.

$$\frac{\partial n(\vec{r},t)}{\partial t} = -\gamma n^3(\vec{r},t) \qquad (4)$$

Following the approximate treatment of Ref. [3], the concentration n in intrinsic material is taken to refer to free electrons or free holes equivalently.

Driven by the huge concentration gradient posed by up to 3 x 10^{20} electrons/cm^3 confined initially within a radius of 3 nm, the electrons diffuse outward, opposed by drift back toward the collection of immobile (on this time scale) self-trapped holes in the example of CsI, or virtually un-opposed in Ge. We incorporated in the model a test to determine on average whether a geminate e-h pair gets ripped apart by the difference in electron and hole diffusion currents at a given radial position and time. By evaluating the

currents at the boundaries of each cell, the model can determine the integrated current flowing through a given cell up to a time *t*. Dividing that current by the electron concentration within the cell gives the average total displacement of electrons comprising the current at that place and time. Since the holes are immobile in the alkali halides on this time scale, electron displacement specifies the average displacement of an electron from its geminate hole partner *attributable to the mismatch of mobility-related electron and hole diffusion currents*. To the extent that this displacement, occurring in the average time t_{Tl} for trapping a carrier on an activator, exceeds the average spacing of Tl^+ activator ions in the crystal, then the electron will on average be trapped on a *different* Tl^+ (forming Tl^0) than will the hole (forming Tl^{++} on a different site). Subsequent recombination via this channel will be 2nd order, will proceed by a slower route of carrier de-trapping and re-trapping, and can be subject to deep trapping or extra nonradiative recombination channels. On the other hand, if the electron and hole are not ripped apart in the contest of diffusion and drift, they are more likely to be captured on the *same* Tl^+ in their vicinity and to undergo prompt monomolecular radiative decay. A related test applies in the more general case of both carriers mobile.

3. Results and Discussion

At room temperature, the average STH jump rate in CsI is 1.7×10^9 s^{-1}.[2] Thus, for purposes of the simulations of band diffusion in $\leq$ 20 ps presented here, the hole mobility in CsI is effectively $\mu_h = 0$. The electron mobility in pure CsI has been measured as $\mu_e = 8$ cm^2/Vs at room temperature[4], and the static dielectric constant is $\varepsilon = 5.65$. We specify thallium doping level (0.3%) because of its role in the test for

geminate-to-independent branching. HPGe has μ_h = 42000 cm^2/Vs and μ_e = 36000 cm^2/Vs at its 77 K operating temperature[5], and ε = 16. The measured Auger rate constant in Ge is $\gamma = 1.1 \times 10^{-31}$ cm^6/s [3]. A measured Auger rate constant is not available for CsI, so we assigned the Ge Auger rate constant to CsI for the sake of comparing purely the diffusion effects on Auger decay, all else being kept the same. Vasil'ev has estimated that the maximum electron-hole pair density produced on axis near the track end of an energetic electron is about 2×10^{20} cm^{-3} in NaI.[1] Therefore we have modeled hole and electron diffusion at initial on-axis concentrations of 2.5 x 10^{18} up to 2.5 x 10^{20} cm^{-3} for CsI:0.3%Tl, and for HPGe (77K). Both cases assume a starting Gaussian radius of 3 nm. For immobile holes as in CsI, the diffusion and drift currents come to a balance at a steady-state time t_{ss} ranging from 9 to 0.4 ps for on-axis carrier densities of 2.5 x 10^{18} and 2.5 x 10^{20} cm^{-3} respectively. Such a steady state distribution is analogous to a *p-n* junction or more specifically a cylindrical *n-intrinsic* junction with depletion zone and built-in electric field, where the role of ionized donors is played by the immobile holes. Just as electrons thermally released from the donors diffuse beyond the sharply-defined boundary of the doped region, setting up charge separation and a built-in electric field, so do conduction electrons excited from the valence band diffuse relative to the sharply confined core of self-trapped holes [1]. By contrast, the e^{-1} radial profile of both carriers in HPGe has already expanded within 1 femtosecond by a factor 6.5 times the starting radius r_{t0}, rendering the Auger decay rate, proportional to $(r_t)^{-6}$, negligible for t > 1 fs.

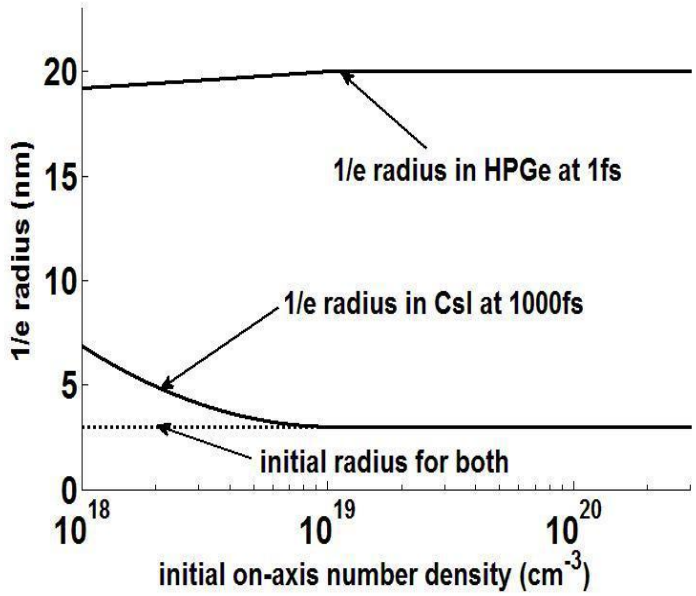

Fig. 1 Comparison of the post-diffusion e^{-1} radius contours of electron population in HPGe after 1 fs and in CsI after 1000 fs, versus initial on-axis density of electrons and holes.

Figure 1 compares the e^{-1} radius of electron distribution versus on-axis initial density n_0 for CsI and HPGe, both having started from the same 3-nm Gaussian distribution. The CsI radius contour is shown at 1000 fs, whereas the Ge contour has already expanded to a much larger radius in 1 fs, and will go out of the range plotted in the next fs. The extreme contrast in the diffusive track expansion rates for these two materials is the first lesson of Fig. 1. As we have pointed out that the 2^{nd} and 3^{rd} order quenching processes are 4^{th} and 6^{th} order in the instantaneous track radius, it makes quite clear at least one reason why HPGe or other intrinsic material with high mobilities will be nearly free of nonproportionality arising from Auger recombination, while a material like CsI:Tl will be much more affected by quenching that is nonlinear in excitation density.

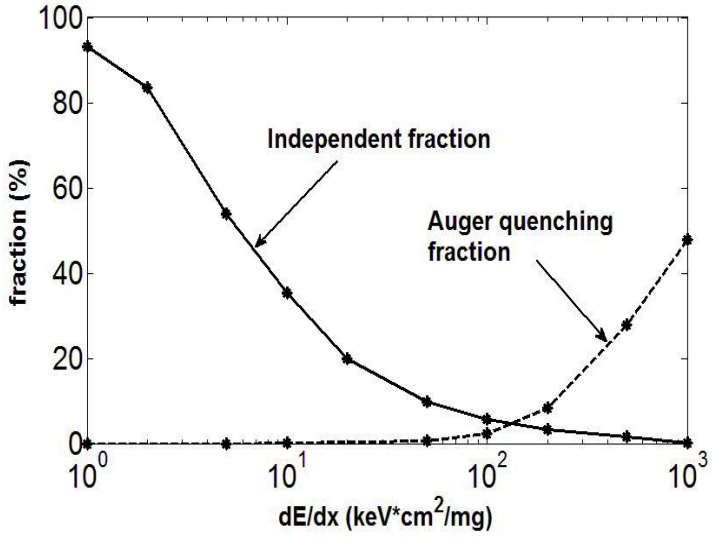

Fig. 2. The dashed curve shows the fraction of geminate e-h pairs driven to trap on activators as independent carriers by differential diffusion displacement of electrons and holes in CsI:0.3%Tl, versus *dE/dx*. The solid curve plots the fraction of carriers quenched by Auger recombination within 10 ps, also vs *dE/dx*. The Auger quenching fraction in Ge is terminated rapidly by diffusion diluting carrier density in the track, and amounts to $< 10^{-6}$ in 10 ps at all *dE/dx* shown.

Yet another lesson that is evident from the comparison in Fig. 1 is the variability of the electron radius contour along the excitation density axis for CsI:Tl, which corresponds to a variation along *dE/dx* or along the particle track. It is fairly well accepted that any properties affecting light yield which vary along the length of an electron track will contribute to nonproportionality. The electron distribution in a material like CsI with immobile holes is shaped like a funnel coming down to its small dimension at the track end. The excitation density is already highest at the track end due to a maximum in *dE/dx* at the valence plasmon energy, but the spatial confinement of electrons preferentially at the small end of the funnel doubly accentuates the rate of nonlinear quenching near the track end compared to earlier parts. Interestingly, HPGe shows a funneling of the electron radial distribution in the opposite trend, but much weaker. This is understandable because $\mu_h > \mu_e$ in Ge, so the holes outrun the electrons

and leave net negative charge in the core. Then the drift and diffusion currents for electrons are both radially outward in Ge, and the drift term becomes relatively more important (hence the electron expansion faster) for high on-axis excitation density. Figure 2 plots the independent carrier fraction and the Auger decay fraction within 10 ps for CsI versus *dE/dx*. The independent carrier fraction has a similar dependence on *dE/dx* as does the electron radius contour, which is not surprising since independence is achieved essentially by the electron outrunning the hole during diffusion before trapping. The integrated Auger decay fraction within 10 ps in HPGe was found to be less than 10^{-6} at all *dE/dx* within the plotted range, i.e. negligible.

4. Conclusions

(a) When holes are immobile, electrons can still diffuse substantially beyond the hole distribution at on-axis initial concentrations such as n_0 = 2.5 x 10^{18} cm^{-3} characteristic of low *dE/dx* at the beginning of electron tracks. This separation of charge immediately reduces the prompt radiative recombination rate. Diffusion reaches a steady state balanced by drift in the self-established field within a few picoseconds. Both the e^{-1} radial extent and the time to achieve steady state *decrease* with increasing on-axis initial concentration. This can be visualized as a diffuse electron distribution which funnels down to a tighter radius toward the end of the track. The reason for this trend can be seen upon examining the n_0-dependence of the diffusion and drift terms in Eq. (1). Diffusion current is linear in n_0 through $\nabla n(\vec{r},t)$, whereas drift current is quadratic in n_0 through the product $n(\vec{r},t)E(\vec{r},t,q_{enclosed})$. Viewed another way in analogy to *n-intrinsic*

junctions, the space charge region becomes narrower as the concentration of ionized donors (self-trapped holes) becomes higher.

(b) When both carriers are highly mobile as in Ge, the radial diffusion in the high concentration gradient of the track will be fast and proceed without limit toward an asymptotically flat gradient. The side-by-side comparison to CsI illustrates the enormous difference in the quantitative rates of expansion and dilution of the carrier concentrations in the track for these two examples, one a highly proportional detector and the other exhibiting both the high- and low-*dE/dx* trends of nonproportionality. Taking Auger recombination as one nonradiative channel that can be compared in the two cases, the simulation confirms that diffusive dilution of carrier concentration renders Auger decay negligible in less than a femtosecond in HPGe, whereas in CsI the track-end diffusion properties actually accentuate the importance of nonlinear decay in that part of the track, thus aggravating nonproportionality.

(c) The simulations show that independent trapped carriers are favored in the low-*dE/dx* (high-E_γ) limit. Conversely, geminate (exciton) trapping is favored near the track end as emphasized for low E_γ. This is consistent with the study of light pulse shape dependence on γ-ray energy in CsI:Tl by Syntfeld-Kazuch et al [6], who resolved the scintillation light pulse in CsI:Tl into a fast, medium, and slow component. 660-keV γ rays produced relatively more amplitude in the slow (16 μs) component, whereas 6-keV x rays produced relatively more of the fast (700-ns) component. Over much of their tracks, the 660-keV γ rays will preferentially produce excitations in the lower density range such as $n_0 = 2.5 \times 10^{18}$ cm^{-3} , at which density our diffusion model shows that a majority of the geminate pairs will be ripped apart to independent status by differential

diffusion. They will tend to trap out on different Tl^{+} sites yielding Tl^{++} and Tl^{0} which enter into the slow hopping bimolecular recombination process. In addition to a slow route of recombination possibly being cut off by the shaping gate width, recombination by thermal detrapping provides additional opportunities for deep trapping or nonradiative recombination, so branching to this path preferentially in the early track suggests an explanation for the phenomenon of falling light yield at low dE/dx in alkali halides.[1] Conversely the 6-keV x rays have energy deposition dominated more by the track ends approaching densities of $n_0 = 2.5 \times 10^{20}$ cm^{-3}, where the simulations show that electrons and holes tend to remain paired and to be trapped on the same Tl^{+} site, entering promptly into monomolecular decay with the characteristic Tl^{+*} lifetime. Our demonstration of the separation of geminate e-h pairs into independent carriers by differential diffusion provides a microscopic mechanism consistent with the finding by Setyawan et al that near equality of μ_h and μ_e correlates generally with better proportionality.[7] Payne et al [8] have shown quite generally that exciton formation from free carriers will be favored increasingly at higher excitation density, as carriers become more likely to be found within the Onsager capture radius of the opposite charge. However this should go on in every material to some degree, so it is not obvious what distinguishes the alkali halide scintillators as the only ones showing the strong depression of light yield at low *dE/dx*. The diffusion-based ripping apart of geminate pairs discussed here introduces unequal carrier mobilities as a determining factor for finding depressed light yield at low *dE/dx*, and this does correlate with the deep hole self-trapping that is known to occur in the alkali halides. We have run model simulations with intermediate values of hole mobility, evaluating carrier independence at different trap-out times. While there is no space to

present those results here, we note that there occurs a rather distinct threshold versus decreasing μ_h/μ_e leading to pair break-up for decreasing *dE/dx*, and the fraction achieving independence depends on the trap-out time as well.

(d) The consideration of band carrier diffusion shows that light yield at the high-*dE/dx* end of the electron response curves becomes flatter if both μ_h and μ_e are large, and light yield at the low-*dE/dx* end becomes flatter if $\mu_h \approx \mu_e$ whatever their magnitude. The lesson with regard to these considerations is that the most proportional scintillators ought to have large and nearly equal electron and hole mobilities, as well as high light yield of course. **k·p** theory associates larger mobilities with smaller band gaps, so we should be led to look to smaller gaps for improved proportionality. For the best proportionality, this points full-circle back to the semiconductor detectors, thus to consideration of semiconductor scintillators in the broad sense. Luryi et al have discussed the prospects for semiconductor scintillators, including both advantages and challenges [9-11]. Kastalsky et al [12] and Luryi [11] point out that in a heavily doped semiconductor scintillator, radiation will effectively produce minority carriers against the large background of extrinsic majority carriers, so Auger recombination, while large, will be linear in the minority carrier concentration and so should not contribute to nonproportionality. The present work shows in addition that *even in intrinsic semiconductors* if the mobilities are high, Auger recombination is reduced to negligible or small levels by the rapid dilution of carrier density in the track due to diffusion. In summary, the present work points to additional reasons based on carrier diffusion that should render semiconductor scintillators highly proportional if the other issues of light extraction and light yield such as discussed by Luryi et al [9-12] can be worked out. In

any case, the traditional wide-gap scintillators represent the material class that **k·p** theory predicts should have some of the poorest mobilities, including the tendency toward self-trapping that comes with flat, narrow bands. Renewed effort at measuring mobilities in candidate materials and orienting searches toward narrower gaps and higher mobilities seems warranted in the quest for better proportionality.

Acknowledgements This work was supported by the National Nuclear Security Administration, Office of Defense Nuclear Nonproliferation, Office of Nonproliferation Research and Development (NA-22) of the U.S. Department of Energy under Contract No. DE-AC02-05CH11231.

REFERENCES

[1] G. Bizarri, W. W. Moses, J. Singh, A. N. Vasil'ev, R. T. Williams, J. Appl. Phys. 105 (2009) 044507:1-15.

[2] S. Kerisit, K. M. Rosso, B. D. Cannon, , IEEE Trans. Nucl. Sci. 55 (2008) 1251-1258.

[3] D. H. Auston, C. V. Shank, P. LeFur, Phys. Rev. Lett. 35 (1975) 1022-1025.

[4] B. P. Aduev, E. D. Aluker, G. M. Belokurov, V. N. Shvayko, phys. stat. sol. (b) 208 (1998) 137-143.

[5] G. Bertolini and A. Coche (eds.), Semiconductor Detectors (Elsevier-North Holland, Amsterdam, 1968).

[6] A. Syntfeld-Kazuch, M. Moszynski, L. Swiderski, W. Klamra, A. Nassalski, IEEE Trans. Nucl. Sci. 55 (2008) 1246-1250.

[7] W. Setyawan, R. M. Gaume, R. S. Feigelson, S. Curtarolo, IEEE Trans. Nucl. Sci. 56 (2009) 2989-2996.

[8] S. A. Payne, N. J. Cherepy, G. Hull, J. D. Valentine, W. W. Moses, Woon-Seng Choong, IEEE Trans. Nucl. Sci. 56 (2009) 2506-2512.

[9] S. Luryi, Int. Journ. High Speed Elect. and Syst. 18 (2008) 973-982.

[10] A. Subashiev, S. Luryi, "Semiconductor gamma radiation detectors: band structure effects in energy resolution" in Future Trends in Microelectronics: From Nanophotonics to Sensors to Energy, ed. by S. Luryi, J. M. Xu, A. Zaslovsky (Wiley Interscience, Hoboken, N. J.) (2010, in press).

[11] S. Luryi, presentation at 2010 Symposium on Radiation Measurements and Applications, Ann Arbor (May 24-27, 2010)

[12] A. Kastalsky, S. Luryi, B . Spivak, Nucl. Inst. and Meth. in Phys. Res. A 565 (2006) 650-656.

CHAPTER 3: A TRANSPORT-BASED MODEL OF MATERIAL TRENDS IN NONPROPORTIONALITY OF SCINTILLATORS

Qi Li, Joel Q. Grim, R. T. Williams, G. A. Bizarri, W. W. Moses

The following manuscript was published in *Journal of Applied Physics* in 2011. Qi Li performed all finite element method calculations and developed the 2D Poisson equation solver. Qi Li and R. T. Williams analyzed the results and prepared the manuscript. I thank G. A. Bizarri and W. W. Moses of Lawrence Berkeley Lab for helpful discussions and reading of the manuscript. Manuscript is reproduced with permission of American Institute of Physcis. Stylistic variations are due to the requirements of the journal.

ABSTRACT

Electron-hole pairs created by the passage of a high-energy electron in a scintillator radiation detector find themselves in a very high radial concentration gradient of the primary electron track. Since nonlinear quenching that is generally regarded to be at the root of nonproportional response depends on the 4^{th} or 6^{th} power of the track radius in a cylindrical track model, radial diffusion of charge carriers and excitons on the ~ 10 picosecond duration typical of nonlinear quenching can compete with and thereby modify that quenching. We use a numerical model of transport and nonlinear quenching to examine trends affecting local light yield versus excitation density as a function of charge carrier and exciton diffusion coefficients. Four trends are found: (1) nonlinear quenching associated with the universal "roll-off" of local light yield *vs dE/dx* is a function of the lesser of mobilities μ_e and μ_h or of D_{EXC} as appropriate, spanning a broad range of scintillators and semiconductor detectors; (2) when $\mu_e \approx \mu_h$, excitons dominate free carriers in transport, the corresponding reduction of scattering by charged defects and optical phonons increases diffusion out of the track in competition with nonlinear quenching, and a rise in proportionality is expected; (3) when $\mu_h << \mu_e$ as in halide scintillators with hole self-trapping, the branching between free carriers and excitons varies strongly along the track, leading to a "hump" in local light yield versus *dE/dx*; (4) anisotropic mobility can promote charge separation along orthogonal axes and leads to a characteristic shift of the "hump" in halide local light yield. Trends 1 & 2 have been combined in a quantitative model of nonlinear local light yield which is predictive of empirical nonproportionality for a wide range of oxide and semiconductor radiation

detector materials where band mass or mobility data are the determinative material parameters.

1. Introduction

Proportionality between scintillator light yield and incident gamma-ray energy is a prerequisite for achieving the best energy resolution consistent with counting statistics in a radiation detector.[1-5] Although it has been known for about 50 years that scintillator materials have an intrinsic nonproportionality of response, [6-10] efforts to understand the physical basis of nonproportionality in order to more efficiently discover and engineer materials with better gamma resolution have intensified in the last decade or so.[11-18] The motivation comes in part from the need for highly discriminating nuclear material monitoring and some types of security scanning, but improved resolution can also benefit medical molecular imaging and particle physics experiments.

It would be very useful if one or more material "design rules" for proportionality could be found. What we mean by a material design rule in this context is a predictive relationship between one independently measurable material parameter and a trend of response affecting nonproportionality, valid across a broad range of radiation detector materials. Such predictive trends or rules would be useful of themselves, but more so because their existence would suggest simple underlying physical mechanisms that can be tweaked and engineered for improved detector resolution.

The sheer number of physical interactions interspersed between gamma-ray energy deposition and the detection of scintillator light pulses, as well as the number of variations of scintillator materials that one can introduce, may make the existence of one or more simple material design rules seem unlikely. In fact, the scintillator nonproportionality problem has seemed so far to be particularly resistive to defining a

single trend that follows from independently measured physical parameters. Payne et al[11,18], Jaffe[19], and Bizarri et al[17], among others, have fit empirical parameterized models to nonproportionality data for a wide range of materials. The data can be fit with a moderate number of empirically determined parameters. For example, Payne et al[18] have fit electron yield data from the SLYNCI (Scintillator Light Yield Nonproportionality Characterization Instrument)[20] experiment for 27 materials using two empirical fitting parameters: in their terms a Birks parameter characterizing how strong the 2nd order dipole-dipole quenching term is, and a branching fraction $\eta_{e/h}$ of initial electron-hole excitations into independent carriers rather than excitons. What is missing so far is the ability to define or calculate those fitting parameters on the basis of independently measureable properties of the material. Bizarri et al[17] chose fitting parameters to be identified with a series of radiative and nonradiative rate constants and branching ratios, but the number of such rate and branching parameters is large and so far the independent measurements of them do not exist in a sufficiently broad material set to allow a good test. Gao et al[21] and Kerisit et al[22,23] have performed Monte Carlo simulations starting from the energy deposition processes. While important to ultimately achieving simulation of the precise light pulse in a given material, the results have not yet been extended to processes such as thermalized band transport of carriers on the ~ 10 ps time scale that we will show are important with respect to nonlinear quenching.

In 2009, we began looking at the effect that electron and hole diffusion occurring in thermal equilibrium within the extreme radial concentration gradient of high-energy electron tracks may have upon nonlinear quenching and the branching from electron-hole pairs to independent carriers.[24-26] Our interest was provoked partly by the anticipated

extreme sensitivity of high-order nonlinear quenching to small changes in the track radius given an initial deposited local carrier concentration on-axis. Since the carrier density is inversely proportional to the square of the track radius, second-order dipole-dipole quenching and third-order Auger quenching depend on the inverse 4^{th} and 6^{th} power, respectively, of a cylindrical track radius expanding by diffusion.[24-26] Even modest diffusion can have controlling influence on nonlinear quenching in such a case, and the extreme concentration gradient promotes substantial diffusion effects even on the ~ 10 ps time scale on which nonlinear quenching typically occurs.[25,27] The carrier mobilities therefore become candidates for physical material parameters that can control nonlinear quenching and through it, nonproportionality.

In section 3 of this paper, we will present results of a numerical model showing how the quenching rates and quenched fractions depend on the carrier mobilities and exciton diffusion coefficient as well as upon excitation density (dE/dx) along the track. It should be noted that carrier mobility is not a single parameter of the material. Electrons and holes have independent carrier mobilities. We will see that the lesser of the two mobilities is an important parameter, as is their ratio. In addition, many important scintillators are anisotropic crystals, so we consider effects of anisotropies in the carrier mobilities.

However, a practical problem for testing the predictions of our diffusion and quenching model against experiment is the scarcity of carrier mobility measurements among scintillators. Scintillators are, as a class, mostly insulators. This situation has arisen as a result of wanting transparency to visible and near-ultraviolet activator emissions, and furthermore selecting large enough host band gap to avoid ionization of

activator-trapped charges to either band edge. Although not impossible, the measurement of mobilities in insulators is challenging, particularly because of the typical lack of ohmic contacts, and so has been performed only in a few inorganic scintillators -- notably the alkali halides[28] including CsI[29] and NaI.[30] In contrast, good mobility data exist for the charge-collecting solid-state radiation detectors such as high-purity germanium (HPGe).[31] Therefore in Refs.[24-26] we used the known mobility data for CsI and Ge with measured rate constants for dipole-dipole[25-27] and Auger recombination[32] to compare our model simulation of nonlinear quenching and its dependence on excitation density (*dE/dx*) in these two paradigms of radiation detectors. The agreement of the model simulation with experiment was very good. The model predicts that carrier diffusion is confined tightly near the track end in CsI:Tl, causing a nonlinear quenched fraction of ~ 60% simulated near the track end. This can be compared with the results of K-dip spectroscopy on the similar scintillator NaI:Tl[33], which shows ~52% quenched at the track-end (~50 eV). In sharp contrast, the high mobilities of both carriers in HPGe resulted in fast diffusion out of the track core, diluting the carrier density to a level that terminated Auger decay within 2 femtoseconds[24-26], rendering nonlinear quenching irrelevant for HPGe. This is in agreement with the excellent resolution of HPGe. Within this set of two materials representing nearly opposite extremes of carrier mobility, the modeled effect of diffusion on nonlinear quenching (~ nonproportionality) was both physically justified and predictive of experiment.

The group of Setyawan, Gaume, Feigelson, and Curtarolo has investigated the link between carrier mobility (actually band effective masses) and nonproportionality concurrently with our modeling studies.[34] Also faced with the scarcity of measured

mobilities or effective masses for most scintillators, they took the course of calculating electronic band structure for a wide range of scintillators in order to deduce effective masses from the band curvatures. They extracted experimental measures of nonproportionality from the literature and plotted the parameters versus the ratio m_h/m_e of the calculated (average) band masses for each material. Excluding most halide materials and also ZnSe:Te, the rest of the (largely oxide and two tri-halide) scintillators were found to fall on an empirical trend line in Ref. 34. A reason for the group of some halides and ZnSe to fall well off the primary trend line was suggested generally in terms of a classification of "excitonic" versus "non-excitonic" materials. They characterized the alkali halides as being excitonic, although Dietrich, Purdy, Murray, and Williams[35] have shown that in NaI:Tl and KI:Tl the majority of scintillation light comes from recombination of independent electrons and holes trapped as Tl^0 and Tl^{++} respectively, changing what had been earlier assumed in the model of Murray and Meyer.[9] Setyawan et al characterized most oxides including YAP ($YAlO_3$, yttrium aluminum perovskite) as transporting energy mainly by free carriers. With the halide and selenide exceptions noted, Setyawan et al found a significant degree of correlation between nonproportionality and the single parameter m_h/m_e coming from calculated band structure.[34] In particular, the materials typified by YAP and YAG ($Y_3Al_5O_{12}$, yttrium aluminum garnet), with $m_h/m_e \approx 1$, peaked up sharply in proportionality compared to the other oxides. Setyawan et al discussed possible reasons for a correlation between nonproportionality and m_h/m_e related to separation of charge carriers with different effective masses, but did not offer a quantitative model.

In the remainder of this paper, we will demonstrate the numerical model basis for trends in scintillator response depending on carrier mobilities. These will include the primary correlation of nonlinear quenching (specifically the amount of yield roll-off versus dE/dx) with the lesser of hole and electron mobility in a panoramic view. A basis for improved proportionality when $\mu_h=\mu_e$ will be described with the help of numerical simulations. We will also present the model basis for finding that the alkali halides have such a uniquely small value of the mobility ratio μ_h/μ_e, that the "hump" in electron yield occurs, and furthermore that it should *improve* the proportionality over what it would be without considering the light yield from independent carriers. Reasons for expecting hole self-trapping to occur generally in the class of halide scintillators and to lead to effects similar to alkali halides in the class as a whole will be discussed. Our recent work on modeling the *anisotropy* of mobilities in scintillators will be discussed. Within the class of halide scintillators, the materials with isotropic band masses empirically have the poorest proportionality while the anisotropic materials have better proportionality, becoming quite good in many of them such as SrI_2:Eu, $LaBr_3$:Ce, $LaCl_3$:Ce, KLC:Ce (K_2LaCl_5:Ce). The model suggests a reason. Finally, we will present a quantitative physical model of nonlinear local light yield which is predictive of empirical proportionality for a wide range of oxide and semiconductor radiation detector materials where band mass or mobility data are the determinative material parameters.

2. Modeling Method

We use time-step finite-element analysis to solve for the diffusion and drift currents, electric field, and local carrier density in the vicinity around the initial

cylindrical distribution of carriers with a radius of about 3 nm produced by the incident electron.[24-26] (Varying the initial radius from 2 to 5 nm had little effect.) The longitudinal dependence is neglected since the characteristic value for the electron track length is generally hundreds of micrometers; while the radial dimension is described in nanometers. The problem can therefore be solved in a cross-section of the track. We evaluate different longitudinal positions along the track by changing the initial carrier density (proportional to *dE/dx*). The equations used are

$$\vec{J}_e(\vec{r},t) = -D_e \nabla n_e(\vec{r},t) - \mu_e n_e(\vec{r},t)\vec{E}(\vec{r},t) \qquad (1)$$

$$\frac{\partial n_e(\vec{r},t)}{\partial t} = -\nabla \cdot \vec{J}_e(\vec{r},t) \qquad (2)$$

for electrons and an equivalent set of equations for holes, $\vec{J}_e$ is the electron number current density (electrons/cm^{2}s), n_e is the electron density (electrons/cm^3), $\vec{E}$ is the electric field. In our earlier simulations with isotropic mobilities[24-26], the electric field could be evaluated from Gauss's law. To handle anisotropic transport in this study, we use the Poisson equation

$$\nabla^2 \phi = -\frac{\rho(\vec{r},t)}{\varepsilon_0} \qquad (3)$$

A fast Poisson solving algorithm is introduced to calculate the potential and electric field at each time step and cell position, where $\rho(\vec{r},t) = e[n_h(\vec{r},t) - n_e(\vec{r},t)]$. The Einstein relation $D = \mu k_B T/e$ gives the diffusion coefficients for electrons and holes in terms of their mobilities μ_e and μ_h. The static dielectric constant ε is used in the Poisson equation.

If the carriers are paired as excitons at concentration n_{ex}, the bimolecular quenching rate due to dipole-dipole Förster transfer can be included in the simulation through the equation.

$$\frac{\partial n_{ex}(\vec{r},t)}{\partial t} = -k_2(t) n_{ex}^2(\vec{r},t) \tag{4}$$

where $k_2(t)$ is the bimolecular quenching rate parameter

$$k_2(t) = \frac{2}{3}\pi^{\frac{3}{2}} \frac{R_{dd}^3}{\sqrt{\tau_R}} \frac{1}{\sqrt{t}} \tag{5}$$

τ_R is the radiative lifetime of the excited stated and R_{dd} is the Förster transfer radius depending on the overlap of emission and absorption bands[36-38]. The fraction of quenched carriers (*QF*) at time τ after excitation is evaluated by

$$QF = \frac{\int_V \int_0^\tau k_2(t) n_{ex}^2(\vec{r},t) dt da dz}{\int_V n(\vec{r},0) da dz} \tag{6}$$

In the very high radial concentration gradient of the track, different diffusion rates of electrons and holes can control whether carriers pair as excitons or become independent. The average displacement of an electron at position $\vec{r}$ and time τ can be evaluated within the diffusion model as

$$\vec{d}_e(\vec{r},t) = \int_0^\tau \frac{\vec{J}_e(\vec{r},t)}{n_e(\vec{r},t)} dt \tag{7}$$

and similarly for holes. We will write the average relative displacement of electrons from holes at a given position and time τ as $\Delta d = \left|\vec{d}_e - \vec{d}_h\right|$. In the case of an activated scintillator, taking CsI:Tl for example, an important question is whether carriers become separated and trap on different Tl^+ producing Tl^0 and Tl^{++}, or whether they remain

geminate and trap together as Tl^{+*}. The time of interrogation τ should in this case be the average trapping time. The independent fraction (*IF*) is hence evaluated as

$$IF = \frac{\int_V n(\vec{r},\tau) \times \min(1, \frac{\Delta d}{s}) dadz}{\int_V n(\vec{r},\tau) dadz} \qquad (8)$$

where *s* is the average spacing between two nearest activators.

Separated and paired charges are subject to different dominant quenching processes, taken as 1st and 2nd order in excitation density, respectively, for the following reasons. The thermalized transport on which this model is based is not primarily the slow hopping transport of activator-trapped and self-trapped carriers during the several microseconds duration of a typical scintillator light output pulse in activated alkali halides. Rather, it is the fast thermalized band transport on the ~ 10 picosecond time scale of nonlinear quenching. The ~ 10 ps time scale of dipole-dipole STE quenching was measured at 2 x 10^{20} e-h/cm^3 excitation density in CsI.[25,27] Were it not for fast transport out of the track,[24-26] a similar time scale would apply for nonlinear quenching in Ge due to its measured Auger rate constant γ = 1.1 x 10^{-31} cm^6/s.[32] As illustrated in our modeled comparison of CsI and Ge, when diffusion of thermalized carriers can significantly dilute the carrier concentration within the track core within ~ 10 ps, the nonlinear quenching is curtailed.

In CsI:Tl, for example, independent trapped charges undergo de-trapping and re-trapping processes until they recombine as Tl^{+*} in order to yield luminescence. This is a different recombination path with different time dependence and perils for quenching or deep-trapping than in the alternate path taken by electron and hole initially trapped as a pair on the same thallium. The longer the path over which hopping migration of

independent charges must occur, the greater is the chance that one or both will encounter a trap that removes them from the light-emission process during the scintillation gate width. We incorporate this trapping hazard for migrating free carriers in the model as a linear quenching fraction k_1 that multiplies the independent carrier fraction *IF* to give the "Independent Nonradiative Fraction," *INF*:

$$INF = IF \times k_1 \qquad (9)$$

Since k_1 was assumed proportional to the migration path between charge-trapping activators, we should expect it to be proportional to [activator concentration]$^{-1/3}$. However, the independent fraction *IF* itself as defined in Eq. (8) depends inversely on the activator spacing *s*, and is thus proportional to [activator concentration]$^{+1/3}$. Thus to lowest order, *INF* is independent of activator concentration. However, the dependence on min(1,$\Delta d/s$) in Eq. (8) leads to moderate dependence on activator concentration at high concentration. We will extend this definition of *INF* to other activated scintillators in the model to be discussed.

In the context of this model, we define "simulated local light yield" (*SLLY*) as follows:

$$SLLY(normalized) = (1 - QF)(1 - INF) \qquad (10)$$

It predicts an upper limit of the local light yield as a function of initial carrier concentration. The most complete set of material parameters is available for CsI:Tl. The electron mobility in pure CsI has been measured as μ_e = 8 cm^2/Vs at room temperature.[29] The static dielectric constant of CsI is 5.65.[39] The trapping time of electrons on Tl^+ in CsI was measured as 6 ps.[40] The bimolecular quenching rate in CsI has been measured as $k_2(t)\sqrt{t} = 2.4 \times 10^{-15}\text{cm}^3\text{s}^{-1/2}$.[25,27] Due to the previously mentioned lack of mobility data

generally in other scintillators, we will in some cases scale mobility values from calculated band masses, and set missing parameters equal to the CsI values for all materials when attempting to illustrate trends versus mobility alone.

3. Material trends affecting nonproportionality based on the transport/quenching model

3.1 Nonlinear dipole-dipole and Auger quenching dependent on min(μ_h,μ_e)

Nonlinear quenching processes such as 2nd-order dipole-dipole transfer and 3rd order Auger recombination are widely regarded to be a root cause of nonproportionality. Therefore we plot in Fig. 1 the simulations of [1-*QF*(10 ps, n_0, μ)], the normalized fraction of electron-hole pairs surviving 2nd order quenching in CsI as of 10 ps. The time of evaluation was chosen because time-resolved measurements on CsI[25,27] showed that the main part of nonlinear quenching is complete in ~ 10 ps. The same measurements have supplied the 2nd-order dipole-dipole rate constant used in these simulations.[27] The curves are plotted versus the local excitation density on axis, n_0, and each curve is for a different value of carrier mobility, assumed for this plot to be equal for the electron and hole ($\mu = \mu_e = \mu_h$). The curves in Fig. 1 roll off toward high n_0 (or dE/dx) in a way very suggestive of the roll-off of electron yield curves[5,18,33] toward low electron energy. While these simulations are not actually electron light yield curves, they express the fundamental cause and generally the magnitude of the roll-off of light yield due to nonlinear quenching from which the main part of nonproportionality is thought to come. In the terminology used by Payne et al,[11,18] these curves are expressing the Birks term of exciton-exciton nonlinear quenching. The effect of carrier mobility within the quenching & transport model described above is very clear in Fig. 1. The underlying cause is simply

that highly mobile carriers can diffuse far enough in the typical 10 ps duration of nonlinear dipole-dipole quenching, that the resulting dilution of carrier density limits the quenching.

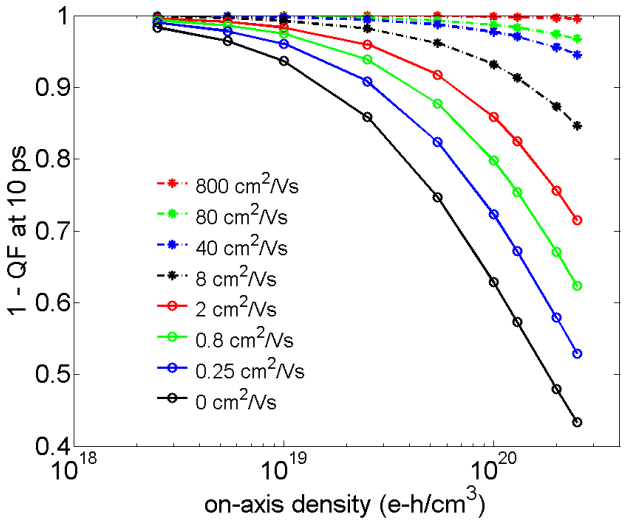

Fig. 1 Probability of survival against 2nd order quenching evaluated at 10 ps, plotted as a function of on-axis excitation density in an electron track deposited in materials having the electron and hole mobilities listed in the legend, in order of the curves from top to bottom. The dipole-dipole quenching rate parameter $k_2(t)$ was held at the value measured in CsI.[25,27]

In Fig. 2, we plot values of (1-*QF*) evaluated at an initial on-axis density of 1 x 10^{20} e-h/cm^3, as a function of carrier mobility (and diffusion coefficient, top) on a logarithmic scale from $\mu = 10^{-4}$ to 10^{+4} cm^2/Vs. Two schemes for handling electron and hole mobility together are compared. In the red continuous curve, $\mu_e = \mu_h$, with μ_h the plotted parameter. In the black broken curve, μ_e is held constant at the measured value of 8 cm^2/Vs for CsI,[29] and μ_h is the plotted parameter. The form of the curve is a high flat plateau for high mobility, a low flat plateau at value (1-QF_{max}) for low mobility, and a transition between them where the entire dependence of nonlinear quenching on min(μ_h, μ_e) occurs. The origin of the high plateau is that the mobility is high enough so that carriers escape the dense track before any significant nonlinear quenching can occur.

Semiconductor detectors such as HPGe (μ_e = 36,000, μ_h= 42,000 cm^2/Vs),[16] CZT (CdZnTe, $\mu_e \approx 1120$, $\mu_h \approx 45$ cm^2/Vs),[41] and CdTe ($\mu_e \approx 945$, $\mu_h \approx 45$ cm^2/Vs)[41] are on the high plateau. Notice that the dashed curve taking μ_e fixed at 8 cm^2/Vs does not approach 1 at high μ_h. This is simply because the modest electron mobility is constraining ambipolar diffusion out of the nonlinear quenching zone when $\mu_h > \mu_e$. The low plateau corresponds to mobilities so low that diffusion cannot compete with quenching, so nonlinear quenching occurs to the maximum extent QF_{max}.

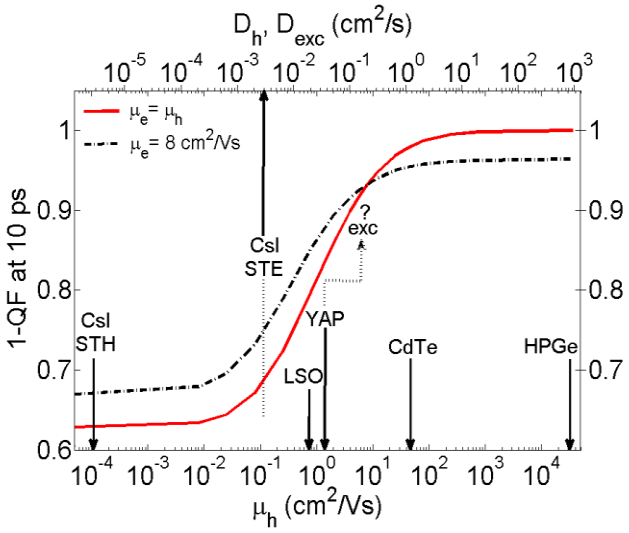

Fig. 2 Survival against 2nd order quenching evaluated at 10 ps for on-axis excitation density of 1 x 10^{20} e-h/cm^3, plotted as a function of hole mobility (bottom) and corresponding diffusion coefficient (top) over 8 decades. The solid curve varies the electron and hole mobility together ($\mu_e = \mu_h$), while the dashed curve keeps electron mobility constant at the value measured in CsI. Five representative radiation detector materials are indicated at their respective hole mobilities, as measured in HPGe[31] and CdTe[41], as deduced from measured self-trapped hole (STH) jump rate[22,42,43] at room temperature in CsI, and estimated from calculated effective band masses[34] in YAP and LSO. An additional marker (CsI STE) indicating the approximate diffusion coefficient of self-trapped excitons at room temperature is also shown.

The self-trapped hole mobility in CsI at room temperature (μ_{STH} = 1.0 x 10^{-4} cm^2/Vs) places it on the low plateau. A self-trapped exciton diffusion coefficient D_{STE} can be deduced from the estimated STE jump rate in CsI[22], as discussed in footnote 44. The value $D_{STE} \approx 2.7$ x 10^{-3} cm^2/s falls near the onset of the low plateau. In either case,

the low plateau appears to be where CsI belongs if we consider *only* the part of its light yield subject to nonlinear dipole-dipole quenching. This seems in disagreement with the data since CsI:Tl does not have worse proportionality than LSO:Ce, for example. But please note that we have so far looked at only the first of the trends, depending on the ability of the least mobile carrier to diffuse out of the nonlinear quenching zone. We shall see when discussing the third trend (Section 3.3), that *independent* carriers are responsible for a significant part of the light yield in CsI:Tl. Splitting geminate pairs into independent carriers because of different electron and hole diffusion rates is a second route protecting them from fast dipole-dipole quenching, and this will be shown to produce a "hump" in local light yield versus *dE/dx*. As a result, the nonlinear quenching (hence nonproportionality) is not as severe for CsI as the single trend in Fig. 2 seems to predict.

Looking at the mobility values constituting the low plateau in Fig. 2, it can be appreciated that only in cases of carrier self-trapping or deep defect trapping will such low mobilities be encountered. Mobilities corresponding to typical band masses, even heavy band masses, fall generally within the transition range of Fig. 2, as exemplified by YAP and LSO. The transition range corresponds to mobilities for which the time to diffuse out of the track is of the same order as the time for nonlinear quenching, so the two are in competition as channels to reduce the excited state concentration. The nonlinear quenching channel destroys excited states, whereas the diffusion channel merely dilutes them, preserving potential light yield.

Nonlinear yield (1-*QF*), and therefore nonproportionality, is a function of mobility in the transition range around $\mu_h \approx 1$ cm^2/Vs corresponding to $D \approx 0.025$ cm^2/s.

By its nature, superlinear decay proceeds rapidly at first but also diminishes rapidly as the population depletes. As noted earlier, the duration of the majority of dipole-dipole quenching in CsI is about 10 ps. We take that as the typical time for nonlinear quenching, τ_{quench}, for purposes of the general trend plot in Fig. 2. The initial track radius at the start of thermalized diffusion has been estimated as r_0 = 3 nm (in NaI) by Vasil'ev[17,36] and we have used it as the initial condition in our previous simulations.[24-26] These two values of τ_{quench} and r_0 fully determine the mobility range over which the transition between plateaus occurs, i.e. the range of dependence of the nonlinear yield (1-*QF*) on mobility or diffusion coefficient.

Upon finding the dependence of nonlinear quenching on carrier mobility exhibited in Figs. 1 and 2, we were at first hopeful that min(μ_e, μ_h) alone might account for the observed variations of nonproportionality. That general trend seems to be weakly manifested when we plot measures of nonproportionality simply versus band masses of the oxide and selenide materials using data from Setyawan et al.[34] But there is sharper detail of material-to-material nonproportionality occurring over smaller changes of m_h, m_e than can be attributed purely to the broader trend in Fig. 2. However, recall that there are 3 more trends depending just on mobility parameters, and other possible material dependences besides. Based just on the magnitude of the mobility effect on nonlinear quenching, we conclude that the gradual trend exhibited in Fig. 2 is an important one applying to all radiation detector materials. It distinguishes the nonlinear response of high-mobility semiconductor detectors from that of mostly oxide scintillators near the middle transition range, and from the scintillators with deep self-trapped carriers (generally halides) at the left end. Fig. 2 expresses the basic background dependence of

nonlinear quenching on how fast ambipolar diffusion can dilute the track core, with the other trends contributing finer detail.

Another example is the pair of scintillators YAP and LSO indicated as lying near hole mobility of ~ 1 cm^2/Vs in Fig. 2. This is the approximate value of hole mobility in these and the other oxide scintillators that we can estimate using the relaxation time approximation

$$\mu = \frac{e\tau_{SC}}{m^*} \qquad (11)$$

with values of hole effective band mass m_h* from the electronic structure calculations of Setyawan et al[34]. The scattering time τ_{sc} = 1.4 x 10^{-15} s is set at the value deduced for CsI from its measured conduction electron mobility[29] and theoretical effective mass.[34] Even with hole band masses differing by a factor 1.9, YAP (m_h* = 1.941m_0, m_e* = 2.335m_0) and LSO (Lu_2SiO_5, m_h* = 3.603m_0, m_e* = 0.545m_0) appear on the "global view" 8-decade mobility scale of Fig. 2 to be at almost the same mobility roughly in the middle of the transition range. But they have quite different proportionality. Setyawan et al listed parameters NP(10/662), representing ratios of light yield for 10 keV and 662 keV gamma rays, of 0.95 in YAP[45]. and 0.62 in LSO,[46] for example. So is Fig. 2 irrelevant? No. We think it correctly predicts where most of the oxide materials (with mobilities proportional to band mass) lie in nonlinear quenching relative to the semiconductor detectors occupying the upper plateau, and relative to how bad CsI would be without trend #3. YAP has an exceptional degree of proportionality relative to its oxide group, which we will attribute in the next section to its having the mobility ratio μ_h/μ_e uniquely close to 1 among current scintillators. This same conclusion was reached empirically by Setyawan

et al plotting NP(10/662) against m_h/m_e.[34] The next section presents a physical mechanism.

3.2 Branching between excitons and independent carriers as a function of μ_h/μ_e

In Section 2, we described the algorithm by which our model of transport in the track region evaluates which pairs will be separated by their different diffusion rates before trapping on activators as independent carriers, and which will remain paired as excitons transporting energy to the activators. Figure 3 plots the independent fraction, *IF*, of carrier pairs created at excitation density n_0 according to the model described in Section 2. It is applied to CsI:0.1%Tl, where all parameters are as measured for CsI except that the hole mobility is declared variable in order to generate the set of model curves plotted. The electron mobility is held constant at the CsI value of 8 cm^2/Vs. The hole mobility varies from 10^{-3} to 10^{+2} cm^2/Vs as plotted on the horizontal axis. The three figures (a-c) are evaluated at three different trapping times: 0.6 ps, 6 ps, and 60 ps. The characteristic time for trapping on the activator is important, because the longer the carriers migrate in the electrochemical potential gradient of the electron track, the more likely they are to become independent. We have experimentally measured 6 ps as the time for electrons to trap on Tl^+ producing Tl^0 in CsI at room temperature,[40] so we direct attention to Fig. 3(b) evaluated at 6 ps.

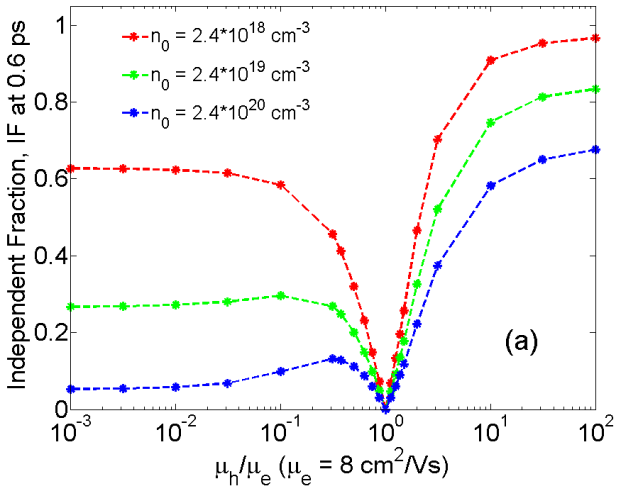
Independent Fraction, IF at 0.6 ps
n_0 = 2.4*10^{18} cm^{-3}
n_0 = 2.4*10^{19} cm^{-3}
n_0 = 2.4*10^{20} cm^{-3}
(a)
μ_h/μ_e (μ_e = 8 cm^2/Vs)

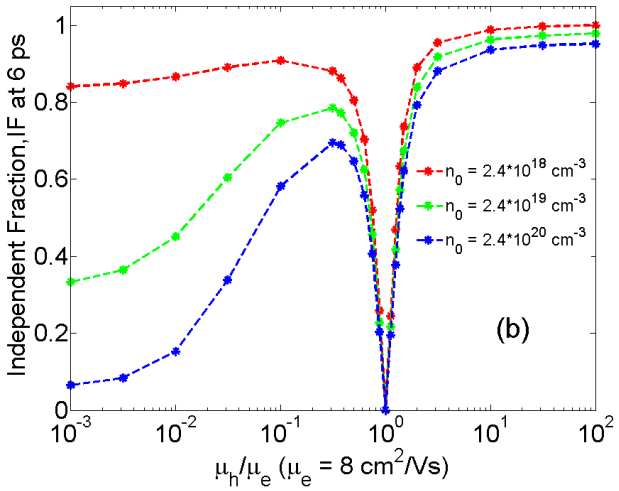
Independent Fraction,IF at 6 ps
n_0 = 2.4*10^{18} cm^{-3}
n_0 = 2.4*10^{19} cm^{-3}
n_0 = 2.4*10^{20} cm^{-3}
(b)
μ_h/μ_e (μ_e = 8 cm^2/Vs)

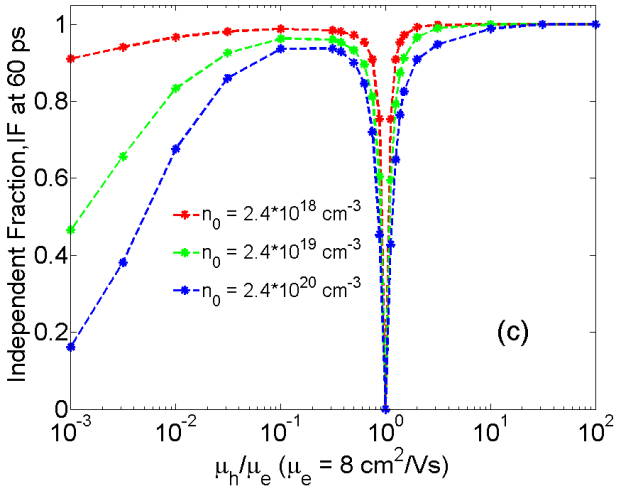
Independent Fraction,IF at 60 ps
n_0 = 2.4*10^{18} cm^{-3}
n_0 = 2.4*10^{19} cm^{-3}
n_0 = 2.4*10^{20} cm^{-3}
(c)
μ_h/μ_e (μ_e = 8 cm^2/Vs)

Fig. 3(a-c) Fraction of carrier pairs driven to independent charge carrier status by different electron and hole diffusion rates in the track, evaluated at (a) 0.6 ps, (b) 6 ps, and (c) 60 ps. The curves are plotted versus hole/electron mobility ratios where electron mobility is held at the CsI value. In each frame, three curves are shown spanning three decades of increasing on-axis excitation density from top to bottom: 2.4 x 10^{18}, 2.4 x 10^{19}, and 2.4 x 10^{20} e-h/cm^3.

The most obvious feature in Fig. 3 is the V-notch taking the independent carrier fraction, *IF*, to zero when electron and hole mobilities are equal. The fraction *IF* plotted in Fig. 3 is the fraction of created e-h pairs that are driven to independence by the differential e/h diffusion rate in the unusually strong carrier concentration gradient represented by electron tracks. In order to illustrate this branching from paired to independent carrier status driven purely by differential e/h diffusion rates, we have neglected the Onsager radius criterion for branching.[11,47] To the extent that the Onsager criterion for carrier pairing retains importance in the face of gradient-driven e-h separation, the V-notch in Fig. 3 should approach a small finite value rather than zero if it were included. We will examine in a future publication the "pairing decision contour" in the presence of a strong e-h concentration gradient and show that it should have a substantially smaller radius than is traditionally determined by setting the e-h pair coulomb energy to *kT*. The electromotive force or gradient of the sum of pair coulomb potential and local chemical potential[48] dominates pairing stability in the presence of a large radial track gradient.

The fraction *IF* corresponds in several ways to the parameter $\eta_{e/h}$ introduced by Payne et al[18] as one of two fitting parameters they used to fit a broad range of electron yield curves. The parameter $\eta_{e/h}$ was defined as the fraction of initial excitations that are "born" as independent carriers. ($\eta_{e/h}$ is the same as η_{EXC} introduced in the earlier Ref. 11.) In our view, the birth of carrier pairs in an environment such as an electron track should

include effects of a few picoseconds worth of diffusion in the extreme concentration gradient. With that proviso, our numerical model for *IF* amounts in some ways to a microscopic material model for $\eta_{e/h}$. However, *IF* and $\eta_{e/h}$ are not simply equivalent. In the Payne et al model, $\eta_{e/h}$ is the multiplier of a term that has variation along the track built in by the Onsager exponential term, which was taken as a fixed dependence for all materials.[18] In the present model, the branching fraction *IF* depends on excitation density and so varies along the track. It can be seen in Fig. 3 that the strong variation of *IF* with *dE/dx* (or n_0) occurs only for $\mu_h/\mu_e << 1$. We argue below that such small mobility ratios are encountered only (or mainly) in the case of self-trapped holes, which are found mainly in halides. For the majority of oxide scintillators, it is a pretty good approximation to regard *IF* as a constant for the track, like $\eta_{e/h}$. But notice that it is a constant close to the value 1 in such cases, predicting mainly independent carrier status for most oxides *in the environment of a radial track gradient*. Summarizing for all materials, our numerical model predicts that except for the "notch" where $\mu_h/\mu_e \approx 1$ (as well as the left side of the plot with $\mu_h/\mu_e << 1$ *and* taking n_0 large), the independent carrier fraction $IF \approx \eta_{e/h}$ generally has a value near unity indicating that *independent carriers dominate energy transport generally in the presence of a strong carrier gradient like the particle track*! This is even true for alkali halides, consistent with the much earlier finding by Dietrich et al.[35] in KI:Tl and NaI:Tl and more recently by Yakovlev et al[49] and Williams et al[40] showing the importance of Tl^0 trapped electrons in excited CsI:Tl. The left side of Fig. 3, where $\mu_h/\mu_e << 1$ causing IF to vary strongly along the track, accounts for the characteristic "hump" found in the electron yield curves of primarily halide scintillators, but that is the third trend, to be discussed in Section 3.3.

Focusing back on the notch seen in Fig. 3(b), our transport model in the track predicts that only for $\mu_h/\mu_e \approx 1$ will the fraction IF ($\approx \eta_{e/h}$) predict dominance of paired carriers (excitons) in energy transport. The finding of an empirical correlation between nonproportionality and the band mass ratio m_h/m_e by Setyawan et al[34] coupled with the sharp V-notch of carrier pairing around $\mu_h/\mu_e = 1$ in Fig. 3, provokes us to look for a reason why exciton transport should give better proportionality than free carrier transport. The reason that we suggest is rooted in the transport & nonlinear quenching model outlined previously, including the first trend discussed in Section 3.1. In addition to what the band mass may predict about the mobility, the real mobility is strongly influenced by scattering, according to Eq. (11) introduced earlier. Independent charge carriers should have strong scattering cross-sections with charged defects[30] and with optical phonons[28,51], whereas neutral excitons may be expected to have smaller scattering cross sections with both[52]. As a hypothesis based on the importance of long-range coulomb scattering, we propose that the diffusion coefficient for energy transport out of the dense nonlinear quenching zone of the track rises when the carriers are excitons rather than free charge carriers. This would move a material with exciton transport in the track environment to the right and upward on the nonlinear quenching trend plotted in Fig. 2, as suggested for YAP by the dashed upward arrow pointing to an exciton diffusion coefficient larger than its carrier mobilities would suggest. Other than YAP, with $m_e/m_h = 1.20$, there are no other scintillators for which band structures have yet been published showing $m_h/m_e \approx 1$. YAG, with a ratio $m_h/m_e = 1.81$, is the closest case among oxides, and it's relatively good proportionality does support the hypothesis. $LaBr_3$, $LaCl_3$ will be discussed separately along with other halides subject to hole self-trapping. It is hard to perform a statistical

test of this trend with so few available examples. But YAP has always seemed exceptional in exhibiting significantly better proportionality than neighboring scintillator hosts with similar structure and chemistry. The fact that it has a nearly unique mobility ratio $\mu_h/\mu_e \approx 1$ and that there is a physical hypothesis relating this to the transport rate out of the track supports its exceptional proportionality. The rarity of examples like YAP supports our conclusion above, that in the special track environment of a scintillator in use, free carriers usually dominate the energy transport. Excitons get ripped apart in the electrochemical gradient of the track unless the material falls in the V-notch (Fig. 3) of $\mu_h/\mu_e \approx 1$.

It was pointed out earlier that our model as presented here ignores the Onsager radius criterion[11,47] for determining whether carriers form excitons or not. That is why the independent carrier fraction in Fig. 3 goes all the way to zero when $\mu_h/\mu_e = 1$. The Onsager radius is found by equating the exciton coulomb binding energy to kT. If an electron is placed close to that radius relative to a hole and given a significant time to statistically explore the area without additional influences, it should eventually settle toward the hole. But in an electron track it does not have that quiet time to make the decision. The electron and hole are on a steep concentration gradient introducing an electrochemical potential gradient.[48] The transport-governed statistical constraints on motion of the carriers outweighs the Coulomb potential over a considerable fraction of the volume within the conventional Onsager sphere, and will win in that volume fraction. We have modeled the random walk of an electron and hole in a radial electrochemical potential gradient representative of a track. The decision radius r_d for stability of the electron-hole pair becomes quite small in the range of $n_0 \approx 4 \times 10^{19}$ e-h/cm^3. The volume

of the decision sphere for survival of a geminate pair is proportional to r_d^3. Details of this simulation will be described in a future publication.

3.3 Variation of carrier independence along the track when μ_h/μ_e << 1, leading to the "hump" for halides

Please focus again on Fig. 3, this time at the left side for mobility ratios μ_h/μ_e << 1. Since the ratio of band masses m_h/m_e compiled by Setyawan et al[34] falls generally within one decade, it may be asked whether factors μ_h/μ_e << 1 are even relevant to experiment. The answer is yes, when self-trapping or small polaron effects come into play.

The one material class in which deep self-trapping of holes is well documented and almost universal is the alkali halides, and then as a further generalization, we may suppose it is similar for most metal halides. The reason for the generalization is fundamentally the highly reactive nature of a halide ion with a photogenerated hole in its valence shell, coupled with the tendency of the halide ions to be packed close to other halide neighbors ready for dimerization, due to the fact that the halide is often the largest-radius component of its highly ionic lattice.[52] Setyawan et al found that the halides formed a separate cluster off their main trend line of nonproportionality versus band mass ratio, where the trend line versus m_h/m_e was deduced primarily for the oxides. The lanthanum tri-halides fell close to their trend line because the electron mass is unusually large in those, rendering the mass ratio close to unity. But if the hole self-traps in the lanthanum tri-halides, the actual mobility ratio will be much different from the band mass ratio. More detailed study of hole self-trapping is needed for many of the halide scintillators. Fortunately, self-trapped holes have been thoroughly studied in the alkali

halides, so we concentrate on alkali halides and specifically CsI in model simulations to illustrate trend #3.

In the plots of Fig. 3, the appropriate carrier mobility ratio for CsI is μ_{STH}/μ_e = 1.2 x 10^{-5}, using the self-trapped hole mobility rather than the hole band mobility. Taking μ_{STH} = 1.0 x 10^{-4} cm^2/Vs for CsI, it can be seen from Fig. 3(b) that the independent carrier fraction *IF* depends strongly on excitation density, represented equivalently by n_0 or *dE/dx*. Therefore at the left side of Fig. 3(b), where $\mu_{STH}/\mu_e << 1$, the independent carrier fraction changes strongly along the primary electron track. The same point is illustrated in another plotting format in Fig. 4 showing *IF* as a function of n_0 for the fixed CsI mobility values. As discussed previously in Refs.[24-26], the reason for this behavior is the drift term in the diffusion-drift equation for current. The drift term is quadratic in n_0 whereas the diffusion term is linear, so drift keeps electrons and holes confined together at high n_0 excitation densities.

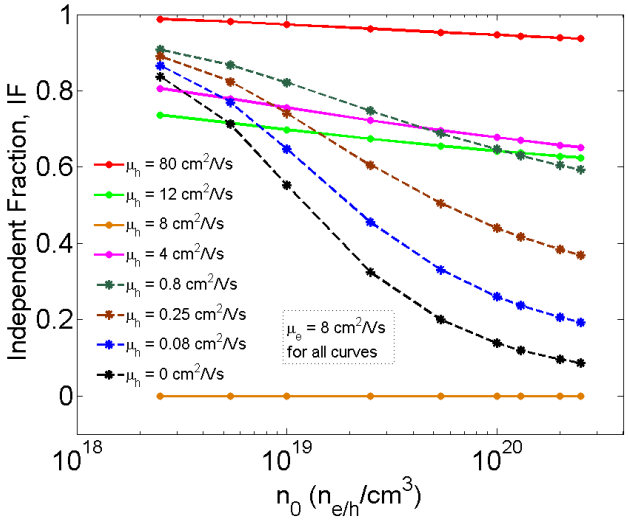

Fig. 4 Carrier fraction driven to independence by differential e/h diffusion rates, plotted versus on-axis excitation density n_0. Since n_0 is proportional to *dE/dx*, this suggests how *IF* should vary along the length of a track for different mobility ratios. Curves are plotted for different μ_h as shown in the legend, holding μ_e constant at the measured CsI value.

To relate the independent carrier fraction to quenching and light yield, we hypothesized in Section 2 that after being independently trapped on different activators (or defects), the carriers hop thermally back toward recombination and during that time are exposed to the hazard of being linearly quenched on deep traps or nonradiative recombination centers. We have represented this linear quenching process in the model by defining the Independent Nonradiative Fraction, *INF*, as the product of a linear trap quenching factor k_1 times the Independent Fraction, as given previously in Eq. (9). Then (1-*INF*) is the normalized probability of surviving the linear trap quenching hazard after carriers become independent. We do not yet have all the information necessary to calculate k_1 from material parameters (requiring knowledge of defects and their cross sections). However, the values of k_1 and of k_2 (nonlinear dipole-dipole quenching) are constrained together by an upper bound. That upper bound is imposed by the total light yield of the crystal expressed in terms of excitation number $E/\beta E_{gap}$, where β is a constant of typical value 2.8. In CsI, k_2 has been measured experimentally,[25,27] so the yield constraint is fully on k_1. In a crystal like SrI_2 which already has a light yield close to the theoretical limit,[15] the constraint on k_1 and k_2 is tight. This is in effect a second reason, beyond counting statistics, why very high light yield should imply good proportionality.

In Fig 5, we plot probability of surviving 2nd order quenching, [1-$QF(n_0)$] and probability of surviving independence and linear quenching, [1-$INF(n_0)$], for CsI:0.1%Tl at 10 ps with fixed electron mobility of 8 cm^2/Vs and a range of assumed hole mobilities as shown. Increasing hole mobility corresponds to the [1-*QF*] curves from bottom to top. Increasing hole mobility corresponds generally to the [1-*INF*] curves ordered top to bottom except near $\mu_h = \mu_e$.

In Fig.6, we plot the product [1-*INF*][1-*QF*] to represent the approximate combined probability of an excitation surviving both nonlinear dipole-dipole quenching and conversion to independent carriers with exposure to linear quenching.

Within a multiplicative constant, the rate of survival against these two quenching hazards should approximate the rate of light emission at the specified excitation density. (We will justify this approximation in Section 3.5.) So Fig. 6 represents simulated local light yield (*SLLY*) as a function of excitation density n_0 (proportional to *dE/dx*). Although not an actual electron yield curve, the local light yield versus excitation density should have qualitative similarity to electron yield curves, and in fact the curve in Fig. 6 for the actual CsI hole mobility $\mu_{hST} \approx 10^{-4}$ cm^2/Vs bears considerable qualitative resemblance to the CsI experimental electron yield curve, complete with the characteristic hump.

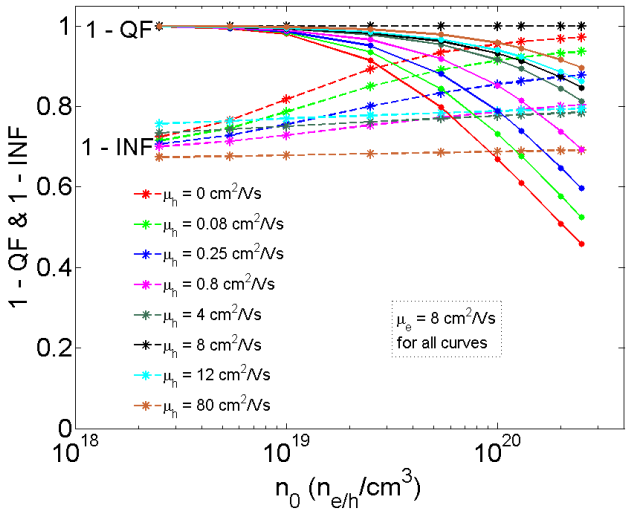

Fig. 5 The probability of surviving 2nd order quenching in 10 ps (1-*QF*) and the probability of surviving the independent carrier route with linear quenching (1-*INF*) are plotted versus on-axis excitation density. The listed hole mobilities increase from bottom to top for (1-*QF*) curves and in a more complicated fashion depending on μ_h/μ_e but roughly top to bottom for (1-*INF*).

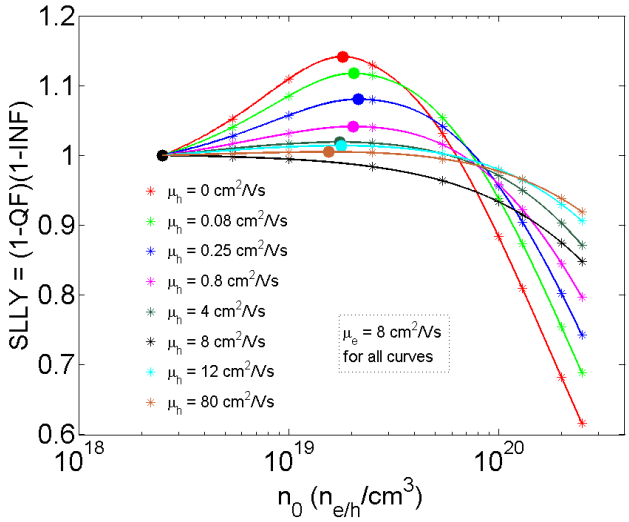

Fig. 6 The product of the two curves in Fig. 5, (1-*QF*)(1-*INF*) is plotted for each hole mobility listed, while keeping μ_e at the CsI value. Increasing μ_h corresponds monotonically to increasing height of the "hump" in this simulated local light yield versus on-axis excitation density (proportional to *dE/dx*).

Notice from Fig. 6 that the hump becomes most pronounced when the hole/electron mobility ratio is very small, as is realized only with deep hole self-trapping found in the alkali halides. More shallow hole self-trapping would lead to the shallower humps shown. The peak of the hump is marked with dots in Fig.6. Notice that changing μ_h/μ_e scales the height of the hump, but the lateral shift of the n_0 value at which the peak of the hump occurs does not have a monotonic dependence on hole mobility.

The effect of the hump on nonproportionality would reasonably come from how it changes the slope of light yield *vs dE/dx* at values of *dE/dx* that matter most. The meaning of the latter qualification is that in scintillators (like the oxides) for which there is no hump, the entire light yield curve is monotonically decreasing with *dE/dx*, like the (1-*QF*) curves in Fig. 1, or like the experimental electron yield curves for oxides. Then the only region of the local yield curve approaching zero slope is the very low excitation density near 10^{18} e-h/cm^3. Vasil'ev has shown that particularly in the high energy (low

dE/dx) part of the trajectory, the energy deposition is clumpy, producing clusters of roughly 3 to 7 electron-hole pairs at each event.[53,17] Gao et al find a similar phenomenon of clumpy energy deposition in Monte Carlo simulations.[21] It is only closer to the mid-range and track end that these clusters begin to overlap to such an extent that the cylindrical or uniform track model becomes truly valid. This means that there may not be so many carriers actually characterized by a local density as low as 10^{18} e-h/cm^3. If so, then by moving the zero-slope region of the local light yield curve squarely into the mid-range of excitation densities, the "hump" could indeed make a significant improvement in proportionality. Payne et al[11] previously made a similar suggestion about how the hump can empirically flatten the electron yield curve over part of its range. A particularly large hump as in the alkali halides will impose a proportionality cost of slope on the way up and on the way down. Therefore as a qualitative goal, a modest hump that puts the flat slope in a good place without introducing big slopes up and down would be ideal in this regard. Something like this might be at work in SrI_2, which we consider in detail under the fourth trend in Section 3.4. There we consider the trend that anisotropy of mobility can move the hump laterally along the *dE/dx* axis.

3.4 Trend produced by anisotropy of mobilities

The alkali halide scintillators CsI and NaI, the alkaline earth fluorides BaF_2 and CaF_2, the garnets YAG and LUAG, and BGO have cubic crystal structure and therefore isotropic mobilities. The majority of other scintillators, especially including high-performance materials in light yield and proportionality like $LaBr_3$, SrI_2, and KLC have noncubic crystal structures and therefore anisotropic mobilities. In the case of

anisotropic mobility and an arbitrary direction of the electron track, there will always be locally definable directions of fast and slow diffusion in the radial direction, usually different for electrons and for holes. One immediate consequence is that electrons and holes may be constrained by anisotropic mobilities to diffuse away from the track in orthogonal directions, producing charge separation and independent-carrier recombination kinetics even if the average magnitudes of their mobilities are similar. Particularly in view of the fact that many of the recent scintillators with very good proportionality have anisotropic mobilities, it is worthwhile to explore the trends affecting proportionality in that case.

Presently, our information on anisotropic mobilities in scintillator materials comes from consideration of effective masses from band structures, such as the survey of scintillator band structures by Setyawan et al[34] and calculations by Singh.[54] The relation between m and μ in the relaxation time approximation is

$$\mu_i = \frac{e\tau_{SC}}{m_i^*} \qquad (13)$$

where m_i* and μ_i are principal components of the tensors resolved along orthogonal axes, and τ is the momentum relaxation time. In CsI, where we know both theoretical m* and experimental μ, the value of τ at room temperature is found to be 1.4 x 10^{-15} s. We will regard this as typical for the scintillators. Often, the bands are degenerate at the band extrema, so that we need to take an average value of contributions to mobility. Setyawan et al[34] computed the average effective mass, which gives a different mobility than taking the average of mobilities (reciprocal effective masses). Their choice was influenced[55] by the fact that the band with larger mass has higher density of states. In our opinion, the rapid carrier scattering time typified by the value noted above assures constant mixing

between the nearly degenerate bands, diminishing the importance of the density of states argument. We have therefore estimated the average mobility as the product of $e\tau_{sc}$ and the average of reciprocal band masses. Working from the band structure diagrams published by Setyawan et al[34] and the assumed value of τ_{sc} = 1.4 x10^{-15} s based on CsI, we deduce approximate values of band mobility along the three orthorhombic axes in SrI_2 as listed in Table I. However, it should be noted here that there are several good reasons to believe that holes self-trap in SrI_2, so the band mobilities may not be quantitatively accurate in fitting the data. Nevertheless, the results should be instructive in a general way.

Table I Estimated conduction and valence band mobilities along the three orthorhombic axes in SrI_2, based on multiplying the average over reciprocal band masses for valence bands degenerate at Γ times $e\tau_{sc}$, where τ_{sc} = 1.4 x10^{-15} s was assumed based on CsI. The rows labeled SrI_2 model-1 (X,Y) are rounded values that were used in simulating "model SrI_2-1" in Figs. 7, 8, and 11. Values are also shown for CsI (cubic isotropic) and YAP (orthorhombic but almost isotropic) band masses.[34,52]

	m_e [m_0]	m_h [m_0]	μ_e [cm^2/Vs]	μ_h [cm^2/Vs]
CsI (band structure)	0.312	2.27	8	1.1
CsI (self-trapping)	0.312	2.5 x 10^4	8	1 x 10^{-4}
YAP (band structure & model-1)	~2.335	~1.941	1.1	1.3
SrI_2 (X- Γ-X)	0.303	0.62	8.2	4.0
SrI_2 (Y- Γ-Y)	0.301	5.699	8.3	0.5
SrI_2 (Z- Γ-Z)	0.259	12.076	9.6	0.2
SrI_2 model-1 (X)	0.312	0.62	8	4.0
SrI_2 model-1 (Y)	0.312	∞	8	0

Figures 7 and 8 display contour plots in the X-Y plane, taken to be transverse to the primary electron trajectory, of hole and electron distributions in SrI_2. The mobilities used are as given in the last two rows of Table I, evaluated after 6 ps of diffusion and drift. For comparison, we also plot carrier distributions in YAP with the mobilities of Table I and in CsI with isotropic electron and self-trapped hole mobilities listed in row 2

of Table I. The different views in Figs. 7 and 8, are for low ($2.5x10^{18}$ cm^{-3}) and high ($2.5x10^{20}$ cm^{-3}) on-axis excitation density n_0, respectively.

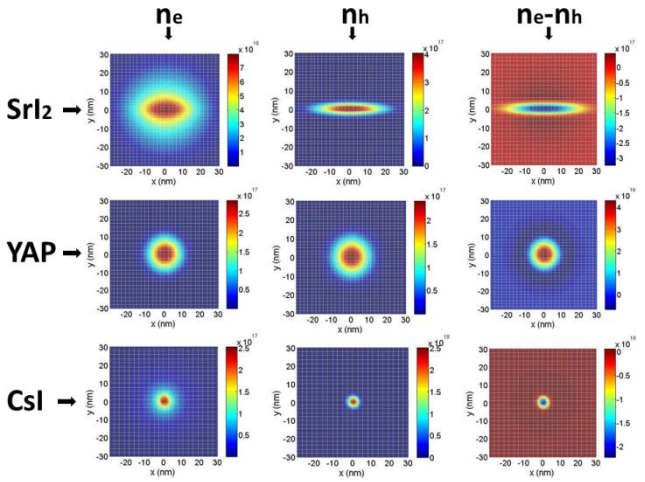

Fig. 7 Cross sections transverse to the track axis showing electron and hole concentration contours for "model SrI_2-1" with the anisotropic mobilities listed in Table I. Cross sections are also shown for YAP with estimated nearly isotropic mobilities listed in Table I, and for CsI with isotropic measured mobilities μ_e = 8 cm^2/Vs, $\mu_{STH} \approx 1 \times 10^{-4}$ cm^2/Vs. In the right hand column, shades of red represent $n_e - n_h > 0$, while shades of blue represent $n_e - n_h < 0$. The on-axis excitation density is 2.5×10^{18} e-h/cm^3.

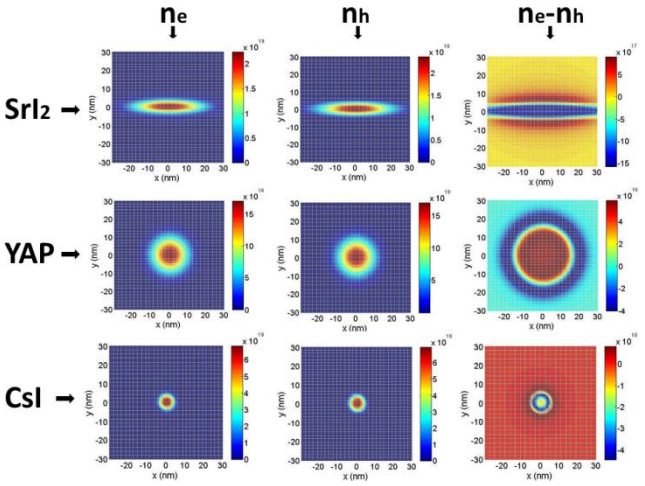

Fig. 8 Cross sections of carrier concentration profile corresponding to Fig. 8, but evaluated for on-axis excitation density 2.5×10^{20} e-h/cm^3.

Figure 9 plots (1-*INF*) and (1-*QF*) for different anisotropic hole mobilities in the range from isotropic to fully anisotropic, where the average hole mobility remains constant. The electron mobility was held constant and isotropic at 8 cm^2/Vs in all cases, while the hole mobilities were chosen to span the extremes from maximum anisotropy to isotropic, while keeping the average hole mobility constant.

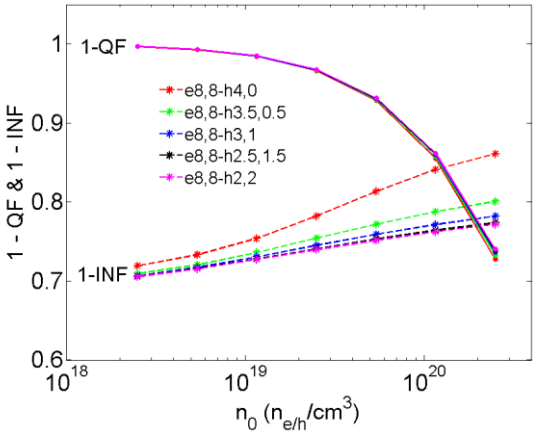

Fig. 9 Survival of the two modeled quenching routes is plotted versus on-axis excitation density for fixed isotropic electron mobility and variably anisotropic hole mobilities, where the average hole mobility is kept constant. The legend lists the four mobility parameters for each curve as μ_{eX}, μ_{eY}-μ_{hX}, μ_{hY}.

When the average hole mobility is kept constant as in Fig. 9, the quenching fraction *QF* is nearly independent of anisotropy. It is the Independent Fraction *IF* that depends on anisotropy for the parameters chosen in Fig. 9. This partly reflects electron and hole diffusion being directed along different crystallographic axes.

Fig. 10 plots the product (1-*INF*)(1-*QF*), indicative of simulated local light yield versus n_0 as discussed in Section 3.3. Five curves are plotted for the indicated combinations of variable anisotropic hole mobility and fixed isotropic electron mobility, where the average of hole mobility over the transverse directions is constant. Fig. 10 should be compared to Fig. 6, which plotted simulated light yield versus hole/electron

mobility ratio. We see only a weak halide "hump" in the curves of Fig. 10 because the average hole/electron mobility ratio is 0.5, but the hump is considerably accentuated for the most extreme anisotropy. The effect of anisotropy in Fig. 10 can be seen to shift the hump consistently toward higher n_0 as anisotropy increases. Thus as a trend, it appears that anisotropy can shift the "halide hump" laterally on the *dE/dx* axis. In qualitative terms, we may anticipate that shifting the hump toward higher *dE/dx* should improve proportionality by counteracting part of the steepest plunge in the nonlinear quenching curve (Section 3.1) that is common to all scintillators.

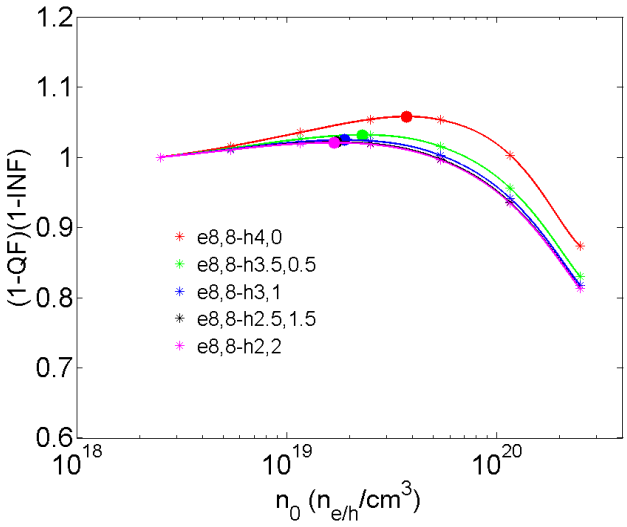

Fig. 10 Simulated local light yield for five assumed degrees of anisotropy in hole mobility, keeping the average hole mobility constant along with the isotropic electron mobility.

3.5 Simulated local light yield versus excitation density for some model scintillators

In Sections 3.1-3.4, we have illustrated four trends in scintillator response depending respectively on $\min(\mu_h,\mu_e)$, $\mu_h/\mu_e \approx 1$, $\mu_h/\mu_e << 1$, and μ_{hX}/μ_{hY}, μ_{eX}/μ_{eY}. In this section, we will use measured mobility parameters (CsI) and values estimated from band structure under approximations discussed above (YAP, SrI_2) for three representative scintillator materials to generate the simulated local light yield as a function of excitation

density, as it has been defined in our model. To justify why the product (1-*INF*)(1-*QF*) evaluated at 10 ps is approximately the local light yield, we first write down the local light yield in a more exact and intuitive form: $1 - (1 - IF)QF - IF(k_1 + AF)$. This states that the normalized local light yield is unity initial population (1) minus that part of the paired (exciton) fractional population ($1 - IF$) which has quenched by fraction *QF* at 10 ps due to 2nd order dipole-dipole interactions, minus the unpaired fraction (*IF*) which has quenched by linear fraction k_1 throughout the whole pulse or by the 3rd order Auger fraction AF which has quenched in 10 ps. Multiplying terms leads to $1 - QF - IFk_1 + IFQF - IFAF$.

The product $(1 - INF)(1 - QF) = 1 - QF - IFk_1 + IFk_1QF$ duplicates the first three terms of the more exact form, and is missing only the Auger quenched fraction of independent carriers (*IFAF*), which we chose to neglect for simplicity (and because Auger rates in scintillators have not been measured) in the present model. With that neglect, the only remaining difference between the two forms is the factor k_1 in the *IFQF* term. Therefore we represent the product $(1 - INF)(1 - QF)$ as approximately indicative of local light yield.

The mobility parameters for each material in Fig. 11 are given as a quartet of values: μ_{eX}, μ_{eY}; μ_{hX}, μ_{hY}. Because the assumption of $\tau_{sc} = 1.4 \times 10^{-15}$ s for all materials was a rough approximation relating band mass to mobility, we chose two trials of the scaling factor between m^* and μ in plotting Fig. 11, shown as YAP-1,2 and SrI_2-1,2.

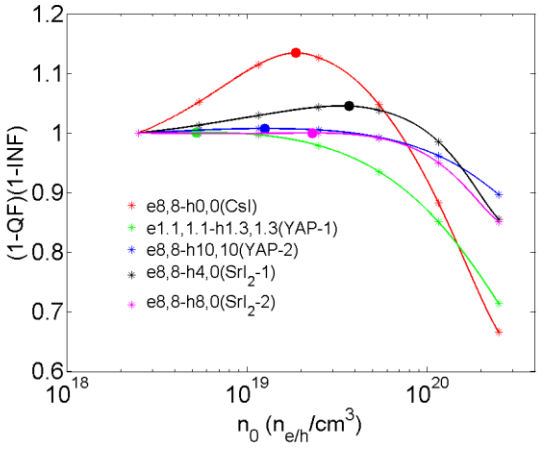

Fig. 11 Simulated local light yield at 6 ps for "model materials" with measured mobilities (CsI) or mobilities estimated with guidance from calculated band masses (YAP and SrI_2). The notation e8,8-h4,0 means, e.g., that the electron mobility is 8 cm^2/Vs in two orthogonal directions transverse to the track, and that the hole mobility is 4 cm^2/Vs on the X transverse axis and 0 cm^2/Vs on the Y axis.

There is an interesting similarity between the curves in Fig. 11 and the shape of experimental electron yield curves if the latter are imagined plotted as a function of *dE/dx* characterizing the suitable cascade average for an electron of the given energy. The curve for CsI:0.1%Tl is particularly significant. It was simulated with measured mobilities[29,42,43,22] and measured 2nd-order dipole-dipole quenching constant.[25,27] Only the linear trap quenching fraction k_1 was an assumed parameter at 0.33, and it is held constant at that value for all the materials plotted. The qualitative shape of the CsI curve bears considerable resemblance to the experimental electron yield for CsI. The distinguishing characteristic that fixes this shape for the CsI curve is the exceptionally low value of its hole mobility, coming from the well established deep self-trapping of holes in alkali halides.

Then, changing nothing else but the mobility parameters shown, and guided in that choice by the available calculated[34] values of m_e/m_h and of m_{eX}/m_{eY}, m_{hX}/m_{hY} for YAP

and SrI_2, it is again remarkable to us that the simulated local light yields plotted particularly for the τ_{sc} choices giving YAP-2 and SrI_2-1 take on the main qualitative characteristics of the experimental electron yield curves for their real namesakes.[18] Namely, "model-YAP" lacks the hump and has a very modest roll-off due to nonlinear quenching, for good overall proportionality. "Model-SrI_2" has a modest "halide hump" and also a modest roll-off due to nonlinear quenching, in line with its good experimental proportionality and its experimental electron yield curve.

The reader may be justifiably skeptical of the actual choices of the linear quench fraction k_1 and the scattering time τ_{sc}. But the significant fact demonstrated in Fig. 11 is that the simulated local light yield versus *dE/dx* can reproduce all the qualitative shapes exhibited by experimental electron yields for CsI, YAP, and SrI_2, by changing only the carrier mobilities, and doing so in a way that corresponds to experiment for CsI and is constrained partly by band structure for YAP and SrI_2.

3.6 Effective diffusion coefficient modeled on mixed excitons and free carriers in the track

The fundamental physical process governing variation of local quenching along the length of a track within the present model is how fast the dense excitations subject to nonlinear quenching in the track core can dilute their effective concentration by radial diffusion. Whether the diffusing species are excitons or free carriers, the dilution rate is governed by a diffusion coefficient,

$$D = \frac{kT\tau_{sc}}{m^*} \qquad (14)$$

where τ_{sc} is the scattering momentum relaxation time and m^* is the effective mass, as defined in introducing the similar Eq. (11) for mobility. Here we choose to deal with diffusion coefficient rather than mobility because we want to generalize to both neutral excitons and charge carriers. Making the simplifying assumption that τ_{sc} is roughly the same for both electrons and holes in a given scintillator, we note that the effective D for *ambipolar* diffusion of electrons and holes will be given by Eq. (14) with m^* being the larger of electron and hole effective mass. We will express this as $m^* = \max(m_h,m_e)$ in Eq. (14), analogous to $\min(\mu_h,\mu_e)$ used earlier in this paper.

Equation (14) also specifies the diffusion coefficient for excitons if we know the appropriate τ_{sc} and m^*. The appropriate effective mass is just the translational mass of the exciton, $m^* = m_{C.O.M.} = m_e + m_h$.[52] When m_e and m_h are very unequal, this reduces to approximately $\max(m_h,m_e)$, as for ambipolar diffusion discussed above. When $m_e = m_h$, then $m_{C.O.M.} = 2\ \max(m_h,m_e)$. But within this difference, which will not exceed a factor 2, we can regard the diffusion coefficient for excitons and for ambipolar carrier diffusion to have nearly the same dependence on the largest effective carrier band mass. The important physical generalization to realize is that even if (as is likely) energy diffuses simultaneously by excitons and free carriers in some mix, the diffusion rate still retains the same basic dependence on the reciprocal of the heaviest band mass! The difference between exciton and carrier diffusion coefficients in a given material just comes down to the scattering time τ_{sc} in lowest approximation.

In justifying trend #2, we pointed out that an exciton should resemble a neutral particle in regard to scattering interactions as its radius becomes small. There is ample evidence in the literature that τ_{sc} should be longer when long-range coulombic scattering

by charged defects[50] and optical phonons[51,52] is turned off. Having established that the diffusion coefficients of excitons and of ambipolar carriers are approximately equal within the proportionality factor of scattering time, we are able to represent the effective diffusion coefficient of the mixture of excitons and free carriers in the track simply in terms of the two scattering times τ_{EXC} and τ_e, and the fractional composition of the mixture. The premise of our model for trend #2 is that the branching between excitons and free carriers *(in the track environment!)* is dominated by mismatch of the rate of diffusion of electrons and holes. We approximate the exciton fraction in lowest order as proportional to the electron/hole mass ratio, m_e/m_h. The limits are reasonable, predicting maximum exciton formation (100% in this model) when there are no diffusional effects tearing them apart, and predicting 0% when electrons and holes have widely different diffusion rates. In a future publication, we will examine how the landscape of electrochemical potential (sum of coulomb potential and chemical potential)[48] supplants the landscape of pure coulomb potential in deciding the critical "Onsager radius" for pairing, and that it leads to a much smaller (and excitation density dependent) effective Onsager radius in the environment of an electron track.

Putting the above considerations together, we can write an effective diffusion coefficient for the "two gas" model of excitation transport as follows:

$$D_{eff} \approx \frac{kT}{\max(m_h, m_e)}\left[\min\left(\frac{m_e}{m_h}\right)\tau_{EXC} + \left(1-\min\left(\frac{m_e}{m_h}\right)\right)\tau_e\right]. \quad (15)$$

The meaning of $\min(m_e/m_h)$ is that the smaller of m_e/m_h or m_h/m_e should be used, since this is meant to be a measure of mismatch. For purposes of data fitting with a bare minimum of one semi-determined parameter τ_{EXC}, we can write the following even

simpler diffusion coefficient which retains similar reasonable limits of branching between excitons and free carriers over the m_e/m_h range for which it will be employed:

$$D_{eff} \approx \frac{kT}{\max(m_h, m_e)} \min\left(\frac{m_e}{m_h}\right)\tau_{EXC} \qquad (16)$$

In this expression, the combined factor $\min(m_e/m_h)\tau_{EXC}$ can be regarded as a variable τ_{sc} in Eq. (14) describing the mixture. The reason Eq. (16) works pretty well with only the one parameter τ_{EXC} is that the oxide, selenide, and semiconductor materials to which we will apply it (lacking self-trapping and so described by band masses) have a minimum m_e/m_h ratio of about 1/7. The best-fit τ_{EXC} turns out to be 6 times the empirical τ_e deduced for CsI and adopted as typical for other materials. Thus over its range of application, Eq. (16) resembles Eq. (14) with an effective scattering time proportional to the mass ratio. It works for fitting about as well as Eq. (15). It has the advantage of containing only one parameter to be determined from the data fit. Even that one parameter, τ_{EXC}, is constrained by how we expect it to relate to the more-or-less known τ_e.

Our purpose for developing a model for the effective diffusion coefficient of the mixture of excitons and ambipolar carriers expressed as functions of band masses is that Setyawan et al[34] have provided an extensive tabulation of calculated band masses along with extracting measured values of the parameter (1-σ_{NP}) from the literature describing proportionality, where σ_{NP} = 0 indicates perfect proportionality. The parameter σ_{NP} is defined[34] in terms of N measurements of light Yield at different gamma energies relative to Yield at 662 keV as

$$\sigma_{NP} = \sqrt{\frac{1}{N}\sum_{i=1}^{N}\left(1-\frac{Y_i}{Y_{662keV}}\right)^2} \qquad (17)$$

For convenience of reference, we have reproduced in Table II the list of all oxide and selenide materials for which Setyawan et al provided both calculated band masses and tabulated empirical σ_{NP} values deduced from the literature.[34] We exclude all the halide materials for now because the halides are likely to be governed by hopping transport of self-trapped species and therefore will not simply follow a trend specified by band masses.

Table II The first 3 columns are tabulated data from Setyawan et al[34] for all of the non-halide scintillators (ZnSe thru BGO) for which they calculated band masses (m_e, m_h) and extracted the proportionality parameter 1-σ_{NP} from the literature. The 4th column, D_{eff}, is the effective diffusion coefficient that we calculate from the effective mass data, using Eq. (16) with the value τ_{EXC} = 8.4 x 10^{-15} s. The diffusion coefficients for CdTe and HPGe are the measured values for free carriers, since the excitons in both materials are very shallow and are thermally ionized even in HPGe at 77 K.

Material	m_e [m_0]	m_h [m_0]	1-σ_{NP}	D_{eff} [cm^2/Vs]
ZnSe	0.146	0.949	0.924	0.065
YAP	1.941	2.335	0.975	0.142
LuAP	0.423	2.094	0.841	0.039
YAG	1.094	1.975	0.912	0.112
LuAG	0.979	2.432	0.864	0.066
YSO	0.699	3.795	0.796	0.019
LSO	0.545	3.603	0.784	0.017
BGO	0.599	3.022	0.776	0.026
CdTe			0.99	1.163
HPGe			1	238.8

Setyawan et al[34] have already plotted (1- σ_{NP}) versus the simple ratio min(m_e/m_h) [actually max(m_h/m_e) by their choice] and were the first to notice an empirical trend of the proportionality parameter (1- σ_{NP}) peaking at YAP, which has m_e/m_h closest to 1 among the scintillators. Having already discussed a rationale for that trend in Section 3.2, we now want to plot the empirical (1- σ_{NP}) values for all the scintillators and semiconductors in Table II. They will be superimposed on the model curve previously plotted in Section 3.1 (Fig. 2), expressing the rate of diffusion out of the track within the

10 ps time window of the majority of nonlinear quenching. The curve from Fig. 2, reproduced in Fig. 12 below is entirely determined by the empirical 10 ps quenching time window as measured in CsI[25,27] and the 3 nm initial radius[17] of the cylindrical electron track. The red curve common to both Figs. 2 and 12 was plotted for assumed equality of m_e and m_h and thus is approximate in that regard for the real data we will compare. There have been no adjustments in the curve of Fig. 2 to try to make it fit the empirical (1- σ_{NP}) data. The agreement of the empirical proportionality data and the model curve of nonlinear quenching is excellent considering the range of materials and diffusion coefficients and that there are no unrestricted parameters in either the quenching model or the D_{eff} model. The single parameter that could be regarded as a fitting parameter is the exciton scattering time τ_{EXC} used to get D_{eff} from the band masses, and we have remarked that it is restricted to be not too different from τ_e and should be larger than τ_e.

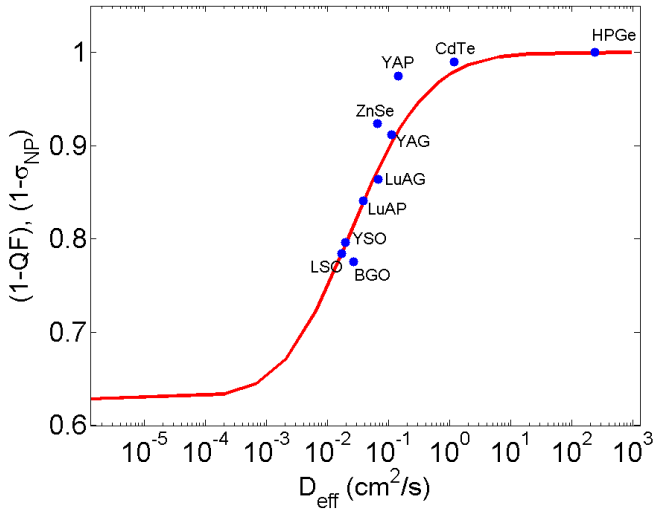

Fig. 12 Empirical measures of proportionality (1- σ_{NP}) tabulated by Setyawan et al[34] for the scintillators shown, together with points for CdTe and HPGe (77 K), are plotted versus effective diffusion coefficient, D_{eff}, deduced from calculated band masses[34] according to Eq. (16) with an assumed exciton scattering time τ_{EXC} = 8.4 x 10^{-15} s. The red curve is the plot of (1-*QF*), the survival probability against 2nd order quenching through 10 ps for on-axis excitation density 10^{20} e-h/cm^3 in a 3 nm Gaussian track. This is the same model curve presented earlier in Fig. 2.

One particular facet we want to point out is that ZnSe was a serious outlier when Setyawan et al[34] plotted (1- σ_{NP}) versus the simple ratio min(m_e/m_h); so much so that they grouped ZnSe together with the halides as a class behaving differently from the main trend. Comparing Eq. (16) with the simple mass ratio, it can be seen that max(m_h,m_e) in the denominator is an important factor that should not be neglected. ZnSe, a semiconductor, has significantly lighter hole and electron masses than the insulators comprising the rest of the table, and so appeared as an outlier in the plot of Ref. 34. Using the diffusion coefficient calculated from Eq. (16) pulls ZnSe right in line with the main trend. The dependence of D on reciprocal mass also takes what appeared to be a very sharp peak in the dependence of (1- σ_{NP}) on m_e/m_h in Ref. 34, and makes it a more gradual slope extending over a larger range of hole masses down to LSO, BGO in the plot versus D_{eff}, matching the model curve in Fig. 12. Speaking of the very sharp empirical peak in Setyawan's (1- σ_{NP}) plot near m_e/m_h = 1, we would like to refer the reader again to the V-notch in Fig. 3 plotting the branching fraction IF to independent carriers in this model.

If the more intuitive two-parameter equation (15) is used to calculate D_{eff} rather than Eq. (16), the quality of fit of (1- σ_{NP}) data points to the red curve is similar, but does not become dramatically better, despite having an additional fitting parameter. The fitting with two scattering times as defined in Eq. (16) yields τ_e = 4.7 x 10^{-16} s and τ_{EXC} = 8.4 x 10^{-15} s characterizing the whole family of fitted scintillators. Notice that the same exciton scattering time best fit value is obtained whether Eq. (15) or Eq. (16) is used.

4. Summary and Conclusions

1. We have presented a numerical model of diffusion and quenching in the track of a high-energy electron, in which the carrier mobilities, nonlinear dipole-dipole quenching rate, and linear defect quenching rate are the parameters. The magnitudes of the effects dependent on mobility are shown to be large enough to significantly affect the nonlinearity of light yield response.

2. We illustrated that combinations of the mobility parameters in the form of $\min(\mu_h,\mu_e)$, μ_h/μ_e, and μ_{hX}/μ_{hY}, each govern an identifiable trend in the dependence of quenching of radiation detector response on local excitation density and on variation of the defined mobility combination.

3. We have plotted a model-based simulation of how the nonlinear quenching fraction depends on the lesser of electron and hole mobility over a global scale of 8 decades that encompasses semiconductor radiation detectors on the right side, scintillators with deeply self-trapped holes on the left side, and oxide scintillators without deeply self-trapped holes in the middle, where the main dependence of nonlinear quenching on diffusion rate occurs.

4. We have identified a microscopic model basis for the observation by Setyawan et al that proportionality is improved for electron/hole mass ratios close to 1, particularly the notable case of YAP.[34] Our numerical model shows that differential diffusion rates in the strong radial gradient will separate electron-hole pairs into independent carriers for all electron/hole mobility ratios except $\mu_h/\mu_e \approx 1$ (and $\mu_h/\mu_e << 1$ when excitation density is high—see #5 below). It is the case of $\mu_h/\mu_e \approx 1$ that predicts excitonic energy transport in YAP almost uniquely among the oxide scintillators. Based

on the experimental fact that Setyawan et al saw the proportionality peaking sharply on YAP and YAG with mass ratios close to 1, we proposed that the remarkable proportionality of YAP follows from the dominance of exciton transport and the tendency that excitons, being neutral, should have higher mobility with respect to scattering from charged defects and optical phonons, than will free charge carriers. Based on trend #1 *vs* $\min(\mu_h,\mu_e)$ already noted, this increased mobility of excitons can help clear out the track core and limit nonlinear quenching, in agreement with the observation in YAP.

5. For the case of mobility ratio << 1, the numerical model predicts that the independent carrier fraction depends on local excitation density, with carrier pairs "ripped apart" by different diffusion rates of electrons and holes early in the track, but remaining paired toward the track end. This produces a light yield trend opposite to nonlinear quenching along the track, and so can have the effect of improving proportionality compared to what one would get from nonlinear quenching of excitons alone. This effect is responsible for the "hump" observed in halides. Band masses alone do not give mobility ratios small enough to get into this hump phenomenon. Band mass ratios typically stay within a decade of $m_h/m_e = 1$. The only way to get hole/electron mobility ratio suitably small to produce the hump is if the hole is deeply self-trapped. (It could be defect-trapped, but then the defect concentration would need to be of order 10^{20} cm^{-3} (~ 1%) to trap most of the holes in the track at once.) The only solid evidence for deep hole self-trapping in activated scintillators (excluding tungstate intrinsic scintillators) is in the alkali halides. As a chemical family, the halides are especially susceptible to self-trapping, so it is likely that the other halide scintillators have self-trapped holes too, but perhaps not as deep.

6. Many of the recent highly proportional scintillators are noncubic with anisotropic mobility. The simulations show that anisotropic mobility can cause electrons and holes to diffuse preferentially along different axes, and this provides another mechanism of spatially separating charge in the track. The unusual effect of anisotropy on simulated local light yield is to move the halide hump laterally toward higher *dE/dx*, which it can be argued may improve proportionality by placing the flat slope of the hump over the steepest part of the nonlinear quenching curve. Even more directly relevant should be the question of where the flat slope of local light yield falls relative to the quantitative spectrum of excitation density versus electron energy, e.g. from Monte Carlo simulations of energy deposition.

7. In short, there is a kind of hierarchy of mobility-dependent trends to look at. The combination of multiple trends depending on different mobility parameters and their ratios introduces apparent complexity of experimental nonproportionality versus mobility. We suggest that this may have disguised the importance of mobility and transport in past considerations.

8. The simulated local light yield as a function of excitation density is suggestive of the qualitative shape of experimental electron yield curves for modeled CsI, YAP, and SrI_2 with only one parameter per material adjustable within a limited range. The most general conclusion of this demonstration is that fast diffusion is a major determiner of local light yield within the model presented.

9. The model presented here is predicated on the importance of radial diffusion in diluting excitations in the dense core region before nonlinear quenching on the 10 ps time scale can take its toll. This leads to a model curve of nonlinear quenched

fraction at 10 ps versus effective diffusion coefficient spanning about 8 decades of exciton and carrier diffusion coefficient. By modeling the effective diffusion coefficient for a mixture of excitons and free carriers in each material determined by the corresponding band mass parameters or measured mobilities as appropriate, we can plot empirical proportionality data for oxide and semiconductor radiation detector materials on top of the model curve for survival of nonlinear quenching. The agreement is unexpectedly good. In our opinion, this is strong confirmation that diffusion of free carriers and excitons is the primary determinant of the variation of nonlinear quenching versus excitation density, and therefore of the material parameter basis of the main part of intrinsic nonproportionality.

Acknowledgements This work was supported by the National Nuclear Security Administration, Office of Defense Nuclear Nonproliferation, Office of Nonproliferation Research and Development (NA-22) of the U.S. Department of Energy under Contract No. DE-AC02-05CH11231. We thank Andrey Vasil'ev (Moscow State University) for many helpful discussions. We thank Steve Payne (Lawrence Livermore National Laboratory) for helpful discussions and for sharing Ref. 18 in advance of publication. We thank Arnold Burger (Fisk University) for helpful discussions and for experimental collaboration on work relating to this topic.

REFERENCES

[1] P. Dorenbos, J. T. M. de Haas, and C.W. E. van Eijk, IEEE Trans. Nucl. Sci. **42**, 2190 (1995).

[2] M. Moszynski, J. Zalipska, M. Balcerzyk, M. Kapusta, W. Mengesha, and J. D. Valentine, Nucl. Instrum. Methods Phys. Res. A, **484**, 259 (2002).

[3] J. D. Valentine, B. D. Rooney, and J. Li, IEEE Trans. Nucl. Sci. **45**, 512 (1998).

[4] W. W. Moses, S. A. Payne, W. –S. Choong, G. Hull, and B. W. Reutter, IEEE Trans. Nucl. Sci. **55**, 1049 (2008).

[5] M. Mengesha, T. D. Taulbee, B. D. Rooney, and J. D. Valentine, IEEE Trans. Nucl. Sci. **45**,456 (1998).

[6] C. D. Zerby, A. Meyer, and R. B. Murray, Nucl. Instrum. Methods **12**, 115 (1961).

[7] P. Iredale, Nucl. Instrum. Methods **11**, 340 (1961).

[8] A. J. L. Collinson and R. Hill, Proc. Phys. Soc. **81**, 883 (1963).

[9] R. B. Murray and A. Meyer, Phys. Rev. **122**, 815 (1961).

[10] J. R. Prescott and G. H. Narayan, Nucl. Instrum. Methods **39**, 51 (1969).

[11] S. A. Payne, N. J. Cherepy, G. Hull, J. D. Valentine, W.W. Moses, and Woon.-Seng. Choong, IEEE Trans. Nucl. Sci. **56**, 2506 (2009).

[12] S. E. Derenzo, M. J. Weber, E. Bourret-Courchesne, and M. K. Klintenberg, Nucl. Insrum. Methods in Phys. Research A **505**, 111 (2003).

[13] J. E. Jaffe, D. V. Jordan, and A. J. Peurrung, Nucl. Instrum. Methods Phys. Res. A **570**, 72 (2007).

[14] C. L. Melcher, Nucl. Instrum. Methods Phys. Res. A **537**, 6 (2005).

[15] P. Dorenbos, IEEE Trans. Nucl. Sci. **57**, 1162 (2010).

[16] M. Moszynski, A. Nassalski, A. Syntfeld-Kazuch, L. Swiderski, and T. Szczesniak, IEEE Trans. Nucl. Sci. **55**, 1062 (2008).

[17] G. Bizzarri, W. W. Moses, J. Singh, A. N. Vasil'ev, R. T. Williams, J. Appl. Phys. **105,** 044507 (2009).

[18] S. A. Payne, W. W. Moses, S. Sheets, L. Ahle, N. J. Cherepy, B. Sturm, S. Dazeley, "Nonproportionality of Scintillator Detectors: Theory and Experiment. II," manuscript to be published (2011).

[19] J. E. Jaffe, Nucl. Instr. and Meth. A **580**, 1378 (2007).

[20] W. –S. Choong, G. Hull, W. W. Moses, K. M. Vetter, S. A. Payne, N. J. Cherepy, and J. D. Valentine, IEEE Trans. Nucl. Sci. **55**, 1073 (2008).

[21] F. Gao, Y. Xie, S. Kerisit, L. W. Campbell, and W. J. Weber, Nucl. Instrum. Methods Phys. Res. A (2010), doi:10.1016/j.nima.2010.08.063.

[22] S. Kerisit, K. M. Rosso, B. D. Cannon, IEEE Trans. Nucl. Sci. **55**, 1251 (2008).

[23] S. Kerisit, K. M. Rosso, B. D. Cannon, F. Gao, and Y. Xie, J. Appl. Phys. **105**, 114915 (2009).

[24] Qi Li, Joel Q. Grim, R. T. Williams, G. A. Bizarri, and W. W. Moses, Nucl. Instrum. Methods Phys. Res. A (2010), doi:10.1016/j.nima.2010.07.074.

[25] R. T. Williams, J. Q. Grim, Qi Li, K. B. Ucer, and W. W. Moses, "Excitation density, diffusion-drift, and proportionality in scintillators," Phys. Status Solidi B, **248**, 426 (2011) / DOI 10.1002/pssb.201000610.

[26] R. T. Williams, Q. Li, Joel Q. Grim, K. B. Ucer, G. A. Bizarri and W. W. Moses, "Role of carrier diffusion and picosecond exciton kinetics in nonproportionality of scintillator light yield," Proc. SPIE 7805, 78050K (2010); doi:10.1117/12.861820.

[27] Joel Q. Grim, Qi Li, K. B. Ucer, R. T. Williams, and W. W. Moses, Nucl. Instrum. Methods Phys. Res. A (2010), doi:10.1016/j.nima.2010.07.075.

[28] R. K. Ahrenkiel and F. C. Brown, Phys. Rev. **136**, A223, (1964); G. T. Jenkin, D. W. Stacey, J. G. Crowder, and J. W. Hodby, "Electronic transport in alkali halides containing F centres," J. Phys. C: Solid State Phys. **11**, 1841(1978).

[29] B. P. Aduev, E. D. Aluker, G. M. Belokurov, V. N. Shvayko, Phys. Status Solidi (b) **208**, 137 (1998).

[30] S. Kubota, F. Shirraishi, and Y. Takami, J. Phys. Soc. Jpn. **69**, 3435 (2000).

[31] G. Bertolini, A. Coche (Eds.), Semiconductor Detectors, Elsevier-North Holland, Amsterdam, (1968).

[32] D. H. Auston, C. V. Shank, P. LeFur, Phys. Rev. Lett. **35**, 1022 (1975).

[33] I. V. Khodyuk, J. T. M. de Haas, and P. Dorenbos, IEEE Trans. Nucl. Sci. **57**, 1175 (2010).

[34] W. Setyawan, R. M. Gaume, R. S. Feigelson, and S. Curtarolo, "Comparative study of nonproportionality and electronic band structures features in scintillator materials," *IEEE Transactions on Nuclear Science***,** vol. 56**,** pp. 2989-2996 (2009).

[35] H. G. Dietrich, A. E. Purdy, R. B. Murray, and R. T. Williams, Phys. Rev. B 8, 5894 (1973).

[36] A. Vasil'ev, IEEE Trans. Nucl. Science, **55**, 1054 (2008).

[37] M. Kirm, V. Nagirnyi, E. Feldbach, M. De Grazia, B. Carre, H. Merdji, S. Guizard, G. Geoffroy, J. Gaudin, N. Fedorov, P. Martin, A. Vasil'ev, A. Belsky, Phys. Rev. B 79 (233103-1) (2009).

[38] V. Nagirnyi, S. Dolgov, R. Grigonis, M. Kirm, L.L. Nagornaya, V. Savikhin, V. Sirutkaitis, S. Vielhauer, A. Vasil'ev, IEEE Trans. Nucl. Sci. **57**, 1182 (2010).

[39] J. H. Schulman and W. D. Compton, Color Centers in Solids (Pergamon Press, Oxford, 1962).

[40] R. T. Williams, K. B. Ucer, Joel, Q. Grim, K. C. Lipke, L. M. Trefilova, and W. W. Moses, IEEE Trans. Nucl. Sci. **57**, 1187 (2010).

[41] J. C. Erickson, H. W. Yao, R. B. James, H. Hermon, and M. Greaves, Journal of Electronic Materials, vol. 29, No. 6, pp. 699-703 (2000).

[42] T. Sidler, J. –P. Pellaux, A. Nouailhat, and M. A. Aegerter, Solid State Comm. **13**, 479 (1973); R. Monnier, K. S. Song, and A. M. Stoneham, J. Phys. C: Solid State Phys. **10**, 4441 (1977).

[43] F. J. Keller and R. B. Murray, Phys. Rev. **150**, 670 (1966).

[44] The mobility of self-trapped holes in CsI at room temperature can be estimated from their thermal hop rate, which is $\tau^{-1} \approx 1.7 \times 10^{9}$ s^{-1} averaged over 180^{o} and 90^{o} jumps.[22,42,43] The respective distances δ for such jumps in CsI are 0.46 and 0.32 nm. Then diffusion coefficient $D_{STH} \approx \delta^2/\tau \approx 2.6 \times 10^{-6}$ cm^2/s and $\mu_{STH} \approx 1 \times 10^{-4}$ cm^2/Vs. Our CsI simulations published previously[24-26] took $\mu_{STH} = 0$ as an approximation. Kerisit et al[22] also estimated the room temperature hopping rate of self-trapped excitons (STE) in CsI. Since there are no direct measurements of this rate in CsI, they made the reasonable approximation that the ratio of STE/STH hopping rates in CsI would be similar to the ratio in NaI, which has been measured. From this ratio and fitting luminescence kinetics in CsI:Tl, they estimated a STE thermal hop rate of $\tau^{-1} \approx 1.8 \times 10^{12}$ s^{-1} in CsI at room temperature. Then $D_{STE} \approx 2.7 \times 10^{-3}$ cm^2/s.

[45] M. Balcerzyk, M. Moszynski, and M. Kapusta, *Proceeding of the 5th Int. Conf. on Inorganic Scintillators and Their Applications*, ed. V. Mikhailin (Moscow State University Press, Moscow, 2000) pp. 167-172.

[46] M. Balcerzyk, M. Moszynski, and M. Kapusta, IEEE Trans. Nucl. Sci. **47**, 1319 (2000).

[47] G. J. Hoffman and A. C. Albrecht, J. Phys. Chem. **95**, 2231 (1991).

[48] A. C. Smith, J. F. Janak, and R. B. Adler, *Electronic Conduction in Solids* (McGraw-Hill, New York, 1967) p. 57.

[49] V. Yakovlev, L. Trefilova, and A Meleshko, J. Lumin. 129, 790 (2009).

[50] E. Conwell and V. F. Weisskopf, Phys. Rev. **77**, 388 (1950).

[51] H. Frohlich, Adv. Phys. **3**, 325 (1954).

[52] K. S. Song and R. T. Williams, *Self-Trapped Excitons,* Springer Series in Solid State Sciences, Vol. 105 (Springer Verlag, 2nd ed., 1996).

[53] A. N. Vasil'ev, "Kinetics of creation of excitons and electron-hole pairs in tracks of ionizing particle," presented at International Conference on Excitonic Processes in Condensed Matter, EXCON 10, Brisbane (July 7-12, 2010).

[54] D. J. Singh, Appl. Phys. Lett. **92**, 201908—1 (2008).

[55] W. Setyawan, private communication.

CHAPTER 4: EXCITATION DENSITY, DIFFUSION-DRIFT, AND PROPORTIONALITY IN SCINTILLATORS

R. T. Williams, Joel Q. Grim, Qi Li, K. B. Ucer, and W. W. Moses

The following manuscript was published as the cover and feature article in the February 2011 issue of *Phys. Status Solidi B.* Qi Li performed all the finite element method calculations. Joel Q. Grim performed all experiments. Qi Li, Joel Q. Grim, and R. T. Williams analyzed the experimental and theoretical results and prepared the manuscript. I thank G. A. Bizarri and W. W. Moses of Lawrence Berkeley Lab for helpful discussions and reading of the manuscript. Manuscript is reproduced with permission of John Wiley and Sons. Stylistic variations are due to the requirements of the journal.

ABSTRACT

Stopping of an energetic electron produces a track of high excitation density, especially near its end, and consequent high radial concentration gradient. The effect of high excitation density in promoting nonlinear quenching is generally understood to be a root cause of nonproportionality in scintillators. However, quantitative data on the kinetic rates of nonlinear quenching processes in scintillators are scarce. We report experimental measurements of 2^{nd} order dipole- dipole rate constants governing the main nonlinear quenching channel in CsI, CsI:Tl, NaI, and NaI:Tl. We also show that the second of the extreme conditions in a track, i.e. radial concentration gradient, gives rise to fast ($\leq$ picoseconds) diffusion phenomena which act both as a competitor in reducing excitation density during the relevant time of nonlinear quenching, and as a determiner of branching between independent and paired carriers, where the branching ratio changes with dE/dx along the primary electron track. To investigate the interplay of these phenomena in determining nonproportionality of light yield, we use experimentally measured rate constants and mobilities in CsI and NaI to carry out quantitative modeling of diffusion, drift, and nonlinear quenching evaluated spatially and temporally within an electron track which is assumed cylindrical Gaussian in this version of the model.

1. Introduction

When an energetic electron is slowed and stopped in a scintillator (or any solid material with a band gap), the track of excitations left behind is characterized by at least two remarkably extreme numbers: (1) very high excitation density and (2) very large concentration gradient of carriers and/or excitations. The first condition of high excitation density has been recognized for some time as crucial for setting rates of 2^{nd} and 3^{rd} order quenching of local light yield in the vicinity of the track. However, with very few exceptions, those rate constants have not been determined. Therefore we present measurements of dipole-dipole quenching rate constants at high excitation density for three halide scintillators in the present work.

In addition to the promotion of nonlinear quenching by high excitation density in a track, the high concentration gradient promotes radial diffusion of electrons and holes, which can limit the nonlinear quenching rates by rapidly diluting carrier concentration, and may affect linear rates by setting up charge separation. We show by numerical modeling of the diffusion and quenching processes together that they compete on similar time scales of the order of picoseconds or less, and that their interplay is a major determining factor in proportionality of the material. We will demonstrate a diffusion- based mechanism for unequal electron and hole mobilities that determines branching between independent trapped carriers and trapped excitons, hence determining branching to subsequent recombination paths in activated scintillators. The branching ratio changes with dE/dx along the track, thus further impacting nonproportionality.

2. Measurement of quenching kinetics at high excitation density

2.1 Background and method

A method for measuring light yield and decay time as a function of e-h density through the range of 10^{18} up to 2 x10^{20} e-h/cm^3 typically deposited along the track of a high-energy electron is to excite with a subpicosecond ultraviolet pulse in the band-to- band or high-exciton region of the scintillator. Such experiments have been reported for $CdWO_4$.[1,2] In the present work, we have applied a method similar to that of Ref. [2] for the study of light yield, spectra, and decay time dependent on excitation density in CsI:Tl, undoped CsI, NaI:Tl, and undoped NaI. There are several reasons for undertaking this study. CsI:Tl and NaI:Tl are widely used scintillators for which detailed data on light yield integrated over electron tracks may be modeled if the kinetic orders and rate constants of the radiative and nonradiative processes can be experimentally quantified. Undoped CsI is also a useful fast-timing scintillator, but there are questions that have been raised about the nature of the room-temperature 300-nm luminescence [3], on which it seems our measurements can supply information. CsI:Tl and NaI:Tl are activated scintillators, whereas $CdWO_4$ and undoped CsI are intrinsic excitonic scintillators. Comparison of luminescence quenching in both activated and intrinsic scintillator materials is of fundamental interest for understanding how excitation transport and recombination kinetics affect nonproportionality.

We have used 0.5-ps pulses of 5.9-eV light to excite carrier densities up to 3 x 10^{20} e-h/cm^3 in CsI, CsI:Tl, NaI, and NaI:Tl. A Hamamatsu C2830 streak camera records partially quenched luminescence from self-trapped excitons (STE) and excited activators (Tl^+*). Having measured the intensity-dependent absorption coefficient of CsI and NaI

in the fundamental band-to-band and exciton region, we can express the quenching of luminescence yield and decay time as a function of N_{max}, the excitation density at the center of the Gaussian beam profile. Vasil ev has derived the following expression for luminescence integrated over a Gaussian transverse profile and exponentially attenuated depth profile of excitation taking into account quenching of a single excited-state species by dipole-dipole Förster transfer: [1,4]

$$I_{lum}(t) = \frac{I_0}{\tau_R} \cdot \exp\left(\frac{-t}{\tau_R}\right) \cdot \frac{-\mathrm{Li}_2\left(-\frac{2\pi}{3} \cdot N_{max} \cdot R^3{}_{d-d} \cdot \mathrm{erf}\left(\sqrt{\frac{t}{\tau_R}}\right)\right)}{\frac{2\pi}{3} \cdot N_{max} \cdot R^3{}_{d-d} \cdot \mathrm{erf}\left(\sqrt{\frac{t}{\tau_R}}\right)} \qquad (1)$$

where τ_R is the radiative lifetime of the excited state and R_{dd} is the Förster transfer radius depending on the overlap of emission and absorption bands. $Li_2(x)$ and erf(x) are the dilogarithm function and error function, respectively. If a family of luminescence decay curves is measured for different values of N_{max}, fitting the entire family yields τ_R and R_{dd}. Within this model [1,2,4], the ratio $R_{dd}^3/\tau_R^{1/2}$ determines the time-dependent rate "constant" for bimolecular quenching:

$$k_2(t) = \frac{2}{3}\pi^{\frac{3}{2}} \frac{R_{dd}^3}{\sqrt{\tau_R}} \frac{1}{\sqrt{t}} \qquad (2)$$

It has been discussed in Refs [4-8], for example, that the bimolecular rate constant itself can have time dependence according to the nature of the recombining species, the initial distribution, mode of recombination, mobility, etc. The particular form of $k_2(t)$ in Eq. (2) applies specifically when there is negligible diffusion, no initial correlation of excitations, and dipole-dipole transfer rate depends on separation r as

$$K(r) = \tau_R^{-1}\left(\frac{R_{dd}}{r}\right)^6 \qquad (3)$$

Equation (2) for $k_2(t)$ has a square root singularity, but $k_2(t)$ is truly singular only in a system where the interacting local excitations have separations distributed continuously down to zero. When we use $k_2(t)$ in numerical modeling of CsI in Section 3, the closest possible separation of STEs on the CsI lattice is just the lattice constant, and this specifies through Eqs. (2) and (3) the maximum physically meaningful value of $k_2(t)$.

2.2 Intensity-dependent absorption coefficients

Our experimental measurements are made as a function of incident laser irradiance, but the relevant parameter determining nonlinear quenching rates is the excitation density (e-h/cm^3). Thus, care is needed to use an accurate uv absorption coefficient and reflectivity to calculate excitation density from irradiance and pulse duration. Spectra of optical density of thin CsI and NaI films at 20 K, 395 K, and 10 K respectively have been reported [9,10], but are lacking quantitative film thickness data needed to extract absorption coefficient, and certainly do not take into account possible band-filling saturation of absorption at high irradiance. The qualitative film thickness characterized by Martienssen [9] as "grössenordnung 20 mμ" did permit our estimating a room-temperature absorption coefficient of $\alpha \approx 4 \times 10^5$ cm^{-1} in CsI at 5.9 eV from his data. The estimate turns out to differ by only 50% from our measurement reported below. To make measurements of absorption coefficient at the laser wavelength (210 nm), we melted CsI films between fused quartz plates and NaI between sapphire plates. (Whereas fused silica can withstand molten CsI, it is chemically attacked by NaI.) Interference observed in a sloping air pocket provided fringe contrast sufficient to deduce accurate change in film thickness of a CsI sample. At low intensity (without amplification), we measured the following

absorption coefficient, reflectance, and optical constants for CsI at 5.904 eV and room temperature: $\alpha = 2.7 \times 10^5$ cm^{-1} ±4%, R = 7.5%, $n_{real} = 1.86$, and $n_{imaginary} = 0.46$.

Performing transmission measurements with the amplified laser, we found optically induced transparency above about 4 GW/cm^2 in CsI. The sample recovers to original absorption after each pulse. We determined the excitation density at the onset of saturation to be about 3×10^{20} e-h/cm^3 for 5.904-eV photons in CsI at room temperature. Fig. 1 shows the transmittance (I/I_0) as a function of 210 nm laser fluence I_0 (on-axis value) in a 500-fs pulse. The onset of saturation occurs at a 0.5-ps pulse fluence of about 1 mJ/cm^2. The reason for optically induced transparency at high intensity is related to electronic band filling also known as the dynamic Burstein effect, illustrated for the simple case of free-carrier excitation in the inset to Fig. 1. Photons at 5.904 eV are very close to the ionization limit of excitons and thus to the onset of band-to-band transitions in CsI at room temperature.

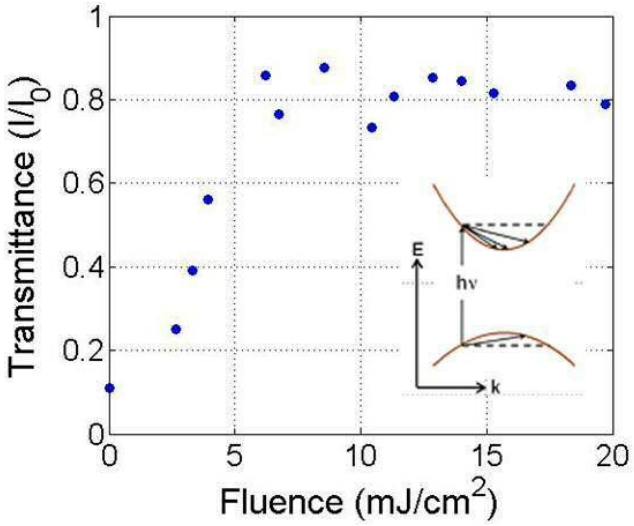

Figure 1 Transmittance versus fluence of a 0.5-ps pulse of 210-nm light incident on an 82-nm film of CsI at room temperature. The low-fluence value of transmittance corresponds to absorption coefficient $\alpha = 2.7 \times 10^5$ cm^{-1}. The inset illustrates the general concept of band filling that we believe accounts for the saturating absorption, although it is more complex with exciton interactions included.

The absorption coefficient $\alpha = 2.7 \times 10^5$ cm^{-1} at pulse fluences below and in the onset of the band-filling regime was used in calculating N_{max}. Although on-axis fluences higher than 2 mJ/cm^2 were used in demonstrating induced transparency of the CsI film in Fig. 1, it was not useful to measure luminescence quenching at such fluences because N_{max} can no longer be increased in the saturated regime. Luminescence decay curves at such conditions were measured but generally fell on top of each other even when increasing the pulse fluence. The quenching curves presented in Fig. 4 below were acquired at $N_{max} = 3.1 \times 10^{19}$ e-h/cm^3 and $N_{max} = 3.1 \times 10^{20}$ e-h/cm^3. The lower of these N_{max} values lies well within the unsaturated regime where the irradiance attenuation profile is exponential with well-defined absorption coefficient 2.7×10^5 cm^{-1}. The upper N_{max} value is just below the onset of Burstein-associated saturation, which is characterized by an energy deposition profile on-axis which starts basically flat from the entrance surface and then transitions to exponential attenuation. For such a profile, an absorption coefficient cannot be strictly defined. The derivation [1,4] of Eq. (1) assumed exponential attenuation described by an absorption coefficient, so the fitting function in Eq. (1) would not be strictly applicable if one pushes above the onset of Burstein behavior. We have chosen in the present paper to restrict analysis to fluence values (and N_{max}) for which Eq. (1) remains valid.

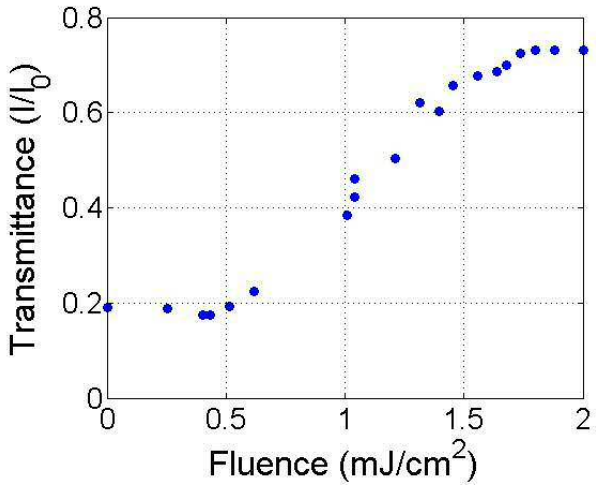

Figure 2 Transmittance versus fluence of a 0.5-ps pulse of 210-nm light on a 5-μm film of NaI at room temperature. The low-fluence value of transmittance corresponds to $\alpha = 3.3 \times 10^3$ cm^{-1}. We were not as fortunate to find a convenient air pocket in a NaI sample, so a combination of determining slope from interference fringes and measuring total mass of NaI from flame emission analysis after dissolving the film in water yielded the thickness that enabled measuring the intensity-dependent absorption coefficient $\alpha = 3.3 \times 10^3$ cm^{-1} for NaI at 210 nm. The dependence of transmittance of a NaI film on pulse fluence is plotted in Fig. 2. Notice that the absorption coefficient in NaI at 5.9 eV has unsaturated value 80 x smaller than CsI and saturates at about 2 x lower fluence (irradiance).

The greater penetration depth of band-edge light at high irradiance has a role in why we are able to see room-temperature STE luminescence excited by 5.9-eV ultraviolet light in CsI and NaI whereas other experiments cannot [11-13, 3]. (See discussion in Section 2.2.)

2.3 Experimental Results and Discussion

Figure 3 compares time-integrated spectra measured on undoped CsI and four different doping levels of CsI:Tl for 5.9-eV excitation at room temperature with 0.5-ps pulses. The band with peak at 500 nm that can be seen to increase in height monotonically with Tl doping concentration is Tl^{+*} luminescence. It appears shifted from the accepted 550-nm CsI:Tl band because the bialkali response of the streak camera has

not been corrected. The luminescence band with peak at 308 nm has maximum intensity in undoped CsI and decreases progressively with Tl doping, but remains observable in all the samples. This band corresponds to the 4.1-eV band attributed by Nishimura et al to the luminescence of equilibrated on-center and off-center STE configurations at room temperature in CsI [11].

The greater penetration depth of band-edge light at high irradiance has a role in why we are able to see room-temperature STE luminescence excited by 5.9-eV ultraviolet light in CsI and NaI whereas other experiments cannot [11-13, 3]. (See discussion in Section 2.2.)

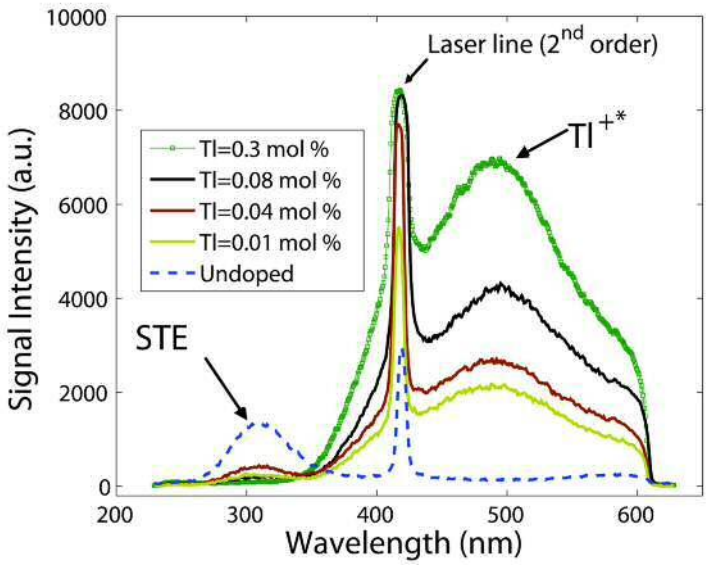

Figure 3 Time-integrated streak camera spectra of luminescence excited by 0.5-ps, 5.9 eV intense pulses at room temperature in CsI samples with Tl doping listed in order of 500-nm band height from top to bottom: 0.3%, 0.08 %, 0.04%, 0.01%, and undoped.

Comparing areas under the bands indicates that the yield of room-temperature STE luminescence in undoped CsI is about 8.3% that of Tl+* luminescence in CsI:0.3%Tl! In comparison, published values of γ-ray induced light yield at room temperature are 2000 photons/MeV in undoped CsI and 54,000 photons/MeV in

CsI:Tl [14], or a ratio of 3.7%. Our ability to excite the 4.1-eV STE luminescence *strongly* with ultraviolet band-edge light compared to inability to excite in that spectrum in Refs. [11,12,3] is attributed in the following discussion to the very high excitation density in the present experiment. This is an important question because it concerns the nature of the luminescence which is the basis for the fast-timing scintillator CsI.

The 302-nm STE decay data are shown in Fig. 4 for excitation densities of N_{max} = 3.1 x 10^{19} and 3.1 x 10^{20} e-h/cm^3, along with a fit of both curves to the dipole-dipole Förster quenching theory represented in Eq. (1). By fitting the family of 9 STE decay curves in CsI for different N_{max}, we obtain empirical parameters $\tau_R \approx 1.4$ ns and $R_{dd} = 2.9$ nm. The problem is that 15 ns rather than 1.4 ns is the STE lifetime in CsI at room temperature measured by Nishimura et al. [11] (However, we note that Belsky et al [3] measured the decay time of fast intrinsic luminescence at 300 nm in CsI at room temperature exciting above 20 eV with synchrotron radiation, and found it to be 1 to 4 ns.) We suggest that the shortening to 1.4 ns in the present study and 1-4 ns in that of Belsky et al is due to use of uv excitation that is absorbed relatively near the surface, but not too close! Nishimura et al [11] and Kubota et al [12] state that STE luminescence was not observable under one-photon uv excitation in the fundamental edge of CsI at room temperature, because of STE diffusion to the surface where impurities and defects are more numerous. In the present experiment with a uv laser pulse at very high excitation density, there is in the first place deeper penetration due to the Burstein effect discussed previously. The finding of Belsky et al [3] that the 300-nm STE luminescence could be produced by uv excitation only above 20 eV seems

in our opinion to reinforce the same conclusion since the uv absorption begins generally decreasing when significantly above the valence exciton region. An additional effect of high density excitation in our experiment is that the finite number of defects can be saturated by an ultraviolet pulse producing 3 x 10^{20} e-h/cm^3 over an extended volume, whereas intrinsic excitons will not be saturated until a much higher excitation level approaching one per unit cell. We have seen just such an effect previously in studies of exciton and defect luminescence in ZnO. [15] Whereas the green luminescence due to defects is commonly seen as a dominant luminescence band under band-edge excitation of ZnO at room temperature, excitation with our 0.5-ps intense band-edge pulses produced negligible green luminescence, but intense free-exciton luminescence, because the limited defect sites were saturated early in the pulse.

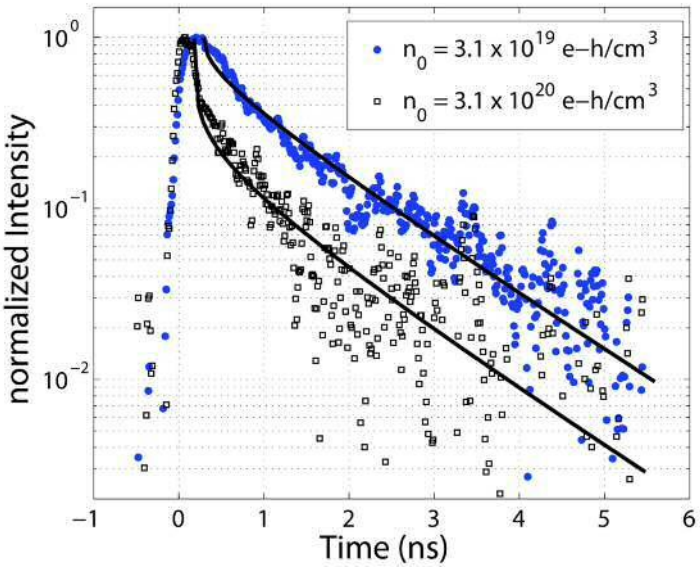

Figure 4 Comparing decay of 302-nm STE luminescence in CsI at room temperature for on-axis excitation densities N_{max} = 3.1 x 10^{19} e-h/cm^3 (blue filled points) and 3.1 x 10^{20} e-h/cm^3 (black open squares). Both curves were fit, along with 7 others for different N_{max}, using a single choice of the Förster transfer radius R_{dd} = 2.9 nm and radiative lifetime τ_R = 1.4 ns in Eq. (1).

Diffusion of at least some STEs to unsaturated nearby surface quenching/trapping sites constitutes an extra de-excitation channel causing the empirical decay time to be reduced, e.g. from 15 to 1.4 ns. It should finally be noted that the bulk-excited decay time of 15 ns [11] is not strictly the radiative lifetime of STEs in CsI either. It is the reciprocal of a sum of radiative and nonradiative decay rates of equilibrated populations of on-and off-center STEs. [11] Thus there remains the problem of what should be taken as the single *radiative* lifetime τ_R appearing in Eqs. (1 & 2). Fortunately, our main goal of determining a quantitative value of the time-dependent bimolecular rate constant for the quenching of STEs by dipole-dipole transfer is a simpler matter than extracting R_{dd} and τ_R individually. Recall from Eq. (2) that $k_2(t)$ is completely specified by the single ratio $R_{dd}^3/\tau_R^{1/2}$, which can be determined as one number by fitting the quenched luminescence decay. Thus, in spite of the more complex issues surrounding multiple components of τ_R, we can extract the time-dependent bimolecular rate constant for quenching of STEs in CsI at room temperature: $k_2(t) = 2.4 \times 10^{-15}$ cm^3 s$^{-1/2}$ $(t^{-1/2})$.

The data and fits of Fig. 4 are re-plotted on an expanded time scale in Fig. 5(a) in order to show clearly that there is a delay in achieving the peak of STE luminescence at 302 nm, and that the delay becomes longer at *lower* excitation density N_{max}. Optical (low-jitter) triggering of the streak camera was used for these measurements, and zero time was identified with the centroid of the streak image of the laser pulse itself. Although the jitter-determined resolution is ~ 60 ps, we can judge centroid shifts better than that, so luminescence peak delay varying in the range of tens of ps relative to the exciting laser pulse is meaningful. The theoretical fitting function defined in Eq.

(1) does not take into account a rise time. Thus as is evident in Fig. 5(a), to get even an approximate agreement of the fast quenching drop in Eq. (1) compared to the experimental data, the zero of time in Eq. (1) would have to be shifted from true time zero (laser pulse centroid) to allow empirically for the slow rise and consequent delayed quenching of STE population. This was done in the approximate fitting to Eq. (1) that we reported in a preliminary analysis [16].

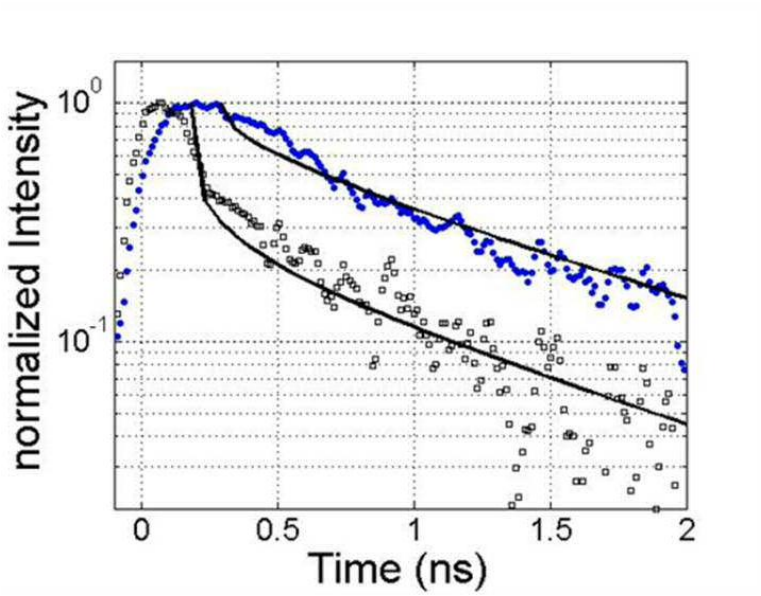

Figure 5(a) The data and fits shown in Fig. 4 are re-plotted on an expanded time scale to highlight the finite rise time of STE luminescence depending on N_{max}, the fact that Eq. (1) itself is steeper than the data, and that it must be shifted in time if one tries to force a single quenching curve of the form of Eq. (1) on the data.

It is necessary to properly identify and parameterize the population growth function and then perform a convolution of the growth and quenching decay to finally compare to data. The justification, derivation, and parameterization of the growth function will be described below. Using it, we present immediately in Fig. 5(b) the comparison of the data to the convolution of the set of quenching curves already determined in Fig. 4 together with expression for the bimolecular rise of STE population from e-h pairs discussed below.

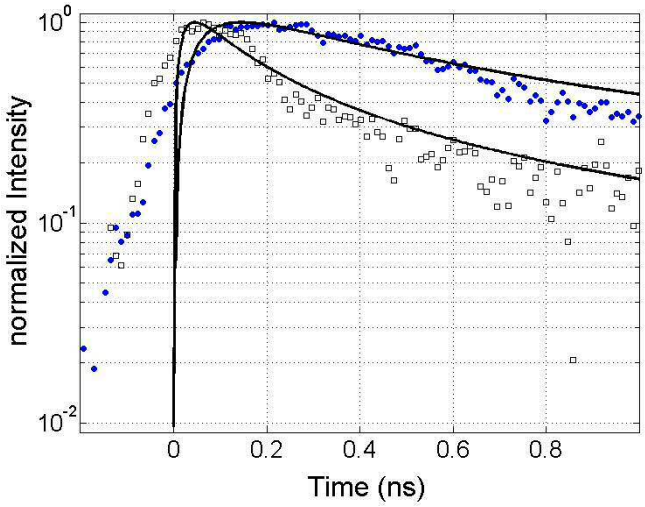

Figure 5(b) Using the bimolecular kinetic expression and parameters for STE formation from e-h pairs as discussed in text and fit in Figs. 6 (a,b), a convolution of STE rise given by Eq. (6) together with quenching given by Eq. (1) is plotted and compared to the data of Fig. 4 on an expanded time scale.

Remarkably, there are only three parameters needed to fit the entire set of 9 normalized *rise and decay* curves within the quality indicated for the 2 curves in Fig. 6(b): the bimolecular rate constant C_2 for creation of STEs, bimolecular rate constant $k_2(t)$ for quenching of STEs, and luminescence lifetime τ_R to fit the long-time luminescence decay. C_2 is a true constant while $k_2(t)$ is a time-dependent (singular) constant , and one can understand quite well why they are of different form. On the relevant time scale of several picoseconds in which growth and quenching take place, the free electrons and holes are moving rapidly and so continually maintain a uniform distribution (hence constant bimolecular rate constant), while the STEs are immobile on this time scale (hence time-dependent singular rate constant). It is worth repeating that there are no other constants beyond C_2, $k_2(t)$, and τ_R to be determined, or fitting parameters needed. The values that produce the entire family of fits illustrated by the two curves in Fig. 5(b) are $C_2 = 8.2 \times 10^{-22}$ cm^3/ps, $k_2(t) = 2.4 \times 10^{-15}$ cm^3 s$^{-1/2}$ ($t^{-1/2}$), and $\tau_R = 1.4$ ns.

Physically, a finite rise time decreasing with excitation density should be expected for formation of STEs by 2nd-order mutual capture of electrons and holes [17]. We have recently measured the rise of infrared absorption induced by sub-picosecond e-h excitation in CsI at room temperature. [18] It was found that the infrared absorption which could be attributed to STEs has a slow growth component with ~ 15 ps rise time. This seems in rough agreement with the present STE luminescence rise time. In Section 3 we will present numerical modeling of diffusion and quenching in the track, and it will be seen that the three processes of exciton formation by electron-hole capture, diffusion in the track s radial gradient, and dipole-dipole quenching all occur on similar time scales of a few ps. Consider a system of electrons and holes, each at density $n(t)$ in intrinsic excited material. They combine as pairs to create excitons of density $E_x(t)$ through bimolecular kinetics with rate constant C_2. Identify $n(t=0) = n_{max}$. From the second order rate equation we can solve for the number of electrons (holes) after time t.

$$\frac{n(t)}{n_{\max}} = \frac{1}{1 + n_{\max} C_2 t} \qquad (4)$$

We can then write the rate constant C_2 in terms of the time $t_{1/2}$ for half of the electrons (holes) to pair up, starting from initial electron (hole) density n_{max}.

$$C_2 = \frac{1}{n_{\max} t_{1/2}} \qquad (5)$$

The time for half the electrons and holes to pair up is identical in this system to the time for half of the excitons to form. The number $E_x(t)$ of excitons formed at time t is given in terms of Eqs. (4) and (5) as

$$E_x(t) = E_x(\infty) \frac{t/t_{1/2}}{1 + t/t_{1/2}} \qquad (6)$$

This describes the bimolecular growth of species which do not decay. In Fig. 6(a), we fit this curve to the rising edge of the luminescence data in order to deduce $t_{1/2}$ for growth to half maximum at each excitation density N_{max}. Here we are making the approximation that $N_{max} = n_{max}$, where N_{max} is the initial excitation density on-axis of the Gaussian laser spot (Section 2), while n_{max} is the excitation density in a uniformly excited sample.

The experimental points that are more than 0.5 ps on the negative side of t = 0 come from the jitter-determined spread of arrivals of 0.5-ps pulses. The fitting is sought on the positive side of t = 0, paying attention to the shift toward later time for lower N_{max}. Then in Fig. 6(b) the values of $1/ t_{1/2}$ are plotted vs N_{max} for the 9 measurements at different N_{max}, and the best-fit slope determines $C_2 = 8.2 \times 10^{-22}$ cm^3/ps, the bimolecular rate constant for creation of excitons from electrons and holes in CsI at room temperature. Then with $t_{1/2}$ substituted by $1/C_2N_{max}$ in Eq. (6), we can perform a convolution of growth according to Eq. (6) and (quenching + radiative) decay according to Eq. (1). The result was shown earlier in Fig. 5(b).

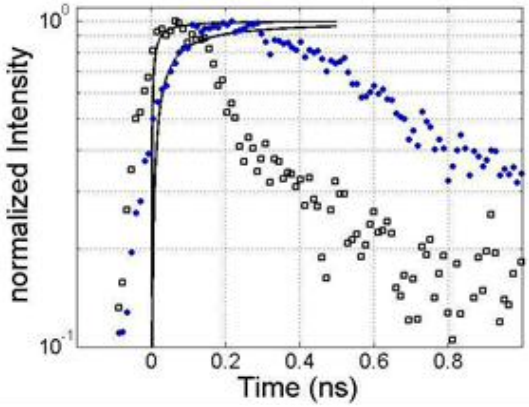

Figure 6(a) The bimolecular growth function in Eq. (6) describing creation of exciton (STE) population from electrons and holes is fit to the rising edge of the CsI luminescence at room temperature for two different N_{max}: 3.1 x 10^{19} e-h/cm^3 (blue filled points) and 3.07 x 10^{20} e-h/cm^3 (black open squares), determining $t_{1/2}$ values for the respective curves. Points to the left of t = 0 are from timing jitter.

Measurements of room-temperature luminescence decay curves as a function of excitation density N_{max} in NaI are shown in Fig. 7 along with the fit to Eq. (1). In the case of NaI, the singlet STE luminescence with τ_{Rad} = 1 ns overlaps the triplet STE luminescence with τ_{Rad} =90 ns, so it was necessary to fit the data to a sum of two functions of the form of Eq. (1) but having different τ_R and different initial singlet and triplet populations. Just as in CsI, we found that the empirical long-time fit requires τ_{fit} shorter than τ_R for the singlet and triplet components, presumably due to diffusion to the surface as previously discussed here and in Ref. [13]. Also as found in CsI, there is a finite growth time which increases at lower N_{max}, and which was determined in the way discussed earlier for CsI.

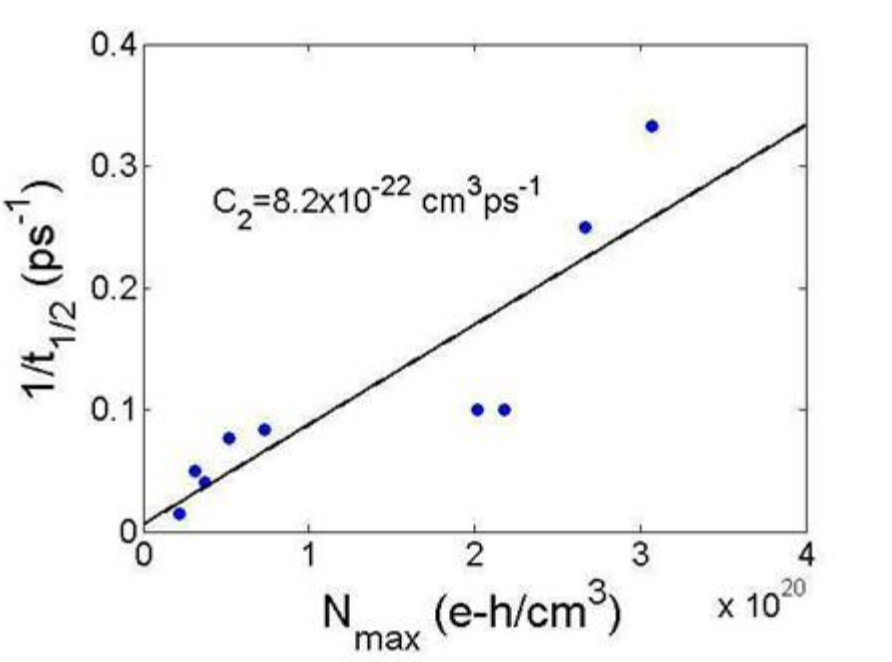

Figure 6(b) For the 9 measurements of CsI STE luminescence decay for different N_{max}, the reciprocal $t_{1/2}$ rise time of the STE growth is plotted versus N_{max} and compared to Eq. (5), which determines the bimolecular exciton creation rate constant C_2.

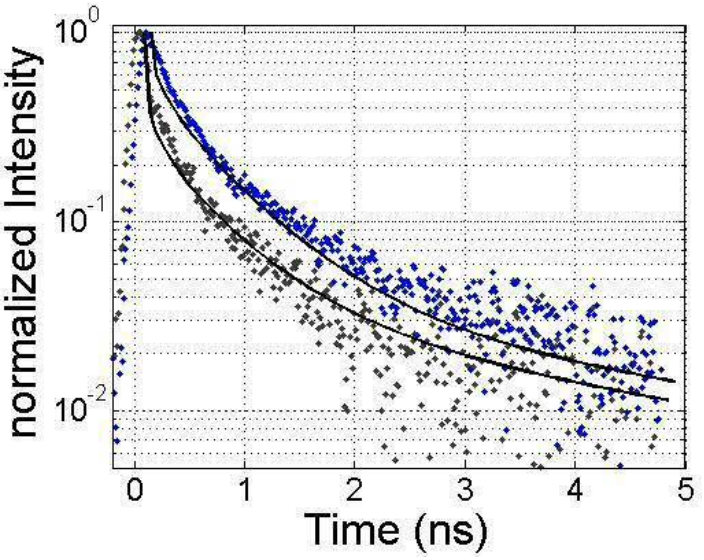

Figure 7 Decay of overlapping singlet and triplet STE luminescence at 295-nm in NaI at room temperature for on-axis excitation densities N_{max} = 1.5 x 10^{19} e-h/cm^3 (blue filled points) and 5.6 x 10^{19} e-h/cm^3 (black open squares). The fit is a sum of dipole-dipole quenching functions of the form of Eq. (1). Fitting parameters are summarized in Table 1.

The creation, quenching, lifetime, and relative population parameters determined from fitting the NaI and CsI data are summarized in Table 1.

Table 1 Parameters for CsI and NaI from fitting the families of curves for STE luminescence intensity versus time for different excitation density. C_2 is the bimolecular rate constant for creation of STEs from electrons and holes, $k_2(t)$ is the time-dependent bimolecular rate constant for dipole-dipole quenching, τ_{fit} is the empirical long-time luminescence decay constant from fitting (including diffusion effects discussed in text), τ_R is the radiative lifetime from literature, and the last column is a number proportional to the initial population of singlet and triplet STEs in fitting NaI, represented as the product of the fraction of initial luminescence intensity times the radiative lifetime of the respective component.

	C_2 cm^3/ps	$k_2(t)$ cm^{3}s$^{-1/2}$(t$^{-1/2}$)	τ_{fit} ns	τ_R ns	$\frac{I_0}{I_{tot_0}} \cdot \tau_R$
CsI	8.2×10^{-22}	2.4×10^{-15}	1.4	15	1
NaI (singlet)	2×10^{-20}	1.7×10^{-14}	0.75	1	0.96
NaI (triplet)	2×10^{-20}	6.6×10^{-15}	5	90	3.6

Figure 8 compares the decay of luminescence in the Tl^{+}* (550 nm) band in CsI:Tl for excitation densities of N_{max} = 3.1 x 10^{19} and 3.1 x 10^{20} cm^{-3}. The most important finding is that there is no excitation-density-dependence of the Tl^{+}* decay time over this range. This is in contrast to the fast decay due to density-dependent quenching seen in the STE population just above. The conclusion is that in the CsI host, the STEs undergo dipole-dipole near-field transfer, whereas the excited Tl activators do not. The Tl^{+*} concentration is capped by 0.3% doping to 3 x 10^{19} Tl^{+*}/cm^{3}, an order of magnitude lower than the maximum host excitation of 3.1 x 10^{20} e-h/cm^{-3}. Correspondingly the average Tl-Tl separation of 3.2 nm at 0.3 mol% is larger than our measured R_{dd} (STE) = 2.9 nm in CsI, so transfer would be strongly discouraged by the 6^{th}-power dependence, relative to the average STE-STE separation in the host of 1.5 nm at N_{max} =3.1 x 10^{20} e- h/cm^{3}. The picture that emerges is of a congestion of STEs waiting to transfer on to a limited number of vacant Tl^{+}, and undergoing dipole-dipole quenching in the meantime.

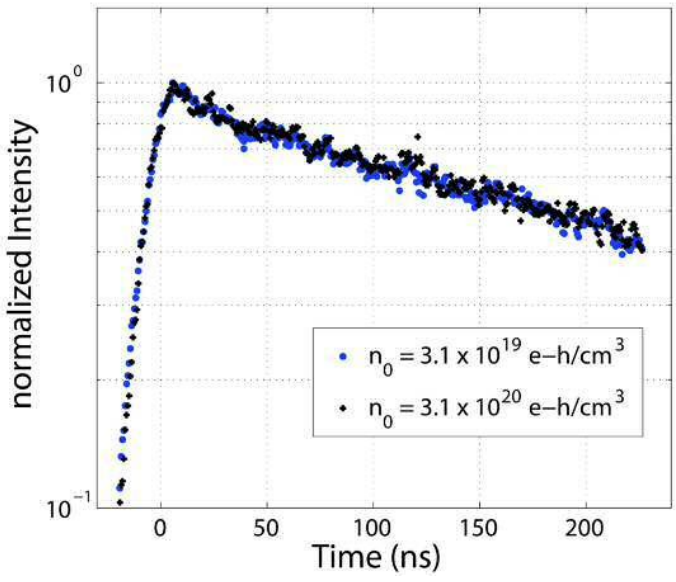

Figure 8 Comparing Tl^{+}* luminescence decay for N_{max} = 3.1 x 10^{19} e-h/cm^{3} (blue closed circles) and N_{max} =3.1 x 10^{20} e-h/cm^{3} (black crosses) in CsI:0.3%Tl.

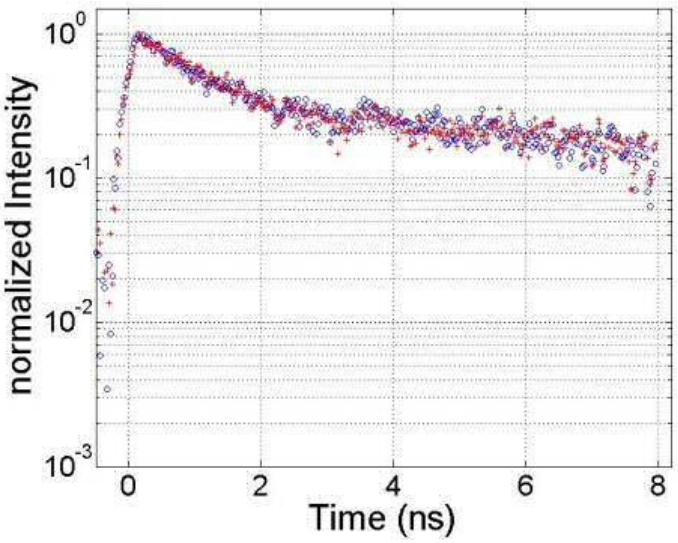

Figure 9 Comparing Tl^{+}* luminescence decay for N_{max} = 1.9 x 10^{19} e-h/cm^3 (blue open circles) and N_{max} =5.6 x 10^{19} e-h/cm^3 (red crosses) in NaI:0.1%Tl.

Figure 8 also shows that there is a substantial delay of ~ 6.2 ns between excitation and the achievement of maximum Tl^{+}* luminescence. To access the full 250 ns time range, electronic streak trigger was used for these data, increasing the jitter width showing to the left of t = 0, but the 6.2 ns delay relative to the laser pulse centroid is unmistakeable. The slow rise of Tl^{+*} luminescence is a known phenomenon in CsI:Tl attributed to thermal hopping transport of energy by means of STE, Tl^{++}, and Tl^{0} at room temperature. [19] Notice that this is nearly 3 orders of magnitude slower than the rise time of STE luminescence in CsI. The slow rise of Tl+* luminescence results from bimolecular recombination of trapped and self-trapped species, whereas the pure STE luminescence results from the bimolecular recombination of electrons and free or self- trapped holes.

Fig. 9 presents data for Tl^{+*} luminescence in NaI:0.1%Tl. The conclusion is similar to that for CsI:Tl. Both the growth and the radiative decay occur on a faster time scale in NaI:Tl compared to CsI:Tl.

The observation of the slow rise of Tl^{+*} luminescence provides very useful confirmation that the 5.9-eV laser pulse excites mainly the CsI host which then transfers energy to Tl^{+}, rather than mainly exciting directly into the D band of Tl^{+}. If the excitation were directly into a thallium absorption band, the Tl^{+*} luminescence should have a prompt rise, as shown by Hamada et al [18] using nitrogen lamp excitation of CsI:Tl in the spectral range 294-407 nm where the host is not strongly absorbing. In contrast, the 210 nm laser light in the present experiment has very high absorption coefficient in the host, $\alpha = 2.7 \times 10^{5}$ cm^{-1}, and does not overlap well with the 5.4-eV D band. The slow rise says that 5.9 eV mainly excites the host and the excitation is subsequently transferred by hopping recombination of trapped species to finally produce an electron-hole pair at one Tl^{+} site, i.e. Tl^{+*}.

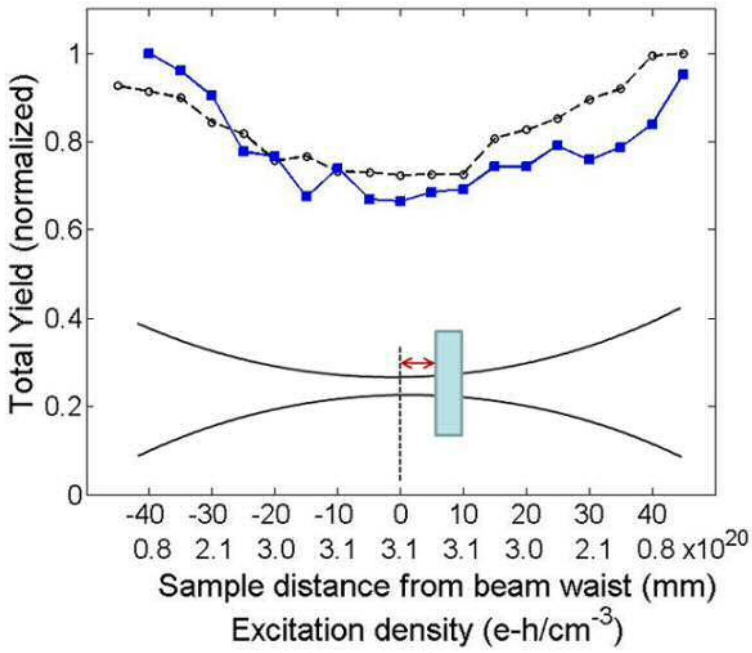

Figure 10 Light yield versus excitation density for 550-nm Tl^{+}* luminescence in CsI:0.3%Tl (black dashed line) and 302-nm STE luminescence in CsI (solid blue line). Inset is a schematic of beam waist translation relative to the crystal to vary spot size.

But the light yield of Tl+* (550 nm) and STE (302 nm) luminescence have the *same* dependence on excitation density in the host, as shown in Fig. 10. These measurements were made for constant total energy in the laser pulses, changing fluence by translating the beam waist to various positions in front of and behind the sample (inset of Fig. 2(a)). An alternative method using a fixed beam size and attenuation by filters yielded consistent results. The conclusion to be drawn is that nonlinear quenching occurs mainly in the STE population, but that this results in diminished production of Tl^{+*} excited activators by STE capture or resonance transfer. Thus the bimolecular quenching rate constant measured in undoped CsI also governs the quenching of Tl^{+*} *light yield* in CsI:Tl.

3. Modeling the competition between fast carrier diffusion and dipole-dipole quencing in CsI and CsI:Tl

We can associate three characteristic time ranges of carrier transport within a particle track with different physical processes of radial diffusion: (1) ballistic transport of carriers created with kinetic energy in excess of kT, lasting for a thermalization time of fs to ps, during which the carriers diffuse a thermalization length l_t [20]; (2) diffusion of carriers with band mobilities in thermal equilibrium, commencing at the end of ballistic transport and continuing until the carrier is recombined with a partner or reduced to slow thermal hopping transport after becoming trapped; and (3) thermal hopping and detrapping on a time scale of nanoseconds to microseconds in room-temperature scintillators.[21] Process (1) of ballistic transport is often folded into the definition of an initial track radius. Vasil ev has estimated a thermalization length $\mathbf{l}_t$ = 3 nm as typical for scintillator materials.[20] It is

the process (2) of band diffusion in thermal equilibrium that is the topic of the simulations to be presented, having importance in ~ 20 ps down to ~ 1 fs depending on mobilities.

The concept of dilution of carrier concentration as a controlling influence on quenching is worth pursuing to its consequences for the highly localized radial distribution of carriers in a particle track. The quenching channels that depend super-linearly on carrier concentration, *i.e.* dipole-dipole transfer (2^{nd} order) and Auger (3^{rd} order), are self terminating by nature. They rapidly drain the excited states, usually within a matter of picoseconds, until the carrier concentration renders nonlinear quenching slower than linear loss channels such as light emission or trapping. But there is a third channel capable of reducing carrier concentration on the same or faster time scale as do the quenching processes, and it is thus capable of terminating them. That third channel is diffusion, and we have shown in a preliminary study of Ge and CsI that it can dilute the carrier concentration in femtoseconds to picoseconds depending on mobilities [22]. Although both diffusion and quenching act to terminate nonlinear quenching rate, there is an important distinction between dilution of carrier concentration and destruction of carrier concentration. The former preserves the total number of excited states that can potentially yield light, whereas the latter does not. Local light yield can be cast in terms of a race to low concentration by two main channels. If diffusion wins, the quenching is terminated but the carriers (excited states) are preserved. If nonlinear quenching beats diffusion, the carriers are lost. To the extent that nonlinear quenching is not terminated by dilution, it will contribute to nonproportionality since dE/dx always varies along the track. If, in

addition, the competition goes differently at different dE/dx along the particle track (and our simulations say it does) then the nonproportionality is compounded at a second level. In both cases, carrier mobilities emerge as important parameters governing proportionality. We have shown that the diffusive separation of electrons and holes due to unequal mobilities is favored at low dE/dx, especially when holes are immobile (self-trapped) [21]. In this way diffusive band transport of electrons relative to holes on the picosecond time scale can explain why the depression of light yield at low dE/dx is a feature peculiar to halide scintillators and is especially strongly expressed in NaI:Tl, CsI:Tl, and CsI:Na where holes are known to be strongly self-trapped.

3.1 Modeling Method

Time-step finite-element analysis was used to solve for the diffusion and drift currents, electric field, and local carrier concentration in cylindrical symmetry around the track of a charged particle. The equations used are

$$\vec{J}_e(\vec{r},t) = -D_e \nabla n_e(\vec{r},t) - \mu_e n_e(\vec{r},t)\vec{E}(\vec{r},t) \qquad (7)$$

$$\frac{\partial n_e(\vec{r},t)}{\partial t} = -\nabla \cdot \vec{J}_e(\vec{r},t) \qquad (8)$$

for electrons and an equivalent set of equations for holes, where the variables and constants have their usual meanings. Gauss s law

$$\nabla \cdot \vec{E}(\vec{r},t) = \frac{\rho}{\varepsilon\varepsilon_0} \qquad (9)$$

serves to evaluate electric field for insertion back into the diffusion/drift equation. The Einstein relation $D = \mu k_B T/e$ gives the diffusion coefficients for electrons and

holes in terms of their mobilities μ_e and μ_h, and the temperature. The static dielectric constant ε of the material is used in Gauss s law.

The finite-element evaluation is applied to cylindrical shells around a starting distribution which is taken to be a Gaussian radial profile initially identical for electrons and holes. The electron and hole number in each cylindrical shell is updated in each time step according to the diffusion and drift currents across the cell boundaries.

Auger recombination can be included as a quenching channel by adding the 3rd order rate

$$\frac{\partial n(\vec{r},t)}{\partial t} = -\gamma n^3(\vec{r},t) \qquad (10)$$

to the right side of Eq. (8). Following the approximate treatment of Ref. [22], the concentration n in intrinsic material is taken to refer to free electrons or free holes equivalently.

If carriers are paired as excitons (free, self-trapped, or activator-trapped) at concentration n_{ex}, the bimolecular quenching rate due to dipole-dipole Förster transfer can be likewise included in the simulation through the equation

$$\frac{\partial n_{ex}(\vec{r},t)}{\partial t} = -k_2(t) n_{ex}^2(\vec{r},t) \qquad (11)$$

where $k_2(t)$ was given in Eq. 3 earlier. This introduces a complication in that the density of carriers paired as excitons, n_{ex}, and thus capable of dipole-dipole transfer, is not identical with the density of free carriers in Eqs. (7-10) describing diffusion and free-carrier Auger recombination. This can be handled approximately in simulations based on the single set of 7 equations described above if we can identify a branching ratio of independent to paired carriers. We have previously shown, and summarize below,

that such a ratio comes naturally from the diffusion model in the high gradient of a particle track, as a function of relative electron and hole mobilities. [21]. The concept can be summarized as follows:

When carriers have unequal mobilities in a region of very high concentration gradient, they may find themselves at quite different radial positions after time t, even accounting for electric field effects. We can evaluate the average radial displacement of each carrier type in the model, and use this to predict whether at expiration of the average trapping time, the electron and hole will be found on different activator sites, or on the same site. Thus we can evaluate whether a geminate electron-hole pair will on average become independent trapped carriers undergoing 2nd order recombination, or if they will remain paired, subject to 1st order kinetics.

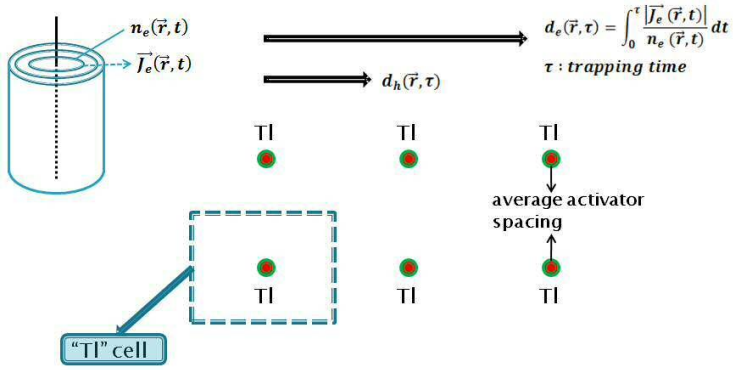

Figure 11 Illustration of the concept of separation of electrons and holes with different mobilities in a strong radial gradient as the basis for diffusion-driven branching from geminate paired to independent carriers at time τ of trapping on an activator.

Briefly stated, the average displacement of an electron at position ***r*** and time τ can be evaluated within the diffusion current model as

$$\vec{d}_e(\vec{r},\tau) = \int_0^\tau \frac{\vec{J}_e(\vec{r},t)}{n_e(\vec{r},t)} dt \qquad (12)$$

and similarly for holes. We will write the average relative displacement of electrons from holes at a given position and time τ as $\Delta d = \left| \boldsymbol{d_e} - \boldsymbol{d_h} \right|$. In the case of an activated scintillator, taking CsI:Tl as the example, an important question is whether carriers trap on different Tl^{+} producing Tl^{0} or Tl^{++}, or whether they trap together as Tl^{+*}. Then the time of interrogation τ should be the average trapping time and we compare Δd to the average Tl-Tl spacing to determine probability that the respective carriers are near the same or different Tl^{+} when trapped. This is different in detail from the question of whether the carriers are independent or paired at times leading up to trapping on activators, but it points the way to similar consideration of the gradient-driven average electron-hole separation compared to exciton radius in a future publication.

3.2 Values of the material parameters

The activation energy for STH jumps in CsI (taking the average for 90 º and 180 º jumps) is 0.20 eV and the frequency factor is estimated to be 5.1×10^{12} s^{-1}. [21] At room temperature, these parameters give the STH jump rate in CsI as 1.7×10^{9} s^{-1}. It will be seen in the results of the simulations that the major redistribution due to diffusion and drift of conduction electrons in CsI is completed to steady state within a few picoseconds. Thus for the relevant time range of these simulations the hole mobility in CsI can be taken as $\mu_h = 0$. The electron mobility in CsI at room temperature is $\mu_e = 8$ cm^2/Vs, measured by a time-of-flight method after 20 ps electron pulse excitation [23]. The static dielectric constant of CsI is $\varepsilon = 5.65$. We specify thallium doping level (0.3%) because of its role in the test for geminate-to-independent branching. Doping with activators can be expected to lower μ_e below the pure-CsI value, but this is neglected for the present illustration because μ_e is not directly available for doped CsI.

3.3 Modeling results and discussion

Figure 12 shows carrier diffusion profiles at two different on-axis excitation densities in CsI:Tl, chosen to span the range of electron-hole concentrations typically produced from beginning to end of a megavolt electron track: 2.5 x 10^{18} and 2.5 x 10^{20} e-h/cm^3. The starting e^{-1} radius is 3 nm. The profile plots in the left column of Fig. 12 display electron density $n_e(r, t)$ (cm^{-3}) at $t = 0$ (identical for the holes) and at t_{SS}, the time at which steady-state balance between drift and diffusion is achieved. The right column displays the radial electron density (cm^{-1}) representing the number of electrons (holes) in a cylindrical shell at radial distance r, of unit length, per shell thickness Δr. It is the azimuthal integral $N_e(r, t) = 2\pi r\, n_e(r,t)$, multiplied by unit track length (1 cm).

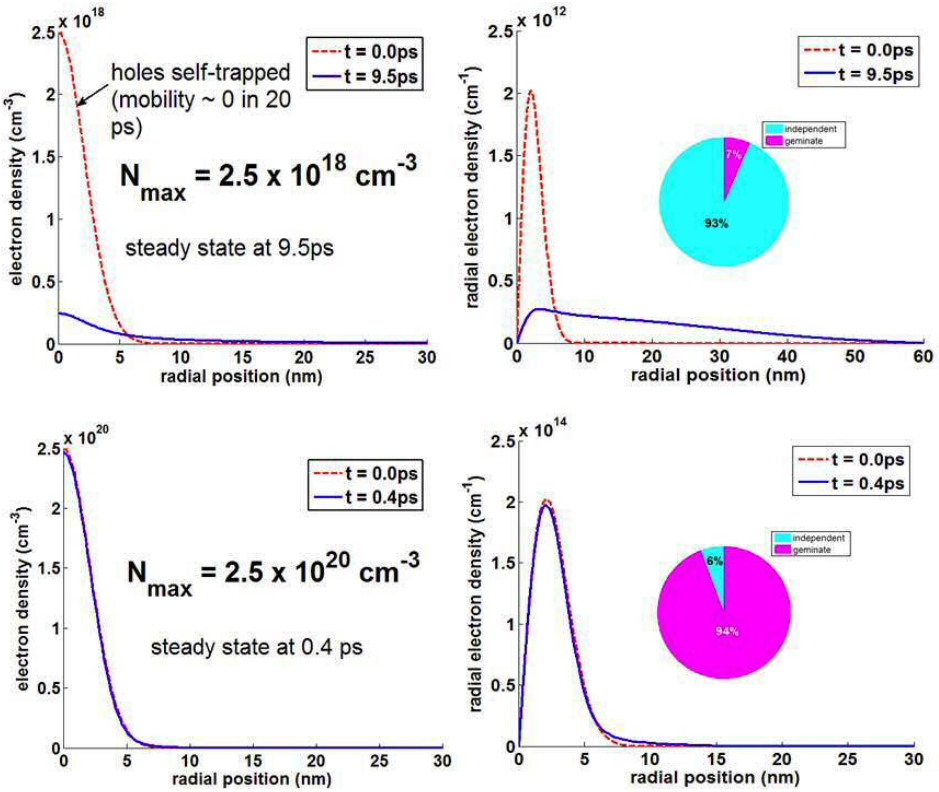

Figure 12 Carrier diffusion profiles at excitation densities of 2.5 x 10^{18} (top panels) and 2.5 x 10^{20} e-h/cm^3 (bottom panels) in CsI:0.3%Tl. The plots in the left column display electron density

$n_e(r,t)$ (cm^{-3}) at t = 0 (identical for the holes) and at t_{SS}, the time at which steady-state balance between drift and diffusion is achieved. The right column displays the radial electron density (cm^{-1}) representing the number of electrons (holes) in a cylindrical shell at radial distance r, of unit length, per shell thickness Δr. It is proportional to r $n_e(r\ t)$. The pie charts show branching ratio to independent electrons and holes (blue light shading) or to paired electrons and holes (purple dark shading).

Since the holes don t move in our model of CsI, and the initial electron and hole distributions are equal, the same two curves can be considered a comparison of the radial distributions of immobile holes and of electrons evaluated at steady-state, respectively. The time to reach steady state depends on the initial excitation density, and can be seen in Fig. 12 to vary from 9.5 ps at the lowest carrier density down to 0.4 ps at the highest density.

In the carrier profile shown for the lower excitation density of 2.5 x 10^{18} e-h/cm^3 in Fig. 12, one can readily see that the electrons have considerably outrun the immobile holes before electric field balances the diffusion. This is reflected in the pie chart as 93% independence of electrons and holes when they trap, i.e. on *different* thallium activators. At the highest plotted excitation density of 2.5 x 10^{20} e-h/cm^3, only a small fraction of electrons have managed to outrun the immobile holes, with the great majority confined by the built-in electric field to almost the same profile as the holes. Thus, carriers tend to remain paired at the time of trapping, and this is shown in the pie chart as only 6% independent, but 94% geminate pairs.

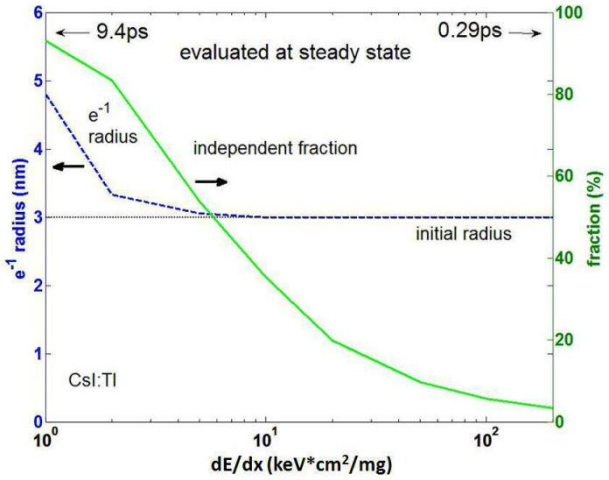

Figure 13 The e^{-1} radius of the electron distribution and independent fraction (fraction of geminate pairs torn apart by differential diffusion) are plotted versus dE/dx for CsI:0.3%Tl. The time to achieve steady-state balance between diffusion and drift is 9.4 ps at the lowest dE/dx and 0.29 ps at the highest dE/dx.

In Fig. 13, we plot the 1/e radius of electron concentration versus linear distance along the particle track in CsI after 10 picoseconds, and find that this contour starts with a larger radius early in the particle track, but closes down to approximately the initial track radius as the track end is approached. Also in Fig. 13, we plot the independent fraction of electrons and holes in CsI:0.3%Tl versus dE/dx along the electron track due to diffusion with the widely different μ_e and μ_h in CsI. There is a strong tendency for geminate e-h pairs to separate into independent carriers early in the track (low dE/dx), due just to differential mobilities. Conversely, there is a strong tendency for association or pairing toward the end of the track (high dE/dx). These tendencies are in the same direction as the trend discussed by Payne et al that is based on comparison of the electron-hole separation to the exciton Onsager radius [24]. Both phenomena are undoubtedly at work.

The diffusion-driven tendency described here is directly tied to relative hole and electron mobilities, and through that to particular material properties like hole self-

trapping in alkali halides. It suggests an explanation for why the alkali halides in particular express a strong slope of light yield at low dE/dx (high gamma-ray energy). The independent trapped carriers can be more susceptible to quenching and delayed afterglow than are paired carriers (excitons) captured at a single Tl activator.

It was shown in Ref. [22] that high purity germanium (HPGe) at 77 K, with μ_h = 42,000 cm^2/Vs and μ_e = 36,000 cm^2/Vs [25], exhibits extremely fast expansion of the track radius with dramatic effect on Auger recombination. The radius expands from 3 nm to 20 nm in 1 femtosecond! As a result, Auger recombination is rendered negligible within 1 fs and at all longer times. Dipole-dipole quenching is insignificant in germanium, so there is virtually no surviving *nonlinear* channel for quenching carriers in HPGe when the carriers are generated within energetic electron tracks and thus are subject to the huge radial concentration gradient driving diffusion. We propose that this is a main reason why semiconductor detectors in general, and HPGe as an outstanding example, are such proportional detectors compared to scintillators. Presently-available scintillators generally cannot compete with semiconductors for high mobility of both carriers.

We have cited extreme cases of low and high mobilities so far. What happens in the intermediate case, where the hole is neither immobile nor equaling the electron mobility? To illustrate, we have set the electron mobility fixed at the CsI value of 8 cm^2/Vs, and let the hole mobility vary from 0 up to 8 cm^2/Vs. We evaluate the independent fraction for the same three on-axis excitation densities as before and plot the the result versus hole mobility in Fig. 14. It turns out that the result depends on when you evaluate it. The physical meaning of time of evaluation for

independence is: when are the carriers trapped? So we plot the simulations for trapping times of 0.5 ps and 10 ps in the upper and lower panels of Fig. 14 respectively. If hole mobility is much smaller than electron mobility, the independence depends very much on the initial carrier density, and thus on location along the electron track. This predicts non-proportional behavior. If electron and hole mobilities are equal, this model predicts zero independence fraction, implying good proportionality. Particularly at longer trapping times, a modest departure from equal mobilities leads steeply to carrier independence, but notice for longer trapping times (e.g. t_{trap} = 10 ps) that the independence for modest inequality of mobilities is about the same for all dE/dx. This also tends to predict proportional behavior.

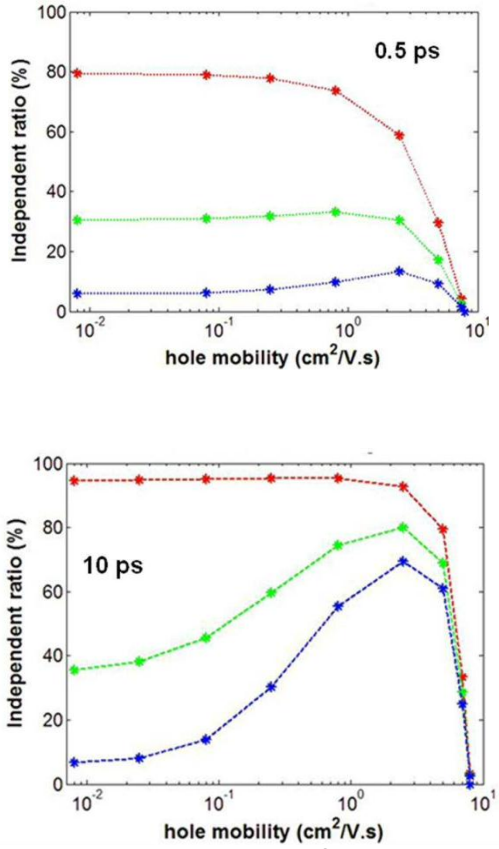

Figure 14 Taking the electron mobility fixed at 8 cm^2/Vs, the independent fraction of electrons and holes evaluated as described above is plotted versus hole mobility, for two values of the trapping time τ at which the independent status is evaluated. The top panel is evaluated at

trapping time τ = 0.5 ps, and the bottom panel at 10 ps. The three curves (from top to bottom) in each panel correspond to initial carrier densities N_{max} = 2.5 x 10^{18} e-h/cm^3, 2.5 x 10^{19}e-h/cm^3, and 2.5 x 10^{20} e-h/cm^3.

However as the trapping time gets shorter, the same mobility ratio begins to predict a strong dependence on dE/dx. Setyawan et al have compared ratios of theoretical electron and hole band masses in a number of scintillators to experimental measures of proportionality and find that near equality of electron and hole band masses (indicative of mobilities) correlates with better proportionality [26].

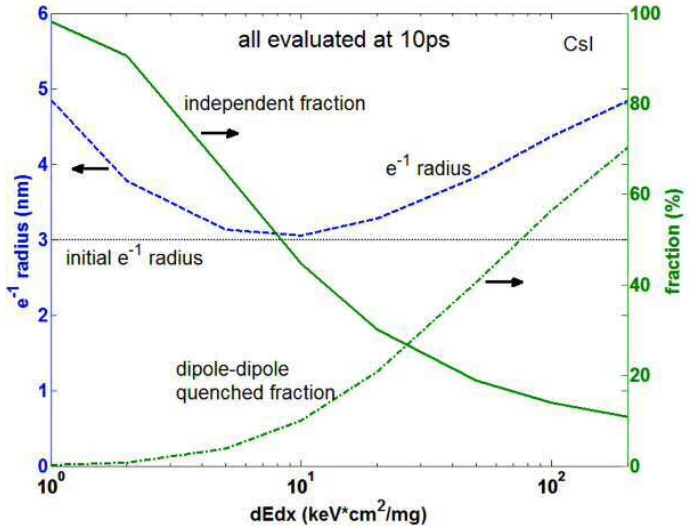

Figure 15 The e^{-1} radius of the electron radial profile, the dipole-dipole quenched fraction of self-trapped excitons, and the independent fraction of electrons and holes (defined earlier), are shown after simultaneous radial diffusion and dipole-dipole quenching with the measured $k_2(t)$ in CsI.

Using the bimolecular quenching rate function $k_2(t)$ measured for CsI in Section 2 of this paper to evaluate quenching and radial diffusion simultaneously within the model described above leads to the results plotted in Fig. 15 versus dE/dx. The results plotted are the e^{-1} radius of the electron profile, the dipole-dipole quenched fraction of self- trapped excitons, and the independent fraction (defined earlier), all evaluated at 10 ps after excitation. The value of dE/dx at the right side of the graph corresponds to on-axis density of 2.5 x 10^{20} e-h/cm^3, and the left side to 2.5 x 10^{18} e-h/cm^3. The

dipole-dipole quenched fraction rises from near zero at the left side up to a value of 70% at dE/dx =200 keV·cm^2/mg characteristic of track ends. Comparison to Auger recombination with an assumed typical Auger rate constant of 10^{-31} cm^6/s (the value for germanium [27]) shows the dipole-dipole quenching is much stronger in CsI than is Auger quenching with the rate constant assumed, at the same excitation density. The e^{-1} radius profile in Fig. 15 behaves in a more complicated way than in Fig. 13. The only difference is that dipole- dipole quenching is present simultaneously with diffusion in Fig. 15, whereas it was absent in the pure transport simulation of Fig. 13. Examination of the detailed profiles shows that at the higher dE/dx values, dipole-dipole quenching becomes so fast that it eats away the central peak of the radial distribuition in a matter of picoseconds and produces a non-gaussian flattened distribution with consequent greater e^{-1} radius.

Acknowledgements This work was supported by the National Nuclear Security Administration, Office of Defense Nuclear Nonproliferation, Office of Nonproliferation Research and Development (NA-22) of the U.S. Department of Energy under Contract No. DE-AC02-05CH11231. We wish to thank Larisa Trefilova of the Institute for Single Crystals, Kharkov, for the CsI and CsI:Tl samples, and Vitali Nagirnyi and Andrey Vasil ev for helpful discussions.

REFERENCES

[1] M. Kirm, V. Nagirnyi, E. Feldbach, M. De Grazia, B. Carre, H. Merdji, S. Guizard, G. Geoffroy, J. Gaudin, N. Fedorov, P. Martin, A. Vasil ev, A. Belsky, Phys. Rev. B **79**, 233103-1 (2009).

[2] V. Nagirnyi, S. Dolgov, R. Grigonis, M. Kirm, L. L. Nagornaya, F. Savikhin, V. Sirutkaitis, S. Vielhauer, A. Vasil ev, IEEE Trans. Nucl. Science **57**, 1182 (2010).

[3] A. N. Belsky, A. N. Vasil ev, V. V. Mikhailin, A. V. Gektin, P. Martin, C. Pedrini, D. Bouttet, Phys. Rev. B **49**, 13197 (1994).

[4] A. Vasil ev, IEEE Trans. Nucl. Science, **55**, 1054 (2008).

[5] L. B. Rubin, O. V. Braginskaya, M. L. Isakova, N. A. Efremov, V. Z. Paschenko, J. Lum. **29**, 399 (1984).

[6] T. R. Waite, Phys. Rev. **107**, 463 (1957).

[7] V. Kuzovkov and E. Kotomin, Rep. Prog. Phys. **51**, 1479 (1988).

[8] M. N. Berberan-Santos, E. N. Bodunov, B. Valeur, Chem. Phys. **317**, 57 (2005).

[9] W. Martienssen, J. Phys. Chem. Solids **2**, 257 (1957).

[10] K. J. Teegarden and G. Baldini, Phys. Rev. **155**, 896 (1967).

[11] H. Nishimura, M. Sakata, T. Tsujimoto, and M. Nakayama, Phys. Rev. B **51**, 2167 (1995).

[12] S. Kubota, S. Sakuragi, S. Hashimoto, and J. Ruan, Nucl. Instrum. Methods A **268**, 275 (1988).

[13] S. Nagata, K. Fujiwara, and H. Nishimura, J. Lumin. **47**, 147 (1991).

[14] for example, www.detectors.saint-gobain.com

[15] J. Wilkinson, K. B. Ucer, R. T. Williams, Rad. Meas. **38**, 501 (2004).

[16] Joel Q. Grim, Qi Li, K. B. Ucer, R. T. Williams, and W. W. Moses, Nucl. Instr. & Meth. in Phys. Res. A (accepted, July 2010).

[17] R. T. Williams, J. N. Bradford, W. L Faust, Phys. Rev. B **18**, 7038 (1978).

[18] R. T. Williams, K. B. Ucer, Joel Q. Grim, Kyle C. Lipke, L. Trefilova, W. W. Moses, IEEE Trans. Nucl. Science **57**, 1187 (2010).

[19] M. M. Hamada, F. E. Costa, M. C. C. Pereira, S. Kubota, IEEE Trans. Nucl. Sci. **48**, 1148 (2001).

[20] G. Bizarri, W. W. Moses, J. Singh, A. N. Vasil ev, R. T. Williams, J. Appl. Phys. **105** 044507-1 (2009).

[21] S. Kerisit, K. M. Rosso, B. D. Cannon, , IEEE Trans. Nucl. Sci. **55**, 1251 (2008).

[22] Qi Li, Joel Q. Grim, R. T. Williams, G. A. Bizarri, and W. W. Moses, Nucl. Instr. & Meth. in Phys. Res. A (accepted, July 2010).

[23] B. P. Aduev, E. D. Aluker, G. M. Belokurov, V. N. Shvayko, Phys. Status Solidi B **208**, 137 (1998).

[24] S. A. Payne, N. J. Cherepy, G. Hull, J. D. Valentine, W. W. Moses, Woon-Seng Choong, IEEE Trans. Nucl. Sci. **56**, 2506 (2009).

[25] G. Bertolini and A. Coche (eds.), *Semiconductor Detectors* (Elsevier-North Holland, Amsterdam, 1968).

[26] W. Setyawan, R. M. Gaume, R. S. Feigelson, S. Curtarolo, IEEE Trans. Nucl. Sci. **56**, 2989 (2009).

[27] D. H. Auston, C. V. Shank, P. LeFur, Phys. Rev. Lett. **35**, 1022 (1975).

CHAPTER 5: ELECTRON ENERGY RESPONSE OF SCINTILLATORS CALCULATED FROM CARRIER MOBILITIES AND MEASURED 1st THROUGH 3rd ORDER QUENCHING

Joel Q. Grim, Qi Li, K. B. Ucer, G. A. Bizarr, W. W. Moses, and R. T. Williams

The following manuscript was published in *Material Research Society Communications Research Letter* (2012). Qi Li performed all the finite element method calculations and helped to set up the GEANT4 calculations and understand GEANT4 results. Joel Q. Grim was mainly responsible for the Monte Carlo simulations of electron tracks using GEANT4. Joel Q. Grim and K. B. Ucer performed z-scan experiments for evaluating 2nd order and 3rd order quenching rate constants. I thank G. A. Bizarri and W. W. Moses of Lawrence Berkeley Lab for helpful discussions and reading of the manuscript. Manuscript is reproduced with permission of Material Research Society. Stylistic variations are due to the requirements of the journal.

ABSTRACT

Intrinsic energy resolution in γ-radiation detectors is limited by nonlinear quenching that varies as the 2^{nd} or 3^{rd} power of local excitation density. Using a numerical model for local light yield depending on measured quenching rates, kinetic order, and carrier mobilities, we employ Monte Carlo simulations of energy deposited at each local excitation density to calculate electron energy response that can be directly compared to Compton coincidence and K-dip experiments. Agreement is found for NaI:Tl and SrI_2:Eu using thermalized carrier diffusion and linear quenched fraction deduced from total light yield. This lays groundwork for testing refinements with recent hot-electron extensions of the model.

In the experimental characterization of energy-resolving scintillator performance, the ratio of total light emission to the initial energy of the electron being stopped, often called electron response , can be measured by several experimental methods including Compton coincidence and K-dip spectroscopy. The Compton coincidence method now implemented in the high-throughput version of the SLYNCI experiment,[1] correlates light yield $Y_e(E_i)$ with total stopping of a Compton electron of initial energy E_i. K-dip spectroscopy [2] yields data to lower electron energy by correlating $Y_e(E_i)$ with the kinetic energy of K-shell photoelectrons excited by tunable synchrotron radiation. The scintillator is said to exhibit nonproportionality of response if $Y_e(E_i)$ varies with E_i. If so, its energy resolution is degraded by fluctuations in the energy deposition process interacting through the nonproportionality of response.[3]

The physical origin of nonproportional response is generally regarded to start with nonlinear quenching proportional to 2^{nd} or 3^{rd} power of the excitation density n. In the defining rate equation for nonlinear quenching, n is expressed in units of $volume^{-1}$, so the linear spatial rate of energy deposition dE/dx must always be converted to n with a factor of dimension $energy^{-1}length^{-2}$ if the nonlinear quenching rate constants K_2 and K_3 are to be relevant. This dimensional conversion is commonly regarded as dividing dE/dx by a factor β times the bandgap and the square of a track radius (r_{NLQ} in Table 1). The radial gradient is very high, so *radius*, thus n, and thus the nonlinear quenching rates $-K_2 n^2$, $-K_3 n^3$ are all functions of time and diffusion coefficients D_e, D_h, and D_{eff} discussed below.

Refs. [4,5] explored the dependence of numerically simulated local light yield $Y_L(n_0)$ upon the local on-axis excitation density n_0 of a track with assumed Gaussian

radial profile. Two major dependences were found: (1) ambipolar carrier diffusion with effective coefficient D_{eff}, and (2) the inequality of electron and hole diffusion coefficients expressed by the ratio D_e / D_h (= mobility ratio μ_e / μ_h in thermal equilibrium).[4] Ambipolar diffusion depending on D_{eff} is universal in all materials and expresses simply how much dilution of n_0 occurs by radial diffusion before nonlinear quenching in the track core takes its toll. This governs the roll-off at high n_0 as seen at the right hand end of the blue solid curve in Fig. 1.

In parallel with the D_{eff} dependence, inequality of D_e and D_h produces radial charge separation. This becomes an especially strong effect in halide compounds where self-trapping of holes reduces D_h to the order of 10^{-6} cm^2/s. Charge separation protects the separated carriers from prompt nonlinear quenching. They can still recombine with light emission during subsequent hopping diffusion under Coulomb attraction. However, diffusion of independent charge carriers in the presence of deep nonradiative traps introduces the hazard of deep trapping, which we characterize by the linear quenched free-carrier fraction k_1. Ref. [4] showed that the n_0-dependence of an Independent carrier Fraction, $IF(n_0, D_e, D_h)$, leads to a rising slope of Y_L *vs.* n_0, where the slope is proportional to k_1 and approximately to D_e /D_h. Combined with the falling slope depending on D_{eff}, this produces the hump seen in the blue curve of $Y_L(n_0)$ calculated for NaI:Tl in Fig.1. This hump qualitatively resembles and is responsible for the halide hump seen characteristically in the experimental electron energy response, $Y_e(E_i)$,[6] of halide materials (those with self-trapped holes). The responsible trends are similar to the Birks and Onsager trends discussed by Payne *et al*[6], but the treatment used here admits expression directly in

terms of nonlinear quenching rate constants and diffusion coefficients since it depends on *volume* energy deposition density *n* rather than linear energy deposition *dE/dx* as in Ref. [6].

Unfortunately there are no direct experiments of *local light yield* $Y_L(n_0)$ over the whole electron track. One must convert $Y_L(n_0)$ to $Y_e(E_i)$ in order to quantitatively compare the local light yield model to experiment. That is the subject of this communication. The lower curves (plotted points) in Fig. 1 are the results of Monte Carlo simulations of the electron energy deposition using Geant4 (version 9.4)[7] at each n_0 in NaI:Tl at three different E_i of 100 keV, 20 keV, and 5 keV. The low-energy Penelope electromagnetic models were used with a 100 eV threshold. See supplementary material for validation of Geant4 *dE/dx* results. The quantity plotted is $F_{e\text{-}h}(n_0,E_i)$, the fraction of all excitations occurring in a bin around n_0 from an electron of initial energy E_i (typically 200 2000 simulations averaged). Note that both $Y_L(n_0)$ and $F_{e\text{-}h}(n_0,E_i)$ are functions of n_0. Then the integral

$$Y_e(E_i) = \int_0^{n_0\,\max} F_{e-h}(n_0, E_i)\, Y_L(n_0)\mathrm{d}n_0 \qquad (1)$$

yields the predicted electron energy response for direct comparison to Compton coincidence or K-dip experimental $Y_e(E_i)$.

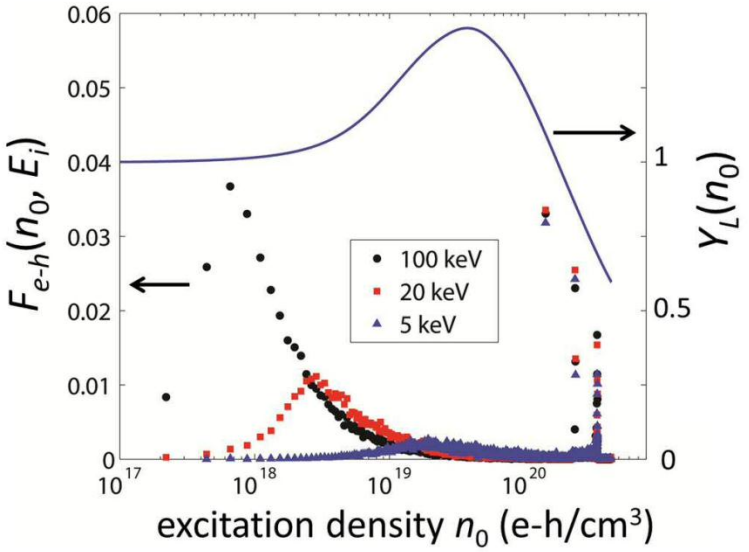

Figure 1 Plotted points (left axis) are distributions $F_{e\text{-}h}(n0,E_i)$ of on-axis e-h density n_0 for 100 keV, 20 keV, and 5 keV electron tracks in NaI. Solid blue curve (right axis) is local light yield $Y_L(n_0)$ for NaI with k_1 = 0.47, 3rd order kinetics with $K_3 = 3 \times 10^{-30}$ cm^{6}s^{-1}, and other parameters in Table I.

In this communication, we present calculated $Y_e(E_i)$ and comparison to experiment for NaI:Tl because it is widely used, and because the necessary input parameters have either been measured or can be scaled from closely similar CsI:Tl as listed and referenced in Table I. We also present calculated $Y_e(E_i)$ for SrI_2:Eu because it has exceptional light yield and proportionality.[8] Its exceptional performance is in interesting contrast to NaI:Tl considering that both materials have similar values for most of the parameters relevant in the model of local light yield due to *thermalized* diffusion.

Table I. Tabulated parameters for NaI:Tl and SrI_2:Eu.

	used NaI:Tl	measured NaI:Tl	method NaI:Tl	Ref.	used SrI_2:Eu
k_1	0.47	0.47	$LY \leq 1 - k_1$	[10]	0.04
K_2 (*t*) (exc.) ($cm^3 t^{-1/2} s^{-1/2}$)	NA	0.7×10^{-15}	z-scan 5.9 eV	present [15]	NA
K_3 (e-h) ($cm^6 s^{-1}$)	3×10^{-30}	3×10^{-30}	z-scan 6.1 eV	present [15]	1×10^{-30}
α (cm^{-1})	4×10^5	4×10^5	thin film	[22]	4×10^5
r_{NLQ} (nm)	3	3	z-scan K-dip	present [15]	3
μ_e (cm^2/Vs)	10	10	photocond.,	[20]	10
μ_h (cm^2/Vs)	10^{-4}	10^{-4}	STH hop 295 K	[23]	10^{-4}
β	2.5	2-3		[13,18]	2.3

There are two ways of getting the linear quenched fraction k_1 from measurements: (1) calculate it from a model based on concentration of deep traps and their cross section, as well as the range of diffusion through a given set of traps, which depends on thermalization time and velocity of hot electrons, depending in turn on host band structure.[9] (2) Alternatively, one may empirically measure an upper limit for k_1 directly from total light yield without a microscopic model. This is the method used to get k_1 in the present calculations. The total light yield as a fraction of excitations cannot exceed $1 - k_1$, i.e. $Y_T/Y_{max} \leq 1 - k_1$, where Y_T is the experimental total light yield and Y_{max} is the theoretical limit determined by βE_{gap}. In NaI:Tl, Y_T = 38,000 photons/MeV[10] gives $k_1 \leq 0.47$, taken here as $k_1 \approx 0.47$. The calculations assumed 0.1% Tl doping in NaI.

Solving Eq. (1) with the full set of $F_{e\text{-}h}$ distributions and the parameters in Table I gives the calculated electron energy response $Y_e(E_i)$ for NaI:Tl shown with black circular points in Fig. 2. Experimental SLYNCI Compton coincidence[1] and K-dip[2] $Y_e(E_i)$ for NaI:Tl are also plotted in Fig. 2. The Compton coincidence curves are the well-known set measured on many different NaI:Tl samples, giving the spread in energy response experimental curves.

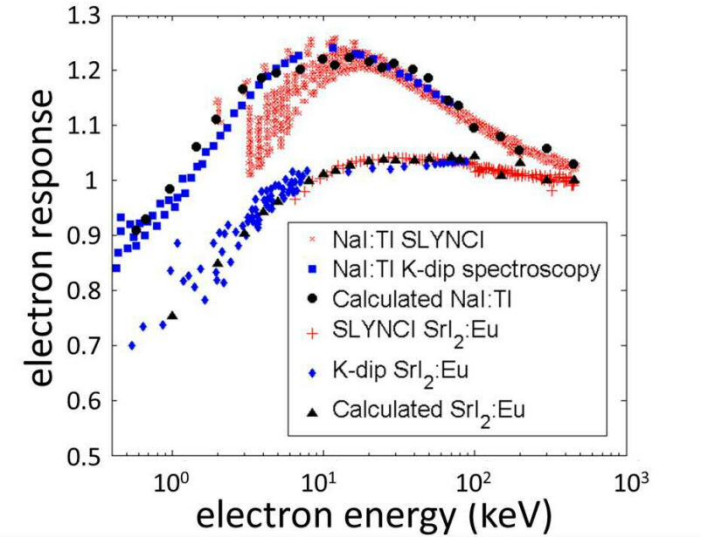

Figure 2. Calculated electron response for NaI:Tl and SrI_2:Eu (black circles and triangles) compared to data from SLYNCI (red asterisks and crosses) and K-dip (blue squares and diamonds) data. Calculated and experimental data normalized at 70 keV, displaced for visibility.

Similarly, we compare the calculated $Y_e(E_i)$ for SrI_2:Eu (black triangles) with both SLYNCI[1] (red dots) and K-dip[11] (blue diamonds). Due primarily to the hygroscopicity of SrI_2:Eu, some of its physical parameters used in the diffusion and quenching model have not yet been measured. At least the important K_3 and k_1 parameters have been measured in SrI_2:Eu, and the other parameters have been assigned NaI values. The comparison of SrI_2:Eu calculations to experiment thus amounts to a test of the importance of K_3 and k_1 in determining its electron response relative to NaI.

STHs have been predicted in SrI_2:Eu,[12] so the assumption of immobile holes is made. SrI_2:Eu has an exceptionally high total light yield of 80,000 ph/MeV, approximately 96% of the theoretical limit.[13] This is consistent with a very small k_1 = 0.04, and that has two effects. First, it decreases the magnitude of the hump in electron response, which improves proportionality. Second, it indicates that most carriers will recombine to give light, thus resulting in high light yield. This is in contrast to NaI:Tl which has a large k_1, therefore a large hump in electron response and lower light yield.

The first and essential conclusion is that taking NaI:Tl input parameters from experiment in a model of competitive diffusion and quenching predicts $Y_e(E_i)$ in good agreement with experimental data. This seems convincing confirmation of the roles of diffusion and quenching in nonproportionality. In a longer publication we will show the systematic effects of varying each material parameter and calculate $Y_e(E_i)$ for more materials as parameters are measured.

Third order quenching together with the measured K_3 contributes to the good match with experiment. This deserves mention, since it will be noted that the K_2 rate constant in Table I was not used for calculating electron response. This is experimentally based, since our recent z-scan experiments measured 2nd order kinetics and a rate constant K_2 for a laser photon energy of 5.9 eV that produces *only excitons* in NaI.[14,15] But using 6.1 eV photons that create free carriers, the quenching kinetics switched to pure 3rd order with rate constant K_3. This should be the applicable kinetics for high-energy electron excitation.

A. Kozorezov *et al*[16] based part of their study of hot carrier diffusion effects on our thermalized local light yield model,[4] but instead of using the thermalized band-

edge mobilities and diffusion coefficients as here, they point out that electrons are not fully thermalized on the time scale of diffusion that competes with nonlinear quenching in at least the heavier halides. They calculated time dependent diffusion coefficients of the thermalizing hot carriers and applied them in the physical context of Ref. [4] to calculate predictions of a hot electron diffusion and quenching model. Kirkin and Vasil ev [17] have also recently discussed the importance of non-thermalized electrons in scintillator response, including the effect of multiple LO phonon modes in complex crystals on speeding up thermalization. Additionally, Wang *et al*[18] have calculated distributions and thermalization effects of hot electrons in the electron track cascade. We agree generally with the reasoning and conclusions of all three groups, and have recently published an extension of our diffusion and quenching model to include hot electron transport, specifically the calculated hot-electron group velocity from band structure in NaI:Tl, SrI_2:Eu, and $LaBr_3$:Ce.[9] Granting the likely role of hot carriers, the results presented here show how well the thermal diffusion parameters and measured 3rd order quenching rates can already match experiments in NaI:Tl and SrI_2:Eu. From this base, hot-electron modifications of the diffusion parameters and resulting local light yield can be calculated in the form of $Y_e(E_i)$ as described here, to look for improved fit with Compton coincidence and K-dip experiments.

Acknowledgements Supported by the National Nuclear Security Administration, Office of Nonproliferation Research and Development (NA-22) of the U.S. Department of Energy, contracts DE-NA0001012 and DE-AC02-05CH11231. Computations were performed on the Wake Forest University DEAC Cluster with support in part by the University.

REFERENCES

[1] G. Hull, W. S. Choong, W. W. Moses, G. Bizarri, J. D. Valentine, S. A. Payne, N. J. Cherepy, and B. W. Reutter: Measurements of NaI:Tl electron response: comparison of different samples. *IEEE Trans. Nucl. Sci.* **56**, 331 (2009).

[2] I. V. Khodyuk, P. A. Rodnyi, and P. Dorenbos: Nonproportional scintillation response of NaI:Tl to low energy x-ray photons and electrons. *J. Appl. Phys.* **107**, 8 (2010).

[3] G. Bizarri, W.W. Moses, J. Singh, A.N. Vasil ev, and R.T. Williams: An analytical model of nonproportional scintillator light yield in terms of recombination rates. *J. Appl. Phys.* **105**, 044507 (2009).

[4] Qi Li, Joel Q. Grim, R. T. Williams, G. A. Bizarri, and W. W. Moses: A transport-based model of material trends in nonproportionality of scintillators. *J. Appl. Phys.* **109**, 123716 (2011).

[5] R. T. Williams, J. Q. Grim, Qi Li, K. B. Ucer, and W. W. Moses: Excitation density, diffusion-drift, and proportionality in scintillators. *Phys. Status Solidi B*, **248**, 426 (2011).

[6] S. A. Payne, W. W. Moses, S. Sheets, L. Ahle, N. J. Cherepy, B. Sturm, S. Dazeley: Nonproportionality of scintillator detectors: theory and experiment. II. *IEEE Trans. Nucl. Sci.* **58**, 3392 (2011).

[7] J. Allison *et al*.: Geant4 developments and applications. *IEEE Trans. Nucl. Sci.* **53** No. 1, 270 (2006); S. Agostinelli et al.: Geant4: a simulation toolkit *Nucl. Instrum. Methods Phys. Res. A*, **506**, No. 3, 250 (2003).

[8] S. A. Payne, N. J. Cherepy, G. Hull, J. D. Valentine, W. W. Moses, W.-S. Choong: Nonproportionality of Scintillator Detectors: Theory and Experiment. *IEEE Trans. Nucl. Sci.* **56**, 2506 (2009).

[9] Qi Li, Joel Q. Grim, K. B. Ucer, A. Burger, G. A. Bizarri, W. W. Moses, and R. T. Williams: Host structure dependence of light yield and proportionality in scintillators on ω_{LO}, μ_e, μ_h, and hot-electron v_g. Submitted to *Physica Status Solidi Rapid Research Letters*.

[10] http://www.detectors.saint-gobain.com/NaI(Tl).aspx

[11] M.S. Alekhin, I.V. Khodyuk, J.T.M. de Haas, P. Dorenbos*:* Non-proportional response of $SrI_2:Eu^{2+}$ scintillators*.* Presented at *11th Intern. Conf. on Inorganic Scintillators and their Applications (2011).*

[12] Babak Sadigh and D. Åberg: First-principles calculations of self-trapping of carriers and excitons in NaI and SrI_2. presented at *IEEE Symposium on Radiation Measurements and Applications* (SORMA West) Oakland, May 14-17 (2012).

[13] P. Dorenbos: Fundamental limitations in the performance of Ce^{3+}-Pr^{3+}-, and Eu^{2+}-activated scintillators. *IEEE Trans. Nucl. Sci.* **57**, 1162 (2010).

[14] Joel Q. Grim, Q. Li, K. B. Ucer, R. T. Williams, A. Burger, P. Bhattacharya, E. Tupitsyn, G. A. Bizarri, W.W. Moses: Nonlinear quenching rates in SrI_2 and CsI scintillator hosts. *Mater. Res. Soc. Symp. Proc.* **1341**, 15 (2011).

[15] Joel Q. Grim, K.B. Ucer, R.T. Williams, A. Burger, P. Bhattacharya, E. Tupitsyn, G. A. Bizarri, W.W. Moses: Measurement of exciton and free carrier nonlinear recombination dynamics in insulators and semiconductors: SORMA West, Oakland, May 16 (2012) and to be published; R. T. Williams, Joel Q. Grim, Qi Li, and K. B. Ucer: Experimental determination of the track-end radius in NaI:Tl and implications for host-structure dependence of nonproportionality in halide scintillators: Presented at International Conf. on Defects in Insulating Materials, Santa Fe, June 25 (2012).

[16] Kozorezov J. K. Wigmore, A. Owens: Picosecond dynamics of hot carriers and phonons and scintillator non-proportionality. arXiv:1206.1780v1. To be published 2012.

[17] R. Kirkin, V.V. Mikhailin, and A.N. Vasil ev: Recombination of correlated electron hole pairs with account of hot capture with emission of optical phonons. *IEEE Trans. Nucl. Sci.* **PP**, no.99, 1, (2012). doi: 10.1109/TNS.2012.2194306

[18] Z. Wang, Y. Xie, B. D. Cannon, L. W. Campbell, and F. Gao, and S. Kerisit: Computer simulation of electron thermalization in CsI and CsI(Tl). *J. Appl. Phys.* **110**, 064903, (2011).

[19] P. Dorenbos, M. Marsman, C.W.E. van Eijk: Non-proportionality in the scintillation response and the energy resolution obtainable with scintillation crystals. *IEEE Trans. Nucl. Sci.***42**, 6, 2190 (1995).

[20] S. Kubota, F. Shirraishi, and Y. Takami: Scintillation Process in NaI(Tl): Comparison with Scintillation Models. *J. Phys. Soc. Jpn.* **69**, 3435 (2000).

[21] S. Kerisit, K. M. Rosso, B. D. Cannon: Kinetic Monte Carlo model of scintillation mechanisms in CsI and CsI(Tl). *IEEE Trans. Nucl. Sci.* **55**, 1251 (2008).

[22] W. Martienssen: Über die excitonenbanden der alkalihalogenidkristalle. *J. Phys. Chem. Solids* **2**, 257 (1957).

[23] H.B. Dietrich, R.B. Murray: Kinetics of the diffusion of self-trapped holes in alkali halide scintillators. *Journal of Luminescence* **5**, 155 (1972).

CHAPTER 6: FIRST PRINCIPLES CALCULATIONS AND EXPERIMENT PREDICTIONS FOR IODINE VACANCY CENTERS IN SrI_2

Qi Li, R. T. Williams, Daniel Åberg

The following manuscript was published as Editor's Suggestions in *Physica Status Solidi B* (2013). Qi Li performed all the first principles with help from Daniel Åberg of Lawrence Livermore National Lab. Qi Li and R. T. Williams developed the method for calculating absorption spectrum and prepared the manuscript. Manuscript is reproduced with permission of John Wiley and Sons. Stylistic variations are due to the requirements of the journal.

ABSTRACT

We present the electronic structure, lattice relaxation, and formation energies of iodine vacancy defects in SrI_2 for the one-electron, two-electron, and ionized charge states. We use a local generalized gradient approximation as well as non-local hybrid functionals within the framework of density functional theory, as it is commonly accepted that the latter can improve accuracy of the band gap and hence relevant energy levels. Comparison is made to published results on chlorine vacancy defects in NaCl calculated with similar methods and functionals, and also to a recent first-principles study of one- and two-electron occupancy in MgO vacancy centers. Using the parameters that are calculable from first principles in SrI_2 as a starting point, we incorporate available experimental data and adaptations of simple models to predict a range of results that can help guide or interpret future experiments such as absorption energy, configuration coordinate curves, vibrational lineshape, thermal trap depth, and Mollwo-Ivey comparison to alkaline-earth fluorides.

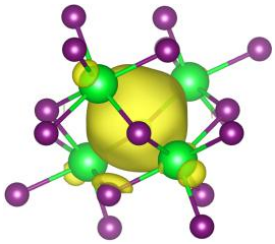

Online title figure: Charge density contour in the F center in SrI_2.

1 Introduction

In 2008, $SrI_2:Eu^{2+}$ became the focus of intense interest in the search to develop higher resolution gamma-ray scintillation spectrometers [1,2] for use in fields such as chemical and isotope security screening, medical molecular imaging, and high-energy physics experiments. For roughly six decades, monovalent alkali iodide scintillators had remained the stalwart choice for many applications in radiation detection. Their light yield and proportionality (both related to energy resolution [3]) were only modest compared to theoretical limiting values and their response was slow. But even the modest values of the first two performance parameters along with ease of crystal growth were enough to keep them ahead of most competing scintillator materials for much of the six decades. Oxide hosts doped with Ce gave faster response and more rugged mechanical characteristics for medical applications beginning from about 1990 [3-5], but still at generally lower light yield (until very recently [6]) and comparable or lower resolution than the alkali halides.[3] Under mounting needs for a breakthrough advance in sensitivity and gamma energy resolution, the discovery of the tri-valent metal halide scintillators $LaCl_3:Ce^{3+}$ and $LaBr_3:Ce^{3+}$ [7,8] finally approached close to theoretical maximum light yield [3] and achieved resolution unprecedented in a scintillator to that time. Then the detailed experimental re-examination and development starting from 2008 of $SrI_2:Eu^{2+}$ scintillation (first discovered decades earlier by Hofstaedter [9]) set a new record in scintillator performance with arguably the best combined light yield and proportionality achieved to date [1-3]. It was soon followed with other discoveries of similar high performance in combined light yield and proportionality, e.g. $BaBrI:Eu^{2+}$

[10], $CsBa_2I_5:Eu^{2+}$[10], $Cs_2LiLaBr_6:Ce^{3+}$[11], $Cs_2LiYCl_6:Ce^{3+}$ [12]. Interestingly, those recent top performers so far are always in host crystals describable as multivalent or complex metal halides.

This distinctive dependence of scintillation performance on the host crystal structure, first noted by Payne et al in summarizing survey measurements of a large number of materials [13], is an interesting puzzle in its own right. We have recently proposed [14] that a main reason for the better performance of complex halides over simple alkali halides involves both hot electron transport within the dense ionization track and the concentration and properties of deep electron traps in the host. Together, the diffusion distance, trap concentration, and capture cross sections determine a *linear quenched fraction* k_1, which was shown in Refs. [15,16] to be a controlling factor in both nonproportionality and the total light yield. Part of the motivation of this paper is to gain understanding of electron traps contributing to the size of k_1 in what is arguably the pre-eminent representative of the high-performance new multivalent halides, $SrI_2:Eu^{2+}$. According to a numerical model of interacting defect traps and carrier diffusion in high concentration gradients of electron traps [15,17], and also an analysis by the method of rate equations [18], k_1 acts both to scale the "halide hump" in measurements of light yield versus initial electron energy and to limit the maximum light yield. Elimination of deep traps and other causes of linear quenching of electrons (k_1), could in principle eliminate the halide hump, which is the main contributor to poor proportionality of alkali halide scintillators, and also increase the potential light yield to very high values [16]. One immediately wonders if the main material advantage of $SrI_2:Eu^{2+}$ as a scintillator host over, e.g., alkali halides might just be a particularly low concentration or cross

section of defects serving as deep electron traps in SrI_2. In any case, as a divalent halide, SrI_2:Eu^{2+} is the next step up in chemical complexity from the alkali halides, bringing a very remarkable change in properties for a short step in chemical complexity but a large step in structural complexity.

With this motivation, we want to characterize the properties of some of the expected common lattice defects in SrI_2. As it turns out, SrI_2 is extremely hygroscopic, and until recently it was moderately difficult to grow good crystals. As a result of these complicating experimental factors and the absence of a strong driving interest until the recent need for improved gamma detectors, there is very little known about defects in SrI_2. Thermoluminescence measurements have been performed [19]. However, optical absorption and EPR spectroscopy of native or radiation induced lattice defects in SrI_2 are basically absent. The first optical absorption spectroscopy on SrI_2 that has been performed in our laboratory is on short-lived species induced by band-gap excitation [20]. The first "defect" calculations on SrI_2 up to now are of an intrinsic transient species, self-trapped excitons [21]. Experiments to introduce and study conventional lattice defects in SrI_2 are being planned, but meanwhile this seems a good occasion for first principles electronic structure theory to lead experiment.

Chen et al. [22] reported results on chlorine vacancy defects in NaCl calculated with similar methods and functionals to those we employ here. Their work provides a useful validation of the accuracy and appropriateness of the computational methods in a similar ionic material where experimental data are abundant. In discussing the data, we will be interested in finding what may be viewed as extensions of behavior seen in the simpler alkali halides, but also new features or characteristics due to the divalent cations

and more complex crystal structure. It is anticipated that spectroscopic defect data on SrI_2 will soon be coming from a number of laboratories. The present calculated predictions should be of help in planning experiments and interpreting the data. Finally, comparison of fully interpreted data with the calculations will provide a retrospective validation or route to improvement of the calculation methods as applied in this material class.

Another useful comparison will be drawn between three types of crystals exhibiting one- and two-electron vacancy centers. In SrI_2, the one- and two-electron centers are termed F and F- respectively in the common nomenclature, where lattice-neutral trapped electron defects are designated F centers. One important case for comparison is the one- and two-electron vacancy centers in MgO, termed F^+ and F respectively. These were the subject of a recent first-principles calculations [23] of optical spectra using the GW approach and the Bethe-Salpeter equation aimed partly at elucidating the experimental observation [24] that the one- and two-electron centers in MgO have almost identical first optical absorption transitions, i.e. the optical binding energy of the second electron in the vacancy is almost the same as that of the first one. This might seem at first counter-intuitive in a static-lattice Coulomb potential picture. We encounter a similar result on examining the optical binding energies of one- and two-electrons in the iodine vacancy of SrI_2. This affects how F and F^- centers both behave as deep electron traps in SrI_2 and so feeds back to the practical consequences for scintillator performance.

2 Material parameters and calculation methods

2.1 Crystal structure and experimental parameters

The crystal structure of SrI_2 is orthorhombic, space group Pbca (No. 61 of the International Tables of Crystallography), with lattice constants 15.22, 8.22, and 7.90 Å, respectively [25]. The experimental band gap of SrI_2 is still being refined, and seems to be converging to about 5.5 eV. Experimental and theoretical values of band gap since 2008 have been quoted as 3.7 eV estimated from absorption and luminescence spectra in thick samples [2], 4.5 eV calculated in DFT with Engel-Vosko GGA[26], 5.7 eV synchrotron luminescence excitation[27], $\geq$ 5.1 eV measured in transmission of a 100 μm crystal [28], and ≈ 5.5 eV deduced from the 1s exciton dip in synchrotron radiation luminescence excitation with estimated 0.26 eV exciton binding energy from dielectric constant [29].

Another experimental parameter that will be used in later analysis and discussion is the LO phonon frequency. Cui et al measured Raman spectra and reported the highest A_g mode to be 124.5 cm^{-1} [30], i.e. the highest-frequency zone-center phonon ω_{LO} = 2.6 $\times 10^{13}$ s^{-1} in SrI_2.

2.2 Computational methods

Our ab-initio calculations are carried out in the projector augmented wave framework in the Vienna ab-initio simulation package (VASP) [31,32]. We employ both screened and unscreened hybrid functionals (HSE06 [33] and PBE0 [34]) and compare the results to the Perdew-Burke-Ernzerhof (PBE) parametrization of the generalized gradient approximation (GGA) [35]. The mixing fraction is 0.25 for both hybrid

functionals and the screening parameter used for HSE06 is 0.2 $Å^{-1}$ following Ref. [33]. The kinetic cut-off energy is 300 eV. A self-consistency convergence criterion of 1×10^{-6} eV is used for all calculations and the structures are relaxed until all force components are less than 0.01 eV/ Å. The bulk properties of ideal SrI_2 are calculated with the primitive unit cell of 24 atoms. A Γ-centered $2 \times 4 \times 4$ Monkhorst-Pack *k*-point mesh is applied for all three exchange-correlation (xc) functionals. To simulate the iodine vacancy, we choose a $1 \times 2 \times 2$ supercell which is roughly cubic in overall shape containing 96 atoms, and remove one iodine atom from a site as specified below. For the defect calculations we use a Γ-centered $2 \times 2 \times 2$ Monkhorst-Pack k-point mesh for GGA-PBE, and only Γ point calculations for hybrid functionals due to the computational complexity. To test the effect of this economization, we calculated with HSE06 the perfect crystal energy with a $2 \times 4 \times 4$ sampling in a unit cell and with $1 \times 1 \times 1$ sampling in the supercell specified above. The energies differed by 1.7 meV/atom. There are two distinguishable iodine sites at the 8c Wyckoff positions: site 1 (−0.202,−0.108,−0.163) and site 2 (0.202,0.108,0.163). We have calculated the formation energy for both of them and they differ by ~0.2 eV. In the current paper, all the results correspond to the lower energy iodine vacancy unless specified otherwise.

2.3 Finite supercell size corrections

In the supercell approximation there are spurious interactions between the defects [22,36,37]. For charged neutral defects, the strain energy is the leading error and scales roughly with L^{-3} [38,39], where L is distance between the periodic defects. Makov and

Payne considered the convergence of the energy of charged species in periodic systems and established a correction on the basis of a multipole expansion as follows. [40]

$$E_f(L) = E_f(L \to \infty) - \frac{\alpha_{\mathrm{Md}} q^2}{2\varepsilon L} - \frac{2\pi q Q}{3\varepsilon L^3} + O(L^{-5}) \qquad (1)$$

where q is the charge of the defect, and Q is the quadrupole moment. The leading term corresponds to the monopole-monopole interaction and can be analytically determined from the Madelung constant α_{Md} of the Bravais lattice of the supercell and the static dielectric constant of the material. Because the F center is lattice-neutral, only small inward displacement of the nearest Sr^{2+} ions occurs on relaxation, so no correction is needed. For the charged iodine vacancies, we choose 5 different supercells with different sizes (containing 48, 96, 144, 288, 432 atoms respectively) and relax the structures for both F^- and F^+ center using GGA-PBE. We calculate the monopole-monopole interaction terms for each of them explicitly using the calculated static dielectric constant tensor [41] and extrapolate the corrected data assuming an L^{-3} dependence. Here L is defined as the cubic root of the supercell volume. Note that this term contains both the quadrupole term of the Makov-Payne scheme and the strain energy [36]. The resulting total correction terms for the F^- and F^+ center of 0.22 eV and 0.06 eV respectively are applied to the hybrid functional results when specifying defect formation energies.

2.4 Chemical potentials, formation energies and thermodynamic transitions

We assume that the crystal is in equilibrium with a reservoir of strontium metal (fcc crystal) and molecular iodine (orthorhombic crystal). The formation energy of an iodine vacancy at charge state q is [22,36,37]

$$\Delta E = E_{\mathrm{d}} - E_{\mathrm{lat}} + \Delta\mu_{\mathrm{I}} + \mu_{\mathrm{I}}(\mathrm{solid}) + q(E_{\mathrm{VBM}} + E_{\mathrm{F}}) \quad (2)$$

where E_{d} is the total energy of a supercell containing one iodine vacancy in charge state q, E_{lat} is the total energy of the perfect supercell. E_{VBM} and E_{F} are valence band maximum (VBM) and electron Fermi energy respectively. To simulate the energy cost of removing one electron from VBM, one needs a sufficiently large supercell to reach the dilute limit.

The chemical potential of the iodine reservoir crystal is μ_{I}(solid). $\Delta\mu_{\mathrm{I}}$ is the change in chemical potential of iodine from the reservoir upon incorporation in SrI_2. $\Delta\mu_{\mathrm{Sr}}$ is the analogous chemical potential change from the strontium reservoir. The formation enthalpy of the SrI_2 crystal is thus

$$\Delta H_{\mathrm{SrI_2}} = \Delta\mu_{\mathrm{Sr}} + 2\Delta\mu_{\mathrm{I}} \quad (3)$$

$\Delta\mu_{\mathrm{I}}$ can vary from ½ $\Delta H_{\mathrm{SrI_2}}$ in the Sr-rich limit up to 0 in the iodine-rich limit. The thermodynamic transition energy, defined by the value of the electron chemical potential at which the charge state of the vacancy changes from q to q', is given by the following expression [22,37].

$$E(q/q') = \frac{E_d(q) - E_d(q')}{q' - q} - E_{\mathrm{VBM}} \quad (4)$$

3 Results

3.1 Crystal structure and experimental parameters

The bulk properties of the ideal crystal are listed in Table I. All three functionals overestimate the lattice constants. PBE0 predicts the smallest deviation of the unit cell volume from experiment. Use of the PBE0 functional produces a close match with the experimental bandgap discussed in section 2.1 above.

Table 1 Lattice constant, deviation of the unit cell volume from experiment, and bandgap (E_g) calculated using three different xc functionals.

	lattice constant (Å)			ΔV(%)	E_g (eV)
	a	b	c		
GGA	15.63	8.31	8.03	5.5	3.85
HSE06	15.53	8.28	7.99	4.0	4.86
PBE0	15.46	8.28	7.98	3.3	5.52
Expt.	15.22[a]	8.22[a]	7.90[a]	--	~5.5[b]

[a]Ref. [25]; [b]Ref. [29]

3.2 Defect formation energies and thermodynamic transition energies

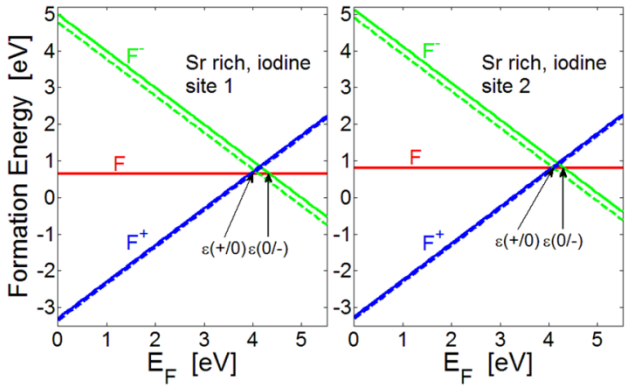

Figure 1 Formation energies of vacancies at iodine sites 1 and 2 under Sr-rich conditions calculated using the PBE0 functional are plotted in (a) and (b). Dashed lines correspond with results as calculated before finite-size correction for charged defects, solid lines indicate results after the correction. The crossing points between F center and charged centers indicate the positions of the thermodynamic transition energies.

The formation energies at the Sr-rich limit for three different charge states as a function of Fermi energy calculated from PBE0 are plotted in Fig.1. Note that there are two distinguishable iodine sites in the crystal -- site 1 has four nearest Sr ion neighbors and site 2 has three nearest Sr ion neighbors. The F center at site 1 has ~0.2 eV lower formation energy than at site 2, so we focus on the type 1 site in the rest of the paper. We can see from Fig. 1 that the thermodynamic transition energies ε(+/0) and ε(0/−) are both within the band gap, which suggests the stability of all three charged states of iodine

vacancy when the Fermi energy is varied within the band gap. We can also see that the finite size correction widens the region of stability for the neutral F center.

In Fig. 2, the thermodynamic transition energies calculated using the three different density functionals are compared. The ε(+/0) level increases from 2.8 eV to 3.74 eV as the band gap widens from GGA-PBE to PBE0, however the energy window between ε(+/0) and ε(0/-) remains similar.

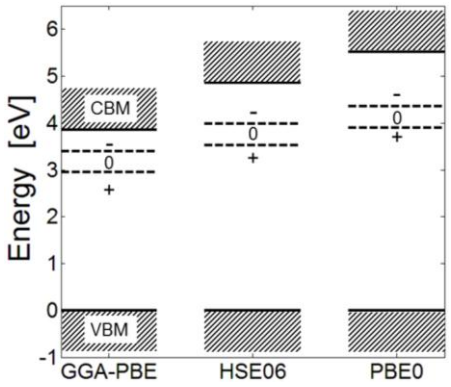

Figure 2 Thermodynamic transition energies between the q = +1, 0, and −1 charge states of the iodine vacancy with respect to the lattice are denoted by the dashed lines.

The calculated formation energies for the iodine vacancy in different charge states are listed in Table 2, for the Fermi energy at the VBM. The dependence of formation energies on choice of functional is more significant for the charged centers. Similar trends have been found in NaCl in Ref. [22].

Table 2 Formation energies (eV) of iodine vacancies in different charge states calculated with different functionals at Sr rich and I rich limits. The Fermi energy is set at E_{VBM}. All results are corrected for finite size effect.

	Sr rich			I rich		
	GGA	HSE06	PBE0	GGA	HSE06	PBE0
F	0.698	0.661	0.647	3.248	3.468	3.498
F^+	−2.295	−2.903	−3.292	0.255	−0.096	−0.441
F^-	4.07	4.636	4.996	6.620	7.443	7.847

3.3 Lattice relaxation and electron density contours around the iodine vacancy

It can be seen in Table 3 that the nearest-neighbor Sr^{2+} ions around the F center remain almost at the perfect lattice distance, since the F center with one unpaired electron is lattice neutral in SrI_2. In the F^+ center, the electron bound to the iodine vacancy has been removed, leaving an effective positive charge at the vacancy. The nearest neighbor Sr^{2+} ions relax outward due to the net repelling potential, and the unoccupied defect level moves closer to the CBM and delocalizes more. When the vacancy is doubly occupied as in the F^- center, the nearest neighbor Sr^{2+} ions see a negative charged potential at the vacancy and relax inward accordingly, as seen in Table 3. Their positive charge and the shrinking confinement cage they represent keeps the doubly occupied defect level well localized despite its negative charge and brings the energy down.

Table 3 Average nearest neighbor Sr^{2+} distance from the vacancy center in the relaxed structures of iodine vacancy in SrI_2 in different charge states calculated in a 96 atom supercell. The last column lists configuration coordinate force constants deduced in Section 3.4.

	average nearest Sr^{2+} distance (Å)			γ (eV/Å^2)
	GGA	HSE06	PBE0	PBE0
F^+	3.74	3.72	3.72	12.82
F	3.38	3.38	3.38	8.58 (8.22)
F^-	3.12	3.00	3.00	5.19
crystal	3.40	3.39	3.39	--

Figure 3 compares the energies of the valence band maximum (VBM), each defect level of specified charge (−1,0,+1), and the conduction minimum (CBM) for each of the three functional choices. The defect level of the F^- center is doubly occupied, and for the

F^+ center it is unoccupied. In spin-polarized calculations, the F center has one spin level occupied (F_{s1}) and the other unoccupied (F_{s2}).

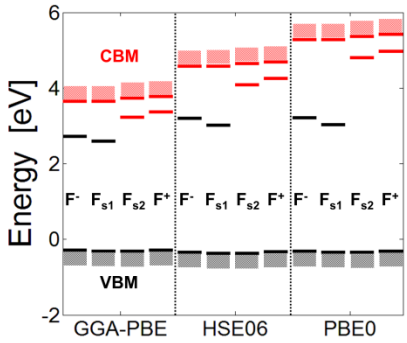

Figure 3 Energy levels relative to E_{VBM} calculated with different xc functionals. For the F center, spin-polarization is turned on and both occupied (F_{s1}) and unoccupied opposite-spin (F_{s2}) levels are shown. Black levels are occupied and red, unoccupied.

It can be seen in Fig. 3 that both electrons of the F^- center in SrI_2 are almost as deeply bound as the single electron of the F center. Furthermore, the isosurface plots in Fig. 4 show that the spatial confinement of the two electrons in the central vacancy of the F^- center is almost the same as in the single F electron. In fact, the Bader analysis below shows that the two electrons in the F^- center are confined in a smaller central distribution than the F center electron. This can be explained by the strong role of the inward relaxing divalent Sr^{2+} ions responding to and stabilizing the net negative charge in the F^-.

The similarity of the F and F^- energy levels in Fig. 3 despite the net charge difference is suggestive of the case of F^+ and F centers in MgO addressed in a very recent first principles study [23] and earlier experiments [24]. In MgO (with divalent anion and cation), the absorption bands of the F^+ center (one electron) and lattice-neutral F center (two electrons) are almost superimposed. In SrI_2, the F (one electron) and F^- (two electron) absorption transitions are similarly close to the same energy.

Fig. 4 shows the charge density contours of the occupied (gold) and unoccupied (red) defect states. Figures on the left show the contour representing 2% of the maximum density; on the right, 10% of the maximum.

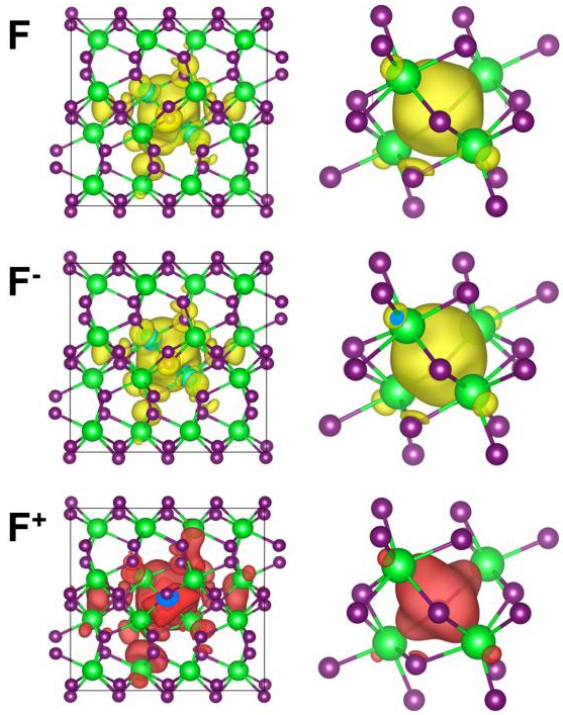

Figure 4 Electron density contours for iodine vacancy centers in SrI_2 in charge states of F, F^-, and F^+. Gold and red denote the occupied and unoccupied defect contours at isosurface levels of 2% (left) and 10% (right). Ions are I-purple, Sr-green.

Henkelman et al. have established a method using Bader analysis to separate the atoms in a crystal according to their electronic charge density [42-44]. In Table 4, we show the integrated electron density at the vacancy and the minimum distance from the vacancy to the Bader surface for the iodine vacancy electron density distribution. For the F^- center, the hybrid functionals predict smaller volume of the iodine vacancy relative even to the F center, which is consistent with the results of the vacancy – nearest neighbor Sr^{2+} ion distance shown in Table 3. More electron density is confined within the

smaller vacancy volume predicted by hybrid functionals. This suggests stronger tendency for localizing electronic states compared to semilocal functionals in which self-interactions are more dominant.

Table 4 Results of the Bader analysis, listing integrated electron density within the Bader surface, D_{Bader}, in units of e, and the minimum distance from the vacancy to the Bader surface, $d_{\min}$ (Å).

	GGA-PBE		HSE06		PBE0	
	D_{Bader}	$d_{\min}$	D_{Bader}	$d_{\min}$	D_{Bader}	$d_{\min}$
F^+	0	--	0	--	0	--
F	0.709	2.128	0.732	2.129	0.736	2.129
F^-	1.417	1.911	1.459	1.867	1.468	1.861

3.4 Configuration coordinate diagram

For first-principles input toward determining approximate optical transitions and vibrational lineshapes (rather than a full Bethe-Salpeter approach as done recently for the F and F^+ centers in MgO [23]) we calculated approximate configuration coordinate curves from the first-principles energies of each of the three defect charge states in the following way. The finite-size corrected formation energies in each different charge state were first calculated at the energy-minimized lattice configuration using PBE0. To describe the procedure farther, we focus specifically on the F center as the ground state and the F^+ center as its ionization limit. The complete set of coordinates of the ground state F (1s) and the ionization limit (F^+) are denoted as Q_0 and Q_+ respectively. We linearly interpolate these two lattice configurations (for all ions) by using 15 intermediate interpolations along the lattice configuration gradient defined by Q_0 and Q_+ as two endpoints. The F and F^+ energies are then calculated at each of the fixed intermediate

lattice configurations. The energy values as a function of interpolated Q are plotted as points superimposed on the fitted F and F^+ parabolas in Fig. 5 and can be seen to match the parabolas very closely. From this fit, we can extract the effective force constant γ, which is listed for each charge state in Table 3 and will be used for calculating vibrational wave functions in Section 4.3.

The configuration coordinate curves for the F center as ground state and the F^+ center as its ionized state are plotted in Fig. 5. The true horizontal axis is the interpolated configuration coordinate Q involving all ion positions. In the lower axis label, this is referred to as configuration coordinate even though it is not representing a specific normal mode. To give a numerical feel, we also plot in Fig. 5 the average nearest-neighbor Sr^{2+} distance from the vacancy (R_{nn}) appearing in each Q configuration of the F center ground state. But this does not imply that the energy change is a function of changing only the nearest-neighbor distance. The Q for the F^- ground state will be along a somewhat different line in configuration space than for the F center ground state.

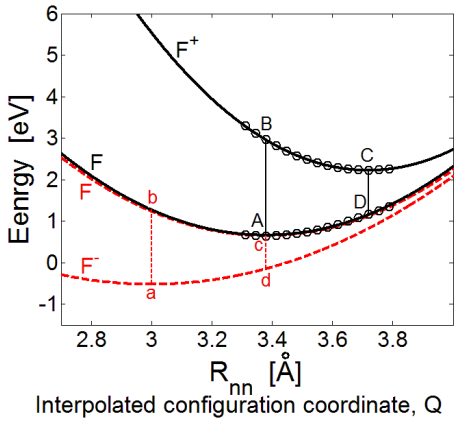

Figure 5 Interpolated configuration coordinate diagram for the F, F^-, and F^+ centers in SrI_2. The Fermi energy is set at the CBM. Finite size corrections are applied. Solid black parabolas fitted to the calculated points represent the F and F^+ energies along the linearized relaxation path between their equilibrium configurations. Dashed red curves give similar representations of F^- and F energies.

4 Discussion

A framework of formation energies, lattice relaxation, charge contour, optical and thermal ionization limits, and curvature (effective force constant) of the configuration coordinate diagram were given by the first principles calculations discussed above. In order to compare to available experiments, or in the case of SrI_2 mostly to prepare for future experiments, we will now go sometimes outside the first principles DFT methods to finish deducing values of transition energies to bound excited states, vibrational lineshape of the transitions, comparison to a particle-in-a-box model by so-called Mollwo-Ivey plots, and activation energies of thermoluminescence. These predictions follow from first principles calculations as the first step, then are supplemented by model extensions and some additional experimental data. At present, they are mostly ahead of experiment in SrI_2. However, some of the same first-principles computational methods have been used for chlorine vacancy centers in NaCl where experimental data do exist. Comparison to experiment in NaCl can provide guidance on which of the xc functional choices are most successful for ionic vacancy defects, and outline the approximate error achieved between theory and experiment. On this basis we will carry over the best NaCl defect calculation methods after confirmation against experiment to the (ground-breaking) predictions about iodine vacancy centers in SrI_2.

4.1 Photo-ionization limit and optical absorption transitions of the F center

Figure 6 shows again the calculated F center configuration coordinate curves based on results with PBE0 hybrid functionals. It now includes additional labels and markings to be referenced in the present discussion. The vertical transition from A to B

represents the optical ionization limit of the F center in the calculated results for SrI_2. In the literature on alkali halide F centers [45,46], the "F band" optical transition is associated with the transition labeled 1s→2p in a hydrogenic model analog of the F center. There is a higher energy "K band" in the optical absorption spectrum that is interpreted as the unresolved envelope of all 1s→np transitions for n = 3, 4, ... ∞. The transition A → B in Fig. 5 represents 1s→∞p in this terminology, and is the essential input provided here from the first principles calculation. For comparison to the F band transition in optical absorption, we need to deduce the 1s-2p energy. The effective mass hydrogenic model for shallow trapped electrons predicts transition energies to p-states of principle quantum number *n* according to [45]

$$\Delta E_{1s\to np} = \frac{e^4 m^*}{2\varepsilon^2 \hbar^2}\left(1-\frac{1}{n^2}\right) \qquad (5)$$

This is useful for shallow trapped-electron centers in solids and for conceptual discussions of F centers, but it is not accurate on its own for the F center. A shortfall of Eq. 5 for F centers is that their radial extent is too small for effective mass theory to apply in the ground state and the effective dielectric constant is between the optical limit for the ground state and tending toward static ε_0 for the excited states. One is then left with m^*/ε^2 in Eq. 5 being an undetermined parameter. In the present treatment, we rely on the first principles calculation to provide the 1s→∞p limit of Eq. 5, thus in an approximate sense determining the undetermined ε parameter. We interpolate Eq. 5 to estimate the 1s→2p transition energy consistent with the calculated ionization limit. The fact that m^*/ε^2 in Eq. 5 still changes somewhat for different transitions is becoming a smaller correction in a

smaller quantity than if ε were required to specify the scaling from a full hydrogen Rydberg of 13.6 eV, as in earlier attempts to apply Eq. 5 without first principles input.

Following the recipe summarized above, the predicted F band absorption transition (1s → 2p) in SrI_2 is estimated to be 75% of the ionization limit calculated from first principles, i.e. $\Delta E_{F(1s\rightarrow 2p)} = 1.67$ eV. This transition of the F center in SrI_2 is sketched in Fig. 5, where the interpolated F(2p) potential curve is approximated with a broken line.

Reference [22] presented a configuration coordinate diagram for NaCl analogous to Fig. 5. As we have also done, they evaluated the transition energy A → B from the F center vertically to the unrelaxed F^+ center using three different choices of DFT xc functionals, GGA, HSE06, and PBE0. However, they compared the ionization transition A → B (1s → n∞) directly to the F band absorption transition in NaCl, $\Delta E_F = 2.77$ eV. Comparing this experimental transition energy in the same column of their Table V with the calculated ionization limits appeared to make the HSE06 prediction of 2.56 eV look better than the PBE0 prediction of 3.50 eV. Similarly, the HSE06 prediction of 1.07 eV recombination emission from the NaCl F^+ state to the F(1s) defect ground state was compared to experimental 0.98 eV emission, which is actually from the relaxed F(2p) state. Comparison to recombination from the ionized state rather than the relaxed excited state made HSE06 look much more successful in matching experiment than PBE0, which predicted 1.88 eV for recombination from ionization. The emission energies will be discussed below and are listed with absorption energies in Table 5.

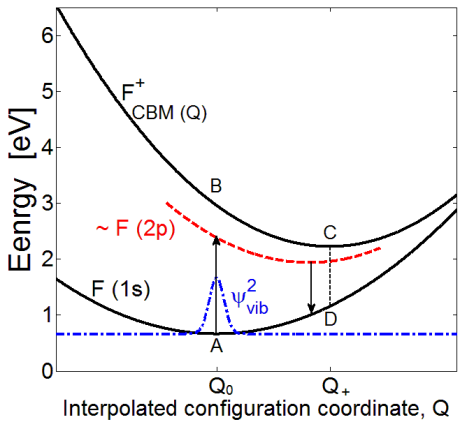

Figure 6 The calculated black solid configuration coordinate curves for the F center and its ionization limit F^+ are reproduced from Fig. 5. The interpolated F(2p) excited state is represented according to the discussion above, in order to illustrate the main absorption and emission transitions that should be compared to experiment. The square of the lowest vibrational wavefunction calculated according to Section 4.3 is plotted in preparation for calculating the F band lineshape in Fig. 7.

What we want to point out, with some importance for applications of the various xc functionals to SrI_2 in the present paper, is that PBE0 gives much better predictions for the experimental absorption transition energy in NaCl if the deduction of 1s→2p F band transition energy is done by the procedure outlined above before comparing to the experimental transition. The experimental emission energy falls between the HSE06 and PBE0 predictions in NaCl. The results for F band (1s → 2p) absorption energies deduced from the Chen et al. [22] calculation of the 1s → ∞p ionization limit for NaCl F centers are shown in Table 5.

Table 5 Transitions E_a and E_e from Ref. [22] multiplied by the 0.75 factor discussed above before comparison to experiment. The last column notes that ZPL from Ref. [22] is the thermal trap depth of the F center, $\Delta E_{f,th}$.

	E_a [22]	0.75 E_a	E_e [22]	0.75 E_e	ZPL
	1s→∞p	1s→2p	∞p→1s	~2p→1s	$\Delta E_{F,th}$
GGA	2.03	1.52	0.65	≥ 0.49	1.19
HSE06	2.56	1.92	1.07	≥ 0.80	1.70

PBE0	3.50	2.63	1.88	≥ 1.41	2.66
Expt.		2.77		0.98	

The experimental emission band is from the F(2p) relaxed excited state to the F(1s) unrelaxed ground state. The relaxed excited state equilibrium configuration is between Q_0 and Q_+. The factor applied in the table above is 0.75 to take account of the excited state being 2p rather than ∞p (ionized, F^+). The " $\geq$ " notation is used on the corrected emission energies because the lattice configuration of the F(2p) excited state is displaced from the F^+ equilibrium configuration. The approximate F(2p) potential curve is suggested schematically in Fig. 6 by the dashed qualitative excited state curve.

4.2 Thermal trap depth of the F center and thermoluminescence data

Referring again to Fig. 5, we review the distinction between the optical trap depth (A→B) and the thermal trap depth (A→C). The optical trap depth can be measured experimentally by photoconductivity spectroscopy or by analysis of the optical absorption series limit. Its final state is on the unrelaxed F^+ potential curve, meaning the crystal with one vacancy per supercell, at the local lattice configuration Q_0 with an electron at the conduction band minimum. This can be equivalently denoted CBM(Q_0) as in Fig. 6. The thermal trap depth from the minimum of the F center ground state (point A in Fig. 5) to the minimum of the F^+ potential curve (point C) can in principle be measured experimentally by thermoluminescence or thermally stimulated current spectroscopy. In the motivating context of this paper, thermoluminescence is important because of its well-established utility for diagnosing scintillator defect properties [47]. In the case of SrI_2 discussed in the Introduction, its good scintillation performance seems to imply a

small linear quenched fraction k_1 [15], and one circumstance giving small k_1 could be if the dominant electron traps such as F centers have small thermal depths. Thus evaluating the F and F^- thermal depths in SrI_2 is one of the practical goals of this paper. The thermal trap depth of the F center can be directly obtained from the first principles calculation. It is the energy of relaxed F^+ minus the energy of relaxed F. For SrI_2 using PBE0, it is $\Delta E_{F,th}$ = 1.56 eV (1.17 eV for F^-center).

The values of thermal trap depth that can be deduced from the calculations by Chen et al. [22] are listed in the last column of Table 5. They labeled this value as ZPL for zero-phonon line. However, our calculated vibrational ground state of the F center in SrI_2 (Section 4.3) shows that there will not be a zero-phonon line associated with optical transitions to the ionization limit nor with the F band (1s→2p) spectrum, and experiments in NaCl have established that there is no ZPL observable from its F center either. These are both cases of strong linear coupling to the lattice. In any case, the energy values of the last column in Table 5 also correspond to thermal trap depth as defined above, and from the calculated results of Ref. [22], we label them as ΔE_{Fth} in the second-line column title.

In SrI_2, thermoluminescence is one of the first defect spectroscopies other than luminescence that has been published [19]. Yang et al. found 9 thermoluminescence peaks in the temperature range 50 K to 259 K, and none in the range 260 K to 550 K. The highest activation energy (thermal depth) in the measured range was 0.431 eV for the 255 K peak. The others were lower than 0.28 eV. None of these are a good match for the calculated F center thermal trap depth in SrI_2. This suggests that the F center and F^- center likely function as deep electron traps (effectively quenchers) in SrI_2 after all. The reason for small k_1 in SrI_2 and other complex halides may lie elsewhere [14, 48]. It has often

been found in thermoluminescence of alkali halides that the F centers are destroyed by more mobile species including halogen interstitial atoms or other hole species before releasing their trapped electrons. Thermoluminescence trap depths for release of electrons from F^- centers were measured in NaF, NaCl, and LiF as 0.72, 0.62, and 1.06 eV, respectively [49].

4.3 Vibrational wavefunctions and modeled optical absorption bands of F and F^- centers in SrI_2

The configuration coordinate diagram in Fig. 6 has a lower potential curve (F center ground state) that is customarily approximated as quadratic in a configuration coordinate Q representing a single most important interacting vibrational mode (usually the symmetric breathing mode).

$$E_{FG}(Q) = \frac{1}{2}\gamma Q^2 \qquad (6)$$

In the present case of first-principles energies minimized for full lattice relaxation at the (e.g. F and F^+) endpoints, Q is a configuration coordinate in the comprehensive sense of a single parameter labeling configurations of all ions in the lattice. We have fit Eq. 6 to the calculated lower CC curve to determine the effective force constants as listed in Table 3. For example, γ = 8.58 eV/Å^2 in the F center ground state. In Fowler's compilation of data on F centers in alkali halides, the local mode frequency that fits the F-band width in each alkali halide is about 1/2 of the LO phonon frequency in that crystal [45]. The basic reason is that the ions neighboring a vacancy with an electron partly in it and partly out see much softer restoring force in breathing mode vibration than the ions surrounding a normal lattice site with a hard rare-gas configuration halide ion in the

center. Cui et al. [30] have measured Raman spectroscopy from which the highest LO phonon frequency in SrI_2, $\omega_{LO} = 2.34 \times 10^{13}$ s^{-1}, is determined. For comparison, $\omega_{LO} = 2.0 \times 10^{13}$ s^{-1} in RbI, where Sr mass is adjacent to Rb. The F center local mode frequency in RbI is $\omega_A = 1.0 \times 10^{13}$ s^{-1} [45]. Scaling in the same way for SrI_2, we arrive at the estimate $\omega_A = 1.17 \times 10^{13}$ s^{-1} for that case. From ω_A and γ, the effective mass M of the mode is found from $\omega_A^2 = \gamma/M$.

The ground state vibrational wavefunction is, in one dimension appropriate to a single normal mode,

$$\psi_{n=0}(Q,\gamma,\omega_A) = C\exp\left(-\frac{\gamma}{2\hbar\omega_A}Q^2\right) \qquad (7)$$

The probability $\psi^2_{n=0}(Q,\gamma,\omega_A)$ based on γ from first principles and ω_A scaled empirically from the experimental highest ω_{LO} in SrI_2 is plotted in Fig. 6.

By comparing the width of the vibrational wavefunction to the displacement ΔQ between the F(1s) and F(2p) minima, we can see that there will be no zero phonon line. The ground state vibrational wavefunction projects up onto the highly excited upper-state vibrational wavefunctions with strong peaks at their classical turning points. We have not done the full vibrational overlap calculation, but regard each classical turning point at high n to be a delta function at that point on the F(2p) curve. In this way, we produce the modeled approximate F(1s→2p) absorption lineshape in SrI_2 at low temperature shown in Fig. 7.

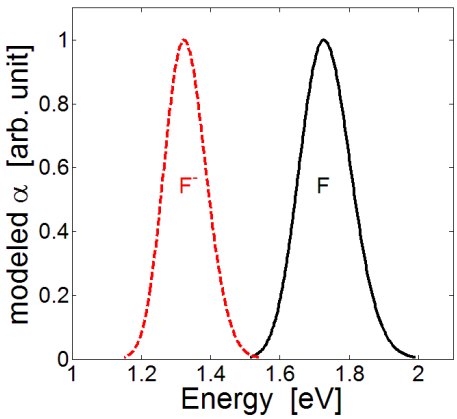

Figure 7 Modeled low-temperature optical absorption bands of F (black solid) and F^- (red dashed) centers in SrI_2.

Figure 7 also plots the lineshape of the $F^-(1s \rightarrow 2p)$ transition (red dashed) obtained in the same way from the F^- configuration coordinate curve and the F curve as its ionization limit. Although Table 3 shows that there is considerable softening of the configuration coordinate curves in the sequence F^+, F, F^-, the degree of softening (fractional change in force constant γ) is about the same at each stage of the sequence, so the band width is predicted to be similar for both the F and F^- first absorption transitions. This is similar to what is found experimentally for the one- and two-electron transitions (F+ and F) in MgO, and different from alkali halides like NaCl, where the F^- transition is significantly wider than the F.

The difference in one-electron and two-electron anion vacancy transition energies in the sequence MgO, SrI_2, and NaCl is ~0.05 eV, ~0.4 eV, and ~0.34 eV. These are experimental and approximately as calculated in MgO and NaCl, but so far only calculated in SrI_2.

4.4 Comparison to a particle-in-a-box model and other halide crystals in Mollwo-Ivey plots

It has been well known in the F center literature that a particle-in-a-box model works reasonably well, maybe even surprisingly well, for predicting variation of the 1s→2p F center transition from crystal to crystal. The point ion potential in the vicinity of the anion vacancy is a flat-bottom well (at the Madelung energy) inside the radial region bounded by the nearest-neighbor cations, and at larger radii it oscillates up and down at each alternate shell of anion and cation neighbors, respectively, with diminishing amplitude. But most of the electron density (70 % in SrI_2) lies within the nearest-neighbor cation bounds, as we have already seen, and so the early developers of the particle-in-a-box model [45,50,51] tried the simple case of an infinite 3-dimensional square well of radius a defined as the distance from the vacancy center to the nearest-neighbor cations. In that model [45,50,51] the 1s→2p transition energy is

$$\Delta E_{1s-2p} = \frac{3\pi^2\hbar^2}{8ma^2} \qquad (8)$$

What counts is the $1/a^2$ dependence, meaning that the F center transition energy should, in this simple model, scale from crystal to crystal as approximately the inverse square of the nearest-neighbor distance. The log-log plot to test whether a power law relation is seen is known as a Mollwo-Ivey plot. In the cubic rock-salt alkali halides, a good linear relation is obtained with the exponent −1.84 [45,51]. Williams et al. [52] made a Mollwo-Ivey plot for both F center and STE absorption transitions in the alkaline-earth fluorides BaF_2, SrF_2, CaF_2, and MgF_2, where the fluorite structures of the first three have a unique nearest-neighbor distance, but MgF_2 has a noncubic structure and three cation neighbors of the vacancy at two slightly different distances. In that case, the average nearest-neighbor cation distance was used, and the F centers in all 4 crystals

formed a good linear Mollwo-Ivey plot, however with exponent −3. To see how SrI_2 fits with the four alkaline earth fluorides, we simply plotted our 1.52 eV and 1.73 eV calculated F center transition energies predicted from HSE06 and PBE0 results, respectively, at the calculated 3.38 eV nearest-neighbor Sr^{2+} distance on the same graph as the alkaline-earth fluoride crystals[52]. The resulting plot is shown in Fig. 8. Considering that the alkaline-earth fluoride F band energies are experimental and SrI_2 calculated, the plot is not bad. If we keep the solid line with slope −3 that fit the alkaline-earth fluoride crystals, the extended fluoride F band line actually intersects the SrI_2 nearest-neighbor distance at an energy prediction of about 1 eV rather than our calculated 1.73 eV PBE0 result. On the other hand if we enforce the slope of -2 dictated by the particle-in-a-box model, the dashed line fits CaF_2, SrF_2, and calculated SrI_2 rather well, while MgF_2 and BaF_2 lie farther off. When experimental optical absorption data on SrI_2 F centers finally emerge, it will be interesting to see whether DFT hybrid functional theory or particle-in-a-box hits it closer.

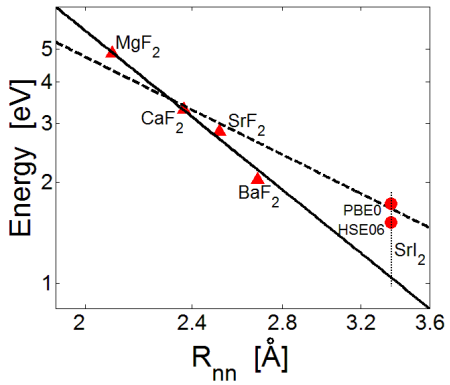

Figure 8 Peak energies of F center optical absorption bands of MgF_2, CaF_2, SrF_2, and BaF_2 from Ref. [52] together with first principles results from this work for SrI_2 are plotted on logarithmic scales as functions of average nearest-neighbor cation distance.

5 Conclusions

Upon comparing results to available lattice constant and band-gap data for SrI_2 and upon analyzing the results of corresponding calculation methods in NaCl for comparison to experimental F center optical transitions, we conclude at the first step that DFT with PBE0 hybrid functionals gives the best predictions of available experimental data for these ionic crystals and their vacancy defects relative to the other approaches tried with GGA-PBE and HSE06. Then continuing with the DFT-PBE0 method, we calculated iodine vacancy defect formation energies in the charge states q = +1, 0, and –1 relative to lattice neutrality, and thermodynamic transition energies between them, predicting stability versus Fermi level. We used an interpolation scheme to construct configuration coordinate diagrams for the F and F^- centers based on the first-principles defect energies at lattice configurations along the linearized configuration path from the potential minimum to the ionized equilibrium configuration for each of the defect charge states. Thermal trap depth and optical trap depth are directly obtained from first principles. Furthermore, construction of the configuration coordinate diagram permits determination of the effective ground and ionized state force constants from fitting the first-principles potential curves. This allows calculating the ground-state and ionized-state defect vibrational wave functions for prediction of optical lineshapes. Departing from first principles methods, but using the results noted above to remove large uncertainties surrounding appropriate ε and m* parameters in the simple hydrogenic model of F center optical transitions, we were able to use that model to make interpolations of excited state energies based on the 2.31 eV energy interval from ground to ionized state of the defect rather than the 13.6 eV Rydgerg basis of the full hydrogenic model. In this way the uncertainties in excited state energies of the F center become of a

tolerable size to make meaningful comparisons and predictions with experiments. For example, the vibrationally broadened 1s→2p optical absorption of the F band in SrI_2 was predicted, as a simpler alternative to the GW and Bethe-Salpeter predictions of F^+ and F bands as has been used in MgO [23], another crystal with divalent alkaline earth cations. The prediction of similar optical binding energies for the one-electron F and two-electron F^- centers in SrI_2 corresponds interestingly to the calculation [23] and experiments [24] for the one-electron F^+ and two-electron (lattice neutral) F centers in MgO. There are far fewer existing experimental data on SrI_2 than on MgO or NaCl, so many of our detailed predictions are just that – predictions waiting for the experiments which should be coming soon given the recently realized importance of $SrI_2:Eu^{2+}$.

Acknowledgements This work was supported by the Office of Nonproliferation Research and Development (NA-22) of the U.S. Department of Energy under contracts DE-NA0001012 (Fisk-WFU), DE-AC02-05CH11231 (LBNL-WFU), and DE-AC52-07NA27344 (LLNL). Calculations were performed on the Wake Forest University DEAC Cluster, a centrally managed facility with support in part by the University. The calculations were performed using the ab-initio total-energy program VASP (Vienna ab-initio simulation program) developed at the Institüt für Materialphysik of the Universität Wien. We thank Natalie Holzwarth, Babak Sadigh, Timo Thonhauser, and Miguel Moreno for helpful discussions.

REFERENCES

[1] N. J. Cherepy, G. Hull, A. D. Drobshoff, S. A. Payne, E. van Loef, C. M. Wilson, K. S. Shah, U. N. Roy, A. Burger, L. A. Boatner, Woon-Seng Choong, and W. W. Moses, Appl. Phys. Lett. **92**, 083508 (2008).

[2] N. J. Cherepy, S. A. Payne, S. J. Asztalos, G. Hull, J. D. Kuntz, T. Niedermayr, S. Prinputkar, J. J. Roberts, R. D. Sanner, T. M. Tillotson, E. van Loef, C. M. Wilson, K. S. Shah, U. N. Roy, R. Hawrami, A. Burger, L. A. Boatner, Woon-Seng Choong, and W. W. Moses, IEEE Trans. Nucl. Sci. **56**, 873 (2009).

[3] P. Dorenbos, IEEE Trans. Nucl. Sci. **57**, 1162 (2010).

[4] C. L. Melcher, U. S. patents No. 4,958,080 (1990) and 5,025,151 (1991).

[5] C. L. Melcher and J. S. Schweitzer, Nucl. Instr. and Meth. in Phys. Res A **314**, 212 (1992).

[6] M. Fasoli, A. Vedda, M. Nikl, C. Jiang, B. P. Uberuaga, D. A. Andersson, K. J. McClellan, and C. R. Stanek, Phys. Rev. B **84**, 081102 (2011).

[7] O. Guillot-Noël, J. T. M. de Haas, P. Dorenbos, C. W. E. van Eijk, K. W. Krämer, and J. U. Güdel, J. Lumin. **85**, 21 (1999).

[8] E. V. D. van Loef, P. Dorenbos, and C. W. E. van Eijk, Appl. Phys. Lett. **79**, 1573 (2001).

[9] R. Hofstädter, U. S. patent No. 3,373,279 (2 March 1968).

[10] G. A. Bizarri, E. D. Bourret-Courchesne, Z. W. Yan, and S. E. Derenzo, IEEE Trans. Nucl. Sci. **58**, 3403 (2011).

[11] U. Shirwadkkar, J. Glodo, E. van Loef, R. Hawrami, S. Mukhopadhyay, A. Churilov, W. M. Higgins, and K. S. Shah, NIMA **652**, 268 (2011).

[12] J. Glodo, E. van Loef, R. Hawrami, W. M. Higgins, A. Churilov, U. Shirwadkar, and K. S. Shah, IEEE Trans. Nucl. Sci. **58**, 333 (2011).

[13] S. A. Payne, W. W. Moses, S. Sheets, L. Ahle, N. J. Cherepy, B. Sturm, S. Dazeley, IEEE Trans. Nucl. Sci. **58**, 3392 (2011).

[14] Qi Li, Joel Q. Grim, K. B. Ucer, A. Burger, G. A. Bizarri, W. W. Moses, and R. T. Williams, Phys. Stat. Solidi Rapid Research Letters, DOI: 10.1002/pssr.201206256.

[15] Qi Li, Joel Q. Grim, R. T. Williams, G. A. Bizarri, and W. W. Moses, J. Appl. Phys. **109**, 123716 (2011).

[16] J. Q. Grim et al., Symposium on Radiation Measurements and Applications, Oakland, May 16 (2012) 11C-3.

[17] R. T. Williams, J. Q. Grim, Qi Li, K. B. Ucer, and W. W. Moses, Phys. Status Solidi B **248**, 426 (2011).

[18] G. A. Bizarri, W. W. Moses, J. Singh, A. N. Vasil'ev, and R. T. Williams, J. Appl. Phys. **105**, 044507 (2009).

[19] K. Yang, M. Zhuravleva, and C. L. Melcher J. Lumin. **132**, 1824 (2012).

[20] K. B. Ucer, A. Burger, P. Bhattacharya, E. Tupitsyn, E. Rowe, V. M. Buliga, L. Trefilova, R. T. Williams, International Conference on Defects in Insulating Materials, Santa Fe, June 24-29 (2012) unpublished.

[21] D. Åberg, P. Erhart, A. Schleife, and B. Sadigh, International Conference on Defects in Insulating Materials, Santa Fe, June 24-29 (2012) unpublished.

[22] W. Chen, C. Tegenkamp, H. Pfnur, and T. Bredow, Phys. Rev. B **82**, 104106 (2010).

[23] P. Rinke, A. Schleife, E. Kioupakis, A. Janotti, C. Rödl, F. Bechstedt, M. Scheffler, C. G. Van de Walle, Phys. Rev. Lett. **108**, 126404 (2012).

[24] Y. Chen, V. M. Orera, R. Gonzalez, R. T. Williams, G. P. Williams, G. H. Rosenblatt, and G. J. Pogatshnik, Phys. Rev. B **42**, 1410 (1990); G. H. Rosenblatt, M.W. Rowe, G. P. Williams, R. T. Williams, and Y. Chen, Phys. Rev. B **39**, 10 309 (1989).

[25] H. Barnighausen, H. Beck, H. Grueninger, E. T. Rietschel, and N. Schultz, Neue AB2-strukturtypen mit siebenfach koordiniertem kation Zeitschrift fur Kristallographie **128**, 430 (1969).

[26] D. J. Singh, Appl. Phys. Lett. 92, 201908 (2008).

[27] V. A. Pustovarov, I. N. Ogorodnikov, A. A. Goloshumova, L. I. Isaenko, and A. P. Yelisseyev, Opt. Mat. 34, 926 (2012).

[28] A. Burger, P. Bhattacharya, E. Tupitsyn, E. Rowe, V. M. Buliga, unpublished.

[29] V. Pankratov, A. I. Popov, L. Shirmane, A. Kotlov, G. A. Bizarri, A. Burger, P. Bhattacharya, E. Tupitsyn, E. Rowe, V. M. Buliga, and R. T. Williams, unpublished.

[30] Y. Cui, R. Hawrami, E. Tuptiysn, P. Bhattacharya, M. Groza, M. Bryant, V. Buliga, A. Burger, N. J. Cherepy, and S. A. Payne, Solid State Commun., **151** 541 (2011).

[31] G. Kresse and J. Hafner, Phys. Rev. B **47**, 558 (1993).

[32] G. Kresse and D. Joubert, Phys. Rev. B 59, 1758 (1999).

[33] J. Heyd, G. E. Scuseria, and M. Ernzerhof, J. Chem. Phys. **118**, 8207 (2003).

[34] J. P. Perdew, M. Ernzerhof, and K. Burke, J. Chem. Phys. **105**, 9982 (1996).

[35] J. P. Perdew, K. Burke, and M. Ernzerhof, Phys. Rev. Lett. **77**, 3865 (1996).

[36] D. Åberg, P. Erhart, A. J. Williamson and V. Lordi, Phys. Rev. B **77**, 165206 (2008).

[37] S. B. Zhang, S.-H. Wei, and A. Zunger, Phys. Rev. B **63**, 075205 (2001).

[38] D. Grecu and P. H. Dederichs, Phys. Lett. **36A**, 135 (1971).

[39] P. H. Dederichs, J. Pollmann and J. Pollmann, Z. Physik **255**, 315 (1972).

[40] G. Makov and M. C. Payne, Phys. Rev. B **51**, 4014 (1995).

[41] Paul Erhart unpublished.

[42] W. Tang, E. Sanville, and G. Henkelman, J. Phys.: Condens. Matter **21**, 084204 (2009).

[43] E. Sanville, S. D. Kenny, R. Smith, and G. Henkelman, J. Comp. Chem. **28**, 899-908 (2007).

[44] G. Henkelman, A. Arnaldsson, and H. Jónsson, Comput. Mater. Sci. **36**, 254-360 (2006).

[45] W. B. Fowler, *Physics of Color Centers* (Academic Press, New York, 1968) chapt. 2 and Appendix B.

[46] D. Y. Smith and G. Spinolo, Phys. Rev. **140**, A2121 (1965).

[47] M. Nikl,, V. V. Laguta, and A. Vedda, Phys. Stat. Solidi (B), 245, 1701 (2008).

[48] A. Kozorezov, J. K. Wigmore, and A. Owens, arXiv:1206.1780v1.

[49] H. Levin, C. C. Berggren, and V. R. Honnold, J. Phys. Chem. **71**, 4228 (1967).

[50] F. Stöckman, Naturvissenschaften **39**, 230 (1952).

[51] H. F. Ivey, Phys. Rev. **72**, 341 (1947).

[52] R. T. Williams, C. L. Marquardt, J. W. Williams, and M. N. Kabler, Phys. Rev. B **15**, 5003 (1977).

CHAPTER 7: HOST STRUCTURE DEPENDENCE OF LIGHT YIELD AND PROPORTIONALITY IN SCINTILLATORS IN TERMS OF HOT AND THERMALIZED CARRIER TRANSPORT

Qi Li, Joel Q. Grim, K. B. Ucer, A. Burger,
G. A. Bizarri, W. W. Moses, and R. T. Williams

The following manuscript was published as a front cover in *Physica Status Solidi Rapid Research Letters* in 2013. Qi Li performed all the band structure and hot electron group velocity calculations. Qi Li, Joel Q. Grim, and R. T. Williams analyzed the results and developed the "scintillator decision tree" model. The original manuscript was prepared by R.T. Williams. I thank G. A. Bizarri and W. W. Moses of Lawrence Berkeley National Lab for helpful discussions and reading of the manuscript. I thank A. Burger for providing the samples and help discussions. Manuscript is reproduced with permission of John Wiley and Sons. Stylistic variations are due to the requirement of the journal.

ABSTRACT

Several outstanding questions, including why complex halide scintillator host structures allow higher light yield and flatter electron energy response than simple monovalent metal halides, have remained unanswered by current models of luminescence in dense ionization tracks. Our measurements of nonlinear quenching kinetic order, recent literature on hot electron transport in scintillators, and calculations presented here of hot electron velocity from band structure of SrI_2 and NaI, lead us to expand our previously described diffusion and nonlinear quenching model to include hot-electron transport. Trends in multivalent versus monovalent metal halides, heavier versus lighter halides, and halides versus oxides versus semiconductors can be predicted based on optical phonon frequency, thermalized band edge mobilities, velocity in the upper conduction bands, and hole self-trapping.

Because excitation density changes dramatically along the track of a slowing electron, luminescence quenching that depends nonlinearly on excitation density is regarded as the root cause for nonproportionality between light emission and initial electron energy. If diffusion of the excitations (carriers) can occur, then the track radius and hence local carrier concentration, *n*, becomes dependent on diffusion coefficients of the carriers. The numerical simulations of thermalized diffusion and nonlinear quenching by Li *et al.* [1-3] showed two primary trends: (a) For all scintillator materials and semiconductor detector materials, there is a competition between the rate of radial ambipolar diffusion diluting the value of *n* and therefore the rate of nonlinear quenching that increases as the 2^{nd} or 3^{rd} power of *n*. (b) For scintillators with large disparity of μ_e and μ_h, especially halide materials with self-trapping of holes, charge separation is produced by diffusion in the radial gradient of the track. This was shown to predict the halide hump of electron energy response, which is a peak in light yield *vs* Compton electron energy [4], corresponding to a peak in local light yield *vs n*. In the model, its size scales both with the disparity of μ_e and μ_h and with the *linear quenched fraction* k_1 due to deep trapping of free carriers [3].

Wang *et al*. have conducted Monte Carlo simulations of the spatial distribution of electrons and holes produced by the primary electron cascade including thermalization by phonon emission [5,6]. Assuming that holes in halide materials self-trap instantaneously at the point of production in the cascade, they found a hole distribution with radius 2.8 nm in NaI [7]. Some of the hot conduction electrons were found to be transported considerably farther out, of order 100 nm in CsI where they calculated thermalization time of 7 ps due to its low LO phonon frequency [5,6].

Kozorezov *et al.* [8] take into account screening and a bottleneck of phonon energy transport from the track, finding somewhat slower thermalization time and from it, an electron-temperature-dependent (thus time-dependent) ambipolar diffusion coefficient. Kirkin and Vasil ev [9] have also recently calculated thermalization and hot diffusion effects on scintillation response, finding that multiple optical phonon modes in complex structures should speed thermalization. Hot electron range before thermalization depends both on the thermalization time, studied in Refs. [5,6,8,9], and on the speed (v_g) of hot electrons of a given energy, studied in this letter. Refs. [5,6,8,9] used parabolic effective mass approximations of hot electron speed.

The physical parameters that are important in a model of thermalized diffusion and nonlinear quenching, such as band-edge effective mass, nonlinear quenching rate constants, and even thermalization time, are in fact rather similar in NaI and SrI_2. Those parameters do not seem to support the dramatic differences [4] that are observed Xin the light yield and proportionality of these two materials. However, Fig. 1(a) illustrates at least one dramatic physical difference between NaI and SrI_2. It is the flatness of the energy bands throughout the hot-electron range. SrI_2 has lower group velocity on average throughout the hot electron range compared to NaI. To quantify this, we have calculated the magnitude of group velocity averaged over the Brillouin zone as a function of energy, using density functional theory. The electronic structures are calculated using VASP [10] with exchange-correlation functionals parameterized by Perdew-Burke-Ernzerhof (PBE) using generalized gradient approximation (GGA) [11]. The group velocity distribution was calculated following the method applied by

Gnini *et al*. to SiO_2 [12]. The $\langle v_g \rangle$ distributions are plotted in Fig. 1(b) along with the parabolic band effective mass approximation of velocity (m_e^*/m_0 = 0.226 and 0.276 respectively, in NaI and SrI_2).

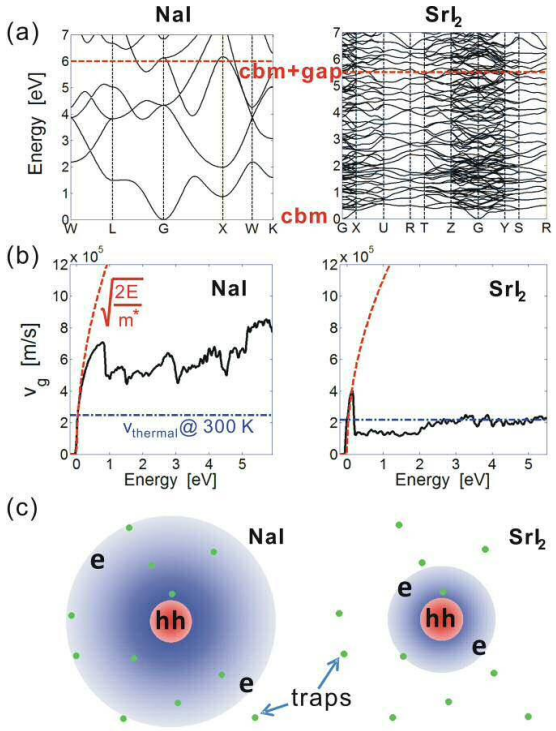

Figure 1 Comparison in NaI and SrI_2 of (a) conduction band structure, (b) group velocity distribution *vs.* energy, and (c) schematic representation of electron track cross sections in halides with self-trapped holes at the core, and thermalization range of hot electrons represented by the larger radial distributions.

Wang *et al*. [5,6] and Kozorezov *et al.* [8] calculated 2-ps and roughly 10-ps electron thermalization times respectively, in NaI. Being an iodide as well, SrI_2 may be expected to have a roughly similar thermalization time, which we assume for the present purpose of comparing effects of $\langle v_g \rangle$ alone.

We have drawn qualitative representations in Fig. 1(c) of the hot electron radial range (outer distribution) which then defines the distance of thermalized diffusion by electrons traveling back to recombine with the track core of self-trapped holes. The randomly placed dots represent deep electron traps, such as iodine vacancies.

Since the hot electrons in SrI_2 did not go out as far before thermalization due to smaller v_g, they should encounter fewer deep traps on the way back to recombination, for assumed equal concentration and cross sections of traps in both materials. The material with smaller hot electron range (here SrI_2) will have a smaller linear quenched fraction k_1. Since k_1 sets an upper limit on Light Yield by $LY \leq 1 - k_1$, and since Ref. [3] showed that the halide hump in electron response is proportional to k_1, SrI_2 is predicted to have the better light yield and flatter electron response based solely on hot electron range. In a full treatment, precise thermalization time in SrI_2 by the methods of Refs. [5,6,8,9] should also be included.

To generalize the present results from the specific pair of NaI and SrI_2, we look for reasons that the whole class of heavier multivalent halides should have lower hot electron group velocity than the alkali iodides, to match the observed electron energy response [4]. The multivalent metal halides generally have a more complex basis and larger real- space unit cells than the simple monovalent halides. In the case of SrI_2, the 24-atom unit cell is much more complex and has lower symmetry than NaI, and one way to understand its flatter conduction bands is because of more frequent flattening at intersections with the smaller Brillouin zone boundaries as well as additional avoided crossings interior to the reduced Brillouin zone of the 58 bands packed between E_{cbm} and $E_{cbm} + E_{gap}$. In addition, many of the multivalent halide scintillators contain lanthanum. We have calculated band structures and group velocity distributions of $LaCl_3$ and $LaBr_3$, finding that the La 4f levels contribute a dense and flat set of bands about 3.5 eV above E_{cbm}, thus low average group velocity in that range.

In Fig. 2, the criterion at the top level is whether hot electron thermalization is fast compared to the picosecond scale of nonlinear quenching. If so, there will be thermalized carriers diffusing with band-edge mobilities during nonlinear quenching and the model of Refs. [1-3] should apply. In that model, the effective ambipolar diffusion coefficient D_{eff} of electron-hole pairs is the important criterion, indicated at the second-level branching on the left side. Since excitons are expected to be formed from the thermalized carriers, 2nd order quenching kinetics such as exciton-exciton Förster transfer can be expected in the oxide scintillators. As shown in Ref. [3], the materials with large D_{eff} have flat electron response curves because the excitations can rapidly escape the track core where nonlinear quenching would be most severe. The conventional oxide scintillators are on the right branch (small D_{eff}) at the second level of the rapidly thermalizing branch. As was shown in Ref. [3], excitons in the oxides linger near the track core subject to nonlinear quenching, so the oxides display the Birks roll-off of light yield *vs.* local excitation density discussed by Payne *et al.* [4].

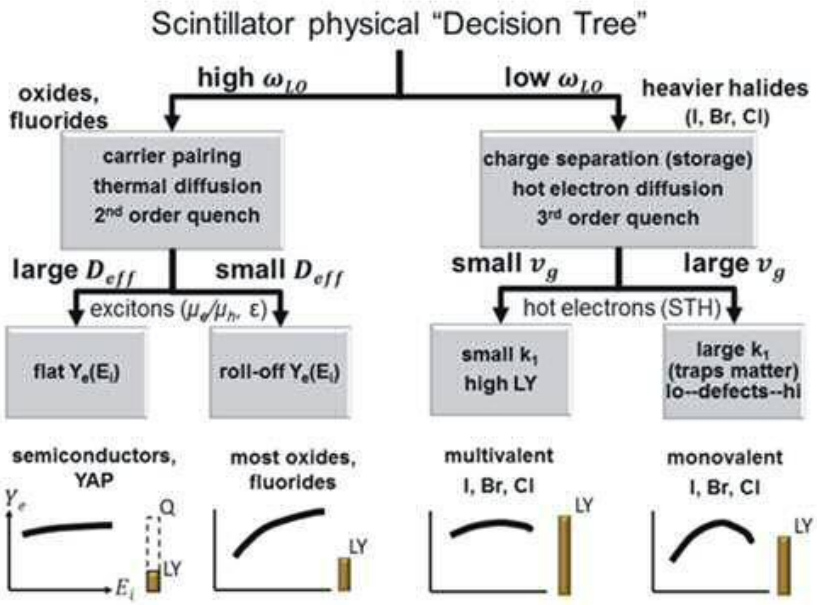

Figure 2 How classes of general behavior in electron energy response (curves) and light yield (*LY*) illustrated along the bottom may result from physical parameter values: ω_{LO} deciding electron thermalization rate -- fast to the left with thermalized diffusion *versus* slow to the right with hot free carriers; subsequent branching in the thermalized half is governed by band-edge diffusion coefficient D_{eff} [3]; whereas the non-thermalized half is controlled by hot-electron velocity and range depending on host structure.

The right-hand branch at the top is toward low ω_{LO}, thus slow thermalization of hot carriers, thus free carriers during nonlinear quenching, and therefore 3rd order Auger quenching should be expected. The scintillators with low ω_{LO} comprise most of those with anions heavier than oxygen or fluorine and cations heavier than lithium. The second level branch on the right is between small and large hot electron group velocity v_g, corresponding to small and large hot-electron range. Thermalization rate (top level) [5,6,8,9] combines with group velocity (second level) to determine hot electron range. If hot electrons have a small thermalization range, their collection in the electric field of the self-trapped holes in the track core will not encounter many traps. Thus light yield will be high and the halide hump (proportional to k_1 [3]) will be small. Furthermore, 3rd order quenching kinetics

contributes in its own right to a flatter electron response and higher total light yield, to be shown in a forthcoming publication.

Experimental evidence for the top-level branch between 2nd order quenching in oxides *versus* 3rd order quenching in iodides has recently been obtained in our laboratory, using an above-gap z-scan method to measure the amount and kinetic order of nonlinear quenching as a function of the density *n* of excitations produced. In SrI_2 and NaI, the nonlinear quenching is 3rd order in excitation density *n* when the laser photon energy is sufficient to create free carriers [13,14]. This is experimental confirmation of the slow thermalization of conduction electrons in the iodides relative to the time scale of nonlinear quenching. The only oxide scintillators whose nonlinear quenching kinetics we have measured so far are BGO ($Bi_4Ge_3O_{12}$) [14] and $CdWO_4$ [2], and both were found to exhibit 2nd order quenching.

Our first conclusion, stated as a hypothesis to be tested by measurements and calculations on more materials, is that heavier halide hosts exhibit 3rd order (free carrier) kinetics of nonlinear quenching due to slow thermalization (low ω_{LO}), while most oxides (and fluorides) exhibit 2nd order kinetics of nonlinear quenching because their high ω_{LO} mediates fast thermalization followed by carrier pairing. The second conclusion of this letter is that hot electron group velocity from electronic structure combines with thermalization time to determine hot electron range and the broad trends among scintillator hosts that are associated with it.

Acknowledgements Supported by the National Nuclear Security Administration, Office of Nonproliferation Research and Development (NA-22) of the U.S. Dept. of Energy, Contracts DE-NA0001012 and DE-AC02-05CH11231. Computations were performed on the Wake Forest University DEAC Cluster with support in part by the University. We thank N. A. W. Holzwarth, Daniel Åberg, and Babak Sadigh for helpful discussions.

REFERENCES

[1] Qi Li et al., Nucl. Inst. and Meth. Phys. Res. A, **652**, 288 (2011).

[2] R. T. Williams et al., Phys. Status Solidi B **248**, 426 (2011).

[3] Qi Li et al., J. Appl. Phys. **109**, 123716 (2011).

[4] S. A. Payne et al., IEEE Trans. Nucl. Sci. 58, 3392 (2011).

[5] Z. Wang et al., J. Appl. Phys. **110**, 064903 (2011).

[6] Z. Wang et al., to be published, preprint courtesy F. Gao (2012).

[7] Fei Gao et al., Symposium on Radiation Measurements and Applications, Oakland, May 14-17 (2012).

[8] J. K. Kozorezov et al., arXiv:1206.1780v1.

[9] R. Kirkin, et al., IEEE Trans. Nucl. Sci. (in press, 2012).

[10] Calculations used the ab-initio total-energy program VASP (Vienna Ab-initio Simulation Program) developed at the Institut für Materialphysik of the Universität Wien.

[11] J. P. Perdew et al., Phys. Rev. Lett. 77, 3865 (1996).

[12] E. Gnini et al., Phys. Rev. B 66, 195205 (2002).

[13] J. Q. Grim et al., Mat. Res. Soc. Symp. Proc. 1341, 15 (2011) DOI: 10.1557/opl.2011.1483.

[14] J. Q. Grim et al., Symposium on Radiation Measurements and Applications, Oakland, May 14-17 (2012).

CHAPTER 8: FIRST PRINCIPLES CALCULATIONS ON Ce, Sr, Sr-F_A, AND F CENTERS IN LaBr3

Qi Li and R. T. Williams

This following manuscript is in preparation for publication. Qi Li performed all first principle calculations. Qi Li and R. T. Williams analyzed the results and prepared the manuscript.

ABSTRACT

LaBr3:Ce is a recently found scintillator material with exceptional light yield and proportionality. The merits of this material are further enhanced with 160 ppm Sr co-doping. Our thermalized and hot electron transport model suggests the carrier capturing mechanism and efficiency on defects is crucial to scintillator performance. In this paper, we calculate the electronic structures and of the Ce activator, Sr-F_A, and F center from density functional theory. Formation energies and optical transition energies are derived. The capturing cross-sections and rates are calculated and analyzed in a carrier transport model.

1. Computational details

Our first principles calculations are carried out in the projector augmented wave framework in Vienna Ab-initio Simulation Package (VASP) [1,2]. For La and Ce 4f electrons, we employ DFT+U techniques to correct the position of these levels. U_{eff} is selected to be 10.3 eV for La 4f [3] and 2.5 eV for Ce 4f [4]. Hybrid functional PBE0 [5] calculations are performed for its stronger ability of charge localization, the mixing factor is chosen as 0.25. In order to obtain more accurate relative energy level positions, G0W0 approximation is used on top of the single particle energies and wavefunctions from DFT+U. The kinetic energy cutoff is 400 eV. All calculations are converged to a self-consistency criterion of 1×10^{-6} eV and force tolerance of 0.01 eV/Å. The defective systems are simulated in a 96 atom supercell with a 2×2×2 Monkhorst-Pack K-mesh sampling. The Ce^{3+} activator is substituted for one La^{3+} in the supercell, which corresponds to a 4% doping level. The F center is simulated by one Br vacancy in the supercell. The electron deficiency of Sr^{2+} relative to La^{3+} for which it substitutes can exist as a hole in the Br valance band, or as a charge-compensating defect such as an adjacent Br^- vacancy. The latter complex of Sr^{2+} and adjacent Br^- vacancy would be called a Sr-F_A^+ center in color center terminology. Calculations of a complex made by removing a neutral Br^0 atom adjacent to substitutional Sr^{2+} were also made. This is termed as a Sr-F_A center. Finally, I also calculated the Sr-F_A^{++} center, where an additional electron is removed from a Br^- ion adjacent to a Sr-F_A^+ center. This amounts to an extrinsic self-trapped hole (STH). In the latter two complexes, there is an overall charge in the

supercell, -1 in the Sr-F_A center and +1 in the Sr-F_A^{++} center. These charges were balanced by introducing a uniform charge of oppsite sign.

2. Results and discussion

2.1 Bulk material

The bulk $LaBr_3$ has an 8 atom P63/m hexagonal unit cell, calculated band gap is 3.55 eV with GGA+U and 5.42 eV with PBE0, both underestimates the experimental band gap of 5.9 eV [6]. Calculated optical dielectric constant is 4.39/4.39/4.80, showing a slightly anisotropic feature.

2.2 Electronic structure and charge localization

In Fig. 1, the charge density contours of the F center and Sr-F_A center in different charge states, as well as the $(Ce^{3+})^*$ excited state, is plotted at the same isosurface level of 0.001 *e*/bohr^3. We can readily see the major difference between the F^+ hole orbital consisting of localized La-5d orbitals and the F_A^{++} hole orbital consisting of more delocalized Br-4p orbitals. The geometric configuration the of Sr-F_A^{++} center exhibits a slight self-trapped hole like feature, and it has a hole binding energy of about 1.4eV according to PBE0 results. The relatively delocalized hole state might account for a large capturing cross-section. This can be tested quantitatively in the future and is crucial to the fact that 160 ppm Sr doping has a prominent impact on the electron response of this material. The electron and hole charge contours of $(Ce^{3+})^*$ shows the features of Ce-5d and Ce-4f orbitals clearly.

2.3 Formation energies

The formation energies are calculated. For example the formation energy E_f of Ce-activators in Br-rich condition is (1):

$$\begin{aligned} &E_f = E_{defect} - E_{host} + \Delta\mu_{La} + \mu_{La} - \Delta\mu_{Ce} - \mu_{Ce} + q(E_{VBM} + \mu_e) \\ &\Delta\mu_{La} + 3\Delta\mu_{Br} = \Delta\mu_{LaBr_3} \\ &\Delta\mu_{Ce} + 3\Delta\mu_{Br} = \Delta\mu_{CeBr_3} \\ &\Delta\mu_{Br} = 0 \end{aligned} \quad (1)$$

where E_{defect} and E_{host} are the total energies of the defective system and the host material in the same supercell without the defect, $\Delta\mu_{\text{La}}$ is the formation enthalpy of La, which is limited by the formation enthalpy of $LaBr_3$ in the second line. In Br-rich condition, the formation enthalpy of Br is set as zero. q is the charge state of the defect, E_{VBM} is the position of valance band maximum and μ_{e} is the electron Fermi energy, which is treated as a variable between zero and one band gap.

In Fig. 2, the formation energies of four defects are plotted in Br-rich and Br-poor conditions respectively. In either case, the 4 defect systems we are studying have lower formation energies in their negative charge states. Therefore, they naturally prefer to exist in the host material in neutral or negative charge states during crystal growth and serve as hole traps.

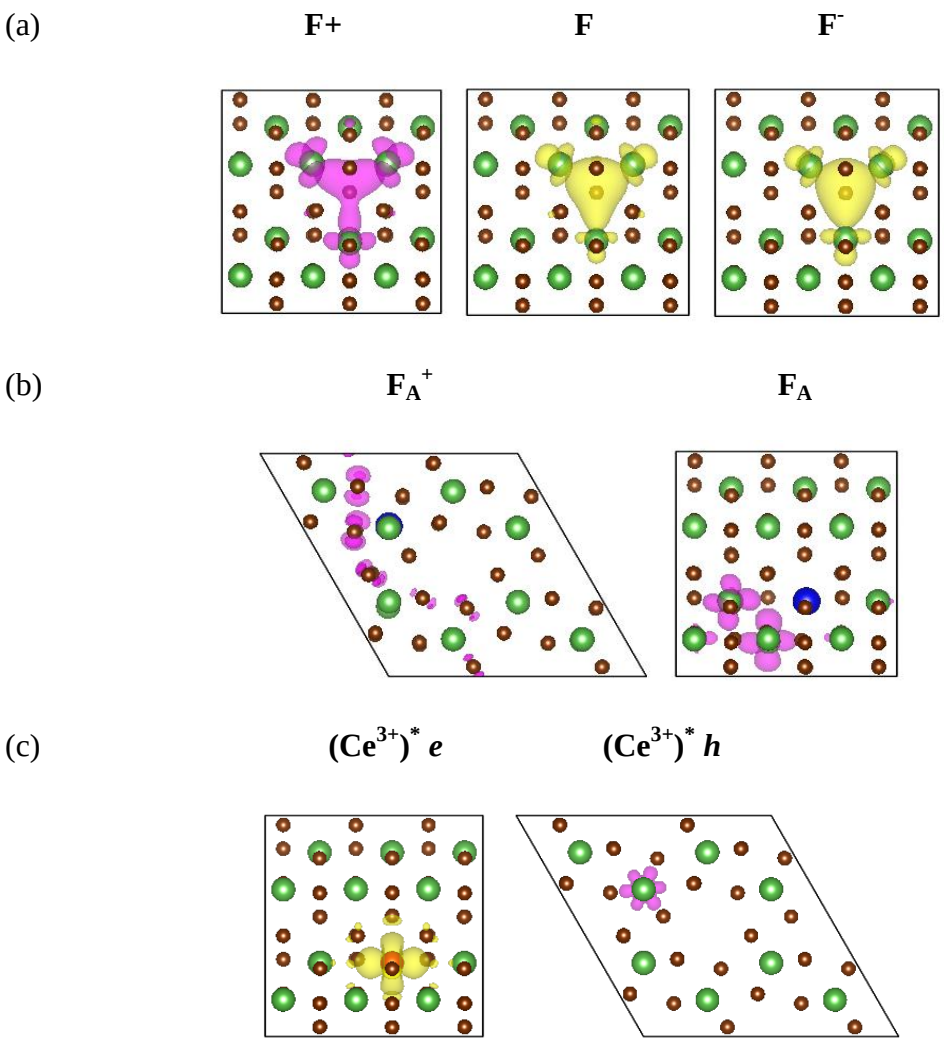

Fig. 1 Electron/hole density contours of (a) F center, (b) F_A center, and (c) $(Ce^{3+})^*$ in different charge states denoted in the figures. Green, brown, red, and blue represent La, Br, Ce, and Sr atoms respectively. All the contours are plotted at isosurface level of 0.001 *e*/bohr^3, purple contours are for unoccupied hole orbitals and yellow contours are for electron orbitals.

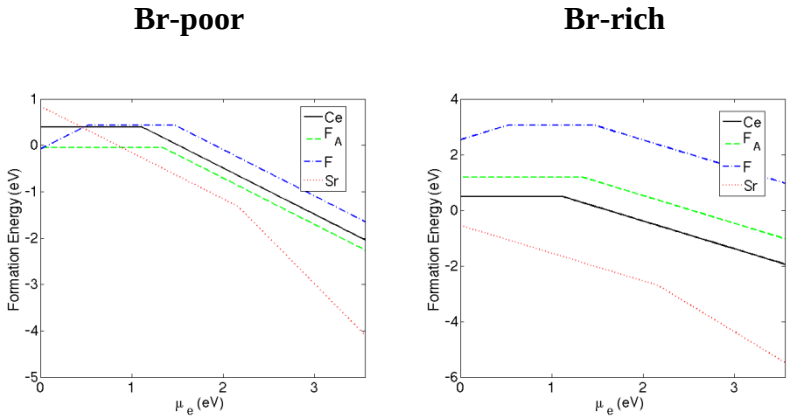

Fig. 2 Formation energies of Ce, Sr-F_A, F center, and plain Sr_{La} in $LaBr_3$ in Br-poor and Br-rich conditions against electron Fermi energy. All four defects are in energetic favor of negative charge states.

2.4 Energy levels and carrier transport analysis

The calculated relevant energy levels from GGA+U and PBE0 of the defect levels in different charge states located inside the fundamental band gap are plotted in Fig. 3. The results from these two different functionals are qualitatively similar. In general, PBE0 results are most accurate in terms of determining these relative energy levels. The F_A^{++} hole level is slightly lower than lowest Ce 4f levels, which means the shallow-trapped holes on F_A^{+} centers are able to eventually land on the Ce centers through tunneling process for example. Our hypothesis of carrier transport in Sr co-doped $LaBr_3$:Ce is as follows: holes are promptly trapped on Sr-F_A^{+} centers due to their large cross-section. The hot electrons with decent upper conduction band group velocity separate from the trapped holes. The existence of the trapped holes form a positive line charge near the center of the electron track helps guide the electrons to drift back and find the holes tunneling to the Ce^{3+} centers.

This process is similar to the characteristic charge separation and drift back mechanism that happens in materials like NaI and CsI. These materials have intrinsic self-trapped holes (STH) and fast hot electrons [6]. The charge separation limits the range of the carrier diffusion and ensures the 3rd quenching feature of these materials, this is the fundamental reason why alkali halides have generally high light yield among all scintillators. $LaBr_3$:Ce itself is already an exceptional scintillator in terms of proportionality and light yield due to its low 3rd order quenching rate and the efficiency of $(Ce^{3+})^*$ 5d-4f transition. We believe the Sr co-doping helps $LaBr_3$:Ce to obtain the additional merits that only halide materials with self-trapping holes had before.

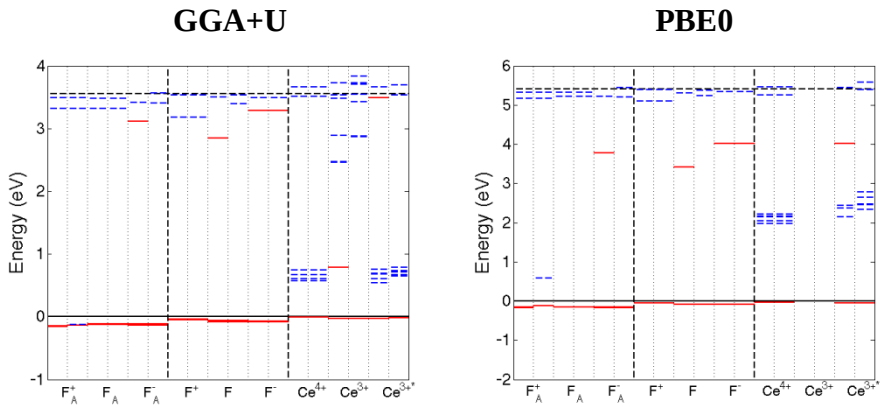

Fig. 3 Defect energies levels of F_A center, F center, and Ce activator in different charge states calculated from GGA+U and PBE0. Red solid lines are for occupied levels and blue dashed line for unoccupied levels.

REFERENCES

[1] G. Kresse and J. Hafner, Phys. Rev. B **47**, 558 (1993).

[2] G. Kresse and D. Joubert, Phys. Rev. B **59**, 1758 (1999).

[3] D. Åberg, B. Sadigh, and P. Erhart, Phys. Rev. B **85**, 125134 (2012).

[4] A. Canning, A. Chaudhry, R. Boutchko, and N. Grobech-Jensen, Phys. Rev. B **83**, 125115 (2011).

[5] J. P. Perdew, M. Ernzerhof, and K. Burke, J. Chem. Phys. **105**, 9982 (1996).

[6] Qi Li, J. Q. Grim, K. B. Ucer, A. Burger, G. A. Bizarri, W. W. Moses, and R. T. Williams, Phys. Status Solidi RRL **6**, 346 (2012).

CHAPTER 9: FIRST PRINCIPLES CALCULATIONS ON SOLID-SOLUTION ALKALI HALIDE SCINTILLATOR MATERIALS

Qi Li, Sam Flynn, R. T. Williams, K. Biswas, E. Rowe, E. Tupitysn, M. Groza, P. Bhattacharya, and A. Burger

This following manuscript is in preparation for publication. Qi Li performed all first principle calculations. A. Burger and his group grew the samples of the mixing crystals. Qi Li, K. Biswas and R. T. Williams analyzed the results and prepared the manuscript.

ABSTRACT

We present a first principles investigation based on density functional theory for alkali halides to predict the formation energies and temperature phase diagram as a function of composition. Special quasi-random structures (SQS) are used to present the alloy systems. We show that the alloying introduces complexity to the band structures and limits overall hot electron group velocity. Based on our hot electron transport model of scintillator materials, this effect has prominent significance for scintillator nonproportionality. Finally, self-trapped exciton and self-trapped hole formation and energy transfer to activators are discussed.

1. Introduction

A. Gektin et al recently directed attention to phenomenological evidence compiled over the last two decades of improved scintillation light yield achieved near the 50% composition point of mixed crystals relative to the two pure-crystal end points [1]. This phenomenon has been noted in at least 10 different solid solution systems. Gektin et al have offered a reason based on limiting hot electron diffusion range so that electrons are more likely to stop within the Onsager radius of the hole, making a geminate pair. They suggested that modification of the phonon spectrum and electron scattering, inhomogeneity of the solid solution, and Anderson localization in the mixed crystal could be responsible factors for the improved light yield of the mixture [1]. Solid solutions such as BaBrI:Eu from the already high-performance family of alkaline earth iodides have been developed and studied by E. Bourret-Courchesne et al. [2] The mixed crystal appears to have higher light yield than the end points and certainly has improved water resistance and mechanical properties relative to the BaI_2 end point. We will discuss a theoretical basis for anticipating improved proportionality as well as light yield in solid solutions of certain systems, particularly alkali iodides, based on concepts introduced in Refs. [3,4]. Solid solutions based on NaI and similar alkali halides are attractive to consider in more detail because the end point compositions are cheap and easy to grow. If some of this quality can be preserved while reaping improved light yield and possibly improved proportionality of the mixture, one version of the goal of better performance at the low price of NaI:Tl might be attainable by such a route. We intend to thoroughly explore the fundamental trends in scintillator material properties within the chosen model

system by theoretical and experimental means, and early results are presented in this paper.

The alloys are simulated by special quasi-random sturctures (SQS's). [5] We first take $NaBr_xI_{(1-x)}$ and $Na_{(1-x)}K_xI$ as examples to illustrate how alloying affects the electronic structures. Br-p and I-p orbitals hybridize near the valence band top of $NaBr_xI_{(1-x)}$, while Na-s and K-s orbitals modify mainly the conduction band bottom. Group velocities as a function of energy are compared among the alloys and hosts.

2. Computational details

2.1 First-principles calculations

Density functional theory (DFT) calculations were carried out in the projector augmented wave pseudopotentials [PAW] and exchange-correlation functionals as parametrized by Perdew-Burke-Ernzerhof [PBE] within the generalized gradient approximation using the Vienna ab initio simulation package (VASP). We employed 16-atom SQS for band structure and group velocity calculations and 64-atom SQS for formation enthalpies. Gamma-centered $6\times6\times6$ and $3\times3\times3$ Monkhorst-Pack k-mesh are used for lattice relaxation of 16-atom cells and 64-atom cells respectively to ensure all the calculations converge within 1 meV/atom with respect to k-point sampling. A self-consistency convergence tolerance of 1×10^{-6} eV is used for all calculations and the structures are relaxed until all the force components are less than 0.01 eV/Å. The lattice parameters are relaxed with the shape of the supercells fixed.

2.2 Group velocity and electron/hole effective mass

Group velocities of $NaBr_{0.5}I_{0.5}$ and $Na_{0.5}K_{0.5}I$ are calculated as a function of energy by averaging over the Brillouin zone (BZ). Using **k**-space coordinates, we can express them as follows:

$$g(E) = \frac{2}{(2\pi)^3} \sum_n \int_{BZ} \delta(E - E_n(\mathbf{k})) d^3\mathbf{k} \quad (1)$$

$$v_g^2(E) g(E) = \frac{2}{(2\pi)^3} \sum_n \int_{BZ} \mathbf{v}_n^2(\mathbf{k}) \delta(E - E_n(\mathbf{k})) d^3\mathbf{k} \quad (2)$$

where $g(E)$ is the density of states, n is the band index, $\mathbf{v}_n(\mathbf{k}) = (1/\hbar)\nabla_{\mathbf{k}} E_n(\mathbf{k})$, and the factor 2 accounts for the spin degeneracy. The k-point sampling for group velocity calculations is $32 \times 32 \times 32$.

The effective masses for electrons (m_e^*) and holes (m_h^*) are calculated from the 2nd derivative of energy with respect to **k**-vector at conduction band minimum and valence band maximum, which are at Γ-point for $NaBr_{0.5}I_{0.5}$ and $Na_{0.5}K_{0.5}I$ and their hosts. We average the inverse of the three diagonal elements ($1/m_{xx}$, $1/m_{yy}$ and $1/m_{zz}$) to get m_e^* and m_h^*. For the host materials, the VBM contains multiple degenerate bands. We average the masses of these degenerate bands to get m_{h1}^* and average the inverse masses to get m_{h2}^* in Table I.

2.3 Formation enthalpy and phase diagram

Formation enthalpies are calculated as [6]

$$\Delta H(A_{1-x}B_xC) = E(A_{1-x}B_xC) - xE(BC) - (1-x)E(AC) \quad (3)$$

where $E(A_{1-x}B_xC)$ is the total energy of the ternary structure of composition x and $E(AC)$ and $E(BC)$ are the total energies of the two binary constituents. The phase diagrams are calculated as in Ref. [6].

3. Results and Discussion

3.1 Electronic structures and group velocities of $NaBr_{0.5}I_{0.5}$ and $Na_{0.5}K_{0.5}I$

To make direct comparison of the electronic structures between the ternary alloys and their hosts, we generated a 16 atom SQS for $NaBr_{0.5}I_{0.5}$ and $Na_{0.5}K_{0.5}I$, and used the exact same cell for the host materials. In Fig. 1, the band structures and the partial density of states are plotted. It is clearly shown that the hybridization of p-orbital of Br and I dominates in $NaBr_{0.5}I_{0.5}$, which breaks more degeneracies and makes more profound change to the valence band. In comparison, in $Na_{0.5}K_{0.5}I$, mixing of cations introduces significant Na-4s and K-3d hybridization in the conduction band. In addition, more compact K-3d orbitals dominate the conduction band of the ternary, resulting in an overall "flatter" conduction band. In Fig. 2, the electron/hole group velocities of the ternaries and the host materials are plotted against energy relative to conduction band minimum (CBM). According to Ref. [3] based on our hot electron transport model, an ideal scintillator should have modestly low hot electron group velocity and high band edge electron mobility, together with self-trapping holes (STH) preferably. The most important shortcoming that limits the resolution of NaI scintillator radiation detectors is that the fast hot electrons are thrown out up to a radial Gaussian range of ~ 50 nm compared to the initial Gaussian distribution of 3 nm. Upon thermalization, these electrons have to travel back to recombine with the holes while in danger of getting

trapped by deep electron traps such as F centers. With mixing cations, we can obtain crystals with significantly lower overall hot electron mobilities as shown in Fig. 2. In Table I, the band edge electron effective masses of the ternaries are calculated and compared to their hosts. We can see that the change of electron effective masses is very limited due to crystal mixing. Additionally, the existence of STH in the host materials has been proved both experimentally and theoretically.

The calculated group velocity and effective mass results make $Na_xK_{1-x}I$ a quite promising scintillator with all the similar features that the existing well performing scintillator -- SrI_2 has. Although it might not be the best choice because of the existence of ^{40}K isotope, we believe the idea of mixing crystal is important for analyzing and designing potentially better scintillators in the future. Experimental study of these mixing crystals will be carried out soon to test our prediction from calculation.

Table I Calculated electron effective mass m_e^* in electron mass m_0 and hole effective mass using two different ways of averaging degenerate bands at VBM, m_{h1}^* and m_{h2}^* in m_0.

	NaI	NaBr	KI	$NaI_{0.5}Br_{0.5}$	$Na_{0.5}K_{0.5}I$
m_e^*	0.27	0.25	0.34	0.31	0.29
m_{h1}^*	1.23	0.88	2.05	1.02	1.11
m_{h2}^*	0.80	0.61	1.13	1.02	1.11

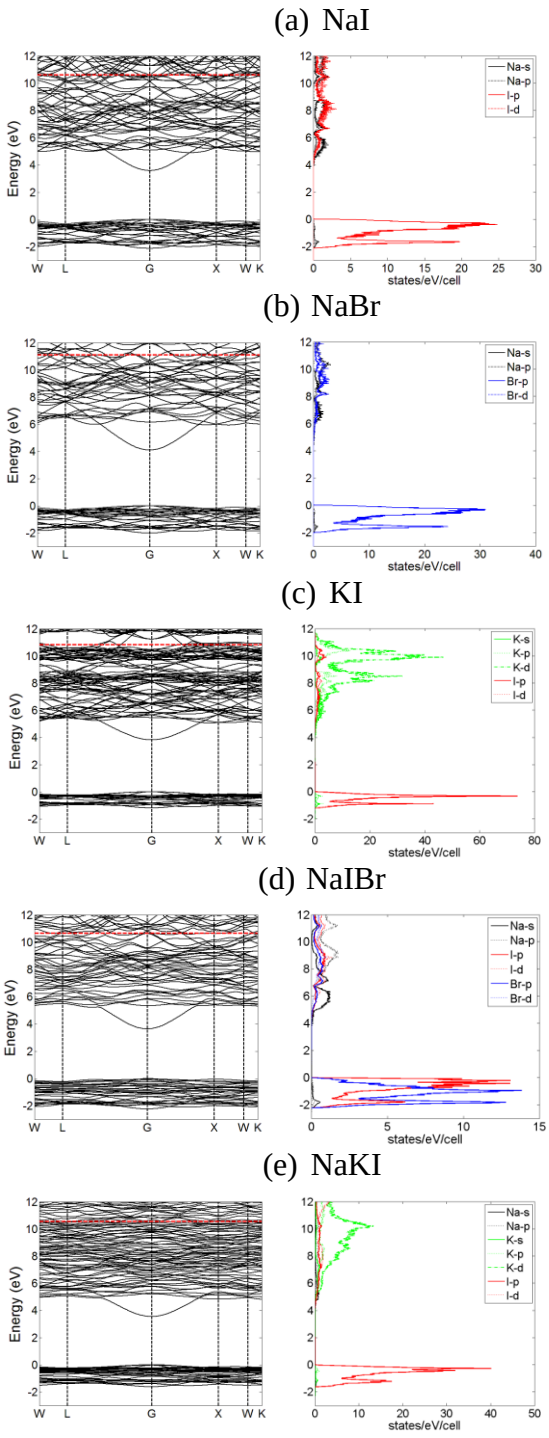

Fig.1 Band structures and partial density of states of (a) NaI, (b) NaBr, (c) KI, (d) $NaI_{0.5}Br_{0.5}$, and (e) $Na_{0.5}K_{0.5}I$. The horizontal red line indicates the position of experimental band gap for NaBr (7 eV), which is the highest among the host materials, above the conduction band minimum (CBM).

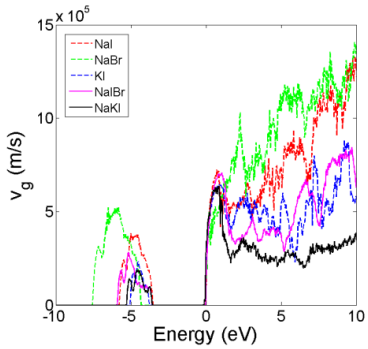

Fig. 2 Hot electron/hole group velocities for the host materials NaI, NaBr, KI and the ternaries $NaI_{0.5}Br_{0.5}$ and $Na_{0.5}K_{0.5}I$. Note that the energy origin is set at conduction band minimum.

3.2 Formation enthalpies as a function of composition

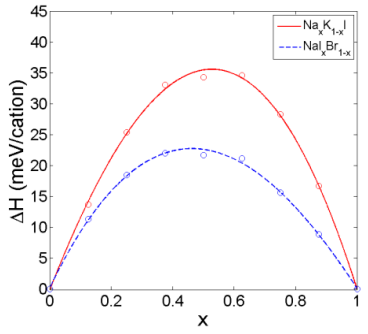

Fig. 3 Formation enthalpies of $Na_xK_{1-x}I$ and NaI_xB_{1-x} as a function of composition *x*. Open circles are data from calculations of 64 atom SQS structures, polynomial fitting is shown with solid lines.

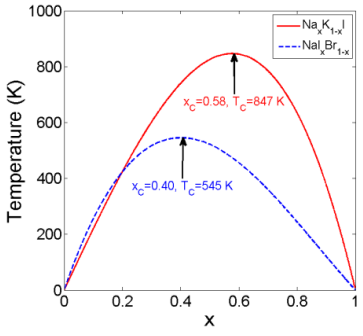

Fig. 4 Simulated temperature phase diagram (spinodal curve) of $Na_xK_{1-x}I$ and NaI_xB_{1-x} as a function of composition *x*. The consolute temperature T_C and corresponding composition x_C are shown for both materials.

The formation enthalpies and temperature phase diagram for $Na_xK_{1-x}I$ and NaI_xB_{1-x} as a function of composition *x* are plotted in Fig. 3 and Fig. 4. These results are done in 64 atom SQS's. We can see $Na_xK_{1-x}I$ has relatively higher formation enthalpy and transition temperature. However, calculated results show that both materials can be grown under reasonable temperature in crystal growth process.

REFERENCES

[1] Gektin, A. Belsky, and A. N. Vasil'ev, IEEE Trans. Nucl. Sci., Proc. SCINT 2013 (in press); SORMA 2012, Oakland, ASM 2013, Kharkov.

[2] E. D. Bourret-Courchesne, G. Bizarri, S. M. Hanrahan, G. Gundiah, Z. Yan, S. E. Derenzo, Nucl. Instr. Meth. Phys. Res. A **613**, 95 (2010).

[3] Qi Li, J. Q. Grim, K. B. Ucer, A. Burger, G. A. Bizarri, W. W. Moses, R. T. Williams, Phys. Stat. Sol. RRL **6**, 346 (2012).

[4] R. T. Williams, J. Q. Grim, Qi Li, K. B. Ucer, G. A. Bizarri, S. Kerisit, Fei Gao, P. Bhattacharya, E. Tupitsyn, E. Rowe, V. M. Buliga, A. Burger, Proc. SPIE Vol. 8852, 88520J-1 (2013).

[5] A. Zunger, S.-H. Wei, G. Ferreira, and J. E. Bernard, Phys. Rev. Lett **65**, 353 (1990).

[6] K. Biswas, A. Franceschetti, and S. Lany, Phys. Rev. B **78**, 085212 (2008).

CHAPTER 10: MONTE CARLO SIMULATION OF HOT ELECTRON TRANSPORT IN SCINTILLATORS

Qi Li, N. A. W. Holzwarth, and R. T. Williams

This following manuscript is in preparation for publication. Qi Li performed all first principle calculations with help from N. A. W. Holzwarth and developed the Monte Carlo simulations package. Qi Li and R. T. Williams analyzed the results and prepared the manuscript.

ABSTRACT

The full band structures of several scintillator materials in respectively alkali halide, alkaline earth halide, and rare earth halide families are determined from density functional theory (DFT) in order to provide necessary parameters for the description of hot electron transport. The density of states and group velocity for the conduction bands from the conduction band minimum (CBM) up to one energy gap (E_g) above CBM are calculated as a function of energy. Based on these results and the knowledge of the optical phonon frequencies (ω_{LO}), a Monte Carlo simulation of hot electron transport in scintillators is carried out. Thermalization time and diffusion range are predicted in different scintillators.

1 Introduction

Electron group velocity (v_g) plays an important role in electron transport which relates to many types of physical systems and applications. For example, v_g has been implicated in high electric field transport systems [1], laser damage [2] and to evaluate the mean free path in metals successfully [3]. In this paper, we use electron group velocity to investigate scintillator materials which are used for radiation detectors and medical imaging systems. The theory of hot electron transport will be tested against experimental results of the optical response of different scintillator materials excited by external energy sources.

Efforts to understand the fundamental origins of scintillator nonproportionality in order to discover better performing scintillator materials have been intense in the last decade. The transport of the electrons in scintillators after being created by stopping of an incident γ-ray can be sub-divided into the hot electron stage with energy range up to one E_g above CBM and the thermalized electron stage with energy very close to CBM. We previously described a nonlinear quenching and diffusion model of thermalized carriers that made quite good predictions between the nonproportionality and effective diffusion coefficient (D_{eff}) of oxides, while it left some ambiguity to both monovalent and multivalent halide materials [4]. A common similarity for almost all these halide materials is that they have been suggested or proved to have self-trapped holes on a time scale of ~1ps by experiment and/or theoretical approaches. Hence we focus mainly on their electron transport. Monte-Carlo modeling for hot electrons losing their energy

mainly by scattering with optical phonons has been done for several halide materials by Wang et al. [5]. They concluded that optical phonon frequency is the key factor controlling the electron thermalization time and hence electron transport length. Velocity calculated from a free electron model is used in their simulations to decide the step length. However, it is demonstrated in Ref. [3] and this work that the inclusion of full band structure significantly improves the result of electron transport velocity with respect to the prediction of a free electron model.

We organize the rest of the paper as follows. In the next section, we discuss the computational detail. Section 3 presents the results for the calculated group velocity for materials in different categories. In Section 4, we present the Monte-Carlo simulation results for CsI, SrI2, and YAP (yttrium aluminum perovskite) scintillators with drastic difference in terms of hot electron transport mechanisms and electron responses.

2 Computational details

We address our calculations on eight materials grouped as follows:

Oxides: SiO_2

Alkali halides: CsI, NaI

Alkaline earth halides: SrI_2

Rare earth halides: $LaBr_3$, $LaCl_3$

Semiconductors: ZnO, CdTe

The electronic structures of these materials are calculated from DFT using the Vienna Ab-initio Simulation Package (VASP) with projector augmented waves (PAW) pseudopotentials and exchange-correlation functionals parameterized by Perdew-Burke-

Enzerhof (PBE) with generalized gradient approximation (GGA). For the Lanthannum compounds, we use DFT+U technique to the La (4f) states to correct their position relative to the La (5d) states. We choose U_{eff} = 10.5 eV in our calculations to reproduce experimental observations. A convergence criterion of 1×10^{-6} eV is used for all the self-consistency calculations. All the crystal structures are relaxed until all force components are less than 0.01 eV/Å. We use Γ-centered Monkhorst-Pack generated kmesh grids for these calculations. In table I, the wavefunction energy cutoff, k-point sampling, and E_g obtained from our calculations together with experimental values are listed. The normal problem of underestimation of E_g is also observed in our calculations. However, since we are only dealing with hot electrons in the conduction band, this problem becomes less relevant and we just apply a scissors correction and use the description of the conduction band calculated from density functional theory.

Table I Crystal structure, wavefunction energy cutoff (E_{cut}), atoms in a single unit cell (N_{atom}), K-point sampling (kp) for cell relaxation and v_g calculations, number of bands (N_{band}) counted in energy range from CBM to CBM + E_{g_exp}, calculated and experimental values of E_g are listed for all materials included.

material	crystal structure	E_{cut} (eV)	N_{atom}	kp_{relax} ($n \times n \times n$)	kp_{vg} ($n \times n \times n$)	N_{band}	E_{g_calc} (eV)	E_{g_exp} (eV)
SiO_2	hexagonal	600	9	4	16	18	5.8	9.0
CsI	Cubic	300	2	6	32	7	3.8	6.1
NaI	Cubic	300	2	6	32	6	3.7	5.9
SrI_2	orthorhombic	300	24	4	12	58	4.0	5.5
$LaBr_3$	hexagonal	400	6	4	16	33	3.6	6.3
$LaCl_3$	hexagonal	450	6	4	16	35	4.5	7.2
ZnO	hexagonal	700	4	6	24	1	0.9	3.3
CdTe	cubic	450	2	6	32	1	0.7	1.4

Based on the relaxed structures, we calculate the density of states and group velocities as a function of energy by averaging over the Brillouin zone (BZ). Using **k**-space coordinates, we can express them as follows [1]

$$g(E) = \frac{2}{(2\pi)^3} \sum_n \int_{\mathrm{BZ}} \delta(E - E_n(\mathbf{k})) d^3\mathbf{k} \tag{1}$$

$$v_g^2(E) g(E) = \frac{2}{(2\pi)^3} \sum_n \int_{\mathrm{BZ}} \mathbf{v}_n^2(\mathbf{k}) \delta(E - E_n(\mathbf{k})) d^3\mathbf{k} \tag{2}$$

where $1/(2\pi)^3$ is the density of states in **k**-space, n is the band index, $\mathbf{v}_n(\mathbf{k}) = (1/\hbar)\nabla_{\mathbf{k}} E_n(\mathbf{k})$, and the factor 2 accounts for the spin degeneracy. We use much denser k-point sampling here to get more accurate information of the conduction band since slopes will be calculated in the vicinity of crossings. Tests have been done to show how the calculated v_g converges with the k-mesh. To evaluate Eqs. (1) and (2), we use Gaussian smearing functions to replace the δ-functions, and convert the integrals to sums of band index and k-points in the Brillouin zone (BZ) weighted by the corresponding volume in **k**-space. We can then rewrite Eqs. (1) and (2) as

$$g(E) = 2\sum_{nk} f(E - E_{nk}) w_k \tag{3}$$

$$v_g^2(E) g(E) = \frac{2}{\hbar^2} \sum_{nk} f(E - E_{nk}) (\nabla_{\mathbf{k}} E_{nk})^2 w_k \tag{4}$$

The function f is a normalized Gaussian function centered at E_{nk} with a smearing of 0.02 eV. The normalized weight factor of each k-point, w_k, is proportional to the volume of each k-point occupying in the irreducible Brillouin zone.

We have also calculated the effective masses for these materials for comparison between the free electron model v_{FEM} and v_g

$$v_{FEM} = \sqrt{\frac{2E_e^{kin}}{m_e^*}} \tag{5}$$

The electron effective mass in each direction is calculated as follows

$$m_\alpha = \frac{1}{\hbar^2}\frac{1}{N}\left(\sum_i \frac{\partial^2 E_i}{\partial k_\alpha^2}\right)^{-1} \tag{6}$$

where index *i* runs over all the degenerate bands at CBM. Then we average the inverse of masses in each direction.

3 Results

3.1 Band structures

The calculated band structures for selected insulators and semiconductors are shown in Fig. 1. We can readily see that the simple halides (NaI, CsI) and semiconductors (ZnO, CdTe) have more dispersive bands than complex halides. 4f electrons in $LaBr_3$ and $LaCl_3$ are extremely compacted, lowering their overall hot electron group velocities.

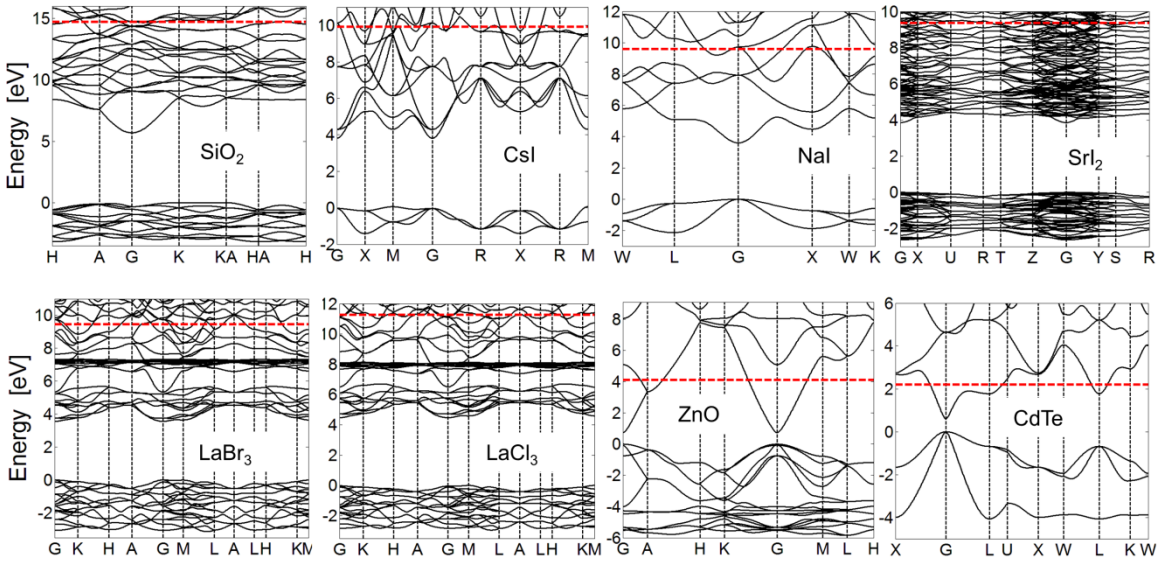

Fig. 1 Calculated band structures for selected insulators and semiconductors. The red dashed line indicates the position of one experimental band gap above conduction band mimimum.

3.2 Group velocity

The group velocity and density of states (DOS) spectra for the selected materials are shown in Fig. 2. The green dashed curve overlays the data with group velocity based on the free electron model with band dedge effective mass. Our results for SiO_2 agree with those in Ref. [1] quite well. The hole group velocity for materials without self-trapped holes (i.e., SiO2, YAP, ZnO, and CdTe) are also included in Fig. 2. The complexity of the material structures has a clear impact on reducing the group velocities. As listed in Table II, the overall group velocities in the range of conduction band minimum up to one band gap above CBM weighted by DOS in simple halides (CsI, NaI) are at least 3 times greater than that in multivalent halides ($LaBr_3$, $LaCl_3$, and SrI_2).

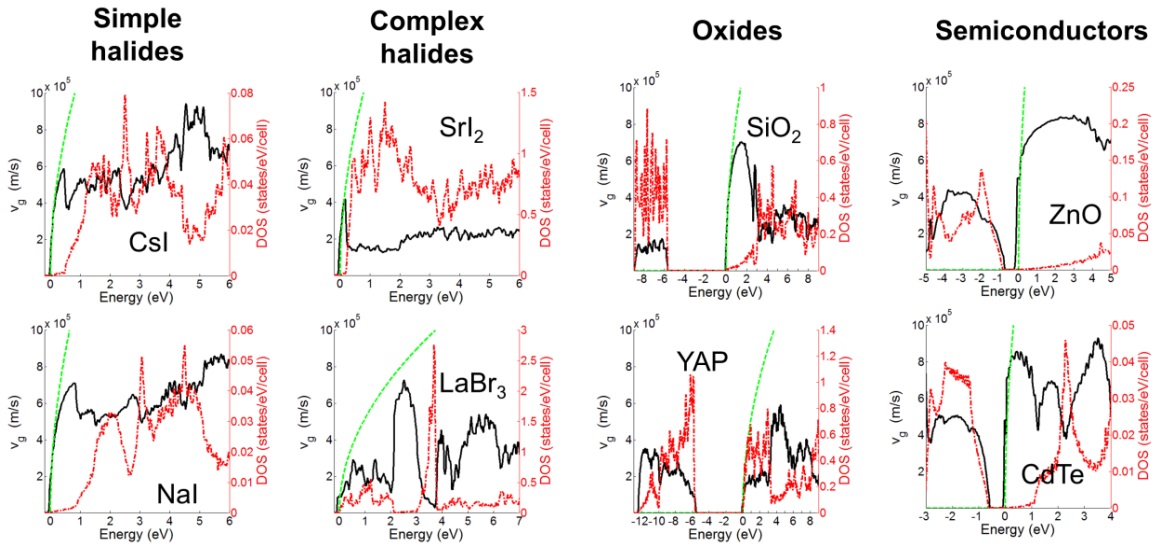

Fig. 2 Group velocity (left axis) and density of states (right axis) as a function of carrier energy in selected insulators and semiconductors grouped as indicated in the figure. The green dashed line is for the band edge electron velocity assuming free electron model and electron effective masses.

3.3 Monte-Carlo simulations

Monte-Carlo simulations are carried out following the routines in Refs. [5,6]. The intial distribution is assumed to be a 3 nm cylinder of independent electron/hole pairs with various on-axis densities. The optical phonon frequencies are calculated from phonon spectra and listed in Table II. In Fig. 3, the simulated thermalization time and diffusion range for CsI, SrI_2, and YAP are plotted. CsI has the longest thermalization time and largest hot electron diffusion range due to its low optical phonon frequency and high hot electron group velocity. Compared to CsI, SrI_2 has significantly more limited electron diffusion range which diminishes the chance of the electrons to be trapped on undesired nonradiative traps during their thermalized diffusion stage to walk back and recombine with the holes. As an example of typical oxide scintillators, YAP has a very high optical phonon frequency which makes the electron thermalization happen very quickly (< 0.2 ps) in this material. This result illustrates that hot electron diffusion is almost irrelevant in materials with high optical frequencies, which validates the conclusions discussed in Refs. [4] and [8]. The thermalized carriers will form a mixture of excitons and independent carriers as discussed in Ref. [4], the diffusion of the mixture keeps going until the carriers are eventually trapped on available trapping centers. The thermalization time and range is almost independent of initial on-axis carrier density. This is a result of the fact that the hot electrons with high kinetic energy can almost move freely with the internal electric field ignored [5].

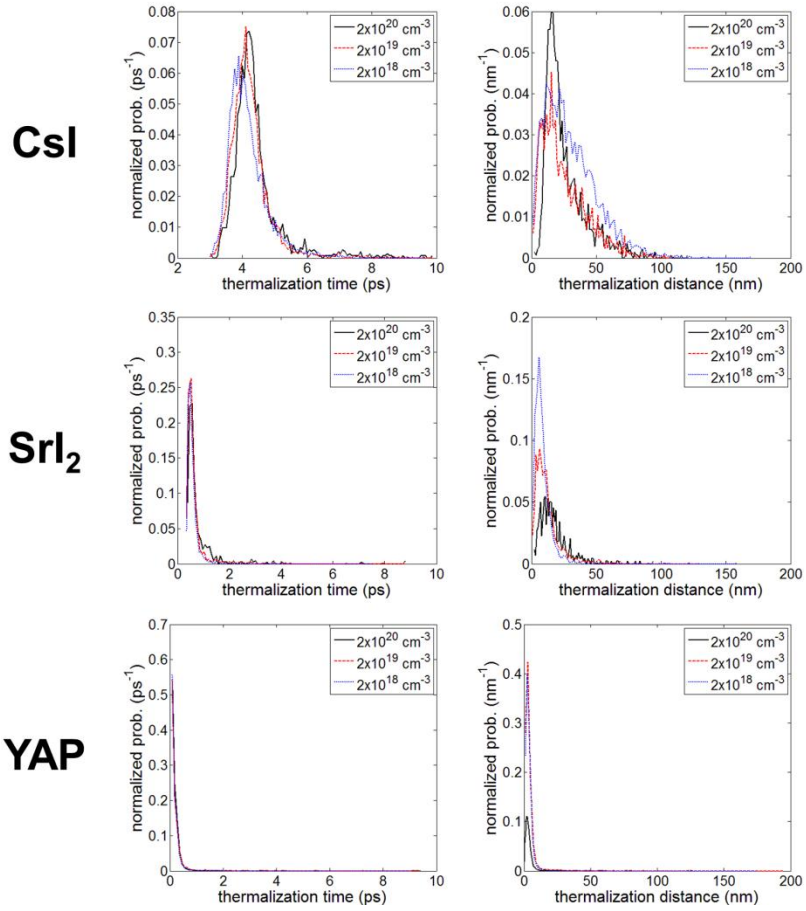

Fig. 3 Hot electron thermalization time and diffusion range statistical distribution of CsI, SrI_2, and YAP scintillators calculated from Monte-Carlo simulations. Calculations are done for three different initial on-axis densities shown in the legends and represented by black (2×10^{20} cm^{-3}), red (2×10^{19} cm^{-3}) and blue (2×10^{18} cm^{-3}) curves.

Table II Simulated group velocity v_g, band edge electron effective mass m^*, phonon frequency ω_{LO}, thermalization time τ and diffusion range before thermalization r for selected scintillators. The existence of multiple modes as discussed in Ref. [6] is also listed.

material	v_g (10^5 m/s)	m^* (m_0)	m'^* (m_0)	ω_{LO} (meV)	multiple modes	τ (ps)	r (nm)
SiO_2	2.6	0.504	0.504	~100	Yes		
CsI	5.4	0.265	0.265	10	No	4.3	28
NaI	6.0	0.226	0.226	23	No	2.2	22
SrI_2	1.8	0.276	0.277	15	Yes	0.8	10
$LaBr_3$	1.5	1.310	1.317	17	Yes	1.1	12
$LaCl_3$	1.6	1.408	1.413	19	Yes	1.2	13
YAP	2.3	1.106	1.243	86	Yes	<0.2	5

4. Conclusion

Group velocity calculated from full band structure calculations are used as a correction parameter in Monte-Carlo simulations of hot electron transport. The hot electron diffusion range is hence predicted to be 25 nm, smaller compared to the results in Ref. [5]. This model is able to solve for the effective diffusion coefficient $D(T_e)$ as a function of electron temperature naturally. In the near future, other T_e dependent parameters will be included in the same model so that light yield will be predicted.

REFERENCES

[1] E. Gnani, S. Reggiani, and M. Rudan, Phys. Rev. B **66**, 195205 (2002).

[2] M. Sparks, D. L. Mills, R. Warren, T. Holstein, A. A. Maradudin, L. J. Sham, E. Loh, Jr., and D. F. King, Phys. Rev. B **24**, 3619 (1981).

[3] V. M. Silkin, E. V. Chulkov, and P. M. Echenique, Phys. Rev. B **68**, 205106 (2003).

[4] Qi Li, J. Q. Grim, R. T. Williams, G. A. Bizarri, and W. W. Moses, J. Appl. Phys. **109**, 123716-1-17 (2011).

[5] Z. Wang, Y. Xie, L. W. Campbell, F. Gao, and S. Kerisit, J. Appl. Phys. **112**, 014906 (2012).

[6] R. Kirkin, V. V. Mikhailin, and A. N. Vasil'ev, IEEE Trans. Nucl. Sci. **59**, 2057 (2012).

[7] Qi Li, J. Q. Grim, K. B. Ucer, A. Burger, G. A. Bizarri, W. W. Moses, and R. T. Williams, Phys. Status Solidi RRL **6**, 346 (2012).

CHAPTER 11: FIRST PRINCIPLES CALCULATIONS ON GGAG:Ce AND GYGAG:Ce SCINTILLATORS

Qi Li, Sam Flynn, K. B. Ucer, and R. T. Williams

This following manuscript is in preparation for publication. Qi Li generated the special quasi-random structures for GGAG and GYGAG and performed all first principle calculations. Qi Li and R. T. Williams analyzed the results and prepared the manuscript.

ABSTRACT

First principles calculations are performed on both undoped and Ce doped GGAG and GYGAG ceramics. The systems are simulated by using special quasi-random structures. We present the electronic structures of the materials from GGA+U and hybrid functional PBE0 methods. Accurate band gaps are determined by GW approximation. The calculated Gd 4f levels in both materials are 1 eV above the conduction band minimum (CBM), in constrast to an earlier hypothesis of a Gd impurity sub-band in the gap that could transport energy. Ga substitution plays an important role in these materials because it forms the conduction band edge and hence determines the band-edge mobilities which are proved to be crucial to the nonlinear quenching for oxide scintillators. Furthermore, the energy levels of substitutional Ce is determined and the calculated Ce 4f-5d transition energies from PBE0 functional correspond well with experimental data.

1. Introduction

Transparent ceramic garnets $Gd_3(Ga,Al)_5O_{12}$ (GGAG):Ce and $(Gd,Y)_3(Ga,Al)_5O_{12}$ (GYGAG):Ce are newly developed scintillators with high light yield (up to 50,000 ph/MeV) and higher energy resolution (4.8% at 662 keV) compared to traditional NaI:Tl scintillators (7% at 662 keV) [1,2]. These materials have their advantages in phase stability, nonhygroscopic nature, and mechanical toughness compared with other newly developed scintillators such as SrI_2:Eu and $LaBr_3$:Ce. Fabrication of the ceramics is cheaper as well. These merits makes Gd garnets an important and promising direction for searching of low-cost energy resolving scintillator radation detectors. Ga^{3+} doping has significant impact on the light yield and proportionality of these ceramic scintillators. Without Ga, $Gd_3Al_5O_{12}$ (GGG) garnet does not exhibit any scintillation [2].

Investigations trying to understand the physical origin of the improvement of scintillation efficiency in $RE_3Al_5O_{12}$ (RE for rare-earth elelements) garnets driven by Ga^{3+} doping has been done in Ref. [3,4]. Density functional theory calculations validate the “band-gap engineering” in order to remove the existence of some shallow electron traps by Ga^{3+} doping in these garnets [3]. However, convincing determination of the relative energy levels of the shallow defects with respect to relevant energy levels of the host material from first principles calculations were not performed. Further experimental evidence shows the amount of Ga^{3+} is responsible for Ce^{3+}/Ce^{4+} ratio of the Ce activators, which also has an impact on the scintillation properties of these garnets [4]. In this work,

we present first principles calculations on the electronic structures of the undoped and Ce doped garnets. The calculations show that Ga 5s levels construct the conduction band edge, which leads to a rather simple but reasonable new path of understanding the impact of Ga^{3+} doping – change of band edge mass/mobilities of the carriers. Simulation done in our group have shown that the band edge mobilities are crucial to the nonlinear quenching and hence proportionality for oxide materials with normally high optical phonon frequencies [5,6]. Accurate band gap results are obtained using GW approximation. The Ce 4f and 5d levels are determined using PBE0 hybrid functionals and compared with experimental data.

2. Computational details

Density functional theory (DFT) calculations were carried out in the projector augmented wave pseudopotentials and exchange-correlation functionals as parametrized by Perdew-Burke-Ernzerhof within the generalized gradient approximation using the Vienna ab initio simulation package (VASP). Hubbard U correction for self energy was applied for strong localized Ce 4f and Gd 4f orbitals. Hybrid functional PBE0 calculations were carried out for more accurate determination of the relevant energy levels in the material. GW approximation was used for accurate results of the band gap. The crystal structure of the $RE_3Al_5O_{12}$ prototype is body center cubic of space group Ia-3d with 160 (80) atoms in the cubic conventional (primitive) cell. 160-atom special quasi-random structures (SQS) were generated to simulate the multicomponent compounds with varying ratio between each element in the garnets. Calculations sampling the gamma-point only were performed but the calculations converge within 1 meV/atom

even so. A self-consistency convergence tolerance of 1×10^{-6} eV is used for all calculations and the structures are relaxed until all the force components become less than 0.01 eV/Å. The lattices parameters are relaxed with the shape of the supercells fixed as cubic.

3. Preliminary results and discussion

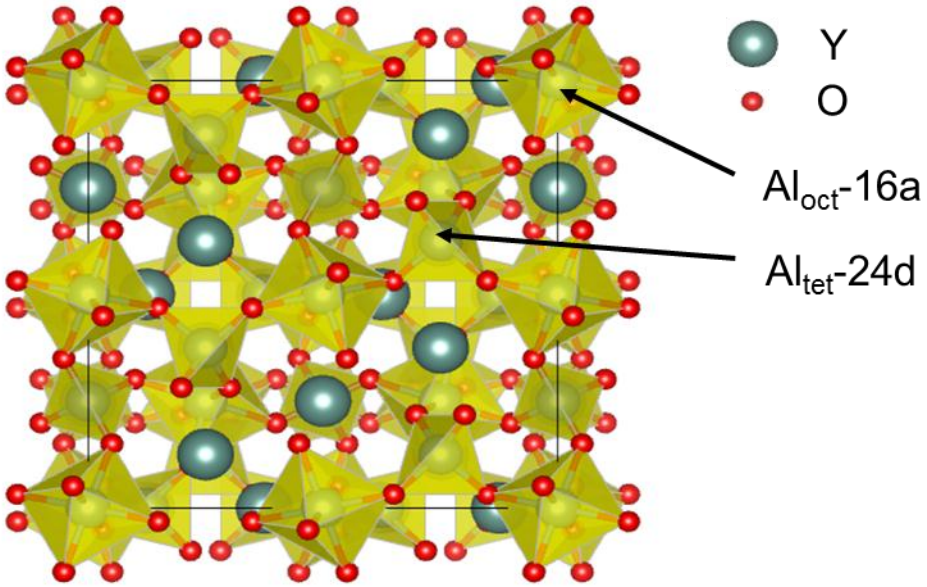

Fig 1. Crystal structure of the YAG prototype in a 160 atom cubic cell. Green atoms are for Y and red for O. Al are at the center of either an octahedral (16a) or a tetrahedral (24d). Y sites can be substitute by Gd and Al sites are substituted by Ga in GYGAG.

The structure of $Y_3Al_5O_{12}$ (YAG), which is a prototype of the GGAG and GYGAG garnets, is shown in Fig. 1. According to Ref. [4], the Ga^{3+} can substitute Al^{3+} and occupy both 16a and 24d sites. Calculated formation energy of Ga_{Al} in $Gd_3Al_5O_{12}$ (GAG) for the two different sites differs only by 17 meV, which is below room temperature. We present both the ordered structure for GGAG in which the Ga only

occupy one type of the Al sites, and SQS structures in which the Ga can randomly occupy both sites. The SQS stuctures are closer to the crystals used in experiments.

Table I Calculated lattice constant (a) and band gaps (b) using different functionals for ordered and randomized GGAG and GYGAG crystals.

(a)

a (Å)	GGAG-ordered	GGAG-SQS	GYGAG-SQS
GGA+U	12.40	12.41	12.28
PBE0	12.28	12.30	12.17
expt.		12.27	

(b)

E_g (eV)	GGAG-ordered	GGAG-SQS	GYGAG-SQS
GGA+U	3.62	3.64	4.04
PBE0	6.35	6.40	6.79
G_0W_0			6.49
GW_0			6.86
expt.		~ 6.70	

The calculated lattice constants and band gaps using different functionals for GGAG and GYGAG are listed in Table I. We can see that both GGA+U and PBE0 overestimate the lattice constant, but PBE0 results are very close to experimental data. The calculated band gaps from GGA+U are severely underestimated. However, PBE0 and GW approximation results are close to available experimental data in Ref. [4].

The calculated band structure and partial density of states (PDOS) using PBE functional without Hubbard U corrections for $Gd_3Ga_2Al_3O_{12}$ (GGAG) garnets are shown in Fig. 2.

We can see that the Gd 4f level in the conduction band is in the band gap and constructs the conduction band minimum. All 7 4f electrons of Gd occupy the same spin state which makes this material highly magnetic.

(a)

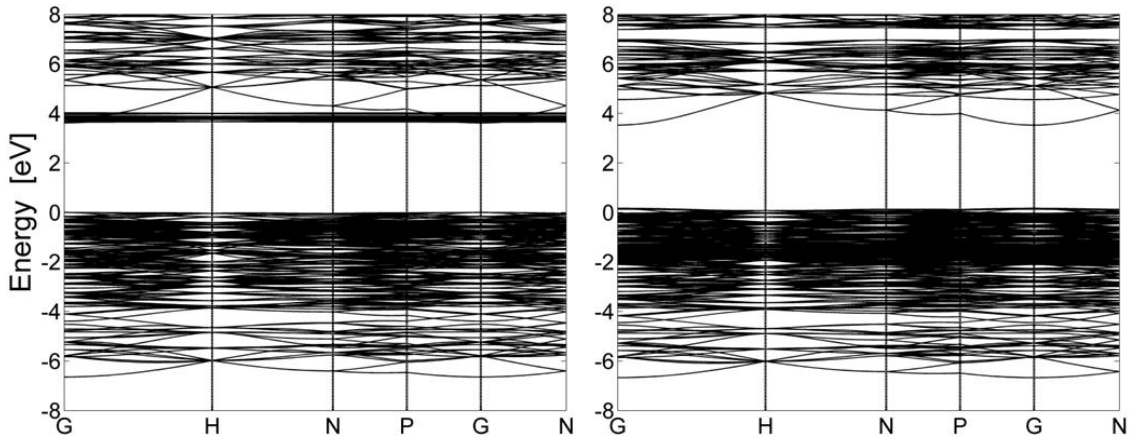

(b)

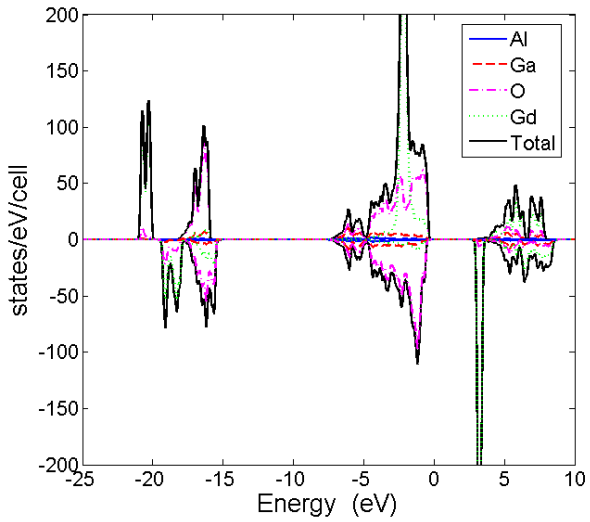

FIG. 2 Calculated band structures and partial density of states for ordered GGAG using PBE functional. The plots show the results for two different spin states. The Gd 4f orbital makes the conduction band minimum in this case.

In Fig. 3, we present the partial density of states of $Gd_{1.5}Y_{1.5}Ga_3Al_2O_{12}$ (GYGAG) calculated from GGA+U functional. The correction of self interaction of the Gd 4f orbitals brings the position of the Gd 4f levels 1 eV above conduction band minimum, which is made by Ga 5s orbitals.

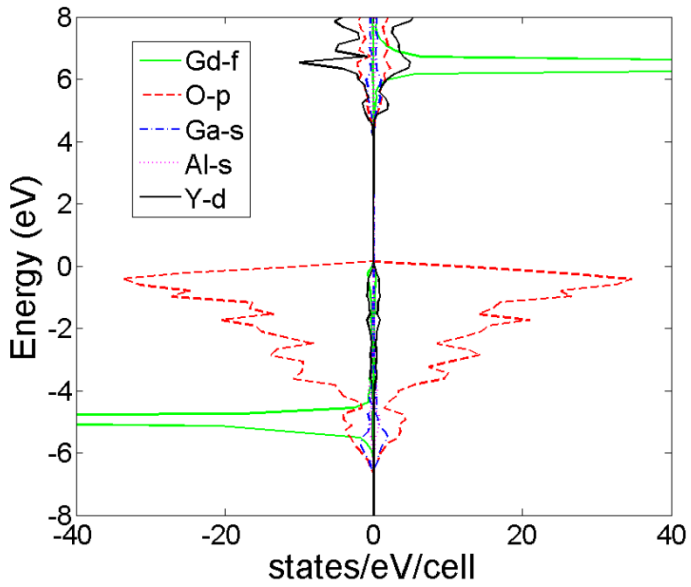

FIG. 3 Calculated partial density of states for SQS-GYGAG using GGA+U functional. The plot show the results for two different spin states. The Ga 5s orbital makes the conduction band minimum in this case.

The scintillation of these garnet scintillators is the Ce 5d to 4f transition. To simulate the optical transition energy, we first determined the position of the Ce substitution by comparing the formation energies of substitutional Ce at all possible sites (Gd, Al-16a, Al-24d, Y). The calculations show Ce_{Al} at 16a sites has the lowest formation energy among all the possible subsitutions and we used this result to determine the optical transition energies for the Ce activators. In Fig. 4, we present the schemetic diagram of the 5d and 4f levels of Ce relative to VBM/CBM. The optical transition energies between 5d and 4f levels are calculated with GGA+U with varing U_{eff} parameter

and PBE0 functionals. PBE0 functional results match the experimental data quite well. The successful determination of the Ce levels leads us to calculate the energy levels related with other electron traps in the crystal, which will give strong evidence of the theoretical validation of the "band gap engineering" in Ref. [3].

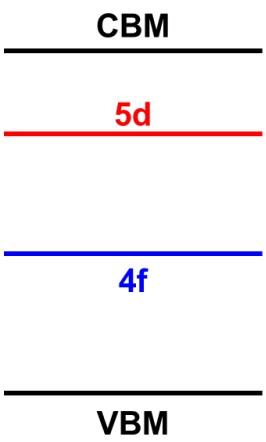

U_{eff} (eV)	4f-CBM (eV)	5d-4f (eV)
0 (GGA)	0.07	
1	0.23	
2	0.54	
3	0.97	
4	1.43	
5	1.95	
PBE0	2.90	2.08
expt.		2.25

FIG. 4 Calculated 4f-CBM transition and 5d-4f transition energies of Ce activators in GYGAG:Ce scintillator

REFERENCES

[1] K. Kamada, T. Endo, K. Tsutumi, T. Yanagida, Y. Fujimoto, A. Fukabori, A. Yoshikawa, J. Pejchal, and M. Nikl, "Composition Engineering in Cerium-Doped $(Lu,Gd)_3$ $(Ga,Al)_5$ O_{12} Single-Crystal Scintillators," Crystal Growth & Design **11**, 4484-4490 (2011).

[2] N. J. Cherepy et al., "Comparative gamma spectroscopy with SrI_2(Eu), GYGAG(Ce) and Bi-loaded plastic scintillators," Nulcear Science Symposium Conference Record (NSS/MIC), 1288 (2010).

[3] M. Fasol et al., "Band gap engineering for removing shallow traps in rare-earth $Lu_3Al_5O_{12}$ garnet scintillators using Ga^{3+} doping," Phys. Rev. B **84**, 081102 (2011).

[4] Y. Wu, J. Luo, M. Nike, and G. Ren, "Origins of improved scintillation efficiency in $(Lu,Gd)_3(Ga,Al)_5O_{12}$:Ce multicomponent garnets: An X-ray absorption near edge spectroscopy study," APL Materials **2**, 012101 (2014).

[5] Qi Li, J. Q. Grim, R. T. Williams, G. A. Bizarri, and W. W. Moses, J. Appl. Phys. **109**, 123716-1-17 (2011).

[6] Qi Li, J. Q. Grim, K. B. Ucer, A. Burger, G. A. Bizarri, W. W. Moses, and R. T. Williams, Phys. Status Solidi RRL **6**, 346 (2012).

CHAPTER 12: CONCLUSIONS AND FUTURE WORK

Numerically Modeling the light yield and nonproportionality for scintillators has been a sub-field in the community for several decades. Starting with the historic expression for light yield L due to Lempicki, Wojtowicz, and Berman [1]:

$$L = \beta' SQ \tag{1}$$

where the electron-hole pair creation efficiency β' is determined to be 2 to 3. S is the transfer efficiency for excitations to transfer to activators and Q is the quantum efficiency of the activators.

The transfer term S implies diffusion, drift in any electric fields, nonlinear and linear quenching along the way, and competitive rates of capture on various things. Furthermore, recent research unveils the importance of electron temperature, especially in heavier halides with slow electron cooling which also make the best scintillators [2,3]. At this point we have already managed to handle thermalized diffusion and drift in the electric fields computationally, and major trends among oxides and semiconductors are reproduced [4]. In order to simulated the hot electron transport, we need the electron-temperature dependence of each of the constants in the master rate equation: diffusion $D(T_e)$, bimolecular exciton formation $B(T_e)$, 2^{nd} & 3^{rd} order quenching $K_2(T_e)$& $K_3(T_e)$, and linear trapping on shallow or "storage" sites, deep traps, and activators $S_1(T_e)$, $K_1(T_e)$, $A_1(T_e)$. The quenching rates can be extracted from z-scan [5]. We also have picosecond absorption [6] experiments for bimolecular exciton formation rate and capturing rates of different capturing centers. $D(T_e)$ is simulated with Monte Carlo codes in Refs. [3,7]. In

principle, we have all the information available to validate the model for some materials such as NaI and CsI with enough known parameters determined. The next step of the building up the toolkit is to use these parameters in a rate equation or Monte Carlo modeling as a function of carrier density. Such simulation will make predictions of the local light yield of the scintillators. The last step is to combine the simulated local light yield results and the GEANT4 data to simulate the SLYNCI data for each scintinllator. The toolkit for modeling scintillators contains the understanding of the fundamental physics of scintillator nonproportionality. Finite element method, Monte Carlo method, GEANT4, and first principles calculations are combined to make predictions of the electron response of scintillator without using any fitting parameter.

Future work is addressed in two main parts: the first part is to improve and complete the Monte Carlo and rate equation model for hot electrons and simulate the light yield for materials with known temperature dependent parameters mentioned above. To generalize and test the model, we would like to obtain the temperature dependent parameters for as many other scintillators as possible. The second part of the future work is to get these parameters from theoretical aspect. First principles calculations of the electronic structures of the different centers will be combined with multi-phonon capturing model in Ref. [8] in order to make predictions of the capturing rates/cross-sections of each capturing center. In addition, Fermi's golden rule can be quantitatively applied to electron/hole states well above/below CBM/VBM to get hot carrier quenching rates from first principles.

REFERENCES

[1] Lempicki, A. J. Wojtowicz, and E. Berman, "Fundamental limits of scintillator performance," Nucl. Instrum. Meth. A **333**, 304-311 (1993).

[2] Qi Li, Joel Q. Grim, K. B. Ucer, A. Burger, G. A. Bizarri, W. W. Moses, and R. T. Williams, Phys. Status Solidi RRL **6**, 346 (2012).

[3] Z. Wang, Y. Xie, B. D. Cannon, L. W. Campbell, F. Gao, and S. Kerisit, J. Appl. Phys. **110**, 64903 (2011).

[4] Q. Li, J. Q. Grim, R. T. Williams, G. A. Bizarri, and W. W. Moses, J. Appl. Phys. **109**, 123716 (2011).

[5] J. Q. Grim, K. B. Ucer, A. Burger, P. Bhattacharya, E. Tupitsyn, E. Rowe, V. M. Buliga, L. Trefilova, A. Gektin, G. A. Bizarri, W. W. Moses, and R. T. Williams, Phys. Rev. B **87**, 125117 (2013).R. T. Williams, J. Q. Grim, Q. Li, K. B. Ucer, and W. W. Moses, Physica Status Solidi (b) **248**, 426 (2011).

[6] K. B. Ucer, G. A. Bizarri, A. Burger, A. Gektin, L. Trefilova, and R. T. Williams, "Electron thermalization and trapping rates in pure and doped alkali and alkaline-earth iodide crystals studied by picosecond optical absorption," submitted to Phys. Rev. B (2014).

[7] Qi Li, J. Q. Grim, N. A. W. Holzwarth, and R. T. Williams, "A model of hot-electron thermalization in electron- and ultraviolet-excited CsI and SrI_2," presented at the International Conf. on Inorganic Scintillators and their Applications (SCINT 2013), Shanghai, April 2013.

[8] A. Alkauskas, Q. Yan, and C. G. Van de Walle, "First-principles theory of nonradiative carrier capture via multiphonon emission," presented in APS 2014, Denver.

APPENDIX I: AB INITIO ENERGETICS AND KINETICS STUDY OF H2 AND CH4 IN THE SI CLATHRATE HYDRATE

Qi Li, B. Kolb, G. Roman-Perez, J. M. Soler, F. Yndurain, L. Kong,
D. C. Langreth, and T. Thonhauser

This following manuscript is published in Phys. Rev. B (2011). Qi Li performed all first principle calculations with help from Brian Kolb and T. Thonhauser. The original manuscript was prepared by T. Thonhauser. Manuscript is reproduced with permission of American Physcis Society.

Ab initio energetics and kinetics study of H_2 and CH_4 in the SI clathrate hydrate

Qi Li,[1] Brian Kolb,[1] Guillermo Román-Pérez,[2] José M. Soler,[2] Felix Yndurain,[2] Lingzhu Kong,[3] D. C. Langreth,[3] and T. Thonhauser[1,*]

[1]*Department of Physics, Wake Forest University, Winston-Salem, North Carolina 27109, USA*

[2]*Departamento de Física de la Materia Condensada, Universidad Autónoma de Madrid, Cantoblanco, E-28049 Madrid, Spain*

[3]*Department of Physics and Astronomy, Rutgers University, Piscataway, New Jersey 08854, USA*

(Received 30 May 2011; revised manuscript received 22 September 2011; published 17 October 2011)

We present *ab initio* results at the density functional theory level for the energetics and kinetics of H_2 and CH_4 in the SI clathrate hydrate. Our results complement a recent article by some of the authors [G. Román-Pérez *et al.*, Phys. Rev. Lett. **105**, 145901 (2010)] in that we show additional results of the energy landscape of H_2 and CH_4 in the various cages of the host material, as well as further results for energy barriers for all possible diffusion paths of H_2 and CH_4 through the water framework. We also report structural data of the low-pressure phase SI and the higher-pressure phases SII and SH.

DOI: 10.1103/PhysRevB.84.153103 PACS number(s): 71.15.Mb, 66.30.je, 84.60.Ve, 91.50.Hc

Clathrate hydrates are crystalline, ice-like structures formed out of water molecules.[1] The water framework creates cavities in which gas molecules—typically O_2, H_2, CO_2, CH_4, Ar, Kr, Xe—can be trapped, which stabilize the framework. The existence of clathrates was first documented in 1810 by Sir Humphry Davy, and clathrates became the subject of intensive studies in the 1930s, when oil companies became aware that clathrates can block pipelines.[2] Nowadays, clathrate hydrates are of particular interest for two reasons: (i) they are formed naturally at the bottom of the ocean, where they are often filled with CH_4.[3] These deposits mean a tremendous stock pile of energy, while—at the same time—representing a possible global warming catastrophe if released uncontrolled into the environment through melting; (ii) clathrate hydrates can be used to store H_2 in its cavities and can be a viable hydrogen-storage material (albeit with moderate hydrogen-storage density).[4] For both cases, an understanding of the interaction between the guest molecule and the host framework is crucial for their formation and melting processes, which are still poorly understood.[5] In this brief report, we present results that elucidate this crucial guest-molecule/host-framework interaction and complement a recent paper by some of the authors.[6] We show additional results of the energy landscape of H_2 and CH_4 in the various cages of the host material, and we show further results for energy barriers for all possible diffusion paths of H_2 and CH_4 through the water framework. We also report structural data of the phases SI, SII, and SH.

At low pressure, the methane-filled clathrate forms the structure SI, consisting of two types of cages. The smaller cage is built of water molecules on the vertices of 12 pentagons with a diameter of approximately 7.86 Å,[7] and we refer to this as 5^{12} cage, or alternatively as *D* cage. The larger cage is built of 12 pentagons and 2 hexagons with a diameter of approximately 8.62 Å, and we call it $5^{12}6^2$ or *T* cage. The unitcell has cubic symmetry and consists of two 5^{12} and six $5^{12}6^2$ cages, with a total of 46 water molecules. At 250 MPa, the structure SI transforms into a new cubic phase SII, consisting of sixteen 5^{12} and eight $5^{12}6^4$ cages, containing 136 water molecules in its unitcell.[2] When the pressure is increased to 600 MPa, the structure undergoes another phase transition to the hexagonal phase SH.[2] This phase has a smaller unitcell of three 5^{12}, two $4^35^66^3$, and one $5^{12}6^8$ cages, with only 34 water molecules. Very nice graphical representations of the different cages and structures can be found in Refs. 2, 4, 6, and 8. While other clathrate-hydrate structures exist, structure SI, SII, and SH are the most common ones.[2]

Guest molecules such as H_2 and CH_4 in the cavities of the clathrate hydrates interact with the water framework through van der Waals forces. But even the water framework itself, i.e., the interaction of water molecules through hydrogen bonds, has a van der Waals component.[9] To capture these effects, we perform here density functional theory (DFT) calculations utilizing the truly nonlocal vdW-DF functional, which includes van der Waals interactions seamlessly into DFT.[10–12] We implemented vdW-DF using a very efficient FFT formulation[13] into the latest release of PWSCF, which is a part of the QUANTUM-ESPRESSO package.[14] For our calculations we used ultrasoft pseudopotentials with a kinetic energy cutoff for wave functions and charge densities of 35 and 280 Ry, respectively. A self-consistency convergence criterion of at least 1×10^{-8} Ry was used. All structures were fully optimized with respect to volume and atom positions, and the force convergence threshold was at least 10^{-4} Ry/a.u. for SI and SH. We have also performed structural calculations on SII, but—due to the large unit cell with 136 water molecules, i.e., 408 atoms—we used a slightly less tight force convergence criterium of 5×10^{-4} Ry/a.u. For SI and SH we used a $2 \times 2 \times 2$ Monkhorst-Pack k-mesh,[15] while for SII we performed Γ-point calculations only.

The empty cages are experimentally not stable, but they have been shown to be a good starting point for calculations like ours.[6] We have calculated the optimized lattice parameters for the SI, SII, and SH structures and the results are collected in Table I. We have also calculated the structures when filled with methane (one methane molecule per cage) and filled with hydrogen (up to four H_2 per cage), but the lattice parameters expand less than 0.1% upon filling, such that we have used the parameters for the empty cages henceforth. Overall, our optimized lattice constants agree well with previous calculations[6] and experiment.[8] In Table I we further analyze the structure of the host materials by calculating the

TABLE I. Calculated and experimental lattice constants a and c for the SI, SII, and SH clathrate hydrates. In addition, calculated and experimental average nearest-neighbor and next-nearest-neighbor distances are given, as well as bond angles. Standard deviations are provided in square brackets. Experimental values for the lattice constants are taken from Ref. 8 for methane-filled cages. Experimental values for the averaged quantities are calculated from the structures given in the supplemental materials of Ref. 8. The experimental distances d^{nn}_{O-H} (d^{nnn}_{O-H}) seem to be underestimated (overestimated), most likely due to the difficulty of accurately determining H positions in x-ray experiments. For SI, neutron scattering experiments suggest $d^{nn}_{O-H} = 0.97$ Å and $d^{nn}_{O-O} = 2.755$ Å.[16] Also note that there is some variation in the experimental results for the lattice constants in Refs. 1, 4, and 8.

		a [Å]	c [Å]	d^{nn}_{O-H} [Å]	d^{nnn}_{O-H} [Å]	d^{nn}_{O-O} [Å]	$\angle_{H-O-H}$[°]	$\angle_{O-O-O}$[°]
SI	Calc.	11.97	–	0.994 [0.001]	1.790 [0.014]	2.781 [0.013]	107.1° [1.0]	108.6° [4.0]
	Exp.	11.88	–	0.861 [0.031]	1.911 [0.022]	2.761 [0.017]	109.3° [3.0]	108.7° [3.7]
SII	Calc.	17.35	–	0.994 [0.001]	1.792 [0.016]	2.784 [0.016]	107.1° [0.6]	109.2° [4.3]
	Exp.	17.19	–	0.812 [0.016]	1.959 [0.025]	2.768 [0.013]	109.5° [2.0]	109.3° [4.0]
SH	Calc.	12.32	10.01	0.994 [0.001]	1.793 [0.015]	2.782 [0.011]	107.2° [0.9]	108.4° [8.5]
	Exp.	12.33	9.92	0.781 [0.040]	1.955 [0.022]	2.775 [0.005]	108.9° [5.1]	108.4° [8.3]

average nearest-neighbor and next-nearest-neighbor distances and important bond angles. In general, the calculated average distances and angles vary only insignificantly among SI, SII, and SH, whereas they show a slightly larger spread for some experimental values. As a side-note, for a single water molecule we calculate $d_{O-H} = 0.973$ Å and $\angle_{H-O-H} = 104.9°$, in good agreement with the experimental numbers of 0.958 Å and 104.5°.[17] Note that vdW-DF is known to give slightly too large binding distances.[18,19] Small deviations are visible in the distances d^{nn}_{O-H} and d^{nnn}_{O-H}, which in sum mostly cancel to give very good agreement with the experimental O–O distances. Reference 8 also gives the O–O distances for all structures explicitly as between 2.725 and 2.791 Å, in remarkable agreement with our calculations. Also, our calculated angles $\angle_{O-O-O}$ agree very well with experiment. However, the good agreement between oxygen distances and angles—which describe the structure as a whole—is closely related to the agreement for the lattice constants.

We next focus on the binding energies of guest molecules in the SI structure. In particular, we study the binding energies of CH_4 and H_2 in the D and T cages as a function of the number of molecules; results are depicted in Fig. 1 for calculations where molecules are added to only one cage in the unitcell, while all other cages are kept empty. Here, we define the binding energy as the energy difference between the "water-framework + guest-molecules" system minus the energy of the single constituents. In case of n-fold occupied cages, we subtract n times the energy of the single molecule. Methane is a large molecule compared to the cage sizes and it can be seen that in both D and T only one methane molecule can be stored. Upon adding another methane molecule, the binding energy increases drastically. The situation is different for the much smaller H_2 molecules. In the smaller D cage we can store up to two H_2 molecules, but increasing the number to three or four results in a positive binding energy; i.e., work is required to place more than two molecules into this cage. Note that the binding energy that we find for double H_2 occupancy is rather small, i.e., −8 meV/per molecule. It is, thus, likely that at nonzero temperatures cages are only singly occupied. Experimentally, while the majority of recent work seems to favor single occupancy of the D cages (see, e.g., Ref. 20), there are also reports that propose double occupancy or that find inconclusive evidence.[21–25] On the other hand, the larger T cage can store four H_2 molecules. If a fifth molecule is added, it escapes through one of the hexagonal faces into the neighboring, empty T cage. Our calculated H_2 storage capacity of four molecules in the T cages is in agreement with experiment.[4] The binding energy for one H_2 molecule compares well with quantum-chemistry calculations on isolated cavities, which give −0.123 eV.[21] Overall, our binding energies are slightly smaller than the ones in Ref. 6. Note that quantum motions have been neglected in our approach, which may play an important role in the binding process and when determining the cage occupancy. A more precise treatment requires the computation of the corresponding thermodynamic partition function, as, for example, shown in Ref. 26. Nevertheless, we consider our calculations for the binding energy an important first step that already reveals important information.

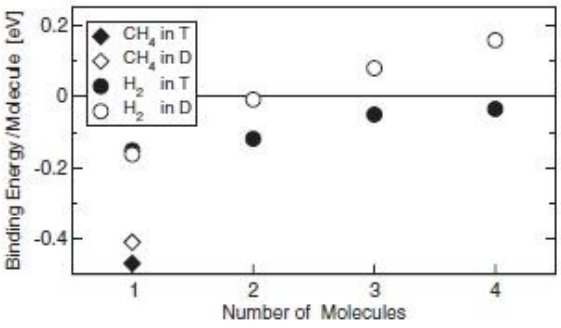

FIG. 1. Binding energies per molecule for different numbers of CH_4 and H_2 molecules in the D and T cages of SI. While the D and T cages can store only one CH_4 molecule, the D and T cage can store up to two and four H_2 molecules, respectively.

It is also interesting to study where and how the H_2 and CH_4 molecules bind in the cages. If only one molecule is present in the cages, it binds in the center of the cage. Rotations and small displacements of H_2 in that situation are on an energy scale of approximately 1 meV and approach the accuracy of our calculations. At room temperature, such

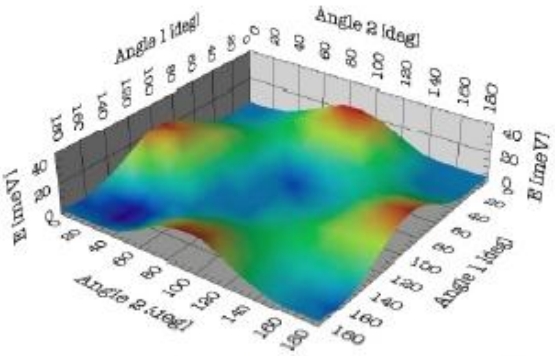

FIG. 2. (Color online) Energy landscape in meV for a rotating methane molecule in a D cage. The x and y axes correspond to rotations about two mutually perpendicular axes. At the (0,0) point of the plot, the hydrogen atoms of the methane point exactly toward four oxygens of the D cage. The difference between the minimum and maximum energy is 22 meV.

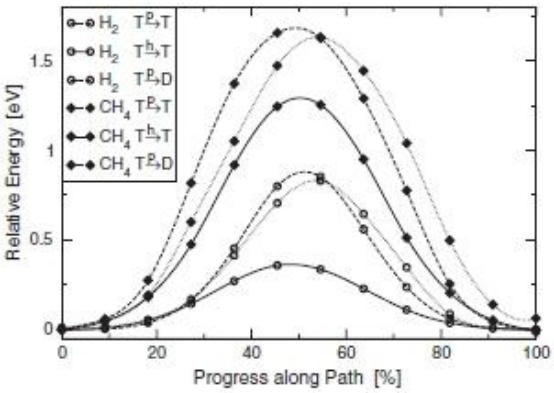

FIG. 3. Barriers to diffusion of H_2 and CH_4 through the water framework along different paths, as a function of the relative progress along the path. The plots are labeled as $A \xrightarrow{x} B$, where A is the type of the starting cage, B is the type of the ending cage, and x refers to either pentagon (p) or hexagon (h), indicating the opening being used for traversing. The symbols are the results from 12-image NEB calculations and the lines are fitted cubic splines, serving as a guide to the eye.

perturbations are thus easily thermally activated. Since the methane molecule is larger, it cannot move/rotate as easily. We have studied the rotation of a single methane molecule centered in the D and T cages as a function of rotation about two mutually perpendicular axes. The energy landscape for this rotation is depicted in Fig. 2 for the D cage. The D cage with its 12 pentagons and the methane molecule have a related symmetry, which allows us to choose the (0,0) point of the plot such that all methane hydrogens point exactly to an oxygen of the host lattice. At this point, hydrogen bonds are created and the total energy is the lowest. Upon rotation of the methane, the hydrogen bonds break and the energy increases. The difference between the lowest and highest point of this energy landscape is 22 meV, suggesting thermal activation of rotations at room temperature and quantifying an experimental assumption.[8] We have also studied the rotation of a methane molecule in a T cage and the results are very similar to the results presented in Fig. 2, with the difference that the maximal energy barrier is slightly smaller, i.e., 18 meV, which is not surprising, as the T cage is slightly larger and the methane molecule can rotate more easily. Calculations for both rotation-energy landscapes have independently also been performed using SIESTA[27,28] and give essentially identical results.

Finally, we present results for barriers to diffusion through the water framework in the SI structure. In the case of H_2 and hydrogen storage this is of much interest, as practical storage solutions require fast kinetics, i.e., low barriers. In the case of CH_4, the barriers can help us understand the natural formation of the filled clathrates. We have calculated the barriers to diffusion with nudged elastic band (NEB) calculations, using 12 images along the path from the center of one cage to the center of the next cage; the results for all possible paths are plotted in Fig. 3. Note that the relaxation of the host lattice is crucial to obtain accurate barrier energies,[6] and NEB calculations allow for such relaxations perpendicular to the path automatically. The plots are labeled as $A \xrightarrow{x} B$, where A is the type of the starting cage, B is the type of the ending cage, and x refers to either pentagon (p) or hexagon (h), indicating the opening being used for traversing. Note that for the path $T \xrightarrow{p} D$ there is only one choice of opening, i.e., a pentagon, and the path is not symmetric as the distance from the center of T to its edge is longer than the corresponding distance in the D cage. Furthermore, this path's end energy is different from its starting energy, since the guest molecules are binding with different binding energies in the cages T and D, as already evident from Fig. 1. The lowest barriers for H_2 and CH_4 diffusion agree well with previous calculations.[6,29] But, our H_2 diffusion barrier is an overestimation with respect to a recent NMR experiment, which gives 0.03 eV and warrants further investigation.[30] The barriers are in general smaller for diffusion through hexagons, simply because these openings are larger.

For hydrogen-storage applications, the low barrier of ~0.3 eV between T cages (going through a hexagon) is important. Through these T-cage channels, which thread through the material in all three dimensions, the hydrogen can quickly be absorbed or released. However, to achieve the material's full storage potential, some hydrogen molecules will also have to get into the D cages, with a much higher barrier of ~0.75 eV. The large barrier of ~1.4 eV for methane diffusion suggests that the methane molecules get trapped while the clathrate is formed, rather than diffusing into an already existing empty clathrate.

To conclude, we have performed an *ab initio* study of structural, energetic, and kinetic properties of the guest molecules H_2 and CH_4 in hydrate clathrates. We have also shown first results for the difficult-to-model, high-pressure phase SII with a large unit cell, finding good agreement with experiment. While we have used vdW-DF for our study, it is conceivable that its successor, vdW-DF2,[19] may further

improve upon our results. We encourage additional studies of the hydrate clathrates using vdW-DF2, also including other types of cages, and more detailed studies of the SII phase, which is one of the more promising phases among the hydrate clathrates for hydrogen-storage applications.

We would like to dedicate this report to the memory of Professor David Langreth, who passed away just days before it was submitted—he is the "father" of vdW-DF and his research inspired many. All calculations were performed on the WFU DEAC cluster.

*thonhauser@wfu.edu

[1]E. D. Sloan and C. A. Koh, *Clathrate Hydrates* (CRC, Boca Raton, 2008).
[2]W. L. Mao, C. A. Koh, and E. D. Sloan, Phys. Today **60**, 42 (2007).
[3]B. Buffett and D. Archer, Earth Planet. Sci. Lett. **227**, 185 (2004).
[4]V. V. Struzhkin, B. Militzer, W. L. Mao, H.-k. Mao, and R. J. Hemley, Chem. Rev. **107**, 4133 (2007).
[5]S. Gao, W. House, and W. G. Chapman, J. Phys. Chem. B **109**, 19090 (2005).
[6]G. Román-Pérez, M. Moaied, J. M. Soler, and F. Yndurain, Phys. Rev. Lett. **105**, 145901 (2010).
[7]Here, we define the diameter as twice the average distance between oxygen atoms and the cage center.
[8]M. T. Kirchner, R. Boese, W. E. Billups, and L. R. Norman, J. Am. Chem. Soc. **126**, 9407 (2004).
[9]B. Kolb and T. Thonhauser, Phys. Rev. B **84**, 045116 (2011).
[10]M. Dion, H. Rydberg, E. Schröder, D. C. Langreth, and B. I. Lundqvist, Phys. Rev. Lett. **92**, 246401 (2004); **95**, 109902(E) (2005).
[11]T. Thonhauser, V. R. Cooper, S. Li, A. Puzder, P. Hyldgaard, and D. C. Langreth, Phys. Rev. B **76**, 125112 (2007).
[12]D. C. Langreth *et al.*, J. Phys. Condens. Mattter **21**, 084203 (2009).
[13]G. Román-Pérez and J. M. Soler, Phys. Rev. Lett. **103**, 096102 (2009).
[14]P. Giannozzi *et al.*, J. Phys. Condens. Matter **21**, 395502 (2009).
[15]H. J. Monkhorst and J. D. Pack, Phys. Rev. B **13**, 5188 (1976); J. D. Pack and H. J. Monkhorst, *ibid.* **16**, 1748 (1977).
[16]C. Gutt, B. Asmussen, W. Press, M. R. Johnson, Y. P. Handa, and J. S. Tse, J. Chem. Phys. **113**, 4713 (2000).
[17]G. Graner, E. Hirota, T. Iijima, K. Kuchitsu, D. A. Ramsay, J. Vogt, and N. Vogt, *2 Inorganic Molecules. Part 4*, K. Kuchitsu, (ed.), SpringerMaterials—The Landolt-Börnstein Database [http://www.springermaterials.com]. DOI: 10.1007/10529543_6.
[18]T. Thonhauser, A. Puzder, and D. C. Langreth, J. Chem. Phys. **124**, 164106 (2006).
[19]K. Lee, E. D. Murray, L. Kong, B. I. Lundqvist, and D. C. Langreth, Phys. Rev. B **82**, 081101(R) (2010).
[20]K. A. Lokshin, Y. Zhao, D. He, W. L. Mao, H.-K. Mao, R. J. Hemley, M. V. Lobanov, and M. Greenblatt, Phys. Rev. Lett. **93**, 125503 (2004).
[21]S. Patchkovskii and J. S. Tse, Proc. Nat. Acad. Sci. USA **100**, 14645 (2003).
[22]T. M. Inerbaev, V. R. Belosludov, R. V. Belosludov, M. Sluiter, and Y. Kawazoe, Comput. Mater. Sci. **36**, 229 (2006).
[23]F. Sebastianelli, M. Z. Xu, Y. S. Elmatad, J. W. Moskowitz, and Z. Bacic, J. Phys. Chem. C **111**, 2497 (2007).
[24]L. J. Florusse, C. J. Peters, J. Schoonman, K. C. Hester, C. A. Koh, S. F. Dec, K. N. Marsh, and E. D. Sloan, Science **306**, 469 (2004).
[25]J. Wang, H. Lu, J. A. Ripmeester, and U. Becker, J. Phys. Chem. C **114**, 21042 (2010).
[26]S. Patchkovskii and S. N. Yurchenko, PhysChemChemPhys **6**, 4152 (2004).
[27]J. M. Soler, E. Artacho, J. D. Gale, A. Garcia, J. Junquera, P. Ordejón, and D. Sánchez-Portal, J. Phys. Condens. Matter **14**, 2745 (2002).
[28]P. Ordejón, E. Artacho, and J. M. Soler, Phys. Rev. B **53**, R10441 (1996).
[29]S. Alavi and J. A. Ripmeester, Angew. Chem. **119**, 6214 (2007).
[30]T. Okuchi, I. L. Moudrakovski, and J. A. Ripmeester, Appl. Phys. Lett. **91**, 171903 (2007).

APPENDIX II: A THEORETICAL STUDY OF THE HODROGEN-STORAGE POTENTIAL OF $(H_2)_4CH_4$ IN METAL ORGANIC FRAMEWORK MATERIALS AND CARBON NANOTUBES

Qi Li and T. Thonhauser

This following manuscript is published in "special issue on Van der Waals interactions in advanced materials" in J. Phys.: Condens. Matter (2012). Qi Li performed all first principle calculations. Manuscript is reproduced with permission of Institute of Physics. Qi Li and T. Thonhauser analyzed the results and prepared the manuscript.

IOP PUBLISHING JOURNAL OF PHYSICS: CONDENSED MATTER

J. Phys.: Condens. Matter **24** (2012) 424204 (8pp) doi:10.1088/0953-8984/24/42/424204

A theoretical study of the hydrogen-storage potential of $(H_2)_4CH_4$ in metal organic framework materials and carbon nanotubes

Q Li and T Thonhauser

Department of Physics, Wake Forest University, NC 27109, USA

E-mail: thonhauser@wfu.edu

Received 4 February 2012, in final form 26 February 2012
Published 3 October 2012
Online at stacks.iop.org/JPhysCM/24/424204

Abstract

The hydrogen–methane compound $(H_2)_4CH_4$—or for short H4M—is one of the most promising hydrogen-storage materials. This van der Waals compound is extremely rich in molecular hydrogen: 33.3 mass%, not including the hydrogen bound in CH_4; including it, we reach even 50.2 mass%. Unfortunately, H4M is not stable under ambient pressure and temperature, requiring either low temperature or high pressure. In this paper, we investigate the properties and structure of the molecular and crystalline forms of H4M, using *ab initio* methods based on van der Waals DFT (vdW-DF). We further investigate the possibility of creating the pressures required to stabilize H4M through external agents such as metal organic framework (MOF) materials and carbon nanotubes, with very encouraging results. In particular, we find that certain MOFs can create considerable pressure for H4M in their cavities, but not enough to stabilize it at room temperature, and moderate cooling is still necessary. On the other hand, we find that all the investigated carbon nanotubes can create the high pressures required for H4M to be stable at room temperature, with direct implications for new and exciting hydrogen-storage applications.

(Some figures may appear in colour only in the online journal)

1. Introduction

The use of hydrogen as an environmentally clean and efficient fuel for mobile applications is a very active research area. But, before a future hydrogen economy can become reality, several crucial challenges need to be addressed, mostly concerning the storage of hydrogen itself [1]. The most important challenges for a practical hydrogen-storage system are: (i) high gravimetric and volumetric storage density (the fuel tanks should be light and small); (ii) good thermodynamics (the hydrogen adsorption/desorption should occur at a reasonable pressure and temperature); and (iii) fast reaction kinetics (tank emptying and refilling should be fast). According to the Department of Energy, addressing these key elements through fundamental research is imperative to achieving a practical hydrogen economy [2]. In this paper we present results that address the gravimetric and volumetric storage density.

A wide variety of materials have been considered as possible hydrogen-storage materials [3–6] (see [7] for a graphical representation of how many articles have been written on the subject). However, amongst all these materials, $(H_2)_4CH_4$—or for short H4M—shows exceptional promise [8]; the H4M system is extremely rich in molecular hydrogen, containing 33.3 mass% molecular hydrogen, not counting the atomic hydrogen in CH_4; including it, we reach even 50.2 mass%. Simply said, H4M holds more hydrogen per mass and volume than any known material except pure hydrogen itself! Unfortunately, H4M is not stable under ambient pressure and temperature. The stability field is reported from approximately 5.8 GPa at room temperature to 10 K for ambient pressure [9, 10], and it has been

shown that moderate cooling can reduce the required pressure significantly [11]. This fact led us to design a novel host + H4M structure in which the host material provides the necessary pressure for H4M to be stable, without the need for excessive cooling. The use of a host material will lower the exceptional volumetric and gravimetric hydrogen-storage density of H4M—it is the main goal of this paper to quantify the tradeoff between lower storage density and stability at closer-to-ambient temperature and explore whether it is worth pursuing.

Since H4M is stable at room temperature under a pressure of 5.8 GPa, we are most interested in this region of the phase diagram and throughout the paper we report results at this pressure. We first consider H4M in nanoporous metal organic framework (MOF) materials [12–15], which provide significant pressure inside their cavities to stabilize H4M. We study MOFs that are isoreticular to (i.e. have the same network topology as) MOF-5, with varying linker length. We find that these MOFs all provide enough pressure to significantly decrease the burden of cooling, but none of them stabilize H4M at room temperature. As a second host material, we consider single-wall carbon nanotubes (CNTs) [16], which are well known for being able to provide high pressure inside their cavities. Specifically, we study zigzag nanotubes with chirality from (10, 0) to (26, 0) and corresponding radii from 4 to 10 Å—while larger nanotubes with radii up to several nanometers can be produced in experiments [17], such systems together with H4M filling inside are, at the moment, not accessible through *ab initio* simulations. Our calculations show that crystalline H4M may be stabilized at room temperature inside nanotubes, opening the door for high-efficiency hydrogen-storage applications.

This paper is organized as follows: after presenting computational details in section 2, we show results for the structure of H4M in its molecular and crystalline forms in section 3. Results for H4M inside the cavities of MOFs and nanotubes are presented in sections 4 and 5, respectively. We conclude and suggest future research in section 6.

2. Computational details

H4M is classified as a van der Waals compound [9]. The study of nanotube interactions [18] and binding of small molecules in MOFs [19] is also strongly determined by van der Waals interactions. As such, an accurate description of van der Waals interactions in these systems is crucial. Thus, we use the recently developed van der Waals density functional (vdW-DF), a truly nonlocal exchange and correlation functional, that incorporates van der Waals forces self-consistently and seamlessly into DFT [20–22]. The vdW-DF approach has shown good transferability for a range of van der Waals systems reaching from simple dimers [23] and physisorbed molecules [24] to DNA [25] and drug design [26]. In particular, it has been applied successfully to answer questions regarding hydrogen storage [27], MOFs [19], and nanotubes [18].

For our calculations we use density functional theory, as implemented in the PWSCF code, which is part of the QUANTUM-ESPRESSO package [28]. We utilize ultrasoft pseudopotentials with a wavefunction cutoff of 475 eV (5700 eV charge-density cutoff) for carbon nanotube related systems and 475 eV (3800 eV charge-density cutoff) for all other cases. A self-consistency convergence criterion of at least 1.4×10^{-7} eV is used. All structures are relaxed until all force components are less than 2.5 meV Å^{-1}. Due to the limitation of calculation size, and the fact that larger MOFs provide less pressure anyway, only the smallest MOF structures are investigated, using a $2 \times 2 \times 2$ Monkhorst–Pack **k**-mesh [29]. For simulations of crystalline H4M itself, we use a $4 \times 4 \times 4$ **k**-mesh. All carbon nanotube related systems are simulated as infinitely long hexagonal nanotube arrays with varying radius/distance, comprised of a short unit cell length in the z-direction, using a $1 \times 1 \times 16$ **k**-mesh. Single molecule calculations on H4M molecules are performed in a $16 \times 16 \times 16$ Å^3 cubic unit cell.

3. Structure of H4M

Although H4M under pressure has been investigated by x-ray diffraction [10], the actual microscopic structure of crystalline H4M remains unknown [9]. The x-ray diffraction experiments suggest a body-centered tetragonal structure [10] and Raman experiments provide further constraints [9]. Here, starting from these experimental guidelines, we report results for *ab initio* calculations of the molecular and crystalline H4M structures. We use a bottom-up approach, where we first find the optimal structure for H4M molecules, which we then assemble to form solids with various symmetries.

3.1. Structure of molecular H4M

We start by investigating the structure of a single H4M molecule. After relaxing the molecule, starting from a variety of initial positions, we always find the same optimal structure: the molecule forms two tetrahedra, sharing the same center with opposite directions. The common center is the carbon atom of the methane molecule, which forms the small tetrahedron. The four hydrogen molecules form a larger tetrahedron, each of them located on one of the vertices, and oriented so that they point to the central carbon atom of the methane. We find the C–H bond of the methane molecule to be 1.091 Å, the H–H bond of the hydrogen molecules to be 0.742 Å, and the distance from the central carbon atom to the closer hydrogen atom of the hydrogen molecules to be 3.295 Å. The optimized structure of the H4M molecule is depicted in figure 1.

In table 1, we list the binding energies as a function of the number of H_2 molecules bound to the central CH_4 molecule. Here, the binding energy is defined as $E_{\text{bind}} = E[(H_2)_n CH_4] - E[CH_4] - n\,E[H_2]$ for the case of n H_2 molecules bound to the CH_4 molecule. We can see that an increase in the number of H_2 molecules leads to an increase in binding energy per H_2 molecule, due to the additional interaction of H_2 molecules. We also report the incremental absorption energy, i.e. the work to absorb each new H_2 molecule. The increasing magnitudes in both columns validate the stability of the H4M molecule.

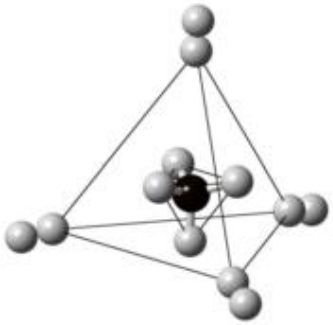

Figure 1. Optimized structure of a single H4M molecule $(H_2)_4CH_4$. The methane molecule forms a small tetrahedron, which sits inside a large tetrahedron formed by the hydrogen molecules. The axes of all hydrogen molecules point toward the centers of the faces of the methane tetrahedron.

Table 1. Binding energies E_{bind} (meV) of H_2 in $(H_2)_nCH_4$ as a function of the number of H_2 molecules attached. We also report the incremental absorption energy $E_{\text{abs}}^{\text{inc}}$ (meV), i.e. the work to absorb each new H_2 molecule.

n	E_{bind}	E_{bind}/H_2	$E_{\text{abs}}^{\text{inc}}$
1	−19.50	−19.50	−19.50
2	−39.58	−19.79	−20.08
3	−60.33	−20.11	−20.75
4	−81.36	−20.34	−21.03

At this point, it is instructive to pause for a moment and analyze the performance of vdW-DF in H4M, the structure and binding of which is very much determined by van der Waals forces. Since this molecule is small enough, we can compare here with the highest level of quantum chemistry. To this end, we have calculated the binding energy of four H_2 molecules to methane—i.e. the last row of table 1—using various approaches and exchange–correlation functionals. As reference, we use MP2 and CCSD(T) calculations, using the aug-cc-pVDZ basis set with counterpoise corrections. For the binding energy we find −85.93 meV with MP2 and −87.75 meV with CCSD(T). These reference numbers are now to be compared with DFT calculations. Using standard LDA [30], we find a very strong erroneous overbinding of −194.37 meV, not untypical when applying LDA to small molecules with van der Waals binding [31]. On the other hand, a standard PBE [32] calculation gives a large erroneous underbinding of only −36.65 meV. From these results it is clear that a simple H4M molecule is a very delicate system that is very much influenced by van der Waals interactions and thus an ideal application for vdW-DF. The corresponding binding energy with vdW-DF is −81.36 meV, in almost perfect agreement with high-level quantum chemistry. These results show that standard functionals such as LDA and PBE are not suited to describe the binding of H4M itself and much less so to study the H4M crystal structure or its properties inside MOFs and nanotubes; thus, in the following we will only report results for vdW-DF.

It is also worth mentioning at this point that vdW-DF is responsible for a small but significant charge transfer; in fact, it seems that vdW-DF is self-consistently rearranging the charge density just right, resulting in the excellent binding energy. Such charge transfers caused by vdW-DF are typically very small, i.e. of the order of 10^{-4} electrons Å^{-3}, where electronic charge gets accumulated between the constituents. A nice presentation of this charge transfer due to van der Waals binding is given in figure 8 of [21].

3.2. Structure of crystalline H4M

It is a complicated task to find the true crystalline structure for H4M. In principle, one should use an approach such as the *ab initio* random structure search (AIRSS) algorithm [33]—which generates random structures biased on chemistry, experimental, and symmetry grounds—to sample the corresponding large phase space. Here, however, we make use of experimentally suggested symmetries [9, 10] and an already existing semiclassical sampling of a large number of possible configurations [34].

Since Somayazulu *et al* suggested a body-centered tetragonal (BCT) structure (with some uncertainty) based on x-ray diffraction patterns [10], research on the precise structure of crystalline H4M seems to have subsided. Fifteen years later, Mao *et al* found a simple orthorhombic unit cell for crystalline H4M from a combined semiclassical/DFT approach by randomly arranging atoms, which resulted in a good agreement between calculated and experimental XRD spectra [34]. They found an optimized unit cell of 332 Å^3 with four H4M molecules, resulting in a molecular hydrogen volumetric density of 0.16 kg H_2/L, in disagreement with their previously published number, which was almost twice as large [8]—which we thus believe to be an error.

Using the above information as a starting point, we generate seven closely related possible unit cells with an H4M molecule as a building block (using the molecular structure described above), i.e. simple/body-centered/face-centered cubic (SC/BCC/FCC), simple/body-centered/face-centered orthorhombic (SO/BCO/FCO), and body-centered tetragonal (BCT). For all seven structures, we internally (atom positions) and externally (unit cell parameters) optimize the unit cells and determine the optimal ratios between the lengths of their edges (b/a and c/a) without pressure; the corresponding results are listed in table 2. Then, we add hydrostatic pressure by changing the cell parameter a, while keeping b/a and c/a constant, and relaxing the atom positions again for each volume. Application of the exact conditions of hydrostatic pressure requires knowledge of all corresponding elastic constants, but test calculations show that H4M is close to isotropic, such that the uniform scaling of all lattice constants is a good approximation[1]. The resulting energy versus volume curves are fitted using a Murnaghan equation of state, enabling us to analyze the structures and their pressure dependence in detail; results are shown in figure 2.

[1] For example, the SO unit cell is almost tetragonal—see table 2—and our calculations show that the corresponding elastic constants c_{22} and c_{33} differ only by a few per cent, while c_{33} differs by about 10%. The numbers are similar for other symmetries.

Table 2. Lattice constant a (Å) and corresponding ratios b/a and c/a for crystalline H4M in various symmetries.

Symmetry	a @ 5.8 GPa	a @ 0 GPa	b/a	c/a
FCC	7.119	9.089	1	1
BCC	5.636	7.166	1	1
FCO	7.791	9.865	0.897	0.843
SC	4.449	5.684	1	1
BCO	6.162	7.741	0.976	0.776
BCT	6.056	7.628	1	0.795
SO	5.174	6.567	0.798	0.784

As can be seen, the BCO and BCT curves are very close to each other due to the similarity of their structures, and they have the lowest energies at zero pressure. However, as the pressure increases, they cross with the SO curve, indicating a pseudo-phase transformation at around 1.8 GPa. At 5.8 GPa—the pressure at which H4M is experimentally stable at room temperature—SO has the smallest volume and slightly higher energy than BCO/BCT. Since at zero temperature the condition for the stable structure at constant pressure is that enthalpy ($H = E + PV$) be minimum [35], we conclude that the SO structure is favored at 5.8 GPa, in agreement with Mao *et al* [34]. The corresponding results for zero pressure and a pressure of 5.8 GPa are listed in table 3. It is striking to see how 'soft' this material is, as is evident by the tremendous volume change upon applying 5.8 GPa of pressure, as is expected for a van der Waals crystal.

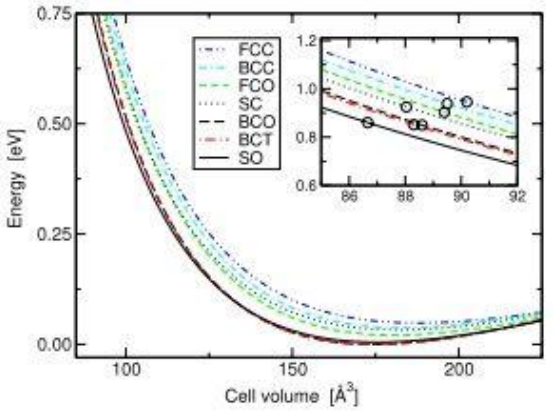

Figure 2. Energy versus volume curve for seven possible symmetries of the H4M crystal. The circles in the small inset indicate the 5.8 GPa point of each structure. Energies are plotted relative to the SO energy at zero pressure.

4. H4M in MOFs

With the H4M crystal structure, we are now ready to position H4M into external host materials, in the hope of stabilizing it at reasonable temperatures. We begin by investigating the possible pressure range that several common MOF materials exhibit. For our study, we limit ourselves to three MOFs of different sizes. The smallest MOF we include is MOF-5, consisting of Zn–O–C clusters at the corners, connected through one benzene linker in a cubic symmetry, depicted in figure 3. From this starting structure, larger MOFs can be built by simply making the chain of benzene linkers longer, while keeping the network topology the same. Such MOFs are referred to as isoreticular, and we have selected irMOF-10 (the linker chain contains two benzene rings) and irMOF-16 (the linker chain contains three benzene rings). For a nice graphical representation and further details of the three MOFs under investigation, see [15]. As the starting point for the three MOF structures, we use experimental atom positions from the supplementary materials of [15].

MOFs can have very large unit cells with hundreds of atoms, which—together with hundreds of atoms from the H4M filling—can quickly render *ab initio* calculations impractical. In order to still be able to make quantitative statements, we begin by investigating empty MOFs and the pressure they can create in their cavities. With the knowledge gained about MOF strength, we estimate their performance when filled with H4M. We verify the results with one full *ab initio* calculation on a small, but complete system of MOF + H4M.

First, we investigate the strength of the bond between the Zn–O–C cluster corners and the connected benzene linker. Knowledge of the strength of this bond allows us to estimate the pressure the MOF can withstand in its cavity. To this end, we perform total energy calculations in which we pull the benzene ring away from the cluster. We keep the structure in the x and y directions constant, and move the benzene ring along the z-axis. To accommodate this, we construct a new tetragonal unit cell with the same cell parameter in the x and y directions (12.916 Å) as the relaxed cubic MOF-5

Table 3. Volume V (Å^3), volumetric hydrogen density ρ_{vol} (kg H_2/L), energy E (meV), and enthalpy H (meV) of crystalline H4M for various symmetries. Energies are reported relative to the values for the SO structure.

	@ 5.8 GPa				@ 0 GPa		
Symmetry	V	ρ_{vol}	E	H	V	ρ_{vol}	E
FCC	90.19	0.1473	88.2	215.9	187.68	0.0708	42.8
BCC	89.49	0.1484	80.5	182.9	184.01	0.0722	32.0
FCO	89.40	0.1486	44.4	143.6	181.47	0.0732	15.4
SC	88.04	0.1509	65.1	114.9	183.62	0.0723	27.4
BCO	88.59	0.1499	−8.1	61.7	175.63	0.0756	−5.3
BCT	88.31	0.1504	−7.3	52.1	176.45	0.0753	−5.3
SO	86.67	0.1533	0.0	0.0	177.16	0.0750	0

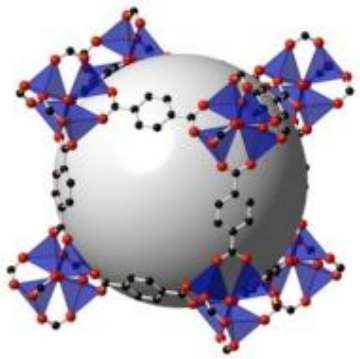

Figure 3. The structure of MOF-5. The unit cell consists of 424 atoms (for clarity hydrogen atoms are not displayed). The Zn–O–C clusters at the corners are connected through one benzene linker. The sphere in the middle serves as a measure for the size of the cavity—we refer to the radius of this sphere as the fixed radius. The free radius is defined as the radius of the largest sphere that fits through the aperture.

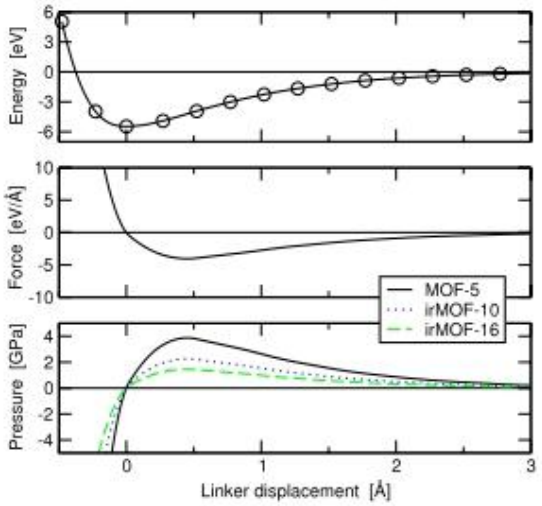

Figure 4. Energy and calculated force/pressure versus benzene ring displacement in the z-direction of simulated MOF-5. The energy is plotted relative to the energy of the completely separated Zn–O–C cluster and benzene ring. In the upper panel, open circles indicate the *ab initio* results; the solid lines are spline fittings.

structure, but with an elongated z-edge with a c/a value of 2.2. This allows us to move the benzene ring several Å, while always keeping a minimum distance of at least 8 Å to the Zn–O–C cluster in the next unit cell. The side of the benzene that would usually connect to the next corner is hydrogen terminated. Throughout the calculations, the relative positions of the atoms in the Zn–O–C cluster and the benzene rings are fixed; the only element that changes is the relative distance between the Zn–O–C cluster and the benzene ring in the z-direction. Results for the total energy versus benzene ring displacement are plotted in the upper panel of figure 4. The force is then calculated by the energy derivative and is plotted in the middle panel of figure 4. From this, we can estimate the possible pressure that MOF-5 can create, as the pressure is the ratio between the force and the area of the square in the cubic unit cell. Note that the connection of the benzene ring to the Zn–O–C clusters at the corners is the same for MOF-5, irMOF-10, and irMOF-16. As such, the energy versus benzene ring displacement plot allows us to estimate the pressure for all three MOFs. Simple test calculations show that the bond between two benzene rings in longer linkers is slightly stronger than the bond between the Zn–O–C cluster and the first benzene ring. In other words, the bond between the Zn–O–C cluster and the first benzene ring breaks before the bond between two benzene linkers. Thus, the corresponding pressures in irMOF-10 and irMOF-16 can easily be estimated by dividing by their corresponding (larger) areas. The pressures, as a function of benzene ring displacement, estimated in this way are depicted in the lower panel of figure 4. The zero point on the horizontal displacement axis indicates the position at which the benzene linker sits in the optimized zero-pressure unit cell. The maximum pressure in the case of MOF-5 is 3.9 GPa, close to the required H4M storage pressure at room temperature. The larger host materials irMOF-10 and irMOF-16 can still produce maximum pressures of 2.3 GPa and 1.5 GPa, respectively, before they break.

We next investigate the possible storage of H4M in these MOF systems. The free and fixed diameters (see figure 3 for a definition of these terms) of the pores in MOF-5 have been reported as 11.2 Å and 18.6 Å, respectively [15]. Since the diagonal length of our calculated SO H4M structure at 5.8 GPa is 7.7 Å, we insert a $2 \times 2 \times 2$ compressed H4M supercell into the pores of MOF-5. The MOF-5 structure itself has 424 atoms; fully filled with the H4M supercell, this corresponds to more than 1000 atoms. Since this is computationally too demanding, we only fill one pore (out of eight) per unit cell, resulting in a 528 atom unit cell. We then perform *ab initio* calculations on this system and find that the unit cell experiences a pressure of 3.9 GPa (the fact that this number is the same as the corresponding maximum pressure in table 4 is accidental). This pressure is lower than the 5.8 GPa compacted H4M supercell that is inserted, simply because the cavity is slightly larger than the H4M supercell. When we further let all atoms relax again in this structure, we find that the unit cell stabilizes at approximately 1 GPa. Note that, upon relaxation, we find only minimal changes in the atom positions of both the MOF and the inserted H4M.

Based on the estimations from above, in table 4, we list the theoretical performance of H4M storage in MOF-5, irMOF-10, and irMOF-16. Since the pore size should be approximately commensurate with the unit cell size of crystalline H4M, we can estimate a possibly largest H4M supercell that would fit in each pore, according to the pore diameters [15]. From that, we calculate the hydrogen mass density—including and not including the hydrogen in CH_4. In addition, with knowledge of the experimentally determined stability field [9] and the possible maximum pressure from above, we estimate to what temperature the systems need to be cooled for the H4M to be stable. Overall, there is a tradeoff

Table 4. Performance of different MOFs as hosts for H4M. The data given are MOF type, free and fixed pore diameter (Å), maximum commensurate size of the H4M supercell for filling, hydrogen mass density ρ_{mass} (mass%) with and without the hydrogen in CH_4, maximum pressure P achievable (GPa), and temperature T (K) to which the system needs to be cooled to stabilize H4M.

System	Free	Fixed	Filling	$\rho^{\text{w}}_{\text{mass}}$	$\rho^{\text{w/o}}_{\text{mass}}$	Max. P	T
MOF-5	11.2	18.6	$2 \times 2 \times 2$	10.0	6.7	3.9	224
irMOF-10	15.4	24.5	$3 \times 3 \times 3$	19.5	13.0	2.3	172
irMOF-16	19.1	28.8	$3 \times 3 \times 3$	15.3	10.2	1.5	126
Pure H4M	—	—	—	50.2	33.3	—	10

between the cooling required and the mass density—the higher the hydrogen mass density is, the more cooling is required. Even though none of those three MOFs stabilize H4M at room temperature, these results are promising: experimentally, pure hydrogen gas absorption using MOF-5 can reach a maximum mass density of 4 mass% [13], while our calculated hydrogen mass density—using H4M as a guest molecule—is significantly higher. This result is related to the fact that most of the pure hydrogen molecules physisorb on the inside walls of the pores, while using H4M makes more efficient use of the entire pore volume.

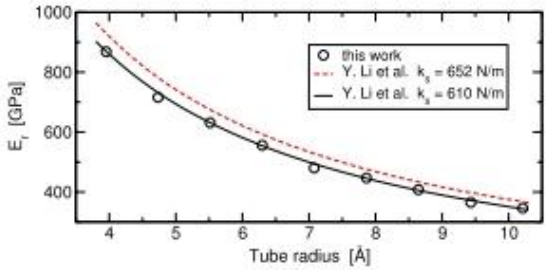

Figure 5. Calculated radial Young's moduli for nanotubes of different sizes.

5. H4M in nanotubes

Nanotubes have been studied extensively and it is well known that they have extraordinary electronic and physical properties [16]. In particular, nanotubes have exceptionally high stiffness and strength and hence the ability to withstand large elastic strains [36, 37]. In the following, we investigate whether carbon nanotubes can provide the necessary pressure to stabilize H4M. We consider zigzag single-wall carbon nanotubes—since they are semiconducting and thus easier to model—with chirality (n, m) ranging from (10, 0) to (26, 0), corresponding to radii from 4 to 10 Å. While larger nanotubes with radii of up to several nanometers can be produced in experiments [17], the filling of such systems with H4M is currently not accessible through *ab initio* simulations, due to the large number of atoms. Similarly to the case of H4M in MOFs, we first model empty nanotubes to find their elastic properties and then investigate their loading with H4M through suitable approximations. Again, we verify our results by one *ab initio* calculation on a small, but complete system of CNT + H4M.

5.1. Radial Young's modulus and strain of carbon nanotubes

The property of most interest to us is the Young's modulus, as it is closely related to the pressure resulting from a small perturbation to the tube's radius. Since the axial Young's modulus has been determined to be 1 TPa [37, 38], we focus on the radial Young's modulus here. We start from the properties of isolated carbon nanotubes, modeling them with a minimum wall-to-wall separation of at least 8 Å. The radial Young's modulus E_r in a hydrostatic pressure model is given by

$$\Delta U_e = \frac{E_r A_0 \Delta r^2}{2 r_0}, \tag{1}$$

where ΔU_e is the relative strain energy, A_0 and r_0 are the original cross-section and radius, and Δr is the amount by which the radius changes. For each nanotube, we first relax the structure and then perform five self-consistent calculations varying the tube radius by 0%, ±0.5%, and ±1%. As expected, ΔU_e and Δr satisfy a quadratic relation in a small vicinity of r_0, allowing us to calculate E_r for each nanotube. Our results are depicted in figure 5, together with recently reported results from analytical calculations [39], where the following fit for E_r of zigzag carbon nanotubes has been found:

$$E_r = \frac{2 n k_s \sin^2(\pi/n)}{3\pi b}. \tag{2}$$

Here, n, b, and k_s refer to the chirality $(n, 0)$, the C–C bond length (in our case 1.42 Å), and the stretching force constant of the covalent bond. The comparison of our results to the results of Li *et al* [39] is already very good, but can be improved if we adjust k_s from its originally published value of 652 N m^{-1} to 610 N m^{-1}.

Knowledge of the radial Young's modulus allows us to estimate what pressure the nanotubes can withstand inside its cavity. In particular, we use the Young's modulus found previously, to calculate the strain necessary to create 5.8 GPa of pressure inside the nanotube—this is the pressure required to stabilize H4M at room temperature. The corresponding strains are given in table 5. Next, we perform simple calculations on the carbon framework to measure how much strain it can withstand before it breaks. In our calculations we investigate strains from 10% to 20% and we find that the carbon network breaks at approximately 15% strain, in good agreement with [40, 41], although other experiments note that breaking occurs at a lower strain of around 5% [37, 42].

Table 5. Theoretically predicted performance of the CNT + H4M systems. The data given are the chirality of the system, the nanotube radius (Å), the largest possible H4M supercell commensurate with the diameter, the mass densities ρ_{mass} (with and without including the hydrogen in CH_4) (mass%), the volumetric densities ρ_{vol} (kg H_2/L), the radial Young's modulus E_r (GPa), and the strain ε (%) required to produce 5.8 GPa.

System	Radius	Filling	$\rho^{\text{w}}_{\text{mass}}$	$\rho^{\text{w/o}}_{\text{mass}}$	ρ_{vol}	E_r	ε
(10, 0)	3.95	$1 \times 1 \times 1$	2.4	1.6	0.028	870	0.7
(16, 0)	6.30	$2 \times 2 \times 1$	5.6	3.7	0.055	555	1.0
(24, 0)	9.43	$3 \times 3 \times 1$	7.9	5.3	0.065	373	1.6
(32, 0)	12.56	$4 \times 4 \times 1$	10.0	6.7	0.070	280	2.1
(40, 0)	15.69	$5 \times 5 \times 1 + 8$	14.6	9.7	0.097	224	2.6
(48, 0)	18.82	$6 \times 6 \times 1 + 12$	16.7	11.1	0.102	187	3.1
(56, 0)	21.96	$7 \times 7 \times 1 + 16$	18.4	12.2	0.103	160	3.6
(64, 0)	25.08	$8 \times 8 \times 1 + 24$	20.4	13.6	0.110	140	4.1
H4M	—	—	50.2	33.3	0.160	—	—

5.2. Binding between nanotubes; optimized separation for a nanotube bundle

We next investigate the binding of nanotubes to each other. To this end we arrange the nanotubes in a hexagonal unit cell and study the energy as a function of separation in such bundles. We start from isolated nanotubes and bring them together incrementally, performing two types of calculation: (i) the atoms in the tubes are fixed and (ii) the tubes are free to deform. From the resulting energy curves, we find that nanotubes bind at a wall-to-wall separation of approximately 3.5 Å, nearly independent of size. Furthermore, larger tubes undergo more deformation at close distance and there is a significant energy gain from the deformation if the separation is less than 3 Å for tubes with chirality larger than (16, 0). Since the deformation only plays a significant role in a region closer than the natural binding distance, we will use a 3.5 Å wall-to-wall distance and start all simulations from undistorted nanotubes in the calculations reported below. From our calculated wall-to-wall separation of nanotubes in bundles, we can then deduce the achievable volumetric hydrogen-storage density; results are given in table 5.

5.3. CNT + H4M system

The length of one of the edges of the SO H4M crystalline unit cell at 5.8 GPa is very close to the unit cell length of carbon nanotubes in the axial direction (4.27 Å). Hence, we compress the H4M unit cell slightly so that the edge is exactly commensurate and scale the other two edges accordingly. We then put $n \times n \times 1$ supercells of H4M inside the carbon nanotubes and relax the whole system. For example, since the diagonal length of the scaled H4M unit cell is 6.6 Å (slightly larger than the radius of the (16, 0) carbon nanotube), it is natural to build the filled structure from a (16, 0) nanotube together with a $2 \times 2 \times 1$ H4M supercell. We slightly adjust the positions of several hydrogen molecules at the corners to prevent steric clashes. The resulting relaxed structure is shown in figure 6. Throughout the relaxation, the structure of H4M changes noticeably. The nanotube also deforms and exhibits a strain of 1.4%, which is more than we estimated in table 5 since we compressed the supercell slightly to make it commensurate; nevertheless, it withstands the pressure created by the H4M inside.

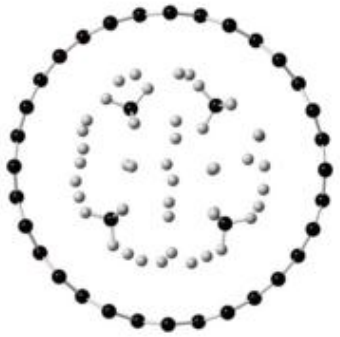

Figure 6. Optimized structure of a $2 \times 2 \times 1$ supercell of H4M inside a (16, 0) carbon nanotube.

In table 5, we list the theoretically possible hydrogen mass densities for the CNT + H4M system for nanotubes up to a radius of 25 Å; even better performance might be achievable for larger tubes. Note that for tubes starting at (40, 0), the filling with supercells of H4M is not simply a square-type pattern corresponding to $n \times n \times 1$, but we can fit in further unit cells on the side to better approximate the circular shape of the tube. The corresponding filling is then reported as $n \times n \times 1 + m$, where m indicates the number of additional unit cells of H4M that we are able to fit in a given tube. According to our estimation, all indicated tubes provide enough pressure to stabilize H4M at room temperature.

6. Conclusions

In this paper we present results of *ab initio* calculations on the H4M system for the purpose of hydrogen storage. While H4M shows exceptional hydrogen mass storage density—well beyond the required Department of Energy target—it falls short in its thermodynamic properties. It either requires very high pressure to be stable at room temperature, or it needs to be extensively cooled at ambient pressure. Our *ab initio* simulations are a proof of concept that external agents such as MOFs and carbon nanotubes can be used

to provide the necessary pressure. We find that certain MOFs provide enough pressure to significantly decrease the burden of cooling, but none of them stabilize H4M at room temperature. On the other hand, we find the very encouraging result that carbon nanotubes may stabilize H4M at room temperature with outstanding gravimetric and volumetric hydrogen-storage densities.

While in this study we have performed basic simulations of possible host materials to stabilize H4M, we have not addressed related practical issues. Questions arise such as: even if these host materials are, in principle, capable of stabilizing H4M at close-to-ambient temperatures, how can we practically place the H4M inside the cavities of these host materials? Also, it is not clear that the radial pressure of the nanotubes alone is practically enough to stabilize H4M; some axial pressure might be necessary. More research is needed to see whether H4M can be crystallized inside these structures, or whether it can form clusters at a low temperature and then diffuse into these cavities.

Acknowledgments

We would like to dedicate this paper to the memory of Professor David Langreth, who passed away in mid-2011—he is the 'father' of vdW-DF and his research inspired many. All calculations were performed on the WFU DEAC cluster. This work was supported by the Department of Energy Grant, Office of Basic Energy Sciences, Materials Sciences and Engineering Division, Grant No. DE-FG02-08ER46491.

References

[1] US Department of Energy Basic Energy Sciences Advisory Committee 2003 *Basic Research Needs to Assure a Secure Energy Future (Washington, DC)* (http://science.energy.gov/~/media/bes/pdf/reports/files/sef_rpt.pdf)
[2] US Department of Energy Office of Basic Energy Sciences 2004 *Basic Research Needs for the Hydrogen Economy (Washington, DC)* (http://science.energy.gov/~/media/bes/pdf/reports/files/nhe_rpt.pdf)
[3] Züttel A 2004 *Naturwissenschaften* **91** 157
[4] Crabtree G W, Dresselhaus M S and Buchanan M V 2004 *Phys. Today* **57** 39
[5] Lim K L, Kazemian H, Yaakob Z and Daud W R W 2010 *Chem. Eng. Technol.* **33** 213
[6] Sakintuna B, Lamari-Darkrim F and Hirscher M 2007 *Int. J. Hydrog. Energy* **32** 1121
[7] Makowski P, Thomas A, Kuhn P and Goettmann F 2009 *Energy Environ. Sci.* **2** 480
[8] Mao W L, Koh C A and Sloan E D 2007 *Phys. Today* **60** 42
[9] Mao W L, Struzhkin V V, Mao H and Hemley R J 2005 *Chem. Phys. Lett.* **402** 66
[10] Somayazulu M S, Finger L W, Hemley R J and Mao H K 1996 *Science* **271** 1400
[11] Mao W L and Mao H K 2004 *Proc. Natl Acad. Sci.* **101** 708
[12] Yaghi O M, Li G and Li H 1995 *Nature* **378** 703
[13] Rosi N L, Eckert J, Eddaoudi M, Vodak D T, Kim J, O'keeffe M and Yaghi O M 2003 *Science* **300** 1127
[14] Zhao X, Xiao B, Fletcher A J, Thomas K M, Bradshaw D and Rosseinsky M J 2004 *Science* **306** 1012
[15] Eddaoudi M, Kim J, Rosi N, Vodak D T, Wachter J, O'Keeffe M and Yaghi O M 2002 *Science* **295** 469
[16] Dresselhaus M S, Dresselhaus G and Eklund P C 1996 *Science of Fullerenes and Carbon Nanotubes: Their Properties and Applications* (New York: Academic)
[17] Cheung C L, Kurtz A, Park H and Lieber C M 2002 *J. Phys. Chem.* B **106** 2429
[18] Román-Pérez G and Soler J M 2009 *Phys. Rev. Lett.* **103** 096102
[19] Yao Y, Nijem N, Li J, Chabal Y J, Langreth D C and Thonhauser T 2012 *Phys. Rev.* B **85** 064302
[20] Dion M, Rydberg H, Schröder E, Langreth D C and Lundqvist B I 2004 *Phys. Rev. Lett.* **92** 246401
Dion M, Rydberg H, Schröder E, Langreth D C and Lundqvist B I 2005 *Phys. Rev. Lett.* **95** 109902 (E)
[21] Thonhauser T, Cooper V R, Li S, Puzder A, Hyldgaard P and Langreth D C 2007 *Phys. Rev.* B **76** 125112
[22] Langreth D C *et al* 2009 *J. Phys.: Condens. Matter* **21** 084203
[23] Thonhauser T, Puzder A and Langreth D C 2006 *J. Chem. Phys.* **124** 164106
Li S, Cooper V R, Thonhauser T, Puzder A and Langreth D C 2008 *J. Phys. Chem.* A **112** 9031
Hooper J, Cooper V R, Thonhauser T, Romero N A, Zerilli F and Langreth D C 2008 *ChemPhysChem* **9** 891
[24] Mura M, Gulans A, Thonhauser T and Kantorovich L 2010 *Phys. Chem. Chem. Phys.* **12** 4759
[25] Cooper V R, Thonhauser T, Puzder A, Schröder E, Lundqvist B I and Langreth D C 2008 *J. Am. Chem. Soc.* **130** 1304
Cooper V R, Thonhauser T and Langreth D C 2008 *J. Chem. Phys.* **128** 204102
[26] Li S, Cooper V R, Thonhauser T, Lundqvist B I and Langreth D C 2009 *J. Phys. Chem.* B **113** 11166
[27] Li Q, Kolb B, Román-Pérez G, Soler J M, Yndurain F, Kong L, Langreth D C and Thonhauser T 2011 *Phys. Rev.* B **84** 153103
[28] Giannozzi P *et al* 2010 *J. Phys.: Condens. Matter* **22** 022201
[29] Pack J D and Monkhorst H J 1976 *Phys. Rev.* B **13** 5188
Pack J D and Monkhorst H J 1977 *Phys. Rev.* B **16** 1748
[30] Perdew J P and Wang Y 1992 *Phys. Rev.* B **45** 13244
[31] Kolb B and Thonhauser T 2011 *Phys. Rev.* B **84** 045116
[32] Perdew J P, Burke K and Ernzerhof M 1996 *Phys. Rev. Lett.* **77** 3865
[33] Pickard C J and Needs R J 2011 *J. Phys.: Condens. Matter* **23** 053201
[34] Mao W L *et al* 2009 *Global Climate & Energy Project Symposium 2009* available at http://gcep.stanford.edu/pdfs/CTISZRP4nww_77Shjd-A2g/WendyMao_Symposium2009.pdf
[35] Martin R M 2004 *Electronic Structure: Basic Theory and Pratical Methods* (Cambridge: Cambridge University Press)
[36] Saito R, Dresselhaus G and Dresselhaus M S 2003 *Physical Properties of Carbon Nanotubes* (London: Imperial College Press)
[37] Yu M F, Files B S, Arepalli S and Ruoff R S 2000 *Phys. Rev. Lett.* **84** 5552
[38] Lu J P 1997 *Phys. Rev. Lett.* **79** 1297
[39] Li Y, Qiu X, Yin Y, Yang F and Fan Q 2009 *Phys. Lett.* A **373** 2368
[40] Grantab R, Shenoy V B and Ruoff R S 2010 *Science* **330** 946
[41] Zhao H, Min K and Aluru N R 2009 *Nano Lett.* **9** 3012
[42] Yu M F, Lourie O, Dyer M J, Moloni K, Kelly T F and Ruoff R S 2000 *Science* **287** 637
[43] Lee S M, An K H, Lee Y H, Seifert G and Frauenheim T 2001 *J. Am. Chem. Soc.* **123** 5059

APPENDIX III: SURFACE MODIFICATION ENABLED CARRIER MOBILITY ADJUSTMENT IN CZTS NANOPARTICLE THIN FILMS

Wenxiao Huang, Qi Li, Yonghua Chen, Yingdong Xia, Huihui Huang,
Chaochao Dun, Yuan Li, David L. Carroll

This following manuscript is accepted for publication on Sol. Energ. Mat. Sol. C in 2014.

Qi Li performed all the calculations for the carrier mobilities in the CZTS-ligand systems and prepared the theoretical part the manuscript. The presented manuscript is in its required submission format.

Surface Modification Enabled Carrier Mobility Adjustment in CZTS Nanoparticle Thin Films

Wenxiao Huang,[1‡] *Qi Li,*[1‡] *Yonghua Chen,*[1] *Yingdong Xia,*[1] *Huihui Huang,*[1] *Chaochao Dun,*[1] *Yuan Li,*[1 b] *David L. Carroll*[1 a]

1. *Center for Nanotechnology and Molecular Materials, Department of Physics, Wake Forest University, Winston-Salem NC 27109, USA*

a. *carroldl@wfu.edu*

b. *liy@wfu.edu*

‡ *These authors contributed equally*

1. Abstract

As the essential building blocks of many electronic devices, solid state thin-films are attracting extensive interest. Soluble nanocrystals (NCs) make it possible to develop robust, low-cost, large-scale fabrication methods for thin-films. However, the organic surface ligands normally used to stabilize the NCs make those thin-films a NC-ligand complex which may possess varied electrical performance compared to a single component system. Previous models could only estimate the charge transportation characteristics in those films quantitatively by considering the capping ligands as a barrier of charges from inter-particle hopping. In this work, we demonstrated that starting from first principles density functional theory, the carrier mobility in a CZTS NC-ligand complex can be determined quantitatively, and guided by this model, we developed a low-cost, low-temperature technique to fabricate CZTS thin films which have a carrier mobility of up to 10.9 $cm^2/(VS)$.

2. Introduction

Semiconductor thin films are the fundamental building blocks for rapidly growing fields involving thin-film-transistors (TFTs), solar cells, and transparent electrodes. While many fabrication methods have been developed, semiconductor nanocrystals (NCs) substantially reduce the cost of thin-film electronic and photovoltaic device fabrication because the soluble NCs 'ink' can be applied to large-scale, low-cost fabrication techniques such as drop casting, dip casting, spin coating, spray casting, and inkjet printing. However, to avoid aggregation caused by their high surface area, the NCs are normally stabilized by organic insulating capping ligands, which introduce a major obstacle in improving the electronic performance of these thin films. To get rid of these organic ligands, many thin-film preparations employ high-temperature annealing: during this aggressive procedure, defects occur in the film formation due to high weight losses[1], and the high annealing temperature limits the choices of substrate. Otherwise, removing the surface capping ligands requires a hazardous and toxic procedure involving hydrazine[2] [3].Therefore, searching for a new low-cost method to improve the NCs thin film electrical performance becomes worthwhile.

One solution is to modify the surface of the NCs by exchanging the long chain insulating ligands with new shorter ligands. Past studies have revealed that the charge transport in a PbSe NC-ligand system can be considered as a series of incoherent tunneling transitions between neighboring NCs[2] [4], using the ligand monolayer as the tunneling barrier. In these previous models, carrier mobility is determined by the site energies, exchange coupling energy between two NCs, and average barrier width. However, given that those parameters are difficult to determine experimentally, these models can only analyze them qualitatively.

In this work, we studied Cu2ZnSnS4 (CZTS) NC-ligand systems. Instead of describing the ligand as an individual tunneling barrier for charge hopping, we coupled it with the NCs and studied how the surface modification influenced the electron structure and the effective mass of charges in this NC-ligand complex. This allowed us to determine the carrier mobility quantitatively.

The kesterite material CZTS possesses promising characteristics to be a conventional absorber for thin film solar cells with the added benefits of being low-cost, non-toxic, and comprised of earth-abundant elements. Various techniques have been developed for the preparation of CZTS thin films, such as sulfurization followed co-sputtering[5], chemical

vapor deposition (CVD)[6], electrodepostion[7], and hydrazine based solution processing[8], which leads to the current highest performing CZTS solar cells (>11% efficiency)[9]. Nevertheless, the nonvacuum, low-toxic preparation of CZTS inks could produce low-cost thin films with superior homogeneous composition. Also, the traditional CZTS ink technique requires a high-temperature procedure which has the same issues that other solution-based NC devices have confronted, but with additional drawbacks: Sn losses through desorption of SnS from CZTS due to high vapor pressure of SnS[10] leads to impurity and defects, and sulfur diffusion into the molybdenum back contact forms MoS2 and yields secondary phases at the CZTS|Mo interface, lowering the performance[11]. Therefore, the theoretical investigation on CZTS NC-ligand systems would not only help us anticipate the electrical performance but also guide us to develop a low-temperature surface modification process that solves the above issues.

3. Discussion

To reveal the origin of how the ligands cap the CZTS NCs and further influence carrier transport in NC-ligand systems, a method based on first principles density functional theory (DFT) is proposed below:

Compared to the bulk material, NC thin films are a complex of organic ligands and nanoparticles. This distinct structure causes great differences between the charge transport features of neighboring particles. Instead of considering the NCs and ligands separately, the CZTS nanoparticles are coupled with different ligands to perform electronic structure calculations for the surface states of CZTS nanoparticles in order to determine the effective mass and then further derive the carrier mobility.

The crystal structure of kesterite CZTS is tetragonal, space group $I\bar{4}$ (No.82 of the International Tables of Crystallography). Our *ab initio* calculations are carried out in the projector-augmented wave framework in Vienna *ab initio* simulation package (VASP)[12] [13]. We employ both hybrid functionals (HSE06 [14] and PBE0[15]) and compare the results to the Perdew-Burke-Ernzerhof (PBE) parametrization of the generalized gradient approximation[16]. The mixing factor is 0.25 for both hybrid functionals. The plane wave kinetic cutoff energy is 300 eV. A self-consistency convergence criterion of 1×10^{-6} eV is used for all calculations and the structures (crystal and crystal-ligand) are relaxed until all

force components are less than 0.01 eV/Å. The bulk properties of ideal kesterite CZTS are calculated with the primitive cell of 8 atoms. A Γ-centered 4 ×4×4 Monkhorst-Pack k-point mesh is applied for all three functionals. Results are listed in the supporting material. The GGA results underestimate the band gap and HSE06 has the closest result to the experimental data. This tendency is also found in Ref. [17]

For the crystal-ligand system simulation, we chose oleylamine (OLA) and a few alkanethiols (1-butanethiol (1-BTT), 1-hexanethiol (1-HXT), and 1-dodecanethiol (1-DDT)), ligands with different chain lengths. OLA is a common ligand used in CZTS NCs synthesis. The alkanethiols have stronger bonding between CZTS NCs than OLA does, so the alkanethiols are potentially capable of exchanging with the surface ligand of OLA-capped CZTS NCs. We first create a non-polarized surface (110) which is favorable to the ligand. This is done by using two new basis vectors ($\overrightarrow{T_1}, \overrightarrow{T_2}$) on the x-y plane of the 16 atom tetragonal conventional cell, where $\overrightarrow{T_1} = \overrightarrow{a_1} - \overrightarrow{a_2}$ and $\overrightarrow{T_2} = \overrightarrow{a_1} + \overrightarrow{a_2}$ and $\overrightarrow{a_1}$ and $\overrightarrow{a_2}$ are the two original basis vectors in the (100) and (010) directions, respectively, while the basis vector in z-direction is unchanged. In Figure 1, $\overrightarrow{T_1}$, $\overrightarrow{T_2}$ are defined as the new X and Y axes, respectively. A supercell is created by stacking three new unit cells in the X direction. Then we remove one hydrogen atom from the amino or thiol group of the ligand molecules and bond the sulfur or nitrogen atom with a copper atom on both sides of the supercell, which are two (110) surfaces of kesterite CZTS. This selection is based on the fact that the Cu^+ existing in bulk CZTS can still provide one more electron to bond with the sulfur or nitrogen atoms of the ligands.

Calculations on the CZTS-ligand complex structure are performed with traditional GGA-PBE functional theory. Although the energy gap calculated from GGA-PBE is not correct, we apply the idea of "scissors operator" [18] and trust the shape of the conduction bands which directly lead to band edge effective masses [19]. The k-point sampling is scaled with the size of the new cells. All atoms are relaxed with the same criteria stated above, and the relaxed structures at the surfaces are shown in Figure 1. As expected, the sulfur and nitrogen atoms from the ligand molecules are bonded most closely with the copper ion of CZTS. In order to simulate the mobilities, we calculated the effective mass at the conduction band minimum. Simulation of electron-phonon scattering time is shown in the supporting

material. The overall mobilities are calculated as the average of the mobilities in the X, Y, and Z directions.

As a result, we combined the electronic structure calculations with the analytical formula for electron-phonon scattering of the NC-ligand complex systems and simulated the electron mobilities quantitatively. The results are listed in Table 1 and shown in Figure 2. Due to the fact that the band masses along the X axis are the largest, we can deduce that carrier transport along the ligand molecules is less efficient than transport on the CZTS-ligand surfaces. The band masses on the Y and Z axes have relatively close values. Furthermore, they are also controlled by the length of the ligand molecules. As a general tendency, longer ligands lead to increasing effective masses at the conduction band minimum and hence sharply decreasing mobility. Inspired by our simulation result, and in order to verify this phenomenon and experimentally calculate mobility, we developed a low-temperature, low-cost technique for CZTS NCs thin-film fabrication. OLA-capped CZTS NCs with size 15~25 nm were synthesized as other literature has described[20]. Then the OLA, bonded to NC surfaces, was replaced by 1-BTT, 1-HXT, and 1-DDT in solution, followed by spray casting onto ITO substrates to make NC thin films (Figure 3).

This ligand exchange has been identified via Thermogravimetric Analysis (TGA) and FT-IR (Fourier Transform Infrared Spectra). Since the C-S bond is not sensitive in infrared spectra measurement, the existence of N-H bond was studied: clearly the N-H peaks disappeared after ligand exchange, revealing that the alkanethiols completely replaced the OLA (see Figure 4(B)). Besides, as shown in Figure 4(A), 1-butanethiol, 1-hexanethiol, 1-dodecanethiol, and OLA-capped NCs contain 3.36%, 4.04%, 5%, and 23.32% organic ligands in total weight of NCs, respectively, indicating that ligands with shorter chains could reduce the amount of insulator in the NC thin films. Also, with the noticeable difference of weight percentage, we can conclude that there are weight losses during the ligand exchange process. With a solutionless ligand exchange method, the weight loss happens during the film formation and leaves many cracks[21]. The SEM image in Figure 5 shows that with solution ligand exchange followed by spray casting, we can fabricate condensed homogeneous films without noticeable cracks. Since the NCs still retain their solubility after the ligand exchange, this is a suitable method for large scale fabrication.

We fabricated the hole-only devices with structure Glass/ITO/CZTS/MoO3/Al since CZTS is p type material. Experimentally, the current-voltage relationship was collected using a Keithley 236 source-measurement unit. The carrier mobility (hole) was then extracted from the J-V characteristics through approximation of the space charge limited current (SCLC) in Eqn. (1) [22]

$$J = \frac{9}{8}\varepsilon_0 \varepsilon \mu_0 \exp\left(0.89\beta\sqrt{V/d}\right)\frac{V^2}{d^3} \tag{1}$$

V is the applied voltage, d is the thickness of the film, μ_0 is the mobility, ε_0 is the permittivity of free space, and ε=6.7 is the dielectric constant[23]. Eqn. (2) gives the efficiency β [22], where T is the temperature in calculation.

$$\beta = \frac{1}{K_B T}\left(\frac{q^3}{\pi\varepsilon_0\varepsilon}\right)^{1/2} \tag{2}$$

The experimental results are superimposed onto Figure 2. Although the lengths of the ligands (1nm~3nm) are much smaller than the diameter of the CZTS NCs (15~25 nm), changing those lengths dramatically influences transportation of carriers in the film. Shifting from OLA to 1-BTT, the carrier mobility improves by a factor of 29. More generally, the mobility increases exponentially while the ligand chain length decreases linearly, which agrees with reported PbSe systems[4]. Not only is the trend consistent with our calculations, but also, the measured values have great agreement with our theoretically calculated values. In other words, the agreement in Figure 2 exemplifies both the qualitative and quantitative validity of our model. Additionally, by developing this low-cost, low-temperature technique we were able to achieve a top mobility of 10.9 $cm^2/(VS)$, which is comparable with that of reported high-temperature processes[24][25][26][27].

Conclusion

In summary, we reported a novel theoretical method to quantitatively estimate the carrier mobility in a NC-ligand complex, and we demonstrated both experimentally and theoretically that simple surface modification could remarkably change the carrier transportation characteristics in the NC thin film. In the CZTS NC-ligand system, we showed that the carrier mobility increases exponentially with decreasing ligand length because the

carrier's effective mass is significantly influenced by the capping ligands. Based on this understanding, we developed a low-cost, low-temperature solution method to fabricate condensed homogenous CZTS thin films. With this method, we illustrated that with the shortest ligand adopted in this report, the carrier mobility of a CZTS thin film could be increased to 10.9 cm2/(VS), which is a 29-fold increase compared to the original OLA-capping NC thin film. It is also pertinent to note that further improvement in carrier mobility would be expected through utilizing ligands which are even shorter than 1-BTT. In conclusion, the present findings proved the importance of the surface state of the NCs in the thin-film device, as it enabled us to adjust the carrier mobility through a simple surface modification of the NCs.

4. Reference

[1] C. Jiang, J. Lee, D. V Talapin, Soluble Precursors for CuInSe2, CuIn1–xGaxSe2, and Cu2ZnSn(S,Se)4 Based on Colloidal Nanocrystals and Molecular Metal Chalcogenide Surface Ligands, J. Am. Chem. Soc. 134 (2012) 5010–5013. doi:10.1021/ja2105812.

[2] D. V Talapin, C.B. Murray, PbSe nanocrystal solids for n- and p-channel thin film field-effect transistors., Science. 310 (2005) 86–9. doi:10.1126/science.1116703.

[3] H. Yang, L. a Jauregui, G. Zhang, Y.P. Chen, Y. Wu, Nontoxic and abundant copper zinc tin sulfide nanocrystals for potential high-temperature thermoelectric energy harvesting., Nano Lett. 12 (2012) 540–5. doi:10.1021/nl201718z.

[4] Y. Liu, M. Gibbs, J. Puthussery, S. Gaik, R. Ihly, H.W. Hillhouse, et al., Dependence of carrier mobility on nanocrystal size and ligand length in PbSe nanocrystal solids., Nano Lett. 10 (2010) 1960–9. doi:10.1021/nl101284k.

[5] H. Katagiri, K. Jimbo, W.S. Maw, K. Oishi, M. Yamazaki, H. Araki, et al., Development of CZTS-based thin film solar cells, Thin Solid Films. 517 (2009) 2455–2460. doi:10.1016/j.tsf.2008.11.002.

[6] T. Washio, T. Shinji, S. Tajima, T. Fukano, T. Motohiro, K. Jimbo, et al., 6% Efficiency Cu2ZnSnS4-based thin film solar cells using oxide precursors by open atmosphere type CVD, J. Mater. Chem. 22 (2012) 4021–4024.

[7] S. Ahmed, K.B. Reuter, O. Gunawan, L. Guo, L.T. Romankiw, H. Deligianni, A High Efficiency Electrodeposited Cu2ZnSnS4 Solar Cell, Adv. Energy Mater. 2 (2012) 253–259. doi:10.1002/aenm.201100526.

[8] W. Yang, H.-S. Duan, B. Bob, H. Zhou, B. Lei, C.-H. Chung, et al., Novel Solution Processing of High-Efficiency Earth-Abundant Cu(2) ZnSn(S,Se)(4) Solar Cells., Adv. Mater. (2012) 1–7. doi:10.1002/adma.201201785.

[9] T.K. Todorov, J. Tang, S. Bag, O. Gunawan, T. Gokmen, Y. Zhu, et al., Beyond 11% Efficiency: Characteristics of State-of-the-Art Cu2ZnSn(S,Se)4 Solar Cells, Adv. Energy Mater. 3 (2012) 34–38. doi:10.1002/aenm.201200348.

[10] A. Redinger, D.M. Berg, P.J. Dale, S. Siebentritt, The consequences of kesterite equilibria for efficient solar cells., J. Am. Chem. Soc. 133 (2011) 3320–3. doi:10.1021/ja111713g.

[11] J.J. Scragg, J.T. Wätjen, M. Edoff, T. Ericson, T. Kubart, C. Platzer-Björkman, et al., A Detrimental Reaction at the Molybdenum Back Contact in Cu2ZnSn(S,Se)4 Thin-Film Solar Cells, J. Am. Chem. Soc. 134 (2012) 19330–19333. doi:10.1021/ja308862n.

[12] G. Kresse, J. Hafner, Ab initio molecular dynamics for liquid metals, Phys. Rev. B. 47 (1993) 558.

[13] G. Kresse, D. Joubert, From ultrasoft pseudopotentials to the projector augmented-wave method, Phys. Rev. B. 59 (1999) 1758.

[14] J. Heyd, G.E. Scuseria, M. Ernzerhof, Hybrid functionals based on a screened Coulomb potential, J. Chem. Phys. 118 (2003) 8207–8215.

[15] J.P. Perdew, M. Ernzerhof, K. Burke, Rationale for mixing exact exchange with density functional approximations, J. Chem. Phys. 105 (1996) 9982.

[16] J.P. Perdew, K. Burke, M. Ernzerhof, Generalized gradient approximation made simple, Phys. Rev. Lett. 77 (1996) 3865.

[17] S. Botti, D. Kammerlander, M. a. L. Marques, Band structures of Cu2ZnSnS4 and Cu2ZnSnSe4 from many-body methods, Appl. Phys. Lett. 98 (2011) 241915. doi:10.1063/1.3600060.

[18] X. Zhu, S.G. Louie, Quasiparticle band structure of thirteen semiconductors and insulators, Phys. Rev. B. 43 (1991) 14142.

[19] Q. Li, J.Q. Grim, K.B. Ucer, A. Burger, G.A. Bizarri, W.W. Moses, et al., Host structure dependence of light yield and proportionality in scintillators in terms of hot and thermalized carrier transport, Phys. Status Solidi (RRL)-Rapid Res. Lett. 6 (2012) 346–348.

[20] Q. Guo, G.M. Ford, W.-C. Yang, B.C. Walker, E.A. Stach, H.W. Hillhouse, et al., Fabrication of 7.2% Efficient CZTSSe Solar Cells Using CZTS Nanocrystals, J. Am. Chem. Soc. 132 (2010) 17384–17386. doi:10.1021/ja108427b.

[21] J.M. Luther, M. Law, Q. Song, C.L. Perkins, M.C. Beard, A.J. Nozik, Structural, optical, and electrical properties of self-assembled films of PbSe nanocrystals treated with 1,2-ethanedithiol., ACS Nano. 2 (2008) 271–80. doi:10.1021/nn7003348.

[22] P. Murgatroyd, Theory of space-charge-limited current enhanced by Frenkel effect, J. Phys. D. Appl. Phys. 3 (1970) 151–156.

[23] C. Persson, Electronic and optical properties of Cu[sub 2]ZnSnS[sub 4] and Cu[sub 2]ZnSnSe[sub 4], J. Appl. Phys. 107 (2010) 053710. doi:10.1063/1.3318468.

[24] C.P. Chan, H. Lam, C. Surya, Preparation of Cu2ZnSnS4 films by electrodeposition using ionic liquids, Sol. Energy Mater. Sol. Cells. 94 (2010) 207–211. doi:10.1016/j.solmat.2009.09.003.

[25] J.C. González, G.M. Ribeiro, E.R. Viana, P. a Fernandes, P.M.P. Salomé, K. Gutiérrez, et al., Hopping conduction and persistent photoconductivity in Cu 2 ZnSnS 4 thin films, J. Phys. D. Appl. Phys. 46 (2013) 155107. doi:10.1088/0022-3727/46/15/155107.

[26] W. Yang, H.-S. Duan, K.C. Cha, C.-J. Hsu, W.-C. Hsu, H. Zhou, et al., Molecular solution approach to synthesize electronic quality Cu2ZnSnS4 thin films., J. Am. Chem. Soc. 135 (2013) 6915–20. doi:10.1021/ja312678c.

[27] T. Tanaka, T. Nagatomo, D. Kawasaki, M. Nishio, Q. Guo, A. Wakahara, et al., Preparation of Cu2ZnSnS4 thin films by hybrid sputtering, J. Phys. Chem. Solids. 66 (2005) 1978–1981. doi:10.1016/j.jpcs.2005.09.037.

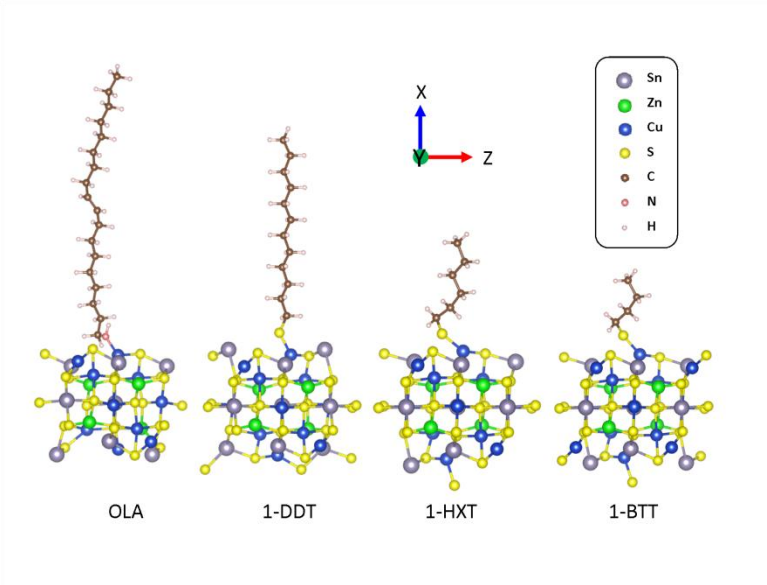

Figure 1 Relaxed surface structures of keresite CZTS ligand complex systems for 4 ligands (OLA, 1-DDT, 1-HXT and 1-BTT) with varying lengths (18, 12, 6 and 4 carbons). The whole unit cell contains a 48 atom supercell arranged along the X axis and ligands on both ends. The anions of the ligands are bonded with the copper ion of CZTS.

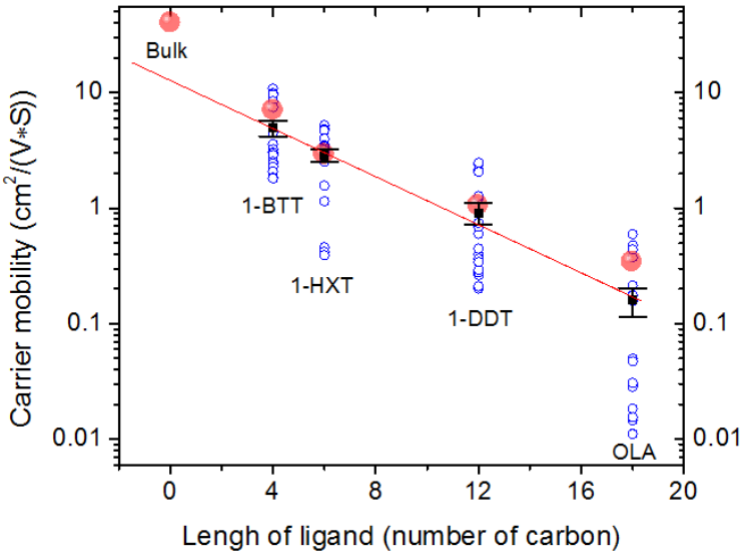

Figure 2 Carrier mobility versus ligand length, from the aspects of theoretical value (red sphere) and experimental statistics (blue hole) with mean (black square). The ligand length is showed in the number of carbon atoms (0, 4, 6, 12, and 18 represents bulk, 1-BTT, 1-HXT, 1-DDT and OLA, respectively).

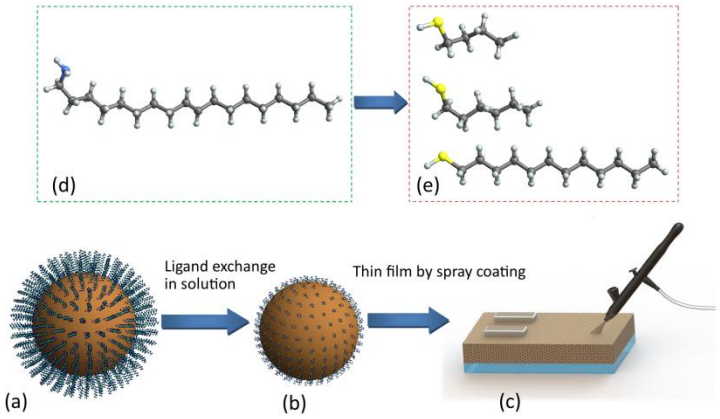

Figure 3 (a)-(b) shows the ligand exchange process in which the longer ligand (d) was exchanged by the shorter ligand (e). After this process, the film can be directly deposited on substrate without post annealing (c).

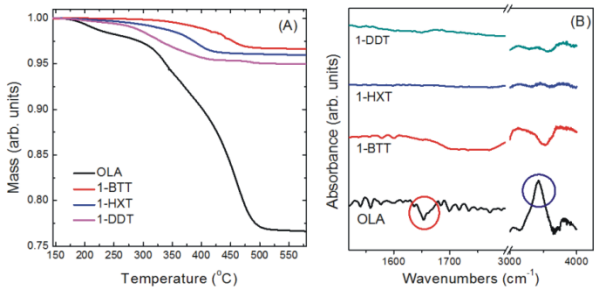

Figure 4 (A) TGA data for different ligand capped CZTS NCs at a constant heating rate of 5°C min^{-1} under argon flow. The samples were retained at 140°C for 30min to avoid the influence of excess solvent. Before measurement, samples were dried in vacuum for 24h. (B) FT-IR of NCs capped by different ligands showing that the N-H stretching (blue circle) and N-H bending (red circle) peaks vanished in thiol ligands-NCs system which indicates that after ligand exchange, OLA is replaced by alkanethiols.

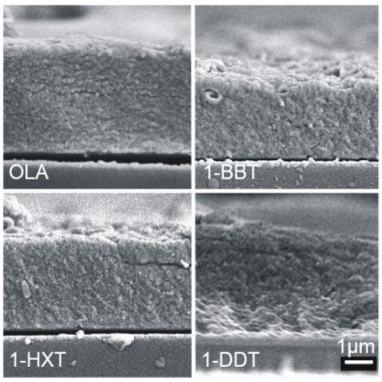

Figure 5 SEM images of CZTS films' cross section with four ligands (OLA, 1-DDT, 1-HXT and 1-BTT).

APPENDIX IV: FIELD ELECTRON EMISSION OF LAYERED Bi_2Se_3 NANOSHEETS

Huihui Huang, Yuan Li, Qi Li, Borui Li, Zengcai Song, Wenxiao Huang, Chujun Zhao, Han Zhang, Shuangchun Wen, David Carrollc, and Guojia Fang

This following manuscript is accepted for publication on Nanoscale in 2014. Qi Li performed all the calculations of the dielectric function of the layered Bi_2Se_3 and simulated the enhance factor. Stylistic variations are due to the requirements of the journal.

Nanoscale

RSCPublishing

ARTICLE

Field Electron Emission of Layered Bi_2Se_3 Nanosheets

Cite this: DOI: 10.1039/x0xx00000x

Huihui Huang,[a,b,△] Yuan Li,[c,△] Qi Li,[c,△] Borui Li,[a] Zengcai Song,[a] Wenxiao Huang,[c] Chujun Zhao,[b] Han Zhang,[b,*] Shuangchun Wen,[b] David Carroll[c,*] and Guojia Fang[a,*]

Received
Accepted

DOI: 10.1039/x0xx00000x

www.rsc.org/

Field electron emission properties of solution processed few-layer Bi_2Se_3 nanosheets are studied for the first time, which exhibits a low turn-on field of 2.3 V/μm, a high field enhancement factor up to 6860 and good field emission stability. These performances are better than the as reported layered MoS_2 sheets and are comparable to single layer graphene films. The efficient field emission behaviours are found to be not only attributed to their lower work function but also related to their numerous sharp edges or protrusion decorated structure based on our simulation results. Besides, the contribution of possible topologically protected single Dirac cone surface states of layered Bi_2Se_3 nanosheets is discussed in this paper. We anticipate that these solution processed layered Bi_2Se_3 nanosheets have a great potential as robust high-performance vertical structure electron emitters for future light weight and highly flexible vacuum micro/nano electronic device applications.

1. Introduction

Field electron emission is a phenomenon that extracts electrons from materials via quantum tunnelling through the surface potential barrier under strong electric field. Applications include flat-panel displays, high energy accelerators, X-ray sources, microwave amplifiers and vacuum microelectronic devices [1-3]. Among the field emission materials, one dimensional (1D) nanostructure materials including ZnO, carbon nanotubes or nanowires have been sufficiently studied for many years [4-10]. Field emission from two-dimensional (2D) atomic crystal materials such as graphene [11-16] and MoS_2 [17] have recently attracted lots of interest due to their atomic-thick sharp edges, unique electronic properties and compatibility with planar device technology.

Most recently, V_2VI_3 compounds like Bi_2Se_3, Bi_2Te_3 and Sb_2Te_3 have received growing attention not only because of their thermoelectric properties but also their unique electronic properties with insulating bulk states and topologically protected single Dirac cone surface states, namely, topological insulators (TIs) [18-23]. Besides, these materials have layered structures due to the weak Van der Waals' force between the quintuple layers (QLs) along the [001] direction. As the thickness reduces to few QLs, its surface properties could be enhanced due to the increase of the ratio of surface area to volume [18-23]. Take Bi_2Se_3 for example, recent literature reported that the square resistance of Bi_2Se_3 nanosheet with few QLs could be as low as 330 Ω, which might be ascribed to a new type of two-dimensional electron gas (2DEG) covered on the surface [21]. The excellent conductivity and atomic-thick sharp edges of layered Bi_2Se_3 nanosheet indicate that it could be a promising excellent field emission material. However, atomic-thick 2D layered structures have not been reported from experiment or theory. In this paper, we experimentally studied the field emission properties of solution processed layered Bi_2Se_3 nanosheets and proposed a theoretical field emission model for this system.

2. Results and discussion

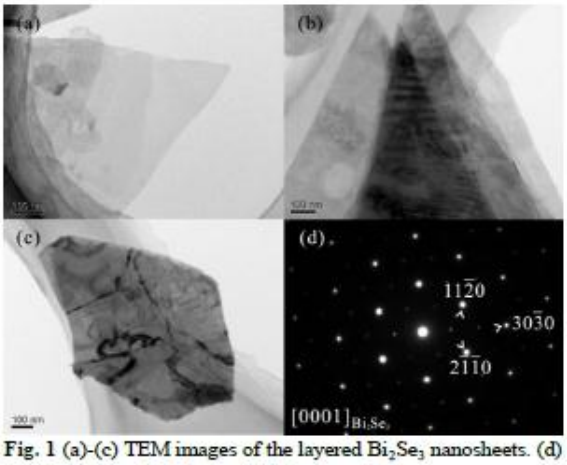

Fig. 1 (a)-(c) TEM images of the layered Bi_2Se_3 nanosheets. (d) SAED pattern of the layered Bi_2Se_3 nanosheets.

Layered Bi_2Se_3 nanosheets were prepared from bulk Bi_2Se_3 crystals by a three-step exfoliation method including mechanical grinding, hydrothermal exfoliation and sonication exfoliation (see the fabrication routing in **Figure S1**). **Figure 1(a)-(c)** show the transmission electron microscope (TEM) images of the layered Bi_2Se_3 nanosheets, which were prepared by directly dropped on the substrate from the dispersion solution (see **Figure S1(d)**). Clearly layered structures with size of several hundred nanometres could be seen from these images. Furthermore, the corresponding selected area electron diffraction (SAED) pattern of the Bi_2Se_3 nanosheets is shown in **Figure 1(d)**. The regular shape of the SAED pattern reveals that the layered Bi_2Se_3 nanosheets are monocrystalline, the wide surfaces are analyzed as {001} planes, which implies that the nanosheets were exfoliated along the [001] (c-axis) direction.

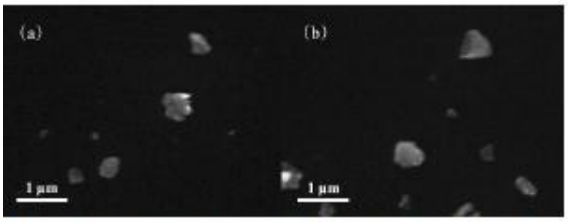

Fig. 2 SEM images of the exfoliated layered Bi_2Se_3 nanosheets spin-coated on Si substrate.

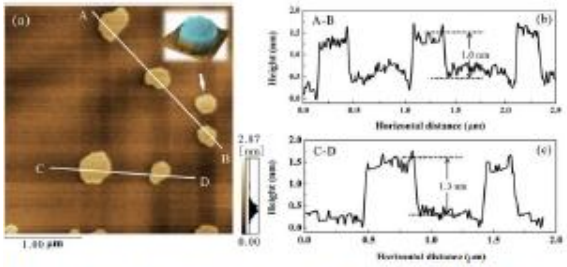

Fig. 3 (a) AFM image and height profile (b-c) of the layered Bi_2Se_3 nanosheets.

Figure 2 shows the scanning electron microscope (SEM) images of layered Bi_2Se_3 nanosheets which were spin-coated on Si substrate from the dispersion solution (see **Figure S1(d)**). Flat layered Bi_2Se_3 nanosheets were dispersed on the Si substrate with sizes up to several hundred nanometers. In order to prove the atomic-thick layered structure of the as-obtained Bi_2Se_3 nanosheets, atomic force microscopy (AFM) techniques were applied to the sample, which is shown in **Figure 3**. **Figure 3(a)** shows the AFM image of dispersed layered Bi_2Se_3 nanosheets, the thicknesses of all the nanosheets in the image are smaller than 2.87 nm. For accurate thickness information, height profiles of Line A-B and Line C-D in the image are shown in **Figure 3(b-c)**. The thickness of the samples in the Line A-B and Line C-D are calculated as ~1.0 nm and ~1.3 nm, respectively. Considering the instrument error, these results imply that the Bi_2Se_3 nanosheets in the image might be made up of 1 or 2 QLs since each planar QL with a thickness of ~0.955 nm [24]. These above results prove that the as-prepared Bi_2Se_3 nanosheets have atomic thick 2D layered structures.

Further, **Figure 4(a)** compares the Raman spectrum of the layered and bulk Bi_2Se_3 in the range of 50~200 cm^{-1}. The three Raman peaks centred at ~70 cm^{-1}, ~130 cm^{-1} and ~173 cm^{-1} could be assigned to the out-plane vibrational mode (A_{1g}^1), the in-plane vibrational mode (E_g^2), and the out-plane vibrational mode (A_{1g}^2) of Bi_2Se_3, respectively[25, 26]. It also can be seen that the relative intensity of the A_{1g}^1 vibrational mode in the layered Bi_2Se_3 spectrum is stronger than that in the bulk Bi_2Se_3 spectrum. Besides, the line width (~11.8 cm^{-1}) of the E_g^2 vibrational mode of the layered Bi_2Se_3 is a little bit broader than that of the bulk Bi_2Se_3 (~10.5 cm^{-1}). These Raman results confirm the few layer structure of the Bi_2Se_3 [26].

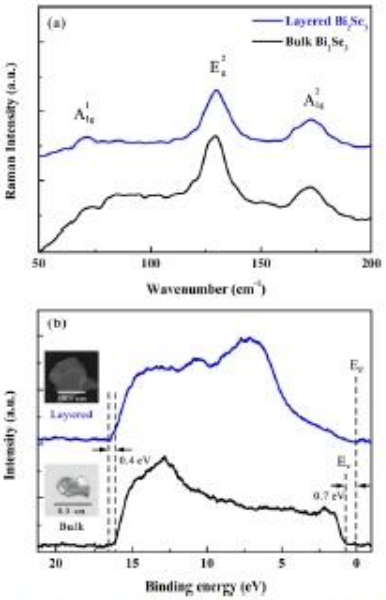

Fig. 4 (a) Raman spectra of layered Bi_2Se_3 and bulk Bi_2Se_3. (b) UPS spectra of layered Bi_2Se_3 and bulk Bi_2Se_3.

In order to investigate the surface electronic states of Bi_2Se_3, ultraviolet photoelectron spectroscopy (UPS) spectra of layered Bi_2Se_3 and bulk Bi_2Se_3 is compared in **Figure 4(b)**. On one hand, the UPS spectrum of layered Bi_2Se_3 shifted about 0.4 eV to higher binding energy compared with that of bulk Bi_2Se_3, indicating a decrease in work function for the layered Bi_2Se_3. On the other hand, the valence band maxinnum (E_v) of bulk Bi_2Se_3 is located 0.7 eV below its Fermi level (E_F), indicating that the bulk conduction band is occupied due to the n-type doping of defects, which also implies that the surface properties of bulk Bi_2Se_3 (with band gap of ~0.3 eV) might be masked by its bulk states. However, no clear energy gap between E_v and E_F could be found in the UPS spectra of layered Bi_2Se_3, which might be caused by the dominated zero-band surface states of the layered Bi_2Se_3 due to its large surface-to-volume ratio. The lower work function and the possible much more conductive

surface of layered Bi_2Se_3 should be related to the changed surface properties including surface energy and surface band structure [21,22], both of which are conducive to the field emission and it will be proved in the following experiments.

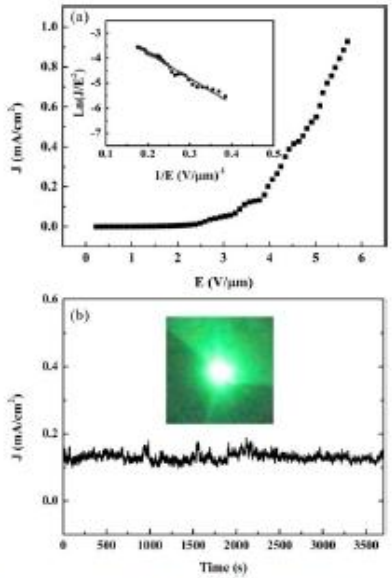

Fig. 5 (a) Typical plot of field emission current density versus electric field (J-E) of the layered Bi_2Se_3 nanosheets. Inset is the corresponding Fowler-Nordheim (FN) plot. (b) The field emission current stability of the layered Bi_2Se_3 nanosheets over time, inset is an electron emission fluorescence image for the layered Bi_2Se_3 nanosheets emitter (a phosphor coated ITO glass was used as the anode in this case).

The electron-field-emission measurement of the layered Bi_2Se_3 nanosheets was carried out in a vacuum chamber with a base pressure lower than 1×10^{-5} Pa at room temperature. In this case, the Bi_2Se_3 nanosheets were spin-coated on pre-cleaned n-type silicon (9.0×10^{-3} Ω·cm) from the dispersion solution (see **Figure S1(d)**). Therefore, the Bi_2Se_3/Si was employed as the cathode and an ITO glass was used as the anode for this measurement. A typical plot of field emission current density versus electric field (J-E) curve at a vacuum gap of ~220 μm is shown in **Figure 5(a)**. As compared in **Table 1**, the turn-on field (E_{to}) of the layered Bi_2Se_3 on flat Si (defined as the emission current density reach 10 μA/cm²) is about 2.3 V/μm, which is smaller than those of layered MoS_2 sheets and is comparable to that of single-layer graphene films[11, 17]. The obtained J-E curve could be further analyzed by Fowler-Nordheim (FN) theory, which can be expressed by the following equation:

$$J = A(\beta^2 E_0^2/\phi)\exp(-B\phi^{3/2}/\beta E_0) \quad (1)$$

Where J is field emission current density, E_0 is the mean field between the cathode and anode, β is the field enhancement factor, ϕ is the work function, A and B are constants ($A = 1.54\times10^{-6}$ A•eV•V^{-2}, $B = 6.83\times10^3$ V•eV$^{-3/2}$•μm^{-1}). The inset of **Figure 5(a)** shows the corresponding FN plot ($\ln(I/E_0^2)$ vs $1/E_0$), which shows approximately a linear relationship with a slope m = -10.1. Since the work function of layered Bi_2Se_3 could be deduced from the UPS results as 4.7 eV, the field enhanced factor β can be calculated as 6860 ($\beta = (-6.8\times10^3)\phi^{3/2}/m$), which is larger than those of single-layer graphene films and layered MoS_2 sheets, as shown in **Table 1**. The emission stability test was performed at a preset value of ~0.13 mA/cm² and the recording interval was 1 s. As shown in **Figure 5(b)**, no obvious emission degradation is observed for over 3600 s and the emission fluctuation is about ~15%. The inset of **Figure 5(b)** illustrates the corresponding electron emission fluorescence image. In the meantime, we also fabricated a flexible field emitter simply by drop casting the layered Bi_2Se_3 dispersion onto carbon cloth (see **Figure S4-S7**), which has a low turn-on field of 2.3 V/μm, a field enhanced factor of 3207, a large field emission current closing to 6 mA/cm² and good emission stability (see **Figure S6**).

In order to investigate the origin of the efficient field emission behaviours of layered Bi_2Se_3 nanosheets, we further proposed a field emission model based on a finite element method with ANSYS v14 software and Comsol 4.3 software [27]. There are two very important issues in the model of layered Bi_2Se_3 field emission: 1). the electrical field distribution on the layered Bi_2Se_3 in field emission. 2). the shape dependence of layered Bi_2Se_3.

First, we simulated the electrical field intensity distributed on a regular circular layered Bi_2Se_3 with a positive voltage of 1000 V applied to the anode (see **Figure S8**). Based on these parameters, especially the permittivity of the involved materials (see **Table S1** in the SI), the edge effect is clearly proved in **Figure 6(a)** with maximum intensity 6.3 V/μm. This also shows edge effect is the key point to field emission of layered

Table 1. Comparison between the performances of relevant field emitters and the layered Bi_2Se_3 nanosheets in this work.

	Turn-on filed (V/μm)	Field enhancement factor (β)	Reference
Single-layer graphene films	2.3 (@10 μA/cm²)	3700	[11]
Layered MoS_2 sheets	3.5 (@10 μA/cm²)	1138	[17]
Layered Bi_2Se_3 on flat Si	2.3 (@10 μA/cm²)	6860	This work
Layered Bi_2Se_3 on flexible carbon cloth	2.3 (@10 μA/cm²)	3207	This work

structural materials. Therefore, could we make more edges to strengthen the effect? We further investigated the irregular shape with more edges, and compared it with regular shape (circular disc). **Figure 6 (b) and (c)** compare the electrical field distributions for two cases. Obviously, irregular shape shows a much more obvious intense edge effect. This probably provides a way to enhance the field emission for layered materials, because unlike bulk material using in field emission having a tip in z direction, layered materials show a plane on the top, meaning that it is very difficult to improve field emission through making a tip toward z direction. In terms of the inspiration from **Figure 6 (b) and (c)**, the field emission in layered material can be tuned via making edges in the crosswise dimension (x, y direction), which is accordance with the experimental results since the solution processed layered Bi_2Se_3 nanosheets have complicated irregular shapes (see **Figure 1-3**). Besides, we also simulated the protrusion decorated structure in **Figure 6**(d), which shows further field enhancements over the sharp edge structures (see **Figure 6**(c)). The above simulation results reveal that the efficient field emission properties of layered Bi_2Se_3 nanosheets fabricated in this work is not only related to its possible 2DEG in the surface and lower work function but also attributed to their abundant sharp edges or protrusion decorated structure.

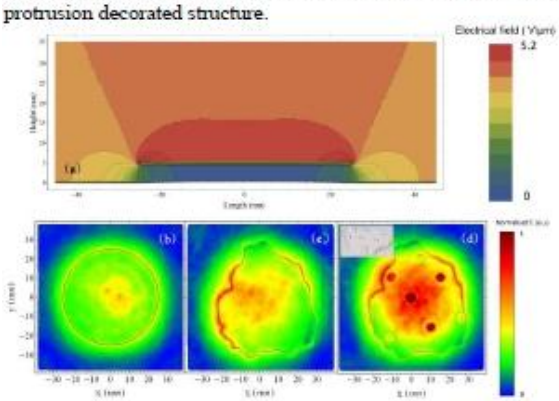

Fig. 6 (a) Sectional drawing of electrical field distribution on Bi_2Se_3 layer (5nm thickness, 50nm diameter); (b-d) Electrical field distributions for layered Bi_2Se_3 with regular shape (b), irregular shape (c) and protrusion decorated structure (d).

3. Experimental

Layered Bi_2Se_3 nanosheets synthesis: Layered Bi_2Se_3 nanosheets were prepared from bulk Bi_2Se_3 crystals by a three-step exfoliation method. Firstly, bulk Bi_2Se_3 crystals (Alfa Aesar) were ground into Bi_2Se_3 powders using an agate mortar (from **Figure S1**(a) to (b)). Then, the Bi_2Se_3 powders were turned into Bi_2Se_3 nanosheet clusters (from **Figure S1**(b) to (c)) by a hydrothermal intercalation and exfoliation method [28] as follows: Bi_2Se_3 powders were placed into a sealed Teflon-lined autoclave with an ethylene glycol solution of lithium hydroxide (8 M). After the autoclave was oven-heated at 200°C for 24 h, Bi_2Se_3 nanosheet clusters were obtained by centrifugation and rinsed with acetone and deionized water to eliminate the residual lithium hydroxide. At last, to get an uniform dispersion of layered Bi_2Se_3 nanosheets, the as-prepared Bi_2Se_3 nanosheet clusters were dried and immediately suspended in isopropanol and sonicated for 30 min to achieve final exfoliation (from **Figure S1** (c) to(d)).

Layered Bi_2Se_3 nanosheets characterization: The morphologies were characterized by a Sirion field emission scanning electron microscopy (SEM: Philips XL30). Transmission electron microscope (TEM) techniques, including the selected area electron diffraction (SAED), were performed using a JEM-2010 electron microscope. Atomic Force Microscope (AFM) measurements were carried out in a SPM-9500J3 system. Raman spectra were obtained by a Horiba-Jobin-Yvon LabRaman HR confocal microscope using 488 nm laser excitation at room temperature. X-Ray photoelectron spectroscopy (XPS) and Ultraviolet photoelectron spectroscopy (UPS) studies were conducted with a Thermo ESCALAB 250xi instrument.

Field emission measurement: Field emission measurements were performed with a two-parallel-plate configuration (Bi_2Se_3/Si as cathode and a phosphor coated ITO glass as anode) in a vacuum chamber with base pressure lower than 2.0×10^{-5} Pa. The cathode and the anode were separated by a 220 μm thick Teflon spacer, and the cathode area is 0.04 cm^2. The current-voltage (I-V) characteristics were measured by a Keithley 6485 picoammeter and a Keithley 248 high voltage supply.

Conclusions

In summary, layered Bi_2Se_3 nanosheets were prepared from Bi_2Se_3 crystals with a three-step exfoliation method. Field emission with a low turn-on field of 2.3 V/μm, a high field enhancement factor of 6860 and good field emission stability was observed from the layered Bi_2Se_3 nanosheets. We further proposed a field emission model to investigate the origin of its efficient field emission behaviours, which found that the irregular shapes of exfoliated layered Bi_2Se_3 nanosheets play a key role in the edge effect that resulting in its efficient field emission. This work suggests that layered Bi_2Se_3 nanosheets with atomic-thick sharp edges have a great potential as high-performance vertical structure field emitters for future light weight and highly flexible electron source such as vacuum electronic device applications.

Acknowledgements

This work was supported by the 973 Program (2011CB933300) of China, the National Natural Science Foundation of China (61376013, 11074194, J1210061). Authors would like to thank Dr. Wei Zeng for his help in coding the program of ANSYS.

Notes and references

[a] Key Lab of Artificial Micro- and Nano-Structures of Ministry of Education of China, Department of Electronic Science & Technology, School of Physics and Technology, Wuhan University, Wuhan 430072 (P. . China), E-mail: gjfang@whu.edu.cn

[b] College of Optoelectronic Engineering, Shenzhen University, Shenzhen 518060(P. R. China), E-mail: hzhang@szu.edu.cn

[c] Center for Nanotechnology and Molecular Materials, Department of Physics, Wake Forest University, Winston-Salem, NC 27109 (U. S.), E-mail: carroldl@wfu.edu

[△] These authors contributed equally to this work.

Electronic Supplementary Information (ESI) available: [details of any supplementary information available should be included here]. See DOI: 10.1039/b000000x/

1 W. B. Choi, D. S. Chung, J. H. Kang, H. Y. Kim, Y. W. Jin, I. T. Han, Y. H. Lee, J. E. Jung, N. S. Lee, G. S. Park and J. M. Kim, *Applied Physics Letters*, 1999, **75**, 3129.

2 K. L. Jensen, *Physics of Plasmas*, 1999, **6**, 2241.

3 C. Hernandez-Garcia, M. L. Stutzman and P. G. O'Shea, *Physics Today*, 2008, **61**, 44.

4 N. S. Xu and S. E. Huq, *Materials Science and Engineering: R: Reports*, 2005, **48**, 47.

5 W. A. de Heer, A. Châtelain and D. Ugarte, *Science*, 1995, **270**, 1179.

6 Y. K. Tseng, C. J. Huang, H. M. Cheng, I. N. Lin, K. S. Liu and I. C. Chen, *Advanced Functional Materials*, 2003, **13**, 811.

7 C. J. Lee, T. J. Lee, S. C. Lyu, Y. Zhang, H. Ruh and H. J. Lee, *Applied Physics Letters*, 2002, **81**, 3648.

8 X. Fang, Y. Bando, U. K. Gautam, C. Ye, D. Golberg and *J Mater Chem*, 2008, **18**, 509.

9 C. Li, G. Fang, N. Liu, J. Li, L. Liao, F. Su, G. Li, X. Wu and X. Zhao, *The Journal of Physical Chemistry C*, 2007, **111**, 12566.

10 S. Fan, M. G. Chapline, N. R. Franklin, T. W. Tombler, A. M. Cassell and H. Dai, *Science*, 1999, **283**, 512.

11 Z. S. Wu, S. Pei, W. Ren, D. Tang, L. Gao, B. Liu, F. Li, C. Liu and H.M. Cheng, *Advanced Materials*, 2009, **21**, 1756.

12 Z. Yang, Q. Zhao, Y. Ou, W. Wang, H. Li and D. Yu, *Applied Physics Letters*, 2012, **101**, 173107.

13 A. Malesevic, R. Kemps, A. Vanhulsel, M. P. Chowdhury, A. Volodin and C. Van Haesendonck, *Journal of Applied Physics*, 2008, **104**, 084301.

14 M. Qian, T. Feng, H. Ding, L. Lin, H. Li, Y. Chen and Z. Sun, *Nanotechnology*, 2009, **20**, 425702.

15 C. K. Huang, Y. Ou, Y. Bie, Q. Zhao and D. Yu, *Applied Physics Letters*, 2011, **98**, 263104.

16 V. P. Verma, S. Das, I. Lahiri and W. Choi, *Applied Physics Letters*, 2010, **96**, 203108.

17 R. V. Kashid, D. J. Late, S. S. Chou, Y. K. Huang, M. De, D. S. Joag, M. A. More and V. P. Dravid, *Small*, 2013, **16**, 2730.

18 H. Zhang, C.X. Liu, X.L. Qi, X. Dai, Z. Fang and S.C. Zhang, *Nat Phys*, 2009, **5**, 438.

19 Y. Xia, D. Qian, D. Hsieh, L. Wray, A. Pal, H. Lin, A. Bansil, D. Grauer, Y. S. Hor, R. J. Cava and M. Z. Hasan, *Nat Phys*, 2009, **5**, 398.

20 Y. Zhang, K. He, C.Z. Chang, C.L. Song, L.L. Wang, X. Chen, J.F. Jia, Z. Fang, X. Dai, W.Y. Shan, S.Q. Shen, Q. Niu, X. L. Qi, S.C. Zhang, X. C. Ma and Q.K. Xue, *Nat Phys*, 2010, **6**, 584.

21 H. Peng, W. Dang, J. Cao, Y. Chen, D. Wu, W. Zheng, H. Li, Z. X. Shen and Z. Liu, *Nat Chem*, 2012, **4**, 281.

22 H. Peng, K. Lai, D. Kong, S. Meister, Y. Chen, X. L. Qi, S. C. Zhang, Z.-X. Shen and Y. Cui, *Nat Mater*, 2010, **9**, 225.

23 J. S. Son, M. K. Choi, M. K. Han, K. Park, J. Y. Kim, S. J. Lim, M. Oh, Y. Kuk, C. Park, S. J. Kim and T. Hyeon, *Nano lett*, 2012, **12**, 640.

24 W. Dang, H. Peng, H. Li, P. Wang and Z. Liu, *Nano Lett*, 2010, **10**, 2870.

25 W. Richter and C. R. Becker, *physica status solidi (b)*, 1977, **84**, 619.

26 J. Zhang, Z. Peng, A. Soni, Y. Zhao, Y. Xiong, B. Peng, J. Wang, M. S. Dresselhaus and Q. Xiong, *Nano Lett*, 2011, **11**, 2407.

27 N. S. Liu, G. J. Fang, W. Zeng, H. Zhou, H. Long and X. Z. Zhao, *Journal of Materials Chemistry*, 2012, **22**, 3478.

28 L. Ren, X. Qi, Y. Liu, G. Hao, Z. Huang, X. Zou, L. Yang, J. Li and J. Zhong, *J Mater Chem*, 2012, **22**, 4921.

Curriculum Vitae
Qi Li

Ph.D. candidate of Physics
1834 Wake Forest Rd., NC 27109
Tel: (336) 758-3372 Fax: (336)758-6142
Email: liq9@wfu.edu

Education

2009	B.S., Physics, Special Class for Gifted Young, University of Science and Technology of China
2014	Ph.D., Wake Forest University

Selected Honors

2011	Member, Sigma Pi Sigma Honorary Society
2011	Lawrence Livermore National Laboratory Computational Chemistry and Materials Science Summer Institute
2012	ICDIM Young Researcher Award, Santa Fe

Invited Talks

2014	SPIE Conference on Hard-Ray, Gamma-Ray, and Neurtron Detector Physics XVI

Selected Publications

R. T. Williams, Qi Li, J. Q. Grim, K. B. Ucer, G. A. Bizarri, and W. W. Moses, "Role of carrier diffusion and picosecond exciton kinetics in nonproportionality of scintillator light yield," Proc. SPIE **7805**, 78050K (2010).

R. T. Williams, Qi Li, J. Q. Grim, and K. B. Ucer, "Dependence of nonproportionality in scintillators on diffusion of excitons and charge carriers," Proc. SPIE **8142**, 81420Y (2011).

Qi Li, J. Q. Grim, R. T. Williams, G. A. Bizarri, and W. W. Moses, "The Role of Hole Mobility in Scintillator Proportionality," Nuc. Inst. Meth. Phys. Res. A **652**, 288 (2011).

J. Q. Grim, Qi Li, K. B. Ucer, R. T. Williams, and W. W. Moses, "Experiments on high excitation density, quenching, and radiative kinetics in CsI:Tl scintillator," Nuc. Inst. Meth. Phys. Res. A **652**, 284 (2011).

R. T. Williams, J. Q. Grim, Qi Li, K. B. Ucer, and W. W. Moses, "Excitation density, diffusion-drift, and proportionality in scintillators," **Feature Article**, Phys. Status Solidi B **248**, 426 (2011).

Qi Li, J. Q. Grim, R. T. Williams, G. A. Bizarri, and W. W. Moses, "Material parameter basis for major and minor trends in nonproportionality of scintillators," MRS Proc. **1341**, mrss11-1314-u04-05 (2011).

J. Q. Grim, Qi Li, K. B. Ucer, R. T. Williams, A. Burger, P. Bhattacharya, E. Tupitsyn, G. A. Bizarri, and W. W. Moses, "Nonlinear quenching rates in SrI_2 and CsI scintillator hosts," MRS Proc. **1341**, mrss11-1314-u08-02 (2011).

Qi Li, J. Q. Grim, R. T. Williams, G. A. Bizarri, and W. W. Moses, "A transport-based model of material trends in nonproportionality of scintillators," J. Appl. Phys. **109**, 123716-1-17 (2011).

Qi Li, B. Kolb, G. Román-Pérez, J. M. Soler, F. Yndurain, L. Kong, D. C. Langreth, and T. Thonhauser, "Ab initio energetics and kinetics study of H_2 and CH_4 in the SI clathrate hydrate," Phys. Rev. B **84**, 153103 (2011).

Y. Li, M. Wang, H. Huang, W. Nie, Qi Li, E. D. Peterson, R. Coffin, G. Fang, and D. L. Carroll, "Influence on open-circuit voltage by optical heterogeneity in three-dimensional organic photovoltaics," Phys. Rev. B **84**, 085206 (2011).

Qi Li and T. Thonhauser, "A theoretical study of the hydrogen-storage potential of H4M in metal organic framework materials and carbon nanotubes," J. Phys.: Cond. Matt. **24**, 424204 (2012).

W. W. Moses, G. A. Bizarri, R. T. Williams, S. A. Payne, A. N. Vasil'ev, J. Singh, Qi Li, J. Q. Grim, and W. Choong, "The origins of scintillator non-proportionality," IEEE Trans. on Nucl. Sci. **59**, 2038 (2012).

J. Q. Grim, Qi Li, K. B. Ucer, R.T. Williams and W. W. Moses, "The roles of thermalized and hot carrier diffusion in determining light yield and proportionality of scintillators," Phys. Status Solidi A **209**, 2421 (2012).

J. Q. Grim, Qi Li, K.B. Ucer, R. T. Williams, G. A. Bizarri and W.W. Moses, "Electron energy response of NaI: Tl and SrI2: Eu calculated from carrier mobilities and measured first-and third-order quenching," MRS Communications **2**, 139 (2012).

Qi Li, J. Q. Grim, K. B. Ucer, A. Burger, G. A. Bizarri, W. W. Moses, and R. T. Williams, "Host structure dependence of light yield and proportionality in scintillators in terms of hot and thermalized carrier transport," **Front Cover**, Phys. Status Solidi RRL **6**, 346 (2012).

Qi Li, R. T. Williams, and D. Åberg, "First principles calculations and experiment predictions for iodine vacancy centers in SrI2," **Editor's Choice**, Phys. Status Solidi B **250**, 233 (2013).

W. Huang, Y. Li, Qi Li, H. Huang, Y. Chen, Y. Xia, C. Dun, and D. L. Carroll, "Surface Modification Enabled Carrier Mobility Adjustment in CZTS Nanoparticle Thin Films," SOL ENERG MAT SOL C, manuscript accepted (2013).

R. T. Williams, J. Q. Grim, Qi Li, K. B. Ucer, G. A. Bizarri, S. Kerisit, F. Gao, P. Bhattacharya, E. Tupitsyn, E. Rowe, V. M. Buliga, and A. Burger, "Experimental and computational results on exciton/free-carrier ratio, hot/thermalized carrier diffusion, and linear/nonlinear rate constants affecting scintillator proportionality," Proc. SPIE **8852**, 88520J (2013).

H. Huang, Y. Li, Qi Li and G. Fang, "Field electron emission of layered Bi_2Se_3 topological insulator," Nanoscales, manuscript accepted (2014).

Qi Li et al., “First principles calculations on F center, Sr-F_A center, and Ce centers in $LaBr_3$ scintillators,” manuscript in preparation (2014).
Qi Li et al., “Modeling hot-electron thermalization in scintillators with exact parameters from first principles calculations,” manuscript in preparation (2014).
Qi Li et al. “First principle calculations on solid solution alkali halide scintillator materials,” manuscript in preparation (2014).
Qi Li et al. “First principle calculations on GGAG:Ce and GYGAG:Ce ceramic scintillators,” manuscript in preparation (2014).